An observational perspective into the nature of short-plateau Type II supernovae

A Thesis
Submitted for the Degree of

Doctor of Philosophy

in

The Department of Physics,
Pondicherry University,
Puducherry - 605 014, India

by

Rishabh Singh Teja

Indian Institute of Astrophysics,
Bengaluru - 560 034, India

October 2024

An observational perspective into the nature of short-plateau Type II supernovae

Rishabh Singh Teja
Indian Institute of Astrophysics

Indian Institute of Astrophysics
Bengaluru - 560 034, India

Thesis title	:	**An observational perspective into the nature of short-plateau Type II supernovae**

Author	:	**Rishabh Singh Teja**
Address	:	Indian Institute of Astrophysics II Block, Koramangala Bengaluru - 560 034, India
Email	:	rishabh.teja@iiap.res.in; rsteja001@gmail.com
Supervisor	:	**Prof. D. K. Sahu**
Address	:	Indian Institute of Astrophysics II Block, Koramangala Bengaluru - 560 034, India
Email	:	dks@iiap.res.in
Co-supervisor	:	**Prof. G. C. Anupama** *(INSA Senior Scientist)*
Address	:	Indian Institute of Astrophysics II Block, Koramangala Bengaluru - 560 034, India
Email	:	gca@iiap.res.in

Declaration of Authorship

I hereby declare that the research contained in this thesis is the result of the investigations carried out by me at the Indian Institute of Astrophysics, Bengaluru, under the supervision of **Prof. D. K. Sahu**. This work has not been submitted for awarding a degree or any other qualification either in this university or any other institution.

Rishabh Singh Teja
Ph.D Student, IIA,
Bengaluru-560034, India

Signed: Rishabh Singh

Date: 16 - October - 2024

Certificate

This is to certify that the thesis titled **"An observational perspective into the nature of short-plateau Type II supernovae"** submitted to the Pondicherry University by Mr. Rishabh Singh Teja for the award of the degree of Doctor of Philosophy, is based on the results of the investigations carried out by him under my supervision and guidance, at the Indian Institute of Astrophysics. This thesis has not been submitted to any other university or institute for the award of any degree, diploma, fellowship, etc.

Prof. D. K. Sahu
Thesis Supervisor,
Indian Institute of Astrophysics,
Bengaluru-560034, India

Signed: ______________________

Date: 16-10-2024.

List of Publications

A). Publications included in this thesis

1. **SN 2020jfo: A Short-plateau Type II Supernova from a Low-mass Progenitor** ; **Rishabh Singh Teja**, Avinash Singh, D. K. Sahu, G. C. Anupama, Brajesh Kumar, & Nayana A. J. *The Astrophysical Journal, Volume 930, Issue 1, id.34, 19 pp.* doi:10.3847/1538-4357/ac610b

2. **Far-ultraviolet to Near-infrared Observations of SN 2023ixf: A High-energy Explosion Engulfed in Complex Circumstellar Material** ; **Rishabh Singh Teja**, Avinash Singh , Judhajeet Basu, G. C. Anupama, D. K. Sahu, Anirban Dutta, Vishwajeet Swain, Tatsuya Nakaoka, Utkarsh Pathak, Varun Bhalerao, Sudhanshu Barway, Harsh Kumar, Nayana A. J., Ryo Imazawa, Brajesh Kumar, & Koji S. Kawabata *The Astrophysical Journal Letters, Volume 954, Issue 1, id.L12, 10 pp.* doi:10.3847/2041-8213/acef20

3. **SN 2018gj: A Short Plateau Type II Supernova with Persistent Blueshifted Ha Emission**; **Rishabh Singh Teja,**, Avinash Singh, D. K. Sahu, G. C. Anupama, Brajesh Kumar, Tatsuya Nakaoka, Koji S. Kawabata, Masayuki Yamanaka, Ali Takey, & Miho Kawabata *The Astrophysical Journal, Volume 954, Issue 2, id.155, 23 pp.* doi: 10.3847/1538-4357/acdf5e

4. **SN 2021wvw: A core-collapse supernova on the sub-luminous, slower and shorter end of Type IIPs**; **Rishabh Singh Teja**, Jared A. Goldberg, D. K. Sahu, G. C. Anupama, Avinash Singh, Vishwajeet Swain, & Varun Bhalerao *The Astrophysical Journal, Volume 974, Issue 1, id.44, 14 pp.* doi: 10.3847/1538-4357/ad67d9

5. **Unravelling the asphericities in the explosion and multi-faceted circumstellar matter of SN 2023ixf**; Avinash Singh, **Rishabh Singh Teja**, T.J. Moriya, K. Maeda, K.S. Kawabata, M. Tanaka, R. Imazawa, T. Nakaoka, A. Gangopadhyay, M. Yamanaka, V. Swain, D.K. Sahu, G.C. Anupama, B. Kumar, R.M. Anche, Y. Sano, A. Raj, V. K. Agnihotri, V.

Bhalerao, D. Bisht, M. S. Bisht, K. Belwal, S. K. Chakrabarti, M. Fujii, T. Nagayama, K. Matsumoto, T. Hamada, M. Kawabata, A. Kumar, R. Kumar, B.K. Malkan, P. Smith, Y. Sakagami, K. Taguchi, N. Tominaga, & A. Watanabe *The Astrophysical Journal [Accepted Sept 2024]* arXiv:2405.20989

B). Conference Proceedings

1. **Observations and modelling of two Type IIP supernovae in M61: Similar yet so different.**; **Rishabh Singh Teja**, G. C. Anupama & D. K. Sahu *Massive Stars Near and Far, Edited by J. Mackey, J.S. Vink and N. St-Louis. Proceedings of the International Astronomical Union, Volume 361, held 8-13 May 2022 in Ballyconnell, Ireland. Cambridge University Press, 2024, pp. 610-611* doi:10.1017/S1743921322002034

D). Other contributed publications [Not part of this thesis]

1. **SN 2020udy: A New Piece of the Homogeneous Bright Group in the Diverse Iax Subclass** ; Mridweeka Singh et al. [including **Rishabh Singh Teja**] *The Astrophysical Journal, Volume 965, Issue 1, id.73, 14 pp.* doi:10.3847/1538-4357/ad2618
2. **Intermediate-luminosity Type IIP SN 2021gmj: a low-energy explosion with signatures of circumstellar material** ; Yuta Murai, Masaomi Tanaka, Miho Kawabata, Kenta Taguchi, **Rishabh Singh Teja** ... *Monthly Notices of the Royal Astronomical Society, Volume 528, Issue 3, pp.4209-4227* doi:10.1093/mnras/stae170
3. **The enigmatic double-peaked stripped-envelope SN 2023aew** ; Tuomas Kangas et al. [including **Rishabh Singh Teja**] *Accepted to A&A* doi:10.48550/arXiv.2401.17423
4. **Characterizing the Ordinary Broad-line Type Ic SN 2023pel from the Energetic GRB 230812B** ; Gokul P. Srinivasaragavan et al. [including **Rishabh Singh Teja**] *The Astrophysical Journal Letters, Volume 960, Issue 2, id.L18, 15 pp.* doi:10.3847/2041-8213/ad16e7

5. **Bridging between Type IIb and Ib Supernovae: SN IIb 2022crv with a Very Thin Hydrogen Envelope** ; Anjasha Gangopadhyay et al. [including **Rishabh Singh Teja**] *The Astrophysical Journal, Volume 957, Issue 2, id.100, 21 pp.* doi:10.3847/1538-4357/acfa94

6. **Observational Properties of a Bright Type lax SN 2018cni and a Faint Type Iax SN 2020kyg**; Mridweeka Singh et al. [including **Rishabh Singh Teja**] *The Astrophysical Journal, Volume 953, Issue 1, id.93, 14 pp.* doi:10.3847/1538-4357/acd559

7. **The unluckiest star: A spectroscopically confirmed repeated partial tidal disruption event AT 2022dbl** Zheyu Lin et al. [including **Rishabh Singh Teja**] *Accepted to The Astrophysical Journal Letters* arXiv:2405.10895

List of other non-refereed publications such as Astronomer's Telegram (ATEL), Classification Reports (TNS), and GCNs can be found in this ADS public library https://ui.adsabs.harvard.edu/user/libraries/USpFMoICSZyKqnMCcL2boA

Conferences

1. **Participant** in *Modern Engineering Trends in Astronomy (META)* conference jointly organized by the National Centre for Radio Astrophysics of TIFR, Raman Research Institutes and the Indian Institute of Astrophysics (IIA) at *IIA Bengaluru* in *September 2019*
2. **Participant** in *39th Meeting of Astronomical Society of India (ASI)* organized virtually in *February 2021*
3. **Participant** in *SuperVirtual-2022* conference organized virtually in *November 2021*
4. **Poster** presented on " ***Observational studies of a short plateau Type IIP supernova 2020jfo***", in the *40th Astronomical Society of India* meeting, organized by *ARIES and IIT Roorkee* at *IIT Roorkee* in March 2022.
5. **Poster** presented on "***Observations and modelling of two Type IIP supernovae in M61***" in *IAU Symposium 361: Massive Stars Near and Far* organized at *Ballyconnell, Ireland* in *May 2022*
6. **Participant** in *META-2022* conference held at *IIA Bengaluru* in *September 2022*
7. **Poster** presented on "***Origins of a short plateau type II supernova, SN 2020jfo: Low mass RSG or binary?***" in *SuperVirtual-2022* conference organised virtually in *November 2022*
8. **Contributed talk** given on "***Panchromatic observations and modelling of two Type II supernovae in M61: Similar origins yet different fates***" in *Young Astronomers' Meet-2022* organised by *ARIES, Nainital* in *November 2022*
9. **Contributed talk** given on "***Understanding Type IIP progenitors with emphasis on short plateau SNe***" in *India/Japan internal collaboration meeting on transients and supernovae* held organised by *Hiroshima Astrophysical Science Center* at the *Higashi-Hiroshima campus in Hiroshima University* in *March 2023*

10. **Contributed talk** given on "***Low mass red supergiants as the plausible origins of Type II supernovae with short plateau***" in *SuperVirtual-2023* conference organised virtually in *November 2023*

11. **Contributed talk** given on "***Nearest supernova in decade 2023ixf: Rapid multi-wavelength follow-up & analysis using space and ground-based facilities***" in *National Space & Science Symposium-2024* organised at *Goa University, Goa* in *Feburary 2024*

12. **Invited talk** given on "***Decadal SN 2023ixf in FUV to NIR: A High-energy Explosion Engulfed in Complex CSM; Early days and beyond***" in *SN 2023ixf, The Decadal Supernova in M101* workshop jointly organized by Weizmann Institute of Science, Israel and ESO, Garching at *ESO in Garching, Germany* in *June 2024*

Schools

1. **Participant** in *SOKENDAI Asia Winter School 2021* held virtually in *February 2021*

2. **Participant** in *ZTF Summer School 2021* held virtually in *August 2021*

3. **Participant** in *ZTF Summer School 2022* held virtually in *July 2022*

Acknowledgements

My journey in IIA, from joining as a research scholar to writing this thesis, has been a joyous ride that I have thoroughly enjoyed. It could not have been possible without the tremendous support of people from all spheres of life, be it my family, friends, supervisors, and others. Everyone has contributed in their own way, whether knowingly or unknowingly! And I would not miss this great opportunity to show my heartfelt gratitude to them. ❑

First and foremost, I am highly indebted to my supervisor *Prof. Devendra Sahu* for his wholehearted support and continuous guidance during this period. He has acted more like a collaborator with an amiable approach, always a call away for discussions or queries, even during off hours. All our mutual agreements, disagreements, and 'occasional' arguments have only led to the betterment of this work. I am forever grateful for his insights into various complex topics related to astrophysics and instrumentation, especially our discussions during scheduled observation nights at CREST. ❑

I am sincerely grateful to my co-supervisor *Prof. G. C. Anupama*, for whom I have great admiration and respect. It wouldn't be hyperbole to say that she had inspired me to take up Astronomy (although indirectly), especially the Time Domain Astronomy. This work would not have seen the light of day hadn't she put in effort, management, motivation, and great discussions. Spearheading the SN group for decades, she has been a key contributor to this work and ensured the accomplishment of goals with time. Her insights into the work and openness to try new things and go beyond the standard have greatly improved this work.❑

Completing this work has been a collective effort based on the contributions of many individuals. First, I thank *Dr. Avinash Singh* for being supportive as a collaborator and, of course, as an excellent personal and professional friend. I also thank *Dr. Anirban Dutta*, with whom I got the opportunity to go for observations on countless occasions. I learned a lot from him during his tenure. I am also grateful to *Dr. Jared Goldberg* as a friend and collaborator. I sincerely thank my collaborators from Japan: *Prof. Koji S. Kawabata, Dr. Tatsuya Nakaoka, Dr. Masayuki Yamanaka, Dr. Takashi J. Moriya, Prof. Masaomi Tanaka, Yuta Murai,* and *Dr. Anjasha Gangpadhyay* for their invaluable insights and contributions to my research and their excellent hospitality during my visit to Japan in 2023. I also acknowledge and appreciate regular discussions and feedback from our SN group, including *Dr. Brajesh Kumar, Dr. Avinash Singh, Dr. Anirban Dutta, Dr. Mridweeka Singh,* and *Dr. Nayana AJ.* For this work, I am also grateful to my collaborators from India: *Prof. Varun Bhalerao, Dr. Harsh Kumar, Vishwajeet Swain* (from IIT-B), and *Judhajeet Basu* and *Dr. Sudhanshu Barway* (from IIA). ❑

I thank my Doctoral Committee members, *Prof. S.V.M.Satyanarayana* (deceased), *Prof. T. Sivarani*, and *Prof. Alok Sharan*, for their insights and guidance in keeping this work's timeline in check. I also thank IIA for this beautiful opportunity and constant support throughout, especially the Director, Dean, BGS chair *Prof. Maheshwar G.*, and BGS office especially *Mr. K Sankara*, who always made sure that things were streamlined and went smoothly. ❑

I am forever grateful to *Dr. Priya Goyal* for her wholehearted support throughout this journey. She has been a great motivator and inspiration at personal and professional levels. ❑

Many thanks to the staff at the *Bhaskara* who made the living comfortable during this half-decade. I further thank my colleagues, batchmates, seniors and juniors for making this journey a very pleasant one by indulging in many festivals, events, trips, treks, gossips, etc. namely my seniors *Avinash, Sandeep, Samrat, Raghu, Priya, Deepak, Partha, Chayan, DVS Phanindra,* and *Swastik*; my batchmates

Anohita, Pallavi, Sambit, Ravi, Dhanush, and *Aratrika*; and my juniors (again in no particular order) *Neeraj, Judhajeet, Sipra, Shubham G., Saili, Rupesh, Nitish, Ajay, Rakshit, Shubham J., Khushbu, Pravash, Manjunath, Saurabh, Shashank, Shatakshi, Reena, Hrishav,* and *Sunit*. I also like to thank my friends and colleagues *Harsh* and *Kshitij* for some wonderful memories. ❑

My heartfelt gratitude to the amazing team of IIA students' e-Magazine *DOOT* for the wonderful opportunity to contribute towards science outreach. I thoroughly enjoyed working with the *DOOT* team for over four years in many different roles, with the most memorable one being the *DOOT's 'Chief Editor'* (2023-2024). ❑

I also thank my dear friends-cum-brothers, *Vikrant, Vaibhav, Kapil, Gaurav, Harshit, Atul, Deepak, Ajay, Ashwani, Sukhdeep* and *Devashish*, who have been a great support (non-academic!) throughout this past decade and continue to do so. ❑

I can not thank my parents enough, *Smt. Usha Devi* and *Mr. Vijendra Singh*, for everything bestowed upon me in this life. Special thanks to my elder sisters, *Mrs. Reshu Devi*, *Mrs. Deepti*, and *Mrs. Shubhi* for their immense love and care. Lastly, I apologize for the many names I might have missed that mattered at some point. Remember that you matter if you come across this and feel the same. ❑

– Rishabh Singh Teja

★❤

Software usage

Data Reduction: Throughout this work, various data reduction softwares have been used extensively. These are utilized to reduce data covering ultraviolet to infrared bands and are as follows: `IRAF` (Tody 1993), `PyRAF`, `HEASoft` (Nasa High Energy Astrophysics Science Archive Research Center (Heasarc) 2014), `ds9` (Smithsonian Astrophysical Observatory 2000), `CCDLAB` (Postma & Leahy 2017), `UVOTPY` (Kuin 2014).

Light Curve & Spectra Modeling: This work also utilizes 1-D stellar evolution software `MESA` (r-15140) (Paxton et al. 2011, 2013, 2015, 2018, 2019) , multi-group radiation-hydrodyanmics software `STELLA` (Blinnikov & Sorokina 2004; Baklanov et al. 2005; Blinnikov et al. 2006), and synthetic spectral generation software `SYNAPPS` (Thomas et al. 2011).

Analysis: For most of the analysis and figures presented in this thesis, various *Python* libraries have been used. Some of the key packages are: *astropy* (Astropy Collaboration et al. 2013, 2018, 2022), *emcee* (Foreman-Mackey et al. 2013), *Jupyter-notebook* (Kluyver et al. 2016), *matplotlib* (Hunter 2007), *numpy* (Harris et al. 2020), *pandas* (Wes McKinney 2010; pandas development team 2020), *scipy* (Virtanen et al. 2020), *seaborn* (Waskom 2021)

Others: Various resources available online such as ADS, WISeREP (Yaron & Gal-Yam 2012), Open Supernova Catalog (Guillochon et al. 2017), ALeRCE (Sánchez-Sáez et al. 2021), ATLAS (Tonry et al. 2018a), and SVO FPS (Rodrigo & Solano 2020) have also been utilized. Related data files (photometry, spectroscopy, models) are available online. *Other data/scripts/jupyter-notebooks used in this work are made available on my personal website: astronomoid.github.io and Github account github.com/Astronomoid*

To my dear mother, father

&

sisters.

(Because of ‘em, I am.)

Abstract

Supernovae (SNe, *singular* SN), the endpoints of stellar evolution, have fascinated humans since time immemorial, with recorded evidence dating back to two millennia. Continuing this quest, modern astronomy and astrophysics have come far in understanding these events and not mere recording for bookkeeping purposes. Astronomers are widely using these violent cosmic deaths in many domains of astronomy. Some common themes are to study galactic chemical evolution, measure cosmological distances independent of other measurements, study natal kicks to compact objects, e.g., white dwarfs, neutron stars, and black holes, sources of various heavier elements, and a few others. These explosions also help to understand the stellar evolution, formation of neutron stars and black holes, host environment, and mass loss mechanisms. Further, SNe are considered one of the sources of gravitational wave radiation and high-energy gamma rays. Even in interdisciplinary areas, their use is becoming eminent in studying metal enrichment in the universe and the possible effects of a nearby SN on Earth and its biosphere.

Evidently, SNe play a crucial role in astrophysics, and hence their study becomes equally essential. Their studies as single events are equally important as studying them as a population. Numerous events do not fit the orthodox classification schemes and require a different explanation with thorough studies. Studying such peculiar events in great detail for better classification and judiciously weeding out contaminant sources from larger samples used in other astrophysical domains is crucial. The recent advent of extensive surveys such as All-Sky Automated Survey for Supernovae (ASAS-SN), Asteroid Terrestrial-impact Last Alert System (ATLAS), Zwicky Transient Facility (ZTF), etc., have led to numerous discoveries, and upcoming surveys like Vera C. Rubin Observatory's Legacy Survey of Space and Time (LSST) would only add more. These require detailed spectroscopic and multi-band photometric follow-up for a clear

understanding. The James Webb Space Telescope (JWST) has recently opened up the SNe domain to much higher redshifts.

Apart from their observational studies, it is critical to model these events with the existing tools to get a detailed picture of them. Only with enough observations, analysis, and modeling of these events could we get much information about them. Studying these single events in great detail is necessary to gather better statistics and say more about different trends in these populations. Hence, we take up this work to observe, analyze, and model such explosions in detail to improve our understanding using observation facilities available in national and international domains. We attempt to analyze and model these events for in-depth understanding using open-source tools as widely as possible.

The thesis is focused on the rarely occurring Type IIP supernovae with shorter plateau duration in their light curve evolution. Various modeling works have theorized that these events could originate from higher-mass red supergiants (RSGs). In this work, we study and understand several short-plateau Type II SNe in detail using multiwavelength observation and 1-D hydrodynamical modeling. It has enabled us to show alternate origins of these events based on observational evidence backed by detailed modeling of these rare events. Further, a great deal of diversity has also been revealed among these events.

The thesis makes use of various national and international observational facilities, both ground and space-based, such as in optical 2-m *Himalayan Chandra Telescope*, 0.7-m *GROWTH India Telescope*, in ultraviolet *AstroSat*, *Swift/UVOT* and 1.5-m near-infrared *KANATA* telescope from Japan. Other publicly available data are also used whenever available. We have used various analytical and modeling tools to estimate several explosion parameters and attempted to know about the progenitor and its properties. The thesis presents detailed studies of SN 2018gj, SN 2020jfo, and SN 2021wvw short plateau SNe, including SN 2023ixf, the nearby decadal supernova.

Contents

Abstract **i**

List of Figures **ix**

List of Tables **xix**

1 Introduction **1**
1.1 Journey of Stars . . . 2
1.2 A Star's Path to Shine . . . 7
1.3 Supernovae Taxonomy . . . 9
1.4 Type II SNe Zoo: Observational Diversity . . . 12
1.5 Powering of Type IIP SNe . . . 13
1.6 Progenitors of Type IIP SNe . . . 16
1.7 Short-plateau Type IIP SNe: Road So Far . . . 18
1.8 Overview . . . 20

2 Methodology **23**
2.1 Introduction . . . 23
2.2 Observation Facilities . . . 24
2.2.1 Himalayan Chandra Telescope (HCT) . . . 24
2.2.2 0.7-m GROWTH-India Telescope (GIT) . . . 27
2.2.3 0.3-m UVOT onboard *Swift* . . . 28
2.2.4 0.4-m UVIT onboard *AstroSat* . . . 31
2.2.5 1.5-m Kanata Telescope . . . 32
2.2.6 Other data sources . . . 32
2.3 Analysis Techniques . . . 33
2.3.1 Nickel Mass Estimation . . . 34
2.3.2 Progenitor Mass from Nebular Phase Spectra . . . 36
2.3.3 Analytical Light Curves Modeling . . . 37
2.3.4 Hydrodyanmical Modeling using `MESA+STELLA` . . . 38
2.3.5 Spectral Synthesis using `SYNAPPS` . . . 41
2.3.6 Distance Estimation using EPM . . . 42

2.3.7 Scaling relation for probable progenitor 44

3 Ordinary Short-plateau SNe 45
3.1 Introduction 45
3.2 SN 2020jfo 46
3.2.1 Observations 46
3.2.2 Host Analysis 50
3.2.3 Light Curve Properties 53
3.2.4 Spectroscopic Evolution 61
3.2.5 Characteristics of the Possible Progenitor 71
3.2.6 Case for a Stripped Low-mass Progenitor 78
3.2.7 CSM Interaction 80
3.2.8 Summary for SN 2020jfo 82
3.3 SN 2018gj 84
3.3.1 Observations 85
3.3.2 Host and Light Curve Analysis 88
3.3.3 Two-Component Analytical Light Curve Model 98
3.3.4 Spectral Analysis 99
3.3.5 Prolonged Blue-shifted Emission 107
3.3.6 Progenitor Mass Estimates Using Nebular Lines 108
3.3.7 Hydrodynamical Modeling 110
3.3.8 Discussion 117
3.3.9 Summary for SN 2018gj 120
3.4 Summary 121

4 Fast Declining Short-plateau SNe 123
4.1 Introduction 123
4.2 SN 2023ixf: From FUV to NIR 124
4.3 Observations 126
4.4 Flash Phase and CSM Characteristics 130
4.5 Early Phase Light Curve Analysis 138
4.6 Photometric Evolution Till Early Nebular Phase 142
4.7 Spectroscopic Evolution Post Flash Phase 150
4.8 Progenitor and Explosion Parameters 159
4.9 Discussion 162
4.10 Summary 165

5 Faint Short-plateau SNe 169
5.1 SN 2021wvw: Introduction 169
5.2 Photometry and Spectroscopy: Data sources 171
5.3 Light Curve Analysis 172
5.4 Spectra 178
5.5 Plausible Progenitor 184

5.5.1 Semi-analytical models 184
5.5.2 Hydrodynamical Modeling 186
5.6 Discussion 191
5.6.1 Scaling relation degeneracies and model differences for short-plateau SNe 191
5.6.2 Fallback during the shock propagation phase 193
5.6.3 SN 2021wvw in the Type II domain 194
5.7 Summary 195

6 Short-plateau SNe: A separate class? 197
6.1 Short-plateau SNe within Type II Class 198
6.2 Progenitors 202
6.3 A Separate Class ? 205

7 Summary and Future Work 207
7.1 Summary 207
7.2 Future Work 210
7.2.1 Long-term Multiwavelength Monitoring Campaigns: 211
7.2.2 Extensive SNe Light Curve Grid 212

Bibliography 217

List of Figures

1.1 Various stages of a star's life are depicted here for low and massive stars along with their resultant remnants. *(Credits:R.N. Bailey-Own work, CC BY 4.0)* . . . 2
1.2 Representative evolutionary track for a 1 $M_\odot$ star on HR diagram. *(Credits: Lithopsian, Wikipedia)* . . . 4
1.3 Representative evolutionary track for a massive star on HR diagram. 5
1.4 A toy model showing the inner layers of an evolved massive star toward the end of the evolution and before the collapse. . . . 8
1.5 Classification scheme for various SNe types and sub-types. . . . 10
1.6 The spectral differences around maximum for some of the common types of SNe are presented. The distinguishing spectral features are highlighted as indicated in the legend. . . . 11
1.7 Absolute V-band light curves of a few Type II SNe. The light blue light curves in the background represent those from the sample presented in Anderson et al. (2014a). . . . 12
1.8 Modeled light curve of a typical Type IIP SN showing contribution from various wavelength regimes [The light curves are obtained using MESA+STELLA framework.] . . . 14
1.9 Type II SNe detected progenitors and upper limits are plotted over stellar evolutionary tracks. Other SNe detections are also presented. (Source: Smartt (2015) and references therein.) . . . 17

2.1 Summary of various facilities utilized for this work from ultraviolet to infrared. . . . 24
2.2 *Left:* Sattelite view render for Astrosat. *Right:* UVIT instrument render showing various parts. . . . 30
2.3 A schematic diagram of a two-component semi-analytical model given in Nagy & Vinkó (2016). . . . 37
2.4 ***Left:*** Effects of changing various initial parameters in the first step (pre-MS to Fe-core evolution) on the resultant bolometric modeled light curves using `MESA+STELLA`. ***Right:*** Variation in the resultant bolometric light curves with changes in the explosion and shock propagation parameters. [***Reference:* *Paxton et al. (2018)***] . . . 39

2.5 Pre-supernova mass fractions for an evolved 12 $M_\odot$ model for different species present in the 'approx21_cr60_plus_co56.net' (approx21) network used in MESA modelling. 41

3.1 The *I* band image of SN 2020jfo in M61 obtained on 2020 May 08. The positions of the three regions of the archival SDSS-spectra [dark orange squares] along with SN 2020jfo [white circle] have been marked. 47
3.2 Panchromatic light curves for SN 2020jfo with photometry from HCT, Swift/*UVOT* and ZTF. The time period for which SN 2020jfo went behind the Sun has been obliterated from the plot and is marked by the discontinuity in the abscissa. Offsets in the apparent magnitudes are for visual clarity. 49
3.3 Estimated Steepness of SN 2020jfo using the functional form from Elmhamdi et al. (2003b). 54
3.4 color evolution of SN 2020jfo from the early rise up to the plateau phase is plotted along with some other Type II SNe. 55
3.5 Absolute *V*-band light curve of SN 2020jfo is plotted with a few other Type II SNe. Distance and extinction correction for individual objects are obtained from their references as provided in Section 3.2.3. The decline rates during the early plateau (s1), late plateau (s2), and nebular (s3) phases determined using linear fit are also mentioned. 56
3.6 Quasi-bolometric light curve (Q-bol) of SN 2020jfo along with other Type II SNe. Q-bol with contribution from UV fluxes and from SuperBol (without BB-corrections) are also plotted. The inset shows Optical and UV+Optical Q-bol during the early phase. . . . 58
3.7 Time evolution of SN 2020jfo spectra from 3 d until 292 d post explosion. Lines have been identified following Gutiérrez et al. 2017a, with some prominent lines marked. All spectra are flux-calibrated and corrected for reddening and redshift. 62
3.8 Early phase (+4.0 d) spectrum of the SN 2020jfo is compared with synthetic spectra generated using TARDIS, indicating the presence of ionized helium. The relative contributions due to different elemental compositions are plotted. In the square brackets, 'e' implies the enhanced abundance of He in the composition. 64
3.9 The pre-maximum (+2.8 d) spectrum of SN 2020jfo compared with the spectra of other Type II SNe around similar epochs. 65
3.10 SN 2020jfo spectrum compared with other Type II SNe during the plateau phase 66

3.11 Line velocity evolution of Balmer, Fe II and Sc II features obtained using their absorption minima are shown here. A comparison with mean Type II SNe velocities from Gutiérrez et al. (2014) is also shown. The solid line represents the mean value, while the shaded region displays the 1-σ scatter from the mean. 67
3.12 Spectrum of SN 2020jfo during the nebular phase (+292.2 d) is compared with other Type II SNe at similar epochs. 69
3.13 Identification of lines in the +292 d spectrum of SN 2020jfo. 70
3.14 Best fitting model curves to the bolometric light curve using a two-component model from Nagy & Vinkó (2016). Individual contributions from the shell and core component are shown with the combined bolometric luminosity. 70
3.15 Nebular spectrum (+292 d) of SN 2020jfo is compared with the model spectra for 12, 15, 19 and 25 $M_\odot$ models, at 250 d since explosion. The model spectra obtained from Jerkstrand et al. (2014) are scaled for distance and nickel mass, and corrected for phase mismatch using the characteristic decay time corresponding to SN 2020jfo. 72
3.16 Multi-component Gaussian fit to the nebular spectrum of SN 2020jfo (+292 d). The fit was performed by having different values of line broadening for [Ca II] and [Fe II]/[Ni II] owing to their differing origins in the ejecta. The FWHM values obtained are mentioned in the figure. 73
3.17 Pre-supernova mass fractions for an evolved 12 $M_\odot$ model for different species present in the 'approx21_cr60_plus_co56.net' (approx21) network used in `MESA` modeling. 74
3.18 Quasi-bolometric light curves obtained from `MESA` + `STELLA` modeling with different values of wsf (1.0, 3.0, 3.2 and 5.0) for the 12 $M_\odot$ ZAMS model. Q-bol of SN 2020jfo is over-plotted for comparison. . 76
3.19 Photospheric velocity evolution as obtained from `MESA` + `STELLA` modeling for two different values of optical depth (τ_{Sobolev}=1.0 and 2.0) compared with the observed photospheric velocities. 76
3.20 ***Left:*** Quasi-bolometric light curves as obtained from `MESA` + `STELLA` modeling for a 12 $M_\odot$ ZAMS progenitor (M_f = 6.6 $M_\odot$) with different CSM configurations. Q-bol light curve of SN 2020jfo is over-plotted for comparison. ***Right:*** Color evolution as obtained from `MESA` + `STELLA` modeling for a 12 $M_\odot$ ZAMS progenitor (M_f = 6.6 $M_\odot$) with different CSM configurations. 78
3.21 Temporal evolution of pEW of Fe II 5018 Å in comparison with models from Dessart et al. (2013) having different metallicities (0.4, 1 and 2 $Z_\odot$). The black solid line represents the mean value of the pEW of Fe II 5018 Å and shaded region shows its dispersion from the extensive sample of Gutiérrez et al. (2017a). 83

3.22 Location of SN 2018gj in the host NGC 6217. The dashed violet line marks the separation between the host center and SN. The image is an RGB color composite utilizing Bessell's V, R, and I filters. . . 85
3.23 Photometric data for SN 2018gj spanning ∼300 d post-discovery. Corresponding spectral epochs are marked along the abscissa. [Violet pentagon markers over-plotted on V and B bands are from Swift UVV and UVB bands, respectively] 86
3.24 V-band light curve evolution of SN 2018gj along with other Type II SNe. Continuous light blue lines are representative of a larger Type II sample from Anderson et al. (2014a) and Faran et al. (2014a). Estimated light curve parameters for V-band viz. OPTd, Pd, s1, s2, and s3 are also shown. Supernovae data used in this plot are mentioned in Table 3.12 92
3.25 Mean color evolution of Type II SNe along with the color evolution of SN 2018gj for different bands are shown. The shaded region with a solid line represents the mean colors from a larger Type IIP sample with $1\,\sigma$ scatter from the mean value. Sources of data have been referenced in the Table 3.12. 94
3.26 Pseudo-bolometric and bolometric light curves for SN 2018gj obtained using multiband photometry are shown. The second plot at the bottom shows the temperature and radius evolution obtained using blackbody fits from the SEDs. 95
3.27 Posterior plot for nickel mass and characteristic time estimates for SN 2018gj using Equation 2.5. 97
3.28 Semi-Analytical model fitting for SN 2018gj using two-component model as described in Nagy & Vinkó (2016). The contributions from the shell and the core are also shown independently. In the inset, best-fitting parameters are listed for reference. The evolution of the light curve without $\gamma-$ray leakage is shown by the cyan dashed line. 98
3.29 Spectral time series for SN 2018gj containing 31 epochs spanning 295 d post-explosion. All spectra have been calibrated with photometry for absolute flux and corrected for host redshift. Some of the prominent spectral lines have been marked for clarity. (The data used to create this figure are available.) 100
3.30 SN 2018gj spectrum during maximum light. Spectra of other Type II SNe around the maximum is shown for comparison. The comparison sample is drawn from Table 3.12. 102
3.31 Spectrum of SN 2018gj during plateau phase is shown in comparison with other Type II SNe. The comparison sample is drawn from Table 3.12. 104

3.32 Temporal velocity evolution of various lines identified in the spectra using the absorption minimum is shown here. The velocities have been compared with the sample from Gutiérrez et al. (2017a) where the solid lines are the mean values from the sample and the shaded area around it in similar color represents the $1-\sigma$ scatter from the mean velocities. 105
3.33 Spectral comparison of SN2018gj with other Type II SNe around similar epochs during the nebular phase. 107
3.34 Focused view of spectral time series for Hα line in SN 2018gj. The black line marked is the rest wavelength for Hα. The spectra are corrected for host redshift, and it is evident that the peak of emission features never reaches the rest wavelength. 108
3.35 ***Left:*** Velocity evolution of blue-shifted Hα emission peak. Velocity evolution for emission features obtained using other ions has also been plotted. ***Right:*** Late phase (+295 d) spectrum of SN 2018gj compared with the model spectra around similar phase to estimate the initial mass of the progenitor. The model spectra are obtained from Jerkstrand, Anders (2017). 109
3.36 Scaling relations (Goldberg et al. 2019) in the context of Type IIP SNe as applicable to SN 2018gj. 110
3.37 Temporal evolution of pseudo-equivalent width (pEW) for Fe II 5169 Å line obtained using optical spectra. Other markers represent the pEWs obtained from models given in Dessart et al. (2013). The solid blue line and the shaded region around it represent the mean pEW and the corresponding 1-σ scatter about the mean for a larger sample of Type II SNe given in Gutiérrez et al. (2017a). 111
3.38 **Left:** One dimensional representation of mass fractions for 13 $M_\odot$ ZAMS model with final mass 7.3 $M_\odot$. The elements are part of the nuclear reaction rates network used in the model's evolution. The abscissa is shown till 4 $M_\odot$ as the trend followed beyond it is the same for the outer hydrogen envelope. **Right:** Effect of mixing with the implementation of Duffell RTI on the ejecta structure just before the breakout is shown for some of the prominent elements for the same model as in the Left panel. 112
3.39 Variations in 13 $M_\odot$ ZAMS model using different parameters to achieve a shorter plateau length. Zoomed out a plot in the bottom left shows the variation in explosion energy for different model light curves around the plateau transition. The second plot in the right inset shows the corresponding Fe 5169 velocities obtained using models. The thicker line represents the model where the expansion velocity could be matched with the observed velocities. 113
3.40 Optical bolometric luminosities obtained using `MESA+STELLA` are plotted along with the optical bolometric light curve of SN 2018gj. The initial rise is not fitting well in the optical regime. 114

3.41 Variations in 19 $M_\odot$ ZAMS model using different parameters to achieve a shorter plateau length. Zoomed out a plot in the bottom left shows the variation in explosion energy for different model light curves around the plateau transition. The second plot in the right inset shows the corresponding Fe 5169 velocities obtained using models. All the 19 $M_\odot$ models underestimate the velocity evolution. . . . 116
3.42 The effect of adding CSM around the progenitor is prominently seen in the early stage and can explain the initial excess in the individual light curves in redder bands. The thicker dashed lines represent the light curves obtained using 120 frequency bins. . . . 120

4.1 RGB composite of the host galaxy M 101 using r' (red), g' (green), and u' (blue) images acquired using 2m HCT. SN 2023ixf and the nearby Giant H II region NGC 5461 are labeled. . . . 124
4.2 Optical spectral evolution for SN 2023ixf from HCT, Perley & Gal-Yam (2023) and Stritzinger et al. (2023). The spectra are corrected for the redshift of the host galaxy M 101, and the epochs are labeled with respect to our adopted explosion epoch. **Top:** *Left:* Early time spectral sequence of flash features in SN 2023ixf with line identification of high-ionization features and Balmer lines. The inset depicts the H α profile on +7.9 d having a broad P-Cygni feature and an Intermediate-width Lorentzian emission. *Right:* Evolution of line-profile of H alpha during the flash phase. **Bottom:** *Left:* Spectral sequence of SN 2023ixf during the photospheric phase. *Right:* Evolution of multi-peaked emission profile of H alpha during the photospheric phase. HV and PV refer to the high-velocity and photospheric velocity components in the blue-shifted absorption wing of H α. . . . 130
4.3 FUV spectral evolution obtained using Astrosat/UVIT and the SYNAPPS fit to the spectrum of ∼ 7 d and ∼ 12 d. . . . 133
4.4 NUV spectral evolution for SN 2023ixf obtained using Swift/UVOT. 135
4.5 Spectral comparison of NUV spectra with other Type II SNe. . . . 137
4.6 *Left*: (Top to Bottom) Multiband photometry is shown along with the data compiled from public sources. The second plot shows the bolometric light curve evolution. The bottom plot shows the color evolution of SN 2023ixf along with the other SNe with observed flash features. *Right:* Best model light curves that could represent the g-band light curve evolution of SN 2023ixf obtained out from a large sample of >170,000 models presented in Moriya et al. (2023) for different progenitor masses. . . . 138

4.7 Multi-wavelength photometry of SN 2023ixf spanning ultraviolet, optical, and near-infrared wavelengths. Template subtraction was performed only in the UV bands ($UVW2$, $UVM2$, and $UVW1$) due to non-negligible contamination. The left panel provides a close-up of the initial rise across all bands, annotated as *blue peak & red shoulder*, and the subsequent *red peak*. 142
4.8 Comparison of absolute magnitude light curves of SN 2023ixf in $UVW2$ and V bands along with the $UVW1 - V$ color evolution compared to other SNe II showing CSM interaction signatures. . . . 145
4.9 `Panel A`: Pseudo-bolometric light curves of SN 2023ixf computed in multiple wavelength bins. `Panel B`: Temporal evolution of UV and NIR flux of SN 2023ixf. `Panel C`: Temperature and radius evolution of SN 2023ixf estimated from blackbody fits to the FUV-Optical-NIR data ($0.16-2.35\,\mu$m). The radius of the line-forming region, i.e., the photospheric radius estimated from Fe II, is over-plotted. The steep rise in temperature and the flat evolution in radius exemplify the shock breakout inside a dense CSM (shaded in grey). 147
4.10 `Left Panel:` Photospheric phase spectral evolution of SN 2023ixf. Prominent spectral features are labeled and depicted using colored shaded areas. `Right Panels:` Comparison of the early and late plateau phase spectrum of SN 2023ixf with other SNe II from the literature with signatures of CSM interaction in the top and bottom panels, respectively. 150
4.11 Temporal evolution of Hβ and Hα profile of SN 2023ixf from the decline of the flash-ionization phase until the late plateau phase. The rest-frame zero-velocity is marked with a grey line. The red lines mark the absorption-minima of the P-Cygni absorption (8,500 km s^{-1}) and the high-velocity absorption (13,500 km s^{-1}) when they first appear simultaneously in the spectra on ~ 16 d. The blue edge of the high-velocity feature (20,000 km s^{-1}) is shown with a blue line. The clumpy features that appear over several epochs are indicated by green boxes in right panels. 152
4.12 Comparison of Fe II λ 5169 line velocity evolution of SN 2023ixf with SNe II from the literature and the mean photospheric velocity evolution for SNe II computed by Gutiérrez et al. (2017a). 155
4.13 `Left Panel`: Nebular spectroscopic evolution of SN 2023ixf from HCT. The marked vertical lines indicate the rest wavelength of the labeled spectral features. `Right Panel:` Comparison of the early nebular phase spectrum of SN 2023ixf with other SNe II from the literature with signatures of CSM interaction. 156

4.14 Evolution of Hα 6563 Å, [O I] 6300, 6364 Å, and [Ca II] 7291, 7324 Å during the early nebular phase of SN 2023ixf. The redshifted excess in H α and [Ca II] $\lambda\lambda 7291, 7324$ is labelled at +5,000 km s^{-1}. The insets show a zoomed view of the peak of the Hα and [Ca II], showing redward attenuation as the SN progressed onto the nebular phase. 157
4.15 *Left Panel*: Hydrodynamical modeling of the light curves of SN 2023ixf with only a compact CSM (dashed line) and including an extended CSM (solid line). The shaded region shows the UV excess from the interaction due to the extended CSM. *Top-right panel*: The density structure of the RSG progenitor, the inner-compact CSM, and the extended CSM. The inner-compact CSM extended to 5×10^{14} cm and the extended CSM extends to 1×10^{16} cm. *Bottom-right panel*: The photospheric velocity estimates from both the hydrodynamic models are compared with the observed evolution of photospheric velocity. (Red vertical dotted line marks the plateau end) 160

5.1 RGB color composite finder chart for SN2021wvw utilizing images in Bessell-BVR filters from HCT. 170
5.2 Light curve evolution of SN 2021wvw for various filters from GIT and HCT is shown. The light curves also include data from ZTF and ATLAS surveys. The constants added to the individual light curves are for visual clarity. 175
5.3 SN 2021wvw r band light curve evolution is compared with the r/R band light curves of other short plateau SNe. We also show the archetypal low-luminosity SN 2005cs and an intermediate-luminosity SN 2021gmj. 176
5.4 Spectral sequence for SN 2021wvw. The spectra have been corrected for absolute flux using corresponding photometry and also de-reddened using Milky Way line-of-sight extinction. 179
5.5 SYNAPPS model fitting to the observed spectra around the mid and end plateau phases. The lower small panels show the model spectra of individual species when the contribution from the rest of the species is turned off. Tellurics marked with grey bands are not considered while fitting. 180
5.6 Spectral comparisons at the early and late plateau phase with short-plateau SNe and with other sub-luminous SNe. 181
5.7 Expansion velocity evolution estimated from several prominent metallic features (including Balmer lines) observed in the spectra. The velocities have been compared with a large sample taken from Gutiérrez et al. (2017a). The shaded region gives the corresponding 1-σ scatter around the sample mean. 183
5.8 Semi-analytical fit for fixed radii of 500 R$_\odot$. The values provided in the inset are for the best-matching models. 184

5.9 Observed and modeled bolometric evolution of SN 2021wvw for 13 $M_\odot$ ZAMS models with different sets of parameters. The inset in the left bottom shows the corresponding modeled and observed Fe II 5169 velocities. 187
5.10 Observed and modeled bolometric evolution of SN 2021wvw for 18 $M_\odot$ ZAMS models with different sets of parameters. The solid red curve gives the best description of the model. The inset in the bottom left shows the corresponding modeled and observed Fe II 5169 velocities. 188
5.11 MESA+STELLA structures for different cases of 18 $M_\odot$ ZAMS models with different RTI parameter. A few species out of the 22 species network used in the modeling are shown here. Solid lines present the mass fraction just after we inject the explosion energy. The other two dashed lines show the final ejecta structure before the shock breakout (SB) for different $\eta_{R,e}/\eta_R$ values. The final ejecta profiles suffer from significant fallback during the shock-propagation phase, which we discuss in Section 5.6.2. 190
5.12 Plausible E_{exp} and M_{ej} ranges plotted for the scaling relations from Goldberg et al. (2019). The scatter points represent the ejecta masses obtained for various models utilized in this work. The energy values for all the evolved models are between 0.1 to 0.3 foe. The shaded regions include the values obtained considering the errors in the observables. 191
5.13 *Left:* Correlation between plateau brightness at 50 d, M_V^{50} and expansion velocities at 50 d after explosion. *Right:* Mid-plateau brightness, M_V versus plateau duration (t_p) for a large sample including a wide range of Type II SNe obtained from Fang et al. (2024). 194

6.1 Plot showing mid-plateau absolute V-band magnitude (M_V) vs the plateau duration (t_p). The sample points are obtained from Fang et al. (2024). 198
6.2 Position of short-plateau Type II SNe shown with other large Type II sample closely following the already established tight correlation between M_{Ni} and mid-plateau luminosity. 199
6.3 Position of short-plateau Type II SNe in the well-established correlation between plateau brightness and expansion velocity (estimated from Fe II 5018) at 50 days. The red 'star' markers show the values obtained by taking measurements at the mid-plateau epoch rather than at 50 days. 200
6.4 Various wind mass-loss schemes used in different models are shown with observational ranges for various stellar types. For typical RSGs the observational wind mass-loss limits are $< 10^{-4}$ $M_\odot$ yr^{-1}. [*Source:* *Smith (2014) and references therein*] 204

6.5 Values for CSM parameters and progenitor mass obtained from various works on SN 2023ixf. 205

7.1 Pseudo-bolometric light curves obtained from a part of a larger grid showing variations due to differences in explosion energies for various ZAMS masses. (Multiple light curves in the same colors are due to variations in other parameters that are not explored/shown here.) 213
7.2 Pseudo-bolometric light curves and velocity evolution shown here for $M_{ZAMS} = 13\ M_{\odot}$ models with differences obtained for rotating and non-rotating models with different explosion energies. ((Multiple light curves in the same colors are due to variation in other parameters that are not explored/shown here.)) 214
7.3 Pseudo-bolometric light curves obtained from a part of a larger grid showing variations due to differences in metallicity for various ZAMS masses. 215

List of Tables

2.1 Multi-wavelength observation details of individual supernovae used in this thesis. . . . 33

3.1 SN 2020jfo: HCT $UBVRI$ photometric magnitudes 48
3.2 SN 2020jfo:*Swift*/UVOT magnitudes 50
3.3 Spectra logs of SN 2020jfo 51
3.4 O3N2-index and E(B-V) estimated from the SDSS spectra of 3 regions in M 61. The regions have been marked in the Figure 3.1. . . . 52
3.5 Peak magnitudes from UV/Optical light curves 53
3.6 Best fit slopes of Q-bol light curve during various phases where decline is conspicuous. Slopes for comparison Type II SNe have also been estimated wherever possible. . . . 60
3.7 Pre-SN parameters for different models 75
3.8 HCT $UBVRI$ magnitudes for SN 2018gj. 87
3.9 Swift/UVOT photometry for SN 2018gj 88
3.10 The JHK_s photometric magnitudes of 2018gj. 89
3.11 Spectra log for SN 2018gj. 90
3.12 Type II SN data used in comparison and estimating mean color evolution. 93
3.13 Parameters for best-fitting two-component model 101
3.14 Parameters for pre-SN/Explosion progenitor models evolved from `MESA` that were used to generate model light curves in `STELLA` . . . 110

4.1 Log of AstroSat observations. 129

5.1 Spectra log of SN 2021wvw obtained from HCT. 171
5.2 Photometric observations of SN 2021wvw from GIT and HCT. . . . 173
5.3 Various slopes obtained for different phases of light curves are presented. Slopes and absolute magnitude for other SNe are also compared. The absolute magnitudes ($M_{r/R}$) are reported from the middle of the plateau. 177
5.4 Core parameters for best matching semi-analytical models 186

6.1 Some of the estimated parameters of well-studied short-plateau Type II SNe from literature and this work. *(The values are quoted as mentioned in the respective works.)* 201

7.1 Summary of various observed/estimated parameters for all short-plateau Type II SNe studied in this work. 209

Chapter 1

Introduction

The static-looking night sky, which appears ever so same, is, in reality, a flourishing stage with many phenomena occurring with every passing moment. The time scale of human life is very minuscule compared to the temporal nature of these phenomena such as galaxy mergers. Interestingly, galaxies hold something more transient, and many such events could be observed in one's lifetime. One such transient phenomenon is commonly referred to as a Supernova (SN), plural Supernovae (SNe). A supernova is a spectacular demise of a star in the form of an energetic explosion. At times, the luminosity of these events is so high that it even outshines the host galaxy. The luminosity around the peak can become equivalent to that of a billion Suns. It could further eject the matter at such high speeds that it could reach fractions of the speed of light, having $\sim 10^{51}$ ergs *(foe)* of kinetic energy. The phenomenon itself is not something new that humanity stumbled upon only after the advent of modern telescopes. In fact, there have been numerous instances in the past where many earlier civilizations have recorded these events in one form or another (Stephenson & Green 2005).

SNe are involved in the metal enrichment in galaxies, the creation of neutron stars or even black holes, cosmic rays origin, and the physical conditions of the interstellar medium (ISM); therefore, they have been explored from various viewpoints. SNe serve as critical tools in various subdomains of astronomy and astrophysics. Exploding stars allow us to perform "stellar autopsies", giving magnificent insights into the stellar interiors that are typically obscured. The observations from different SN layers enable us to investigate pre- and post-SN stages. Furthermore, SNe, being the terminal stages of stellar evolution, provide a key understanding of the evolutionary pathways. They also influence the physical evolution of galaxies by forming long-lived SN remnants with the swept-up ambient CSM and ISM by the SN ejecta. A few widely known SN remnants are the Crab Nebula and Cassiopeia A. SNe are crucial for enriching the Universe with heavy elements, which are synthesized both prior to and during their explosions. Moreover, their luminosity makes them one of the crucial indicators of extragalactic distances, helping further in measurements of the Hubble constant (H_0).

1.1 Journey of Stars

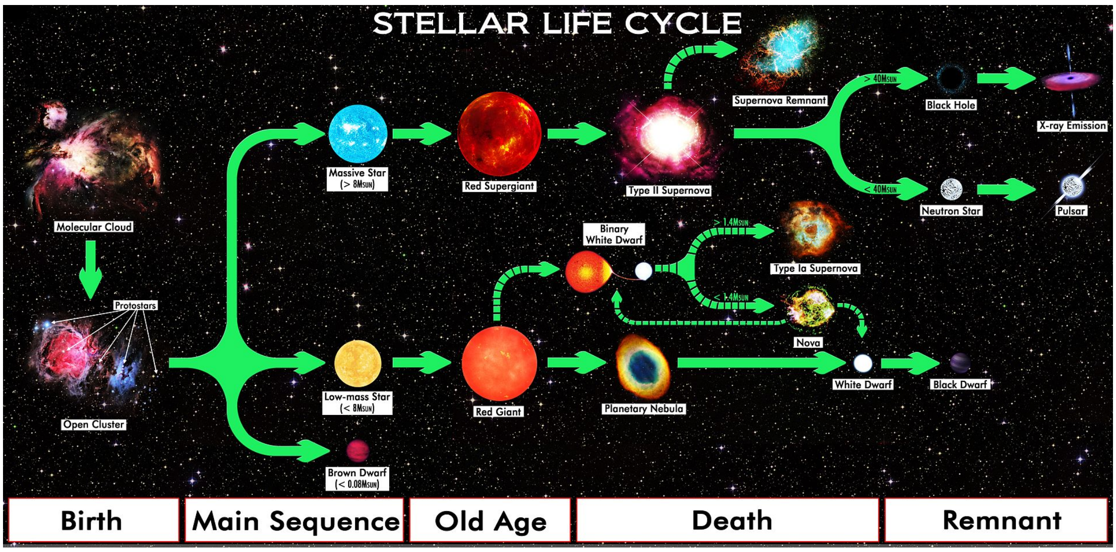

FIGURE 1.1: Various stages of a star's life are depicted here for low and massive stars along with their resultant remnants. *(Credits:R.N. Bailey-Own work, CC BY 4.0)*

Before a star starts its life cycle, it is buried inside a cool dense core of molecular cloud, in the form of a protostar. These protostars are the results of local instabilities in the cloud. Eventually, millions of years go by as protostars reach a state of equilibrium, becoming a main-sequence star and burning hydrogen in their cores. Based on their initial masses, also known as ZAMS (zero-age-main-sequence) mass, these stars are termed as low-mass (< 8 $M_\odot$) or massive ($\gtrsim 8$ $M_\odot$) stars (Figure 1.1).

Birth of a White Dwarf

A low-mass star spends a significant lifetime ($\gtrsim 90\%$) burning hydrogen, which leads to helium development in the core. As the H gets depleted in the core, the thermal equilibrium is disrupted. As a result of this, the core contracts and heats up, igniting hydrogen shell-burning. During this phase, the star is known to be in the *subgiant* phase because of resultant expansion and a decrease in surface temperature. The core continues to contract while the outer layers expand further, resulting in increased luminosity. The star evolves and becomes a *red giant star.*

As helium gets piled up in the core, it becomes dense and hot so that helium burning is feasible. Helium burns much faster than hydrogen in the core. Eventually, helium in the core also gets depleted, leading to further contraction and heating in the core. The resulting star is even more luminous and redder (Figure 1.2). The stellar core now comprises oxygen and carbon, and no further burning is feasible due to its low temperature and density. In this phase, the star reaches the *"Asymptotic Giant Branch (AGB)"* with helium being burnt in the inner shell and hydrogen in the outer shell. This leads to the star becoming unstable, resulting in expelled outer layers in the form of *planetary nebulae*, and the core evolves further to become a remnant *white dwarf (WD).* The crucial nuclear reactions in the hydrogen and helium burning phases are discussed in the successive section.

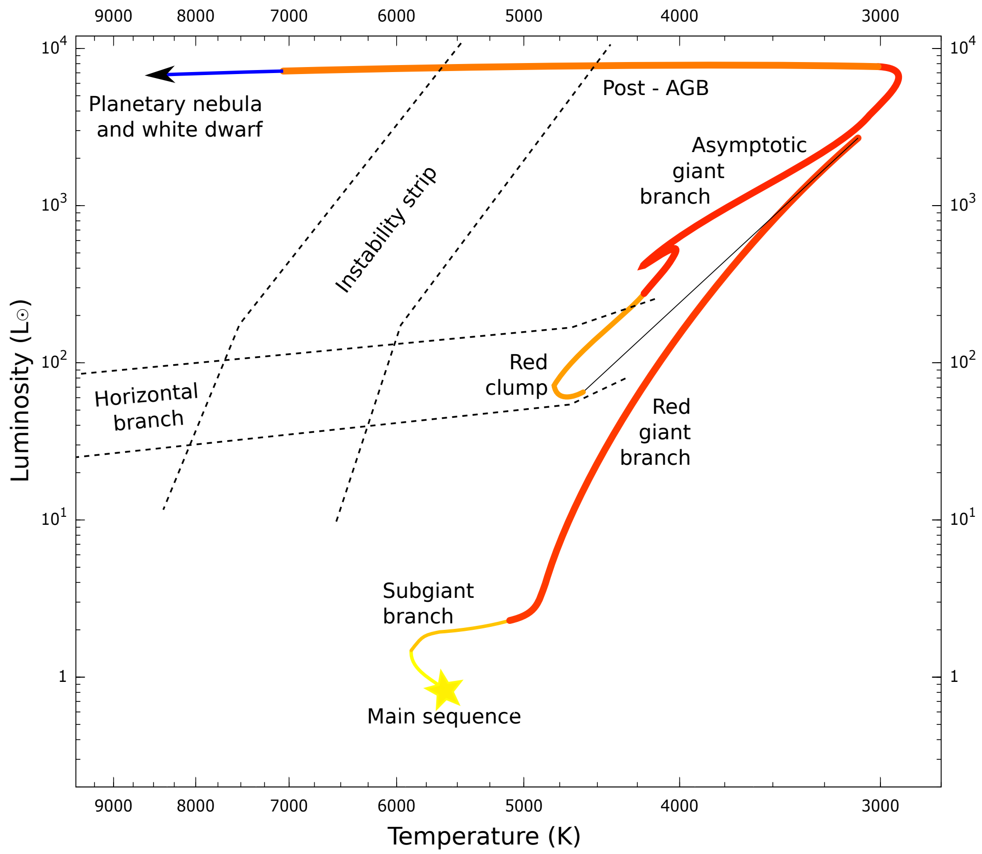

FIGURE 1.2: Representative evolutionary track for a 1 $M_\odot$ star on HR diagram. *(Credits: Lithopsian, Wikipedia)*

Now, we describe the evolution of massive stars, particularly red supergiant (RSG) stars, in detail.

Life of Massive Stars

Understanding RSG evolution is important in understanding CCSNe, particularly Type II. The main sequence evolution of massive stars is similar to the stars with lower masses but massive stars evolve much faster. The late-phase evolution of massive stars ($M_{ZAMS} \gtrsim 8\ to\ 10\ M_\odot$) is quite distinctive from the low-mass star evolution. Towards the late-stage evolution in less massive stars, the electron (e^-) degeneracy pressure supports the internal structure, and the degenerate core stops contracting, eventually becoming a WD. On the contrary, in a massive star evolution due to the gravitational force being more dominant, a significant e^- degeneracy is never achieved in its core throughout all the advanced nuclear burning stages. Hence, in that case, the evolution continues with increased temperature, fusing heavier elements until the point when the core formed is essentially comprised of iron. Understanding these pre-SN evolutionary stages is as crucial as getting insights into the SN itself. Some of the core nuclear-burning stages, from hydrogen to other heavier elements, are described here, along with the required conditions.

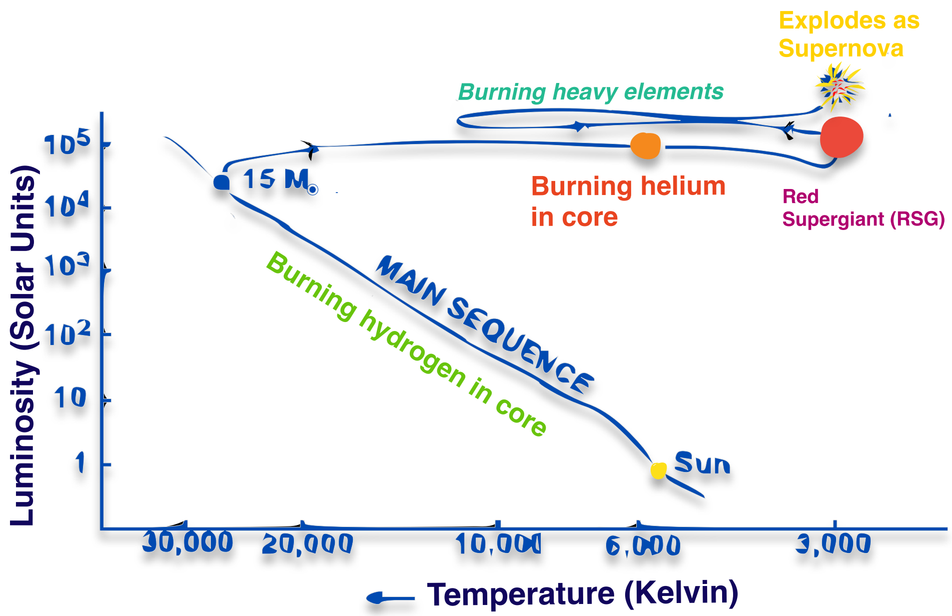

FIGURE 1.3: Representative evolutionary track for a massive star on HR diagram.

Core Hydrogen Burning: The hydrogen burning stage lasts longest in massive stars, almost 90% of their entire lifetime. For mass range $13 - 120$ M$_\odot$, this phase usually lasts for about $\sim 10^7 - 10^6$ yr. The lifetimes are higher for low-mass stars. This nuclear burning phase is dominated by the carbon-nitrogen-oxygen (CNO) cycle with the temperatures of the order $\sim 10^7$ K. The main reactions occurring in the CNO cycle are as follows:

$$
\begin{aligned}
{}^{12}_{6}\mathrm{C} \; + \; {}^{1}_{1}\mathrm{H} &\rightarrow \; {}^{13}_{7}\mathrm{N} \; + \; \gamma && + 1.95 \; MeV \\
{}^{13}_{7}\mathrm{N} &\rightarrow \; {}^{13}_{6}\mathrm{C} \; + \; \mathrm{e}^{+} \; + \nu_{\mathrm{e}} && + 1.20 \; MeV \\
{}^{13}_{6}\mathrm{C} + {}^{1}_{1}\mathrm{H} &\rightarrow \; {}^{14}_{7}\mathrm{N} \; + \; \gamma && + 7.54 \; MeV \\
{}^{14}_{7}\mathrm{N} + {}^{1}_{1}\mathrm{H} &\rightarrow \; {}^{15}_{8}\mathrm{O} \; + \; \gamma && + 7.35 \; MeV \\
{}^{15}_{8}\mathrm{O} &\rightarrow \; {}^{15}_{7}\mathrm{N} \; + \; \mathrm{e}^{+} \; + \; \nu_{\mathrm{e}} && + 1.73 \; MeV \\
{}^{15}_{7}\mathrm{N} + {}^{1}_{1}\mathrm{H} &\rightarrow \; {}^{12}_{6}\mathrm{C} \; + \; {}^{4}_{2}\mathrm{He} && + 4.96 \; MeV
\end{aligned}
$$

Additional 2.04 MeV is produced when the two e^{+} annihilate with two ambient e^{-}, therefore one cycle releases 26.73 MeV, out of which ≈ 25 MeV becomes available to give luminosity and the rest ($\sim$ 1.7 MeV) is taken away by neutrinos (ν_e). There are other CNO cycles that are described as minor branches as well. For massive stars, minor branches of CNO cycles that involve unstable ${}^{18}_{9}\mathrm{F}$ and ${}^{19}_{9}\mathrm{F}$ are significant.

Helium Burning: Once the core H depletes, there is an outward shift in the mass of shells burning H. This results in increased He in the core. The He core contracts continuously while heating up until the He-burning reactions are initiated. The fusion of He in the core is realized by a three-particle response, also known as the triple-alpha process. Carbon starts to build up as a product of He burning, but at hot enough temperatures, ${}^{12}\mathrm{C}(\alpha, \gamma){}^{16}\mathrm{O}$ reactions subsume part of the carbon converting C into O, depending on the mass of the stars. More massive star implies more O. As a result, the carbon-to-oxygen ratio decreases near the end of helium burning in massive stars (Ekström 2021). The He-burning in the core lasts for about $10^{6} - 10^{5}$ yr, typically for stars that fall in between $13 - 120$ $\mathrm{M}_{\odot}$ range (Limongi 2017).

Advanced Nuclear Burning: After depletion of He in the core, heavier elements build up and fuse further to create heavier elements. Starting with **C burning** involving the two ^{12}C nuclei fusion resulting in the production of compound nuclear states of ^{24}Mg. It decays into ^{23}Mg, ^{20}Ne, and ^{23}Na. The C-burning stage typically lasts for a few hundred years. Following C burning phase, core composition consists primarily of ^{16}O, ^{20}Ne, and ^{24}Mg. Before the fusion temperature for O is achieved, $^{20}\mathrm{Ne}(\gamma, \alpha)^{16}\mathrm{O}$ becomes more feasible (Woosley et al. 2002) and energy is generated by rearrangement as: $2\ ^{20}\mathrm{Ne} \rightarrow ^{16}\mathrm{O} + ^{24}\mathrm{Mg} + 4.59$ MeV. The lifetime for **neon burning** phase is several months. The next element in line to burn post-Ne burning phase is **oxygen**. Fusion of oxygen results in ^{32}S compound nuclear states that decay further into sulfur, phosphorus, and silicon. Core O burning typically lasts for a few months (Ekström 2021). Eventually, the **silicon burning** is ignited. Before that, there are two large nuclei clusters, one of which is a nuclei group from total nucleons ranging from 24 to 46, while the other one has heavier nuclei from the Fe group. Post Si burning lasting for about a day, these groups merge into one large iron group elements (Woosley et al. 2002; Ekström 2021). The final structure of massive stars resembles an 'onion' depicting different layers of elements.

1.2 A Star's Path to Shine

Stars span a wide mass range and several evolutionary stages and evolve in different environmental conditions. However, physical processes, that lead these stars to their ultimate demise as SNe, can be broadly placed into two major categories: ***thermonuclear SNe*** and ***core-collapse SNe***

Thermonuclear Supernovae: *Firstly, the detonation/deflagration of an accreting white-dwarf star resulting from the thermonuclear runaway as it exceeds*

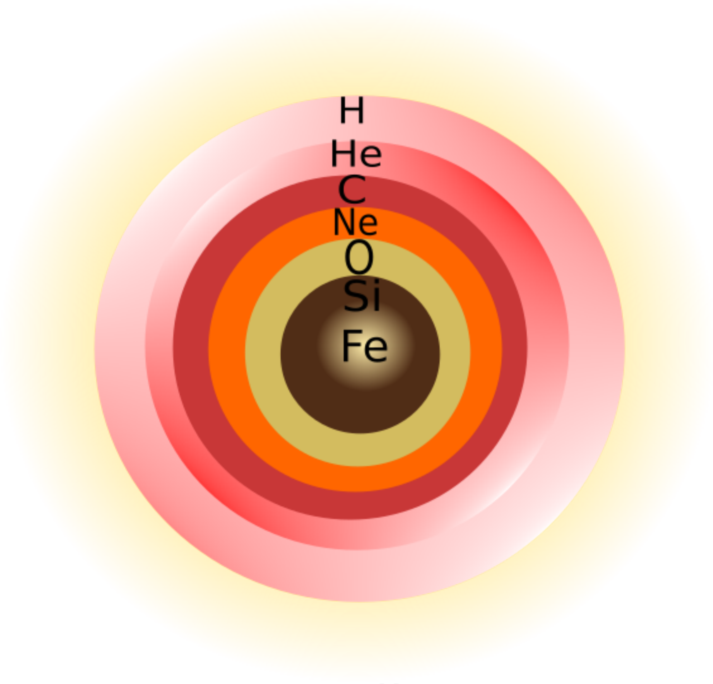

FIGURE 1.4: A toy model showing the inner layers of an evolved massive star toward the end of the evolution and before the collapse.

its Chandrasekhar mass limit (Type Ia) (Mazzali et al. 2007). As mentioned earlier, low-mass stars end up as white dwarfs. If this WD exists in a binary configuration, it can accrete matter from the binary counterpart, which could either be an MS* star or even another WD. The accretion process increases the white dwarf mass, and when this mass approaches the Chandrasekhar mass limit, a thermonuclear runaway is imminent. Due to this, the thermonuclear burning becomes unstable both dynamically and thermally. The star goes through *'detonation'* resulting from the supersonic shock wave, or through rapid but subsonic combustion known as *'deflagration'*, or probably a combination of both. This explosion shatters stellar structure without leaving any compact remnant. The result of this is observed as a Type Ia SN.

Core-Collapse Supernovae (CCSNe): *Core-collapse supernovae (CCSNe) are the powerful explosions of evolved massive stars ($\geq 8\ \mathrm{M}_\odot$) (Arcavi 2017, and*

*Main Sequence

references therein). The massive star core collapsing gravitationally initiates the explosion, as no further energy-generating nuclear fusion reactions can occur once iron (Fe) forms in the core, leading it to collapse under its own gravity (Burrows & Vartanyan 2021; Janka 2012). Depending on the progenitor's mass, it collapses either into NS or BH. Rebound shock from such a proto-neutron star expels the ejecta very energetically, leading to a core-collapse supernova. Various routes have been proposed for such events: electron-capture supernovae (SNe), Fe-core collapse SNe, γ-ray burst SNe, and pair-instability SNe (Janka 2012). The initiation of core collapse is highly sensitive to the lepton-to-baryon ratio and the entropy. Weak interaction, β-decay, and e^{-}-capture are the dominant factors for the above properties.

1.3 Supernovae Taxonomy

SNe are primarily classified based on specific features in their spectrum obtained close to peak brightness (Minkowski 1941; Filippenko 1997). They are primarily classified into two categories, Type I and Type II, distinguished by the absence or presence of prominent hydrogen Balmer lines (e.g., $H\alpha$, $H\beta$) in their spectra, respectively. Type I class can be further subdivided based on other dominant features. The SN is classified as Type Ia if there is a strong Si II λ 6355 Å present in the spectrum around peak light. Type Ia SNe are further classified into subcategories depending on distinctive features and evolution. Further, objects that show weak or no Si II lines but with strong helium lines in the spectra are termed Type Ib, and objects with no helium but O I absorption are called Type Ic SNe.

Type II events are further classified based on their observed light curves, as Type IIP if a *plateau* phase of constant or very slow declining luminosity is observed and

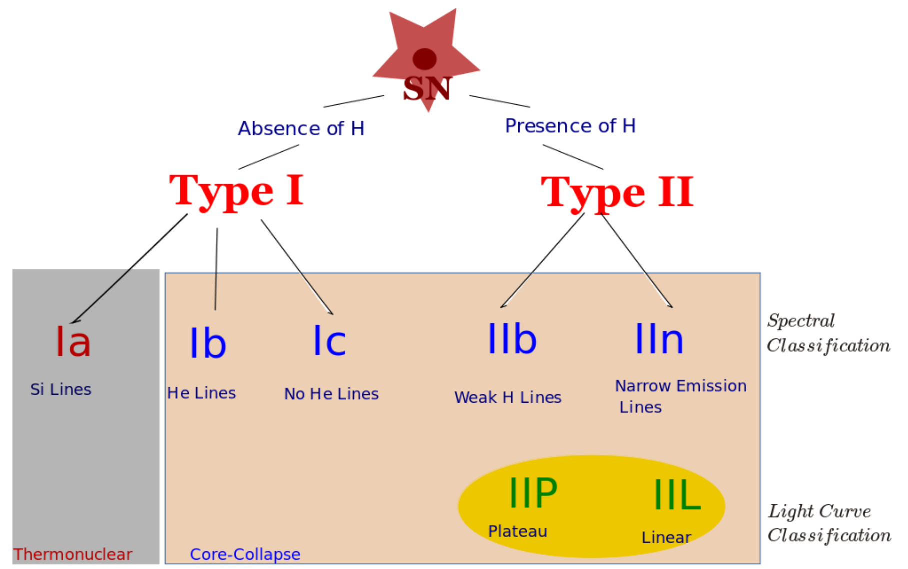

FIGURE 1.5: Classification scheme for various SNe types and sub-types.

Type IIL when the decline from the light curve peak to radioactive decay powered tail phase is *linear*. Type IIP SNe are more commonly observed with a definitive plateau of around 100 days, but with varied luminosity, before falling to the tail phase. While there are clear differences in Type IIP/L SNe light curves, it remains unclear whether the two classes are fundamentally distinct. Many studies of samples of the Type II SNe (for example, Anderson et al. 2014a; de Jaeger et al. 2019) indicate the two sub-classes (IIP and IIL) are observed to be in a continuous sequence. In contrast, a few studies present (subtle) differences in these sub-classes, both photometrically and spectroscopically (Faran et al. 2014a,b). However, studies involving larger supernova populations tend to support the existence of a continuous distribution of these events† (Gutiérrez et al. 2017a). In addition, some events labeled Type IIb show H lines initially in their spectra, which weaken in the later phases, and as the spectra evolve, strong helium features appear.

Apart from these typical classes, there have been numerous instances where narrow emission spectral features are superimposed over the usual broad emission features

†In this thesis, we use Type II and Type IIP interchangeably at many places.

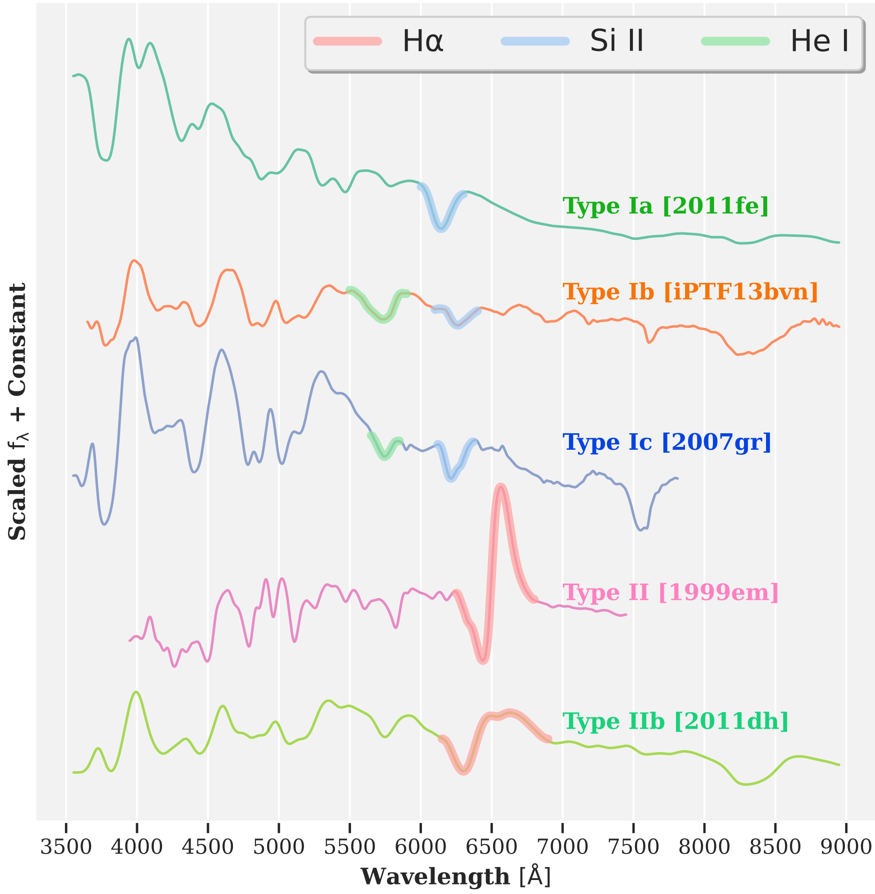

FIGURE 1.6: The spectral differences around maximum for some of the common types of SNe are presented. The distinguishing spectral features are highlighted as indicated in the legend.

in the spectra. These narrow emission lines are assumed to be the product of interaction between the SN ejecta and the CSM around the star that exploded as SN, leading to their classification as interacting supernovae, or Type IIn. (Filippenko 1997) or even Type Ibn, 'n' implying *narrow* spectral features. There are some other extreme events with very high expansion velocities, but their spectra resemble that of Type Ic objects. These are referred to as broad-lined Type Ic supernovae (Ic-BL). A few of these events are known to be associated with GRB[‡] sources. Some typical classes of SNe, as classified based on their spectra, are shown in Figure 1.5.

[‡]Gamma Ray Burst

1.4 Type II SNe Zoo: Observational Diversity

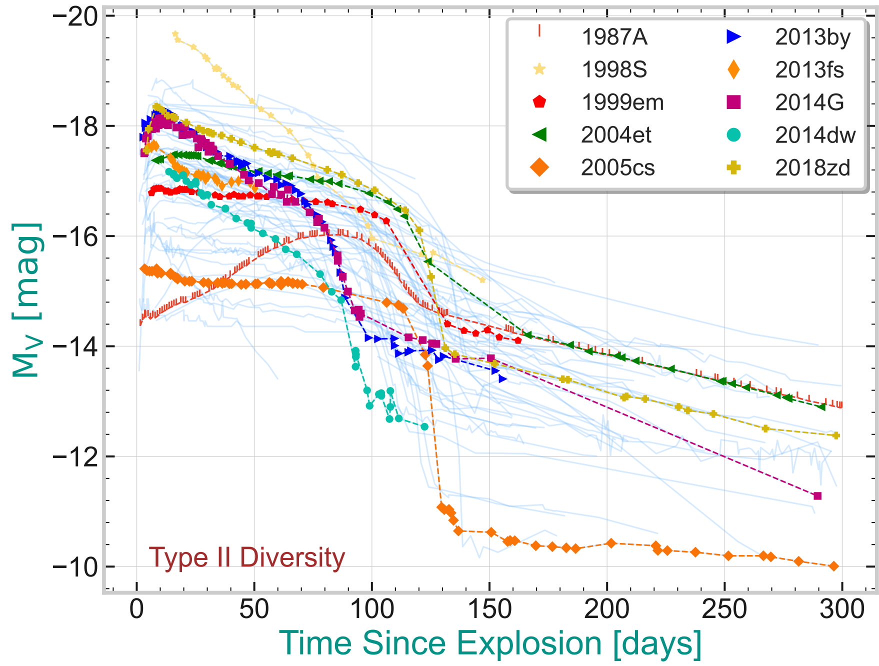

FIGURE 1.7: Absolute V-band light curves of a few Type II SNe. The light blue light curves in the background represent those from the sample presented in Anderson et al. (2014a).

Intrinsically, the Type II SNe covers most of SNe occurring in the local universe, with more than 50% out of all SNe (Li et al. 2011). However, as noticed in observations, Type Ia SNe dominate the space (79%, Li et al. 2011) due to their consistent and higher inherent brightness. The overwhelming number of SNe observed has also revealed significant diversity within the Type II class. Although categorized under the same umbrella based on their spectral features, there is heterogeneity in many of their observed properties. Figure 1.7 illustrates the distinct variations in light curve evolution among different Type II SNe. We find that maximum absolute magnitudes vary by more than 4 mag ($-19 \lesssim M_V$ [mag] $\lesssim -14$). Significant differences are observed in the decline rates during both the plateau and nebular phase light curve evolution (Anderson et al. 2014a). Many modern surveys have brought out differences in the very early light curves as well in terms of their rise times and brightness. Apart from the light curve differences, there are differences in the spectra at similar epochs in terms of features, profiles, and expansion velocities (Gutiérrez et al. 2017a).

There are several factors due to which the observed differences arise. One of the key causes is the progenitor and its properties such as the initial mass, rotation, evolutionary track, metallicity, presence of companion, amount of hydrogen envelope retained, and explosion energy. Apart from the progenitor, the SN environment equally affects the light curve and spectral properties and contributes to the diversity. The crucial external factor is the existence of CSM in the proximity of the progenitor. The evidence of CSM in Type II is usually seen early on in the form of highly ionized lines dubbed as *'flash features'*, high-velocity absorption features in spectra, narrow emission lines, and enhanced luminosity in light curves (Bullivant et al. 2018; Singh et al. 2019a; Zhang et al. 2022). Furthermore, it has been established that sometimes only a few of these features are present while others are missing altogether (Dong et al. 2021; Andrews et al. 2019). With the increasing number of supernovae observed early enough, the fraction of supernovae showing flash ionization features is also increasing ($> 36\%$, Bruch et al. 2022), indicating the existence of CSM proximal to the explosion site is common in these SNe (Morozova et al. 2018). The presence of spatially confined CSM likely results from increased mass loss from the end phases of the progenitor before going as SN.

1.5 Powering of Type IIP SNe

Several primary radiation sources, along with a few secondary sources (Zampieri 2017), contribute to the total observed flux for typical Type IIP SNe and its evolution. Type IIP SNe light curves are powered primarily by three components:

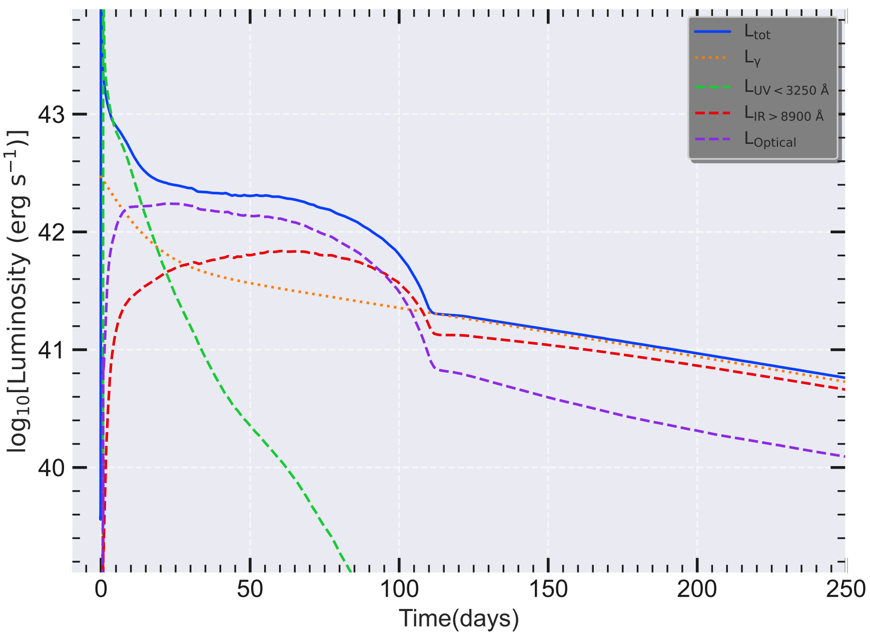

FIGURE 1.8: Modeled light curve of a typical Type IIP SN showing contribution from various wavelength regimes [The light curves are obtained using MESA+STELLA framework.]

- **Shock breakout**: A rebounded shock is generated when the stellar layers of the progenitor star collapse onto a newly formed proto-neutron star. This shock traverses through successive layers of the star (depicted as an onion-like structure) and eventually reaches the outermost stellar layers. When it leaves the stellar structure, it emits brief pulses of X-ray as well as UV radiation, surviving minutes to hours or, at times, even days, depending on the external environment. The physics of this phase is not well understood yet, but there have been several attempts, including 3-D modeling (Waxman et al. 2007; Cowen et al. 2010).

- **Shock cooling and ejecta recombination:** Energetic shock traversing through the ejecta (stellar layers) deposits energy in the ejecta, accelerating, expelling, heating, and ionizing it. This ionized, hot material starts to cool gradually and eventually recombines and emits radiation. The H-rich envelope is optically thick to radiation for a sufficient time after the explosion, and diffusion approximation holds (Arnett 1980, 1982; Zampieri 2017). This shock also assists in synthesizing ***heavy radioactive*** ^{56}Ni ***nuclei*** (Arnett 1980). ^{56}Ni is the most significant contributor whose decay results in the daughter nuclei ^{56}Co with half-life $\sim$6.1 d. These daughter nuclei then finally decay to ^{56}Fe with half-life $\sim$77.3 d ($^{56}\mathrm{Ni} \Longrightarrow^{56} \mathrm{Co} \Longrightarrow^{56} \mathrm{Fe}$). This radioactive cascade of ^{56}Ni primarily dominates the late-time luminosity in Type II SNe. The luminosity during this recombination phase, which is a sum of several components, can be given as:-

$$L_{tot} = L + L_{rec} + L_{\gamma} \tag{1.1}$$

The diffusion luminosity L is then given by :

$$L = -\frac{4\pi r_i(t)^2 c}{3\kappa\rho}\left(\frac{\partial w_0}{\partial r}\right)_{r_i} = \frac{4\pi c a_R T_0^4}{3\kappa\rho_0}\zeta\frac{R_0}{R} r_i(t)\phi(t) \tag{1.2}$$

where, $a_R = 4\sigma/c$ is radiation constant and σ being the Stefan-Boltzmann constant, T_0, ρ_0, R_0 are initial temperature, density and radius at t_0, respectively, $\zeta = \left[-\frac{d\psi}{dy}\right]_{y=1}$ and $y = r/r_i$ with r being the radial coordinate of outermost layers, $w_0 = a_R T^4$ is the radiation energy density (LTE) and $\phi(t)$ is the time-dependent solution for the energy equation.

Further, the energy output during the recombination process (radiative + advection) is given by:

$$L_{rec} = 4\pi r_i(t)^2 v_i(a_R T_{rec}^4 + \rho Q_{ion}), \tag{1.3}$$

where v_i refers to wavefront velocity and Q_{ion} implies energy/mass released during recombination.

Additionally, the energy released by the decay of freshly formed radioactive substance can be approximated as:

$$L_{\gamma} = (1 - e^{-\tau_{\gamma}})Q_{\gamma} \tag{1.4}$$

$$where,\ Q_\gamma \approx [A \times e^{-t/\tau_{Ni}} + B \times (e^{-t/\tau_{Co}} - e^{-t/\tau_{Ni}})]$$

where τ_{Co} and τ_{Ni} are the respective characteristic lifetimes. A equals 3.9×10^{10} $erg\ s^{-1}$ and B is 7.2×10^{9} $erg\ s^{-1}$.

In the *nebular phase*, once the recombination wavefront approaches inward of the ejecta and eventually to the base, radiation from the radioactive decay of heavy nuclei becomes the main source of luminosity. The luminosity produced can also be expressed as Equation 1.4.

- **Secondary factors**: There are other sources that can also contribute to the luminosity, such as CSM interaction with ejecta (Moriya et al. 2011), accretion-induced luminosity when the inner layer falls onto the central remnant (Gerling-Dunsmore & Ott 2015), the possibility of radiation due to slowing down of magnetar formed during the collapse (Soker 2022), and others.

There are several pathways to model these light curves, from semi-analytical modeling to the full radiation hydrodynamical approach, considering these radiation sources under different approximations, which we discuss in subsequent chapters.

1.6 Progenitors of Type IIP SNe

One of the fundamental questions related to SN is about its progenitor. What kind of star would have given birth to the SN studied? What would have been its initial mass? What were the environmental conditions? Was it part of a binary system? Many other questions related to the progenitor are always around when we study SNe. Detailed modeling works have well established that the majority of massive stars ranging from $8-30$ $M_\odot$ end up as Type II SNe, forming a neutron star in their center, while beyond this mass range, the star would typically collapse

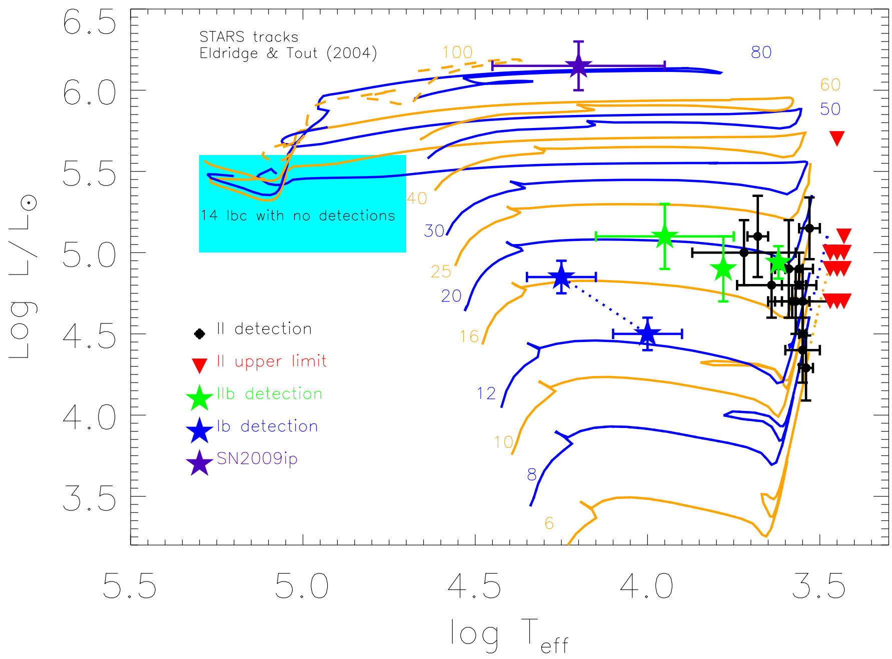

FIGURE 1.9: Type II SNe detected progenitors and upper limits are plotted over stellar evolutionary tracks. Other SNe detections are also presented. (Source: Smartt (2015) and references therein.)

to a BH. Although there exist certain mass gaps in 1-D modeling works within this range where models do not explode, leading to failed SNe, instead, these models directly collapse to black holes (Sukhbold et al. 2016). Theoretically, it is plausible to obtain Type II SNe with long-lasting plateaus from progenitors of masses up to 30 $M_{\odot}$. However, this is not the complete picture, as the observational evidences indicate this upper mass limit to be much lower.

The Hubble Space Telescope (HST) has revolutionized our views about the progenitors of various SNe. The archival images from various SN fields already observed by HST, along with accurate astrometry, have been utilized time and again to identify probable progenitors of SNe occurring in the local universe (for example Van Dyk et al. (2002), Smartt (2009)). Smartt (2015) obtained the upper bounds on the mass limit of the observed RSGs, which are confirmed as Type II SNe progenitors. The limit is obtained by utilizing 13 such directly identified progenitors. A similar number (13) of progenitors were also presented with an upper limit on detection. It was shown that there are no progenitors detected with luminosity greater than $\log(L/L_\odot) \sim 5.2$ translating to $\lesssim 19\ M_\odot$ using stellar evolution tracks (Smartt 2015; Van Dyk 2017). Whereas the RSGs observed in nature go well beyond this mass (empirical luminosity limit is $\log L/L_\odot = 5.5$). In fact, in the Local Group galaxies, RSGs have been observed up to mass 25 $M_\odot$ (Smartt et al. 2009; Rodríguez 2022). Hence, the lack of directly detected progenitors beyond 19 $M_\odot$ even with RSGs being present in nature above this mass has led to a dilemma. This has been termed as the 'missing mass gap' or the *Red Supergiant Problem* in literature. However, recent works revisit the statistical significance of this limit (Davies & Beasor 2020a) and attribute a less than $2-\sigma$ significance to this RSG problem.

Although there are challenges, both theoretically and observationally, it is fairly understood that the RSG stars are the progenitors of Type IIP supernovae. Even with a typical single RSG, depending on the progenitor properties and environmental conditions, these SNe come with great diversity. Stellar evolution theory has given a lot of insights into their working and the different factors affecting the RSG evolution and the resultant SN.

1.7 Short-plateau Type IIP SNe: Road So Far

As indicated earlier, the typical plateau lengths for most Type IIP SNe have been observed to be ~100 days. With the modern high cadence and deep night-sky surveys, SNe are being discovered at an early phase. Their rigorous follow-up programs have revealed that the plateau lengths of some Type IIP SNe are considerably shorter ($\sim 50-75$ days). These objects have been termed as short plateau Type IIP SNe. Theoretical (Eldridge et al. 2018) and large sample observational works (Anderson et al. 2014b) provide 4% as an upper limit for the short plateau IIP SNe among all Type II SNe, implying the rarity of these events.

The shorter plateau length in Type IIP SNe is usually explained by considerable stripping of the hydrogen envelope. The stripping of the outer hydrogen layer is possible in all mass ranges of red-supergiants (RSGs) via various mechanisms, viz. wind mass loss, presence of a secondary star, episodic mass losses, etc. The short-plateau SNe had not been paid that much attention until recently. There have been several theoretical works where we find the emergence of short-plateau SNe and their rarity. Dessart et al. (2010) evolved an extensive set of progenitors models. In these models, we find the high mass progenitors ($M_{ZAMS} \approx 25-30\ M_{\odot}$), with a natural tendency to lose more mass during evolution, result in SNe with plateaus ranging from 53 to 80 days. However, these models do not include any ^{56}Ni in their structure, which has been found in many cases to lengthen and even brighten the plateau. Recent work by Curtis et al. (2021) also obtained short-plateau SNe in their massive star ($M_{ZAMS} \approx 27-32\ M_{\odot}$) models. However, these models have very extended envelopes (1000 $R_{\odot}$) and very high SNe luminosities (peak $L_{bol} \sim 10^{43}$ erg s^{-1}). Hiramatsu et al. (2021a) studied three short-plateau SNe in detail with high intrinsic brightness, faster decline rates during the plateau phase, and high estimated ^{56}Ni mass. They further showed these events could arise from RSG progenitor ranging between $18-22\ M_{\odot}$.

In totality, some theoretical works have shown (directly or indirectly) high mass RSGs as progenitors of short plateau SNe (Curtis et al. 2021; Hiramatsu et al. 2021a) as, with the usual single-star evolutionary scenario with "typical" mass-loss, only the much heavier stars can achieve stronger winds required to strip enough hydrogen to cause a shorter plateau. Massive RSGs as progenitors for the short plateau could address the "RSG problem" (Hiramatsu et al. 2021a), although in general, there is no consensus with regards to its statistical significance (Eldridge et al. 2013; Beasor et al. 2020; Kochanek 2020).

With this work, we study several short-plateau Type II SNe in detail and add to the limited sample of these rare events. We further look into the intrinsic diversity of these short-plateau SNe and where they stand as sub-types in the Type II scenario. With detailed observations and modeling of the increasing number of short plateau Type IIP SNe, we attempt to explore their progenitor properties and origin.

1.8 Overview

Numerous SNe are being discovered regularly by the current dedicated night sky surveys such as ASAS-SN, Gaia, ATLAS, Pan-STARRS, Global Supernova Search Team (GSNST), ZTF, etc., and with the upcoming telescopes and survey facilities such as Vera C. Rubin Observatory, this number is certainly going to increase manifolds. They would reveal more such events that are termed rare as of current understanding. Some of the recent observational findings, including some exotic classes of SNe, hypernovae, and γ-ray associated SNe, along with their theoretical modeling, have given a whole new dimension to SN studies. This work presents extensive multi-wavelength observations and detailed modeling of rarely occurring short-plateau Type II SNe with different traits. The primary aim is to understand the influence of various physical processes that lead to these short-plateau SNe and their diversity. With observations and hydrodynamical modeling, this work sheds more light on the nature of these rarely occurring short-plateau Type II SNe. The overall thesis is divided into the following Chapters:

- Chapter 2 provides a brief methodology that includes details of various observational facilities, key instruments, and data processing techniques. This Chapter also describes various analysis tools and techniques to obtain key SN and progenitor parameters, including hydrodynamical modeling.

- Chapter 3 focuses on two short-plateau SNe, namely SN 2020jfo and SN 2018gj, that show similar traits to typical Type IIP SNe. The content of Chapter 3 is based on Teja et al. (2022) and Teja et al. (2023a), which are published in *The Astrophysical Journal*.

- Chapter 4 contains a detailed work on the nearby, fast declining, short-plateau SN 2023ixf. The results based on its evolution from the very early phase till the nebular phase are presented in this Chapter. The content of Chapter 4 is adapted from Teja et al. (2023b) published in *The Astrophysical Journal Letters* and Singh et al. (2024) which has been *accepted for publication* in *The Astrophysical Journal*.

- Chapter 5 deals with SN 2021wvw, a unique intermediate-luminosity SNe also showing a short plateau phase. The content of this Chapter comes from Teja et al. (2024), published in *The Astrophysical Journal*.

- Chapter 6 discusses short-plateau SNe with respect to normal Type II SNe and where these stand in various correlation spaces. It also tries to ascertain the plausible progenitors for these SNe.

- Chapter 7 provides a brief conclusion for this work and discusses future prospects.

Chapter 2

Methodology

2.1 Introduction

The thesis is based on good quality, high-cadence observational data, covering far-ultraviolet (FUV) to near-infrared (NIR) bands, acquired using various national and international facilities. The various facilities and relevant instruments used for acquiring data are briefly described in the subsequent sections of this chapter. This work has also used public/archival data for the objects whenever available. The data have been reduced using standard techniques, usually with the help of custom scripts to process the files in batch mode. The observational data are used to estimate several parameters, which are modeled with the help of various open-source tools to derive the explosion parameters and progenitor properties. Eventually, this exercise resulted in collecting new data and a detailed analysis of four core-collapse supernovae: SN 2018gj, SN 2020jfo, SN 2021wvw, and SN 2023ixf.

This chapter briefly provides information about the various observational facilities,

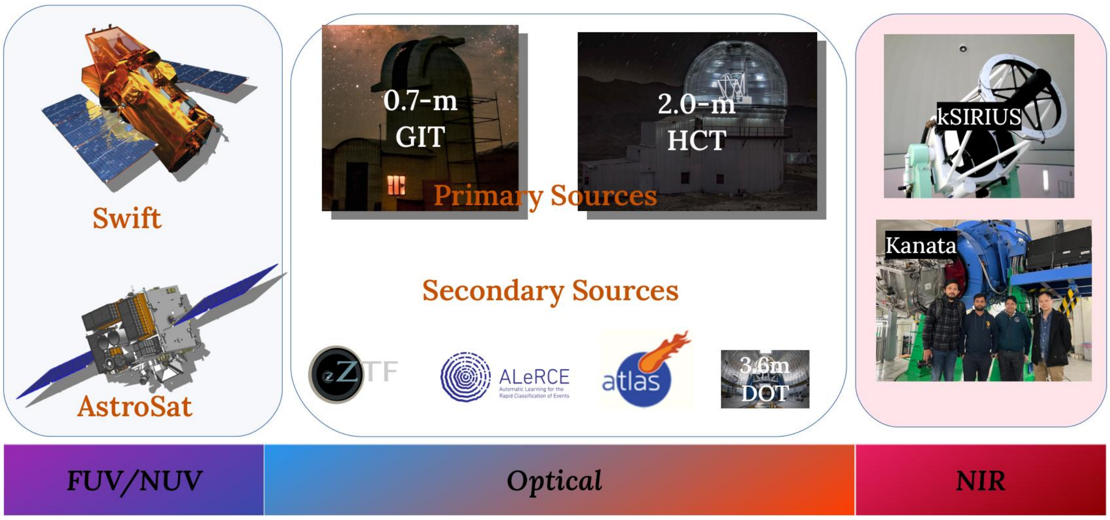

FIGURE 2.1: Summary of various facilities utilized for this work from ultraviolet to infrared.

the types of data obtained, and their reduction procedures. Later on, various analysis and modeling techniques are also described. Combinedly, this chapter forms the technical basis for this work, providing a methodology to proceed further.

2.2 Observation Facilities

2.2.1 Himalayan Chandra Telescope (HCT)

HCT* is an optical-infrared telescope with an aperture diameter of ∼2-m. The IAO†, Hanle, located on Mt. Saraswati, hosts this telescope with observatory coordinates being 32°46′46″ N (lat) and 78°57′51″ E (long). IAO boasts an altitude of 4500 m. Observations from HCT are performed remotely from the CREST campus of IIA located in Hosakote, Karnataka, India, which is connected via an exclusive satellite link. There are three instruments available with the HCT namely,

*https://www.iiap.res.in/centers/iao/facilities/hct/
†Indian Astronomical Observatory

- Himalaya Faint Object Spectrograph Camera (HFOSC),
- Hanle Echelle Spectrograph (HESP), and
- TIFR Near Infrared Spectrometer and Imager (TIRSPEC).

Out of these three instruments, the optical imager cum spectrograph HFOSC was used for this study.

HFOSC comes with a SITe CCD chip consisting of a pixel array with dimensions 2K $\times$ 4K. The CCD comes with a liquid nitrogen cooling setup. Gain and readout noise parameters of this CCD are $1.22\,e^-\,ADU^{-1}$ and $4.8\,e^-$, respectively. Imaging is conducted using a central region of 2K $\times$ 2K pixels, which encompasses a $10' \times 10'$ FOV[‡] with a plate scale of $0.296''$/pix. Prior to 2023, the imager was equipped with Bessell-$UBVRI$ filters, and now it is replaced by the $ugriz$-prime (SDSS) filter system. The spectrograph system is equipped with multiple slits and grisms. For this work, the low-resolution spectroscopic ($\sim$10 Å) data were obtained using a setup consisting of $1.92''$ slit with grisms, Gr7 and Gr8 covering $3500-7200$ Å and $5800-9500$ Å wavelength range respectively.

Data Acquisition & Processing

Photometry

The data used in this thesis are observed under numerous regular and Target of Opportunity (ToO) proposals. During every observing run, depending on the brightness of the supernovae, they were observed through multiple filters. In addition to object frames, calibration frames like bias and sky-flats were also taken at each epoch. The data were pre-processed by performing the standard tasks

[‡]Field of View

such as subtraction of bias from all the frames, flat fielding individual images by creating a master flat for different filters, and removal of cosmic rays through packages available in IRAF implemented through pyRAF using the custom scripts (Singh 2021). During certain epochs, particularly in the later period, more than one frames for the individual bands were obtained. To enhance the SNR[§] ratio in the SN frames, multiple images taken were aligned and then combined into a single exposure frame. Standard star calibration fields from Landolt (1992) were also obtained on several epochs under photometric conditions, which are utilized to calibrate secondary standards present in the object frame. We utilized DAOPHOT 3 (Stetson 1987) to conduct PSF photometry on the standard fields. Calibration of the secondary standards was carried out using the mean atmospheric extinction coefficient for the location (Stalin et al. 2008), along with standard stars that have a magnitude extent of $12.02 \leq V \leq 16.25$ mag and a color span of $-0.22 \leq B - V \leq 2.53$ mag. For SNe relatively isolated in their host galaxy, the magnitudes were extracted using PSF photometry. If the SN was embedded in the host or significantly contaminated by host flux, image subtraction was performed using host templates from previous observations, if available. Otherwise, a new set of templates was obtained when the SN faded sufficiently. We conducted aperture photometry on the template-subtracted SN fields, and the extracted magnitudes were differentially calibrated against the secondary standard in the supernova field.

Spectroscopy

We obtained low-resolution optical spectroscopic data on several epochs for each SNe in their different phases. In addition to the 2-D object spectra, we obtained several bias frames, as well as arc-lamps spectra. Attempts were made to observe spectro-photometric standards also on each night. The observed spectroscopic data were bias-corrected, and 1-D spectra were obtained from the 2-D spectra

[§]signal-to-noise

frames in concordance with the optimal extraction procedure (Horne 1986). Dispersion solutions derived from arc lamps (such as FeNe, and FeAr) spectra were used to carry out the wavelength calibration of the 1-D spectra earlier obtained in the pixel scale. The sky emission lines such as λ 5577 Å , λ 6300 Å, etc. were used to verify calibration accuracy, applying minor shifts where necessary. The instrumental response was corrected using observed spectro-photometric standards. Response curves from adjacent nights were utilized for nights that lacked standard star observations. The flux and wavelength calibrated spectra from Gr7 and Gr8 grisms were median-combined, using an overlapping area for statistics, to create a single spectrum covering the entire optical range. The flux of the resulting spectra was matched to the photometric flux by scaling. It places the spectra on an absolute flux scale. These reduction and calibration steps were accomplished using various tasks given in `IRAF` and custom `python` scripts.

2.2.2 0.7-m GROWTH-India Telescope (GIT)

GIT (Kumar et al. 2022), located at IAO, is an automated telescope dedicated to Time Domain Astrophysics (TDA) for studies of various transient phenomena, for example, Gamma Ray Burst, Supernovae, Novae, and GW optical counterpart. It is equipped with a back-illuminated *'Andor iKon-XL 230'* CCD camera of 16.8 megapixels (4K $\times$ 4K). It provides a wide FoV (field of view) covering 0.7° of the night sky. SDSS-*ugriz* prime filters integrated into a filter wheel are available for photometric observation.

Data Acquisition & Processing

We conducted regular monitoring campaigns for nearby SNe in the targeted observation mode. By default, GIT is operated in an automated mode for nightly observations. The objects are observed in a queue-based mode. Before the observations start, a detailed list of objects with relevant information regarding coordinates, exposures, filter sequence, priority order, etc., is parsed to the scheduling computer. Based on these inputs, the computer automatically performs the observations. Along with the object frames, multiple flat and bias frames were also obtained. GIT data processing and photometry are achieved via a dedicated `python` based pipeline, which performs the standard pre-processing tasks such as bias subtraction, flat fielding, cosmic ray correction, solving for WCS (World Coordinate System) via `astrometry.net`. Further, differential photometry is done on the cleaned images with nightly zero points for each image estimated via querying Pan-STARSS or SDSS catalogs. The detailed procedure to carry out these tasks is described in the GIT instrument paper (Kumar et al. 2022).

2.2.3 0.3-m UVOT onboard *Swift*

Three of the SNe studied in this thesis were also monitored by the UVOT[¶] (Roming et al. 2005) onboard the *Swift* (Gehrels et al. 2004) observatory. UVOT is a 30 cm aperture telescope that covers the wavelength range of 1600 – 6000 Å. Its detector consists of an intensified CCD, which has 385 × 288 pixels, of which 256 × 256 are utilized for science purposes. It provides a $17' \times 17'$ FoV with each pixel of $4'' \times 4''$ on the sky. It has seven filters for photometry and two grisms setups for spectroscopy. In this study, data obtained with near UV filters: $UVW2$, $UVM2$, and $UVW1$, optical filters: UVU, UVB, and UVV along with UV grism data whenever available are used.

[¶]Ultraviolet Optical Telescope

Data Acquisition & Processing

Level I (raw) data and Level II (reduced) data from *Swift* data are made available publicly on the Swift Archives‖. The supernova files along with auxiliary files were obtained from the archive portal to further perform photometry and spectroscopy on the object of interest.

Photometry

The images obtained from the *Swift* data portal were processed using the High Energy Astrophysics Software (HEASOFT, v6.27) package with the most recent calibrations for the *UVOT* instrument. For the processing tasks, the procedures followed were obtained from Poole et al. (2008) and Brown et al. (2009). To extract source magnitudes, we utilized the `UVOTSOURCE` tool. For the source region, we took a $5''$ aperture centered around the source, and a similar aperture in a nearby source-free region was taken to estimate the background counts. Saturated or bad quality data can be checked and discarded further by the `saturate` and `sss_factor` flags from the output. If there is host contribution in the SN flux, it can be removed by utilizing earlier images if available or using late-time images when the SN has faded enough.

Spectroscopy

Spectroscopic data reduction for *Swift* UV-grism data was performed using the standard `UVOTPY` package, which includes the latest grism calibrations and corrections (Kuin 2014). For 1-D spectrum extraction from 2-D images, the `getSpec` function in the `uvotpy.uvotgetspec` module of the `UVOTPY` package is used. The output of this provides three graphs along with output spectra files. The obtained graphs contain the following information:

‖ https://www.swift.ac.uk/swift_portal/

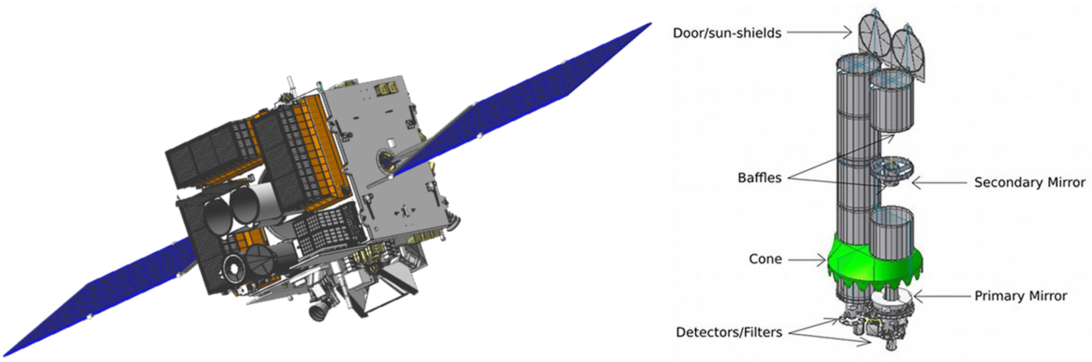

FIGURE 2.2: *Left:* Sattelite view render for Astrosat. *Right:* UVIT instrument render showing various parts.

- The first plot shows the extraction position on the 2-D image with each order marked with crosses.
- The second plot provides the extracted raw total counts without background subtraction and exposure scaling.
- The third plot shows the spectrum, which is flux-calibrated.

Due to inherent positional inaccuracies in the UV grism, there could be slight wavelength offsets in the final spectrum. These minor wavelength offsets are corrected using `adjust_wavelength_manually` function, which provides a graphical interface with multiple prominent lines shown at their rest wavelengths. A few lines can be identified (for example, Mg II), and wavelength can be adjusted accordingly with the help of a slider. Moreover, multiple spectra obtained intra/inter-night can be summed using `uvotspec.sum_PHAfiles` function for a better SNR.

Note: *All Swift/UVOT data utilized are from public archives, and no triggers were performed from our end.*

2.2.4 0.4-m UVIT onboard *AstroSat*

The UltraViolet Imaging Telescope (UVIT; Kumar et al. 2012; Tandon et al. 2017) on board *AstroSat* was also utilized for observations in both imaging and spectroscopic modes. UVIT is primarily an imaging instrument with a primary mirror of effective aperture of ~ 0.37 m. It has the capability to image simultaneously in 3 channels: a) *FUV* (1300-1800 Å), b) *NUV* (2000-3000 Å), and c) *VIS* (3200-5500 Å). All channels are equipped with intensified C-MOS type detectors (512×512 pixels). UVIT has a $\sim 28'$ FOV in a circular shape with an FWHM (spatial resolution) $< 1.8''$. In the 3 channels, several filters are available for observations. There is also a provision for low-resolution slitless spectroscopy (~ 100) in *FUV* and *NUV* channels. We have incorporated data from the *FUV* channel for both photometry and spectroscopy.

Data Acquisition & Processing

The data were obtained using the Target of Opportunity (ToO) mode. The ToO observations are typically made public typically within a week at the ISSDC[**] portal. We have used the Level 1 (raw) and Level 2 (processed) data files available at ISSDC in this work. The two gratings used for spectroscopy (*FUV* Grating-1 and *FUV* Grating-2) are mounted on the *FUV* filter wheel at positions F4 and F6, respectively (Kumar et al. 2012) and have perpendicular dispersion axes. The *AstroSat-UVIT* data were pre-processed with `CCDLAB` (Postma & Leahy 2017) following the steps described in Postma & Leahy (2021). Aperture photometry was performed using a 12-pixel ($5''$) aperture and calibrated following the procedures mentioned in Tandon et al. (2020). Spectral extraction and calibrations were performed manually following the procedures from Tandon et al. (2020) and Dewangan (2021) using `IRAF` and some custom scripts `python`.

[**]Indian Space Science Data Center

2.2.5 1.5-m Kanata Telescope

Near Infrared (NIR) data were acquired with the HONIR[††] (Akitaya et al. 2014), installed at the Kanata Telescope (aperture 1.5 m), operated by the Hiroshima Astrophysical Science Center (HASC) of Hiroshima University. The NIR arm has a HgCdTe VIRGO-2K array with 2K × 2K pixels (pixel size 20 × 20 μm, plate scale of 0.295″/pixel) with 11.6 e^-/ADU and 24 e^- as gain and readout noise, respectively. The NIR data was also reduced using the standard IRAF tasks with similar steps taken for optical photometry. The secondary standard stars for J, H, and Ks bands were calibrated against the magnitudes provided by the 2MASS catalog (Skrutskie et al. 2006).

2.2.6 Other data sources

We also supplemented our data with those from various other facilities, night-sky surveys, and other publicly available sources. The key facilities utilized were ZTF public data obtained through ALeRCE[‡‡] (Sánchez-Sáez et al. 2021) and ATLAS$-c$, and $-o$ fluxes were obtained from forced photometry server (Tonry et al. 2018a) maintained by ATLAS. We have also obtained data from the Devasthal Optical Telescope (Omar et al. 2019; Sagar et al. 2019), which has an aperture of 3.6 m and is being operated by ARIES, Nainital.

Table 2.1 summarizes the data sources in various bands and modes (Imaging/Spectroscopy) for the SNe included in this thesis.

[††] Hiroshima Optical and Near-InfraRed Camera
[‡‡] Automatic Learning for the Rapid Classification of Events

TABLE 2.1: Multi-wavelength observation details of individual supernovae used in this thesis.

Object	**Facility**	**Mode**[a]	**Data Sources**[b]	**Wavelengths**
SN 2018gj	HCT	Img & Spec	Obs	Optical
	Kanata	Img	Obs	Near Infrared
	Swift/UVOT	Img	Public	Near-UV & Optical
	ATLAS	Img	Public	Optical
SN 2020jfo	HCT	Img & Spec	Obs	Optical
	DOT	Spec	Obs	Optical
	ZTF	Img	Public	Optical
	Swift/UVOT	Img	Public	Near-UV & Optical
	SDSS	Spec	Public	Optical
SN 2021wvw	HCT	Img & Spec	Obs	Optical
	GIT	Img	Obs	Optical
	ZTF	Img	Public	Optical
	ATLAS	Img	Public	Optical
SN 2023ixf	HCT	Spec	Obs	Optical
	GIT	Img	Obs	Optical
	ASTROSAT	Img & Spec	Obs+Public	Far-UV
	KANATA	Img	Obs	Near Infrared
	ZTF	Img	Public	Optical
	Swift/UVOT	Img & Spec	Public	Near-UV & Optical

[a] Img: Photometry mode; Spec: Spectroscopy [b] Obs: Observations taken through our proposals or in collaboration; Public: Data utilized from public sources both in raw and science-ready form

2.3 Analysis Techniques

With the help of multiband photometry and spectroscopy, numerous aspects of supernovae and its progenitor can be explored. There are various straightforward observables that could be estimated from the light curves, such as peak magnitude, decline rates, plateau duration and magnitude, color evolution, etc. Spectral evolution can be used to study the presence/absence of various metals in the ejecta, asymmetries in the ejecta through line profiles, ejecta velocities, temperature, etc. Further, a detailed analysis involving more physical processes is applied to obtain various parameters of the SN as well as its progenitor. Some key parameters and the methods to obtain these are described in brief.

2.3.1 Nickel Mass Estimation

There are several ways that can be employed to estimate the mass of synthesized ^{56}Ni (M_{Ni}).

- Firstly, we used the following relations by Hamuy (2003):

$$\frac{M(^{56}Ni)}{M_{\odot}} = \frac{L_t}{L_*} \exp\left[\frac{(t_t - t_{exp})/(1+z) - t_{1/2}(^{56}Ni)}{t_{e-folding}(^{56}Co)}\right] \quad (2.1)$$

  where $L_* = 1.271 \times 10^{43}\,\mathrm{erg\,s^{-1}}$ factor comes from the decay energy, t_{exp} is the estimated explosion epoch, $t_{1/2}$(^{56}Ni) is 6.1 d. L_t is the observed tail luminosity at time t_t. The $t_{e-folding}$(^{56}Co) is 111.26 d.

- We can also compare the late-phase quasi-bolometric or bolometric luminosity of the observed SNe with that of very thoroughly studied nearby SN 1987A. Due to proximity and detailed multiwavelength observations, the overall luminosity and ^{56}Ni mass of SN 1987A produced in the explosion is estimated with significant accuracy (0.075 $M_{\odot}$, Turatto et al. 1998). Assuming that the γ-ray deposition in SNe is similar to SN 1987A, mass of ^{56}Ni in any SNe can be estimated using,

$$M_{Ni}(SN) \approx M_{Ni}(SN\ 1987A) \times \frac{L_{1987A}(t)}{L_{SN}(t)} \quad (2.2)$$

- It was empirically seen that the ^{56}Ni mass shows anti-correlation with the steepness parameter's maximum ($S = dM_V/dt$) obtained from the end plateau to the nebular phase transition. Singh et al. (2018) further refined the relation by incorporating a larger Type IIP SNe sample, including low-luminosity events as

$$\log M(^{56}Ni) = -(3.5024 \pm 0.0960) \times S - 1.0167 \pm 0.0034 \quad (2.3)$$

This relation is also used to obtain ^{56}Ni mass yielded in the explosion.

- Maguire et al. (2012) show the mass of ^{56}Ni is correlated with FWHM of Hα emission feature during the late nebular phase. The FWHM of the Hα line can be measured in the spectrum obtained at late nebular phases by fitting a Gaussian profile. The observed FWHM is corrected for instrumental broadening using the line width of the skylines present in the spectrum. ^{56}Ni mass can be obtained by using:

$$M(^{56}Ni) = A \times 10^{B \times FWHM_{corr}}\ M_{\odot} \tag{2.4}$$

where $A = 1.81^{+1.05}_{-0.68} \times 10^{-3}$ and $B = 0.0233 \pm 0.0041$

- Further, if there is incomplete trapping of $\gamma-$rays, the following equation from Yuan et al. (2016) can be utilized, which incorporates the characteristic time (t_c) of $\gamma-$ray escape:

$$L_{obs} = L_0 \times M_{Ni} \times \left[e^{-(\frac{t-t_0}{t_{Co}})} - e^{-(\frac{t-t_0}{t_{Ni}})} \right] \times \left(1 - e^{(-\frac{t_c^2}{(t-t_0)^2})} \right) \tag{2.5}$$

where t_{Co} and t_{Ni} are the respective half-lives with t_0 being the explosion epoch, and t_c is the time when the optical depth for $\gamma-$rays approaches unity (Yuan et al. 2016). L_0, t_{Co}, and t_{Ni} are explosion epoch, 1.41×10^{43} erg s^{-1}, 111.4 d and 8.8 d, respectively.

- Semi-analytical models and hydrodynamical simulations can also be employed for more precise estimates of the nickel mass. These methods are discussed in detail in the following sections.

2.3.2 Progenitor Mass from Nebular Phase Spectra

The plausible mass of the progenitor star that eventually ended as SN could be determined from several independent methods. One such approach is to utilize the nebular phase spectra, which can provide insight into the metallic lines that arise from stellar nucleosynthesis. In CCSNe, the mass of calcium synthesized is insensitive to the initial progenitor mass (or ZAMS mass), whereas the mass of oxygen synthesized relies on it. The observed [Ca II] $\lambda\lambda\,7291,\ 7324$ Å/ [O I] $\lambda\lambda\,6300,\ 6364$ Å flux ratio can serve as a proxy to estimate the progenitor mass (Fransson & Chevalier 1989). The lower the value of the estimated ratio, the heavier the progenitor could have been. Jerkstrand et al. (2014) generated synthetic spectra using radiative transfer calculations in NLTE. These are applied to ejecta obtained from various explosion models of progenitors with varying ZAMS masses. Hence, to constrain the progenitor mass, we can compare the nebular phase spectrum of SN with model spectra. The model spectra for different progenitor masses (12, 15, 19, and 25 $\mathrm{M}_{\odot}$) are scaled with respect to ^{56}Ni mass and the distance of respective SNe (in contrast to 5.5 Mpc used for model spectra). In order to account for the difference in phase between the model spectra and the observed spectrum, the observed spectrum is scaled by the brightness difference due to dissimilarity in phases determined from the characteristic time scale (t_c) obtained from the ^{56}Ni-decay powered phase of the light curve using $f_{corr} = f_{obs}/(1 - e^{-(t_c/phase)})$ (Singh et al. 2019a). The comparison of [Ca II] / [O I] line fluxes of the observed spectra with the spectral models are then used to put rough constraints on the progenitor mass range.

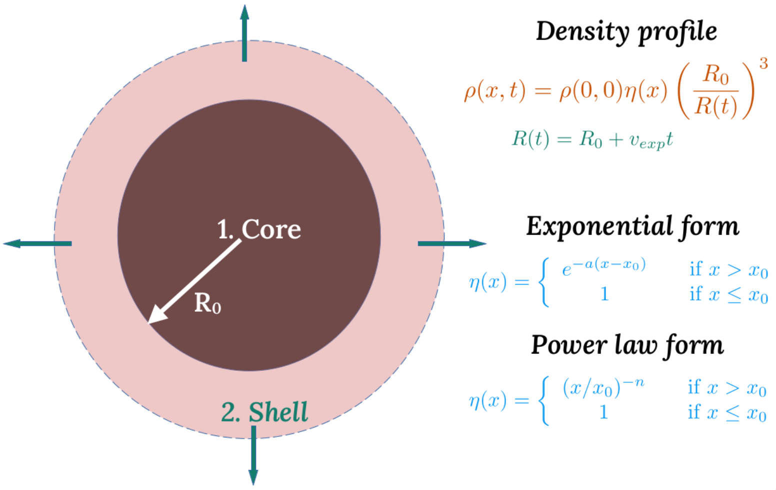

FIGURE 2.3: A schematic diagram of a two-component semi-analytical model given in Nagy & Vinkó (2016).

2.3.3 Analytical Light Curves Modeling

Nagy & Vinkó (2016) formulated a two-component progenitor model that could be utilized to compare the observed light curves of Type IIP SNe semi-analytically. This formulation is based on the seminal work by Arnett & Fu (1989), which had been subsequently modified by Popov (1993), Blinnikov & Popov (1993) and Nagy et al. (2014). It can be utilized to get approximate estimates on synthesized ^{56}Ni mass (M_{Ni}), ejecta mass (M_{ej}), progenitor radius (R_0), and total energy (E_{tot}). The formulation divides the homologously expanding and spherically symmetric SN ejecta into an inner faction with a flat (constant) density configuration and an outer region with power law or exponential density profile (Nagy et al. 2014). Both these spherically symmetric components have different masses, radii, energies, and densities but a common center. The outer region is an extended envelope (Nagy & Vinkó 2016). Contribution to bolometric luminosity is primarily by energy released due to recombination and radioactive decay of ^{56}Ni. During the nebular phase, if there is full trapping of $\gamma-$rays, we get 0.98 mag (100 day)$^{-1}$ as light curve decline rate. But usually, this isn't the case due to partial trapping of $\gamma-$rays; this results in the escape of γ-rays, and a steeper decline rate is observed. The effect of $\gamma-$ray leakage on the nebular phase flux is introduced using the A_g parameter in this formulation. This parameter reflects the effectiveness of $\gamma-$ray trapping (Chatzopoulos et al. 2012) whereas, in luminosity equation, it could be shown as $\mathrm{L_{bol}} = \mathrm{L_{Ni}}(1 - \exp{(-\mathrm{A_g}/\mathrm{t}^2)}) + \mathrm{L_{rec}}$. Physically, it is related to the characteristic time scale ($\mathrm{T_0}$) of the $\gamma-$rays as $\mathrm{A_g} = \mathrm{T_0^2}$. A representative structure for this model describing both shell and core components is shown in Figure 2.3

2.3.4 Hydrodyanmical Modeling using `MESA+STELLA`

We also perform detailed hydrodynamical modeling to understand better the progenitor, its evolution, mass loss history, and its immediate environment. We used the publicly available 1-D stellar evolution code `MESA` revision r-15140 to evolve and explode progenitor stars. We further use a simplified version of `STELLA` included with MESA to calculate light curves and photospheric velocities of various progenitors exploded as SNe. `MESA + STELLA` has been successfully used in many studies to investigate properties of CCSNe progenitors (Goldberg et al. 2019; Hiramatsu et al. 2021a). We also apply this framework to get more insights about the progenitor of some of the SNe studied in this work. Prescriptions used for various parameters in these hydrodynamical simulations are as follows:

1. The built-in nuclear reactions rates used in the progenitor models were taken from 'approx21_cr60_plus_co56.net'. Nuclear reaction rates are mostly from the Nuclear Astrophysics Compilation of Reaction rates, (NACRE, Angulo 1999) and the Joint Institute for Nuclear Astrophysics, JINA reaction rates (REACLIB, Cyburt et al. 2010).

2. Cool and hot wind schemes for the Red Giant Branch or Asymptotic Giant Branch phase are considered 'Dutch', as described in MESA IV. This wind scheme for massive stars combines results from work by various Dutch authors. The particular combination chosen is from Glebbeek et al. (2009).

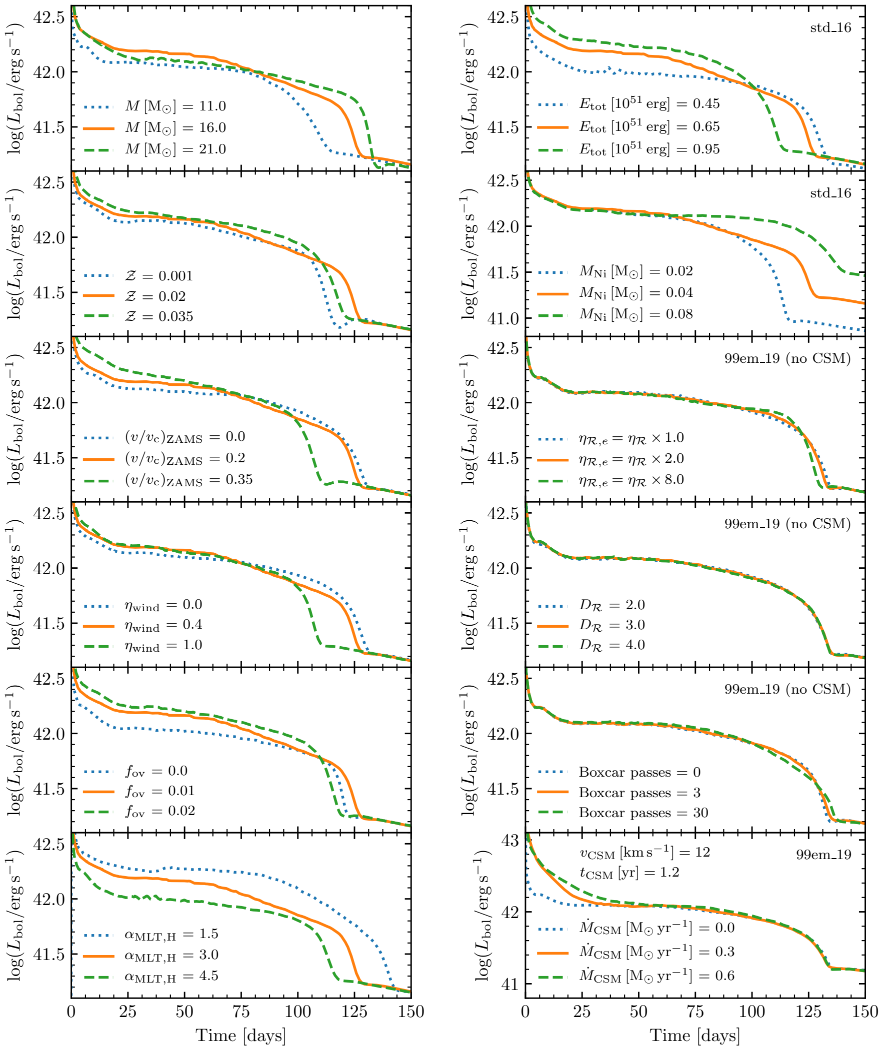

FIGURE 2.4: ***Left:*** Effects of changing various initial parameters in the first step (pre-MS to Fe-core evolution) on the resultant bolometric modeled light curves using `MESA+STELLA`. ***Right:*** Variation in the resultant bolometric light curves with changes in the explosion and shock propagation parameters. [***Reference: Paxton et al. (2018)***]

Typically, if the surface hydrogen has a mass fraction less than 0.4 and an effective temperature greater than 10^4 K, the prescription used is from Vink et al. (2001), otherwise it is taken from Nugis & Lamers (2000). The wind efficiency is controlled by the η_{wind} parameter.

3. The mixing length parameter (`MLT_option`) is set to *Henyey*, which came from the work by Henyey et al. (1965), with $\alpha_{\rm MLT}$, the ratio of mixing length to the pressure scale height ($= \mathrm{P}/\mathrm{g}\rho$), as its critical parameter.

4. To determine the position of the convective boundaries, the default *Ledoux* criterion is used.

5. Various other factors such as metallicity (Z), convective overshoot (f_{ov}), and rotation ($v/v_{cricitcal}$) are also controlled during evolution from pre-MS to the development of Fe-core. The influence of these individual parameters on the resultant bolometric light curves is shown in Figure 2.4 (*Left*).

From the evolution of the pre-main-sequence star to finally retrieving the multi-band/bolometric light curve post-explosion, the modeling process is completed in the following broad steps: progenitor evolution, synthetic explosion, shock propagation, shock breakout, and ejecta evolution inside the `MESA+STELLA` framework.

First, a pre–MS star is evolved till the Fe-core developed. It is followed by an initiation of swift infall of the iron core. These steps are accomplished using `'make_pre_ccsnIIp'` test suite provided in MESA. Default values of the controls in `inlists` are used with slight variations in individual models (described in subsequent Chapters) to reach convergence with some of the inputs from Farmer et al. (2016).

Since the explosion is not achieved directly by MESA, we utilize the second step, which closely follows the `'ccsn_IIp'` test suite. In this step, a section of the core is removed, which would have eventually collapsed onto a proto–NS. This center section is removed from the models based on the entropy. The model section where entropy per baryon is $4\mathrm{k_B}$ with k_B being the *Boltzmann's constant*, the central section is excised from there.

Later, the explosion is induced by the synthetic injection of energy into a narrow region of $\approx 0.01\,\mathrm{M_\odot}$ located at the inner boundary for about 5 ms, and the rate is scaled such that the $\mathrm{E_{exp}}$ reaches the desired input value. Shock then proceeds

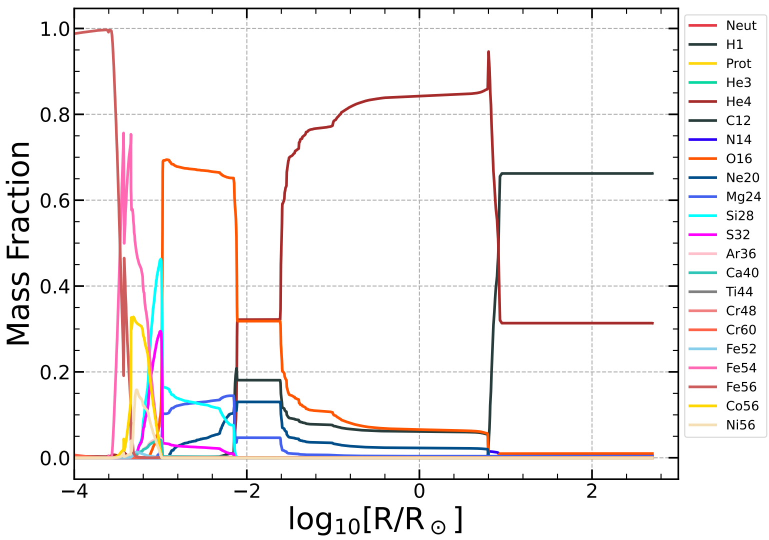

FIGURE 2.5: Pre-supernova mass fractions for an evolved 12 $M_\odot$ model for different species present in the 'approx21_cr60_plus_co56.net' (approx21) network used in MESA modelling.

through various steps until it reaches just below the surface, where the hand-off is performed from MESA to STELLA (Paxton et al. 2018). STELLA then deals with the shock-breakout and post-explosion evolution. Eventually, we obtain multiband light curves, bolometric luminosities, Fe II λ 5169 Å line velocities, and we compare these with the observations. Various explosion parameters such as explosion energy (E_{tot}), ^{56}Ni mass synthesized (M_{Ni}), shock propagation, structure smoothing, and addition of circumstellar material are also varied to obtain light curves satisfying the observations. The influence of some of these individual parameters on the resultant light curves is shown Figure 2.4 (*Right*). In most of our models, we utilize 400 zones for STELLA with 40 extra zones in the case of CSM. For the case of bolometric light curves, we used 40 frequency bins.

2.3.5 Spectral Synthesis using SYNAPPS

We generated synthetic spectra using SYNAPPS/Syn++ to ascertain better the presence/absence of species in the observed spectra. SYNAPPS and Syn++ are direct implementations of parameterized spectral synthesis code `SYNOW` (Parrent et al. 2010). It assumes a spherical symmetry for the ejecta, which is expanding homologously. The emission of photons is from a sharp photosphere, with the optical depth taken as a function of velocity:

$$\tau_{ref}(v) = \tau_{ref}(v_{ref}) \exp\left(\frac{v_{ref} - v}{v_e}\right)$$

where v_{ref} is reference velocity for parameterization and v_e is the maximum velocity allowed at the outer edge of the line-forming region (Thomas et al. 2011). For a particular optical depth, the reference line profile is estimated for a given ion with the remaining lines following Boltzmann statistics (Parrent et al. 2010). `SYNAPPS` iteratively generates synthetic spectra based on a provided input file with parameters such as ions list, blackbody temperature, expansion velocities, opacities, etc. The synthetic spectra thus obtained are compared with the observed spectra after each iteration. The procedure is automated and requires only initial input parameters with user-defined ranges for each parameter to constrain the parameter space physically. `SYNAPPS` has been predominantly used to model stripped-envelope and thermonuclear SNe spectra but has been successfully utilized in several hydrogen-rich SNe cases as well (Takáts & Vinkó 2012; Sahu et al. 2013; Bostroem et al. 2019; Dastidar et al. 2021).

2.3.6 Distance Estimation using EPM

Apart from Type Ia SNe 'standard candles', Type IIP SNe can also be utilized as independent distance probes using various methods. One widely used method is the expanding photosphere method, which can give distances to the Type IIP SNe. The implementation of the EPM is followed as per the details given in Hamuy et al. (2001) and Dessart & Hillier (2005a). This formalism involves measurements of two radii associated with SN: i) a photometric angular radius (θ) and ii) a spectroscopic physical radius (R). With the aid of these two radii, the distance to SN could be derived. The angular radius (θ) is given as:

$$\theta = \frac{\mathrm{R}}{\mathrm{D}} = \sqrt{\frac{\mathrm{f}_\lambda}{\pi \mathrm{B}_\lambda(\mathrm{T}) 10^{-0.4\mathrm{A}(\lambda)} \zeta_\lambda^2}},$$

where, D represents SN distance, $\mathrm{B}_\lambda(\mathrm{T})$ is Planck function at the corresponding color temperature, T, $\mathrm{A}(\lambda)$ is dust extinction, f_λ represents apparent flux density, and ζ_λ is the dilution factor to account for the deviation from a black body (Hamuy et al. 2001). The above equation could be transformed in terms of apparent magnitudes (m_λ) for multiband photometry as:

$$\mathrm{m}_\lambda = -5\log(\zeta_\lambda) - 5\log(\theta) + \mathrm{A}_\lambda + \mathrm{b}_\lambda(\mathrm{T}),$$

Now, for different filter sets (S), the above equation was minimized with b_λ values being taken from Hamuy et al. (2001), and dilution factors have been considered from these three different works: Hamuy et al. (2001), Dessart & Hillier (2005a) and Vogl et al. (2019). We then minimize the following quantity:

$$\varepsilon = \sum_{\lambda \epsilon \mathrm{S}} \left[\mathrm{m}_\lambda + \log(\theta_\mathrm{S}\zeta_\mathrm{S}) - \mathrm{A}_\lambda - \mathrm{b}_\lambda(\mathrm{T}_\mathrm{S})\right]^2$$

Finally, the expansion velocity (v) measured using spectra could be used in the following equation:

$$\frac{\theta_i}{v_i} \approx \frac{(t_i - t_0)}{D},$$

where subscript i implies for each epoch available. A straight line could be fit for multiple epochs, and the resulting slope is used to get a distance estimate.

2.3.7 Scaling relation for probable progenitor

Goldberg et al. (2019) obtained scaling relations combining various observables that could give a set of probable explosion properties. These explosion properties could yield an observed bolometric light curve that can be used for initial model guess in MESA models. Otherwise these can be utilized to obtain crude limits on various explosion parameters. These relations are solved to obtain E_{exp} and M_{ej} as a function of L_{50}, t_p, M_{Ni}, and R as:

$$\log(E_{51}) = -0.728 + 2.148 \log(L_{42}) - 0.280 \log(M_{Ni}) - 1.632 \log(R_{500}) + 2.091 \log(t_{p,2})$$

$$\log(M_{10}) = -0.947 + 1.474 \log(L_{42}) - 0.518 \log(M_{Ni}) - 1.120 \log(R_{500}) + 3.867 \log(t_{p,2})$$

where E_{51} is explosion energy in the units 10^{51} ergs, M_{Ni} has $M_\odot$ unit, L_{42} = Luminosity at 50 days/10^{42} erg s^{-1}, R_{500} = Progenitor Radius/500 $R_\odot$, M_{10} is the ejecta mass in the units 10 $M_\odot$, and $t_{p,2}$ = Plateau length/100 d.

Chapter 3

Ordinary Short-plateau SNe

3.1 Introduction

Type IIP SNe are usually observed with a characteristic light curve plateau duration of 100 d, while the short plateau events (as indicated earlier) have a plateau duration around 50–80 d or less. Apart from the apparent short plateau length as one of the key characteristics, their spectra consist of very conspicuous P-Cygni profiles from multiple elements. The short-plateau SNe, although few in number so far, do show differences in their observed properties. While the numbers are not large enough to group them into distinct sub-categories, for the ease of this study, we have grouped them into three categories, namely, ***"ordinary"***, ***"fast-declining"*** and ***"faint"*** short-plateau SNe. The basis of this division is their additional distinctive properties other than being a short-plateau SNe.

In this Chapter, we discuss the ordinary short-plateau events, defined as those events in which, except for the plateau duration, all other parameters such as the plateau phase decline rate, synthesized nickel mass, luminosity, and spectral feature bear resemblance to the normal Type IIP SNe. We analyze two such SNe, namely, SN 2020jfo and SN 2018gj.

3.2 SN 2020jfo: A short plateau Type II supernova from a low mass progenitor

ZTF discovered SN 2020jfo (also known as ZTF20aaynrrh) on 2020 May 06 in the galaxy M61 (NGC 4303) at $\alpha = 12^h21^m50^s.479$, $\delta = +04°28'54''.14$ ($J2000$). It was discovered at an AB magnitude of 16.0 mag in ZTF r-band. Merely within a day after the discovery, spectroscopic classification of SN 2020jfo was performed by the ZTF group (Perley et al. 2020) using spectra obtained with LT/SPRAT, NOT/ALFOSC, and P60/SEDM. Spectral matching with the `SNID` (Blondin & Tonry 2007) library showed Type IIP supernova SN 1999gi as a good match, about 7 days before maximum light. SN 2020jfo was suggested to be a young Type II supernova.

3.2.1 Observations

Optical Photometry with the 2-m HCT

A quick follow-up of SN 2020jfo began on 2020 May 07 (JD 2458977.2), i.e., $\sim$ 2 days after discovery, with HFOSC+HCT. It was monitored in two phases. In the first phase, it was observed until 2020 July 14 (JD 2459044.1), after which it went into Solar conjunction. When it reappeared in the night sky, the second phase of observations was carried out from 2020 November 14 (JD 2459167.5) to 2021 January 26 (JD 2459241.5). Panchromatic observations in Bessell-$UBVRI$

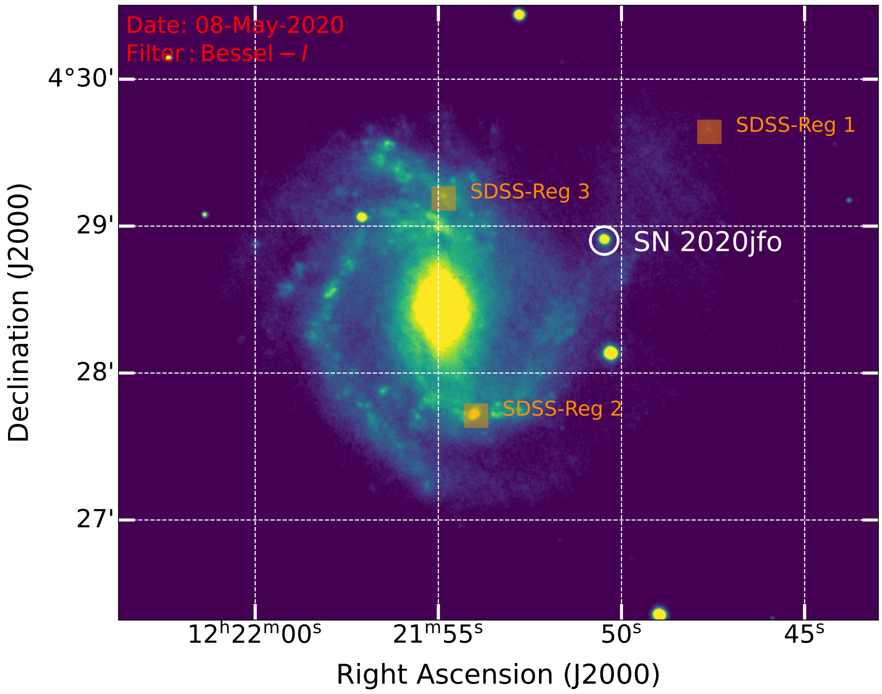

FIGURE 3.1: The I band image of SN 2020jfo in M61 obtained on 2020 May 08. The positions of the three regions of the archival SDSS-spectra [dark orange squares] along with SN 2020jfo [white circle] have been marked.

filters were obtained for a total of 23 epochs. The HCT optical data presented here are supplemented with data from the ZTF-g and $-r$ bands, obtained through ALeRCE (Sánchez-Sáez et al. 2021).

Since SN 2020jfo is situated in an outer spiral arm of M61, the host brightness could significantly affect the supernova luminosity, especially during the late phase. Hence, we used host template images, obtained during our monitoring program of SN 2008in, which occurred in the same galaxy, to remove the contribution from the host. The template images were registered to the field of SN 2020jfo, with the background subtracted, PSF matched, and subsequently scaled. The templates were subtracted from object frames, isolating the SN in the resulting frames. Aperture photometry was conducted on the SN, and the derived magnitudes were calibrated based on the nightly zero points determined from the original observations. The template subtraction procedure adopted is given in Singh et al. (2019a). The estimated magnitudes are noted in Table 3.1 and shown in Figure 3.2.

Table 3.1: SN 2020jfo: HCT $UBVRI$ photometric magnitudes

JD (2458900+)	**Phase†** (d)	U (mag)	B (mag)	V (mag)	R (mag)	I (mag)
77.2	3.2	13.89 ± 0.17	14.63 ± 0.05	14.85 ± 0.05	-	14.84 ± 0.01
78.3	4.3	-	14.57 ± 0.02	14.80 ± 0.03	14.74 ± 0.07	14.68 ± 0.02
79.2	5.2	-	14.51 ± 0.03	14.61 ± 0.04	14.57 ± 0.04	14.48 ± 0.05
80.2	6.2	13.84 ± 0.08	14.55 ± 0.03	14.61 ± 0.03	-	14.34 ± 0.05
81.1	7.1	13.85 ± 0.02	14.57 ± 0.02	-	14.32 ± 0.05	-
83.1	9.1	-	14.57 ± 0.01	14.59 ± 0.01	14.38 ± 0.02	14.36 ± 0.03
85.1	11.1	14.09 ± 0.05	14.63 ± 0.01	14.57 ± 0.02	-	14.39 ± 0.02
86.1	12.1	-	14.55 ± 0.03	-	-	14.30 ± 0.03
87.1	13.1	-	14.72 ± 0.02	-	14.46 ± 0.04	-
89.3	15.3	14.41 ± 0.07	14.80 ± 0.02	14.70 ± 0.03	14.42 ± 0.02	14.36 ± 0.03
90.2	16.2	14.54 ± 0.06	14.84 ± 0.02	-	14.47 ± 0.04	-
100.2	26.2	15.64 ± 0.11	15.35 ± 0.03	14.80 ± 0.03	14.47 ± 0.03	-
102.3	28.3	15.66 ± 0.13	15.47 ± 0.05	14.80 ± 0.05	14.50 ± 0.02	14.35 ± 0.03
104.3	30.3	-	15.57 ± 0.04	14.82 ± 0.02	14.51 ± 0.02	14.33 ± 0.14
109.2	35.2	16.28 ± 0.11	15.69 ± 0.02	14.86 ± 0.02	14.54 ± 0.02	14.35 ± 0.02
111.1	37.1	16.46 ± 0.06	15.70 ± 0.01	14.91 ± 0.02	14.53 ± 0.03	14.36 ± 0.04
119.2	45.2	16.77 ± 0.13	15.96 ± 0.03	15.01 ± 0.02	14.62 ± 0.05	14.40 ± 0.03
130.2	56.2	-	16.36 ± 0.04	15.20 ± 0.03	14.79 ± 0.03	14.51 ± 0.02
144.2	70.2	19.04 ± 0.14	18.15 ± 0.03	16.90 ± 0.01	16.14 ± 0.02	15.89 ± 0.04
267.5	193.5	-	19.50 ± 0.07	18.67 ± 0.03	17.71 ± 0.06	17.54 ± 0.04
280.5	206.5	-	19.51 ± 0.02	18.71 ± 0.04	17.92 ± 0.02	17.85 ± 0.05
309.5	235.5	-	19.75 ± 0.04	19.21 ± 0.03	18.40 ± 0.04	18.36 ± 0.01
316.4	242.4	-	19.50 ± 0.49	19.48 ± 0.29	18.46 ± 0.17	18.55 ± 0.26
341.4	267.4	-	-	19.71 ± 0.05	18.93 ± 0.04	-

†Phase= JD − t_{exp}, where t_{exp} = JD 2458974±2

*S*wift/UVOT photometry

SN 2020jfo was observed with the *Swift*/UVOT in all bands starting from 2020 May 07 (JD 2458976.6) and continued till 2020 August 08 (JD 2459069.6). Template subtraction for UVOT images was performed using the mean background flux estimated at the SN 2020jfo location from the archival images of M61 obtained during the follow-up of SN 2014dt. A similar flux was also obtained at the SN location as the light curve in the UV filters* flattened out during the post-plateau

*$UVW2$, $UVM2$, and $UVW1$

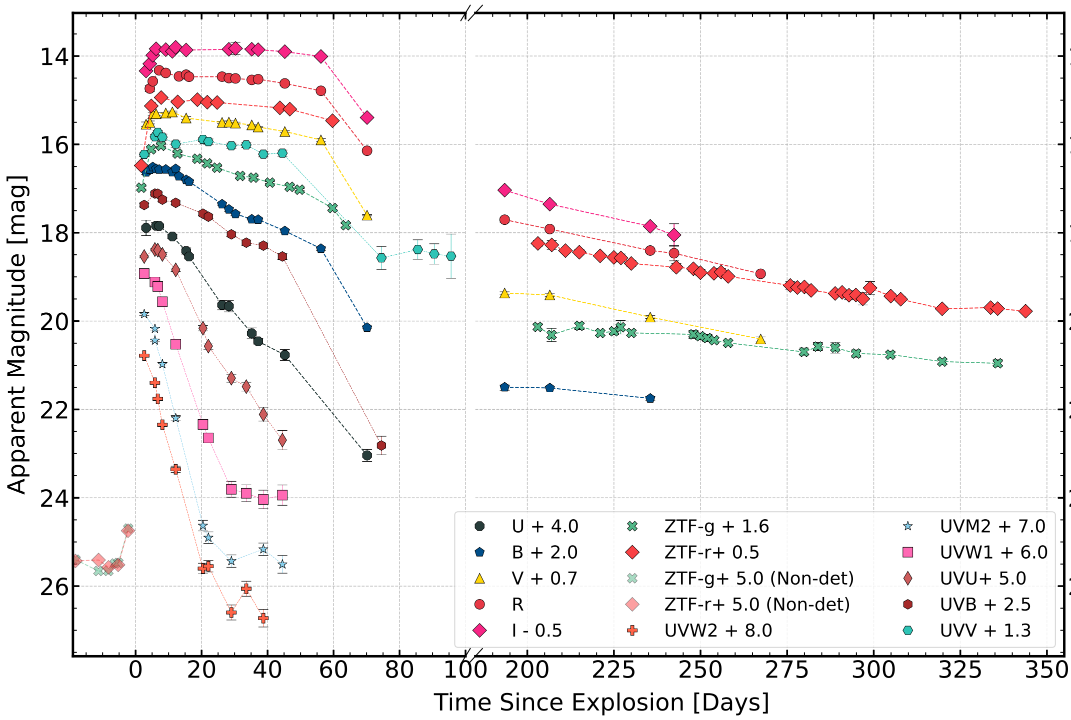

FIGURE 3.2: Panchromatic light curves for SN 2020jfo with photometry from HCT, Swift/*UVOT* and ZTF. The time period for which SN 2020jfo went behind the Sun has been obliterated from the plot and is marked by the discontinuity in the abscissa. Offsets in the apparent magnitudes are for visual clarity.

phase ($\gtrsim 60$ d).

Spectroscopic Observations

Spectra of SN 2020jfo were primarily obtained with the HCT starting from 2020 May 07 (JD 2458977.1) to 2021 January 26 (JD 2459241.4), using HFOSC with grisms Gr7 and Gr8. One spectrum at the nebular phase was obtained on 2021 February 21 (JD 2459266.5) with the ADFOSC instrument mounted at the 3.6 m DOT. The spectra of SN 2020jfo were redshift corrected using host $z = 0.00502$ (Perley et al. 2020). A log of spectroscopic observations is provided in Table 3.3.

TABLE 3.2: SN 2020jfo:*Swift*/UVOT magnitudes

JD (2458900+)	**Phase†** (d)	***UVW2*** (mag)	***UVM2*** (mag)	***UVW1*** (mag)	***UVU*** (mag)	***UVB*** (mag)	***UVV*** (mag)
76.6	2.6	12.78 ± 0.02	12.84 ± 0.03	12.92 ± 0.03	13.54 ± 0.03	14.87 ± 0.03	14.93 ± 0.05
79.9	5.9	13.39 ± 0.03	13.17 ± 0.03	13.11 ± 0.03	13.38 ± 0.03	14.61 ± 0.03	14.53 ± 0.05
80.7	6.7	13.76 ± 0.03	13.44 ± 0.03	13.22 ± 0.03	13.39 ± 0.03	14.62 ± 0.03	14.43 ± 0.04
82.1	8.1	14.34 ± 0.04	13.98 ± 0.04	13.56 ± 0.04	13.49 ± 0.04	14.75 ± 0.04	14.54 ± 0.07
86.2	12.2	15.35 ± 0.07	15.20 ± 0.06	14.52 ± 0.05	13.84 ± 0.04	14.82 ± 0.05	14.69 ± 0.07
94.4	20.4	17.60 ± 0.13	17.63 ± 0.12	16.34 ± 0.09	15.16 ± 0.06	15.06 ± 0.04	14.59 ± 0.05
96.0	22.0	17.55 ± 0.13	17.90 ± 0.13	16.64 ± 0.11	15.57 ± 0.07	15.14 ± 0.04	14.63 ± 0.06
103.0	29.0	18.59 ± 0.17	17.43 ± 0.14	17.81 ± 0.18	16.29 ± 0.09	15.54 ± 0.05	14.73 ± 0.06
107.5	33.5	18.05 ± 0.17	-	17.89 ± 0.19	16.48 ± 0.10	15.72 ± 0.06	14.71 ± 0.06
112.7	38.7	18.72 ± 0.20	18.16 ± 0.14	18.04 ± 0.21	17.11 ± 0.15	15.79 ± 0.06	14.92 ± 0.06
118.5	44.5	-	18.50 ± 0.20	17.94 ± 0.23	17.70 ± 0.22	16.04 ± 0.07	14.90 ± 0.07
148.5	74.5	-	-	-	-	20.31 ± 0.21	17.27 ± 0.26
159.5	85.5	-	-	-	-	-	17.08 ± 0.22
164.5	90.5	-	-	-	-	-	17.18 ± 0.23
169.6	95.6	-	-	-	-	-	17.23 ± 0.50

†Phase= JD $-$ $t_{\rm exp}$, where t_{exp} = JD 2458974±2

3.2.2 Host Analysis

Reddening, Distance, and Metallicity

The reddening within the Milky Way in the direction of the host M61 is $E(B-V)_{\rm MW} = 0.0194 \pm 0.0001$ mag which is obtained from IRSA† Galactic Dust Reddening and Extinction map (Schlafly & Finkbeiner 2011). We also noted a prominent Na I D absorption feature due to host with pseudo-equivalent width, EW= 1.14 ± 0.04 Å, in the co-added spectrum obtained from three early phase spectra, spanning 11 to 15 d from explosion date (see Section 3.2.3 for explosion epoch). The host galaxy reddening ($E(B-V)_{\rm host}$) is estimated using two independent methods. The empirical relations between $E(B-V)$ and Na I D absorption lines EW provided by Barbon et al. (1990) and Poznanski et al. (2012) were used to

†NASA/IPAC Infrared Space Archive

TABLE 3.3: Spectra logs of SN 2020jfo

JD *(2458900+)*	**Phase†** *(d)*	**Wavelength** *(Å)*
77.1	3	4000–8000; 5200–9000
78.3	4	4000–8000; 5200–9000
79.2	5	4000–8000; 5200–9000
81.2	7	4000–8000; 5200–9000
85.1	11	4000–8000; 5200–9000
86.2	12	4000–8000; 5200–9000
89.3	15	4000–8000; 5200–9000
102.2	28	4000–8000; 5200–9000
110.1	36	4000–8000; 5200–9000
112.1	38	4000–8000; 5200–9000
119.2	45	4000–8000; 5200–9000
129.2	55	4000–8000; 5200–9000
144.1	70	4000–8000
270.5	196	4000–8000
276.5	202	4000–8000; 5200–9000
309.4	235	4000–8000; 5200–9000
341.4	267	4000–8000; 5200–9000
366.4	292	4000-9000 [DOT]

†Phase= JD − $t_{\rm exp}$, where t_{exp} = JD 2458974±2

infer $E(B-V)_{\rm host}$ of 0.29 ± 0.01 mag and 0.30 ± 0.08 mag, respectively. Secondly, reddening was also estimated using Balmer decrements, with host galaxy spectra from three regions, marked in Figure 3.1, obtained from the SDSS archive. The ratio of Hα and Hβ line fluxes were measured, and the color excess was estimated using the relation given by Domínguez et al. (2013), which resulted in an $E(B-V)_{\rm host} = 0.25 \pm 0.02$ mag. The extinction obtained using the two independent methods agrees within errors. A weighted mean from the above estimates gives $E(B-V)_{\rm host} = 0.27 \pm 0.08$ mag. The total $E(B-V) = 0.29$ mag reddening is adopted in this work.

A plethora of distance measurements to the host galaxy M61 are provided on the NED[‡], with variation from 7.59 Mpc (Bottinelli et al. 1984) to 35.50 Mpc (Sparks 1994) including both redshift-dependent and redshift-independent measurements.

[‡]NASA/IPAC Extragalactic Database http://ned.ipac.caltech.edu

Recent redshift-independent measurements based on SN 2008in constrain the distance to 12-20 Mpc (see Rodríguez et al. 2014; Bose & Kumar 2014). A simple mean of all these estimates could not be adopted as the values are not continuous but at extremes. Steer (2020) has defined a robust method to get enhanced mean estimate distances (MED) using the weighted mean for the distances from various primary and secondary sources. From the various means, we have estimated MED 7, which is a combination of the unweighted (MED 2), error-weighted (MED 3), and date-weighted (MED 4) means with weights of 1:2:4, respectively. The distance obtained is, $D_L = 16.45 \pm 2.69$ Mpc ($\mu = 31.08 \pm 0.36$ mag).

TABLE 3.4: O3N2-index and E(B-V) estimated from the SDSS spectra of 3 regions in M 61. The regions have been marked in the Figure 3.1.

Regions	**O3N2-index**	**12+log[O/H]**	***E(B-V)***
SDSS-Reg 1	1.16	8.36	0.28
SDSS-Reg 2	-0.32	8.83	0.22
SDSS-Reg 3	-0.48	8.88	0.26

To estimate the host environment properties, we used archival SDSS spectra of the three regions in M61, as indicated earlier (refer Figure 3.1). Fluxes of the strong emission lines from Hα, Hβ, [N II] 6584 Å and [O III] 5007 Å were measured and the O3N2 index (Pettini & Pagel 2004) was estimated which provided gas-phase O abundance (12+log[O/H]) Pettini & Pagel (2004). The metallicity estimates for all three regions are noted down in Table 3.4. It was observed that towards the outer edge of the galaxy, the metallicity is sub-solar with an oxygen abundance of ~ 8.36 dex($\sim 0.5\,Z_{\odot}$)[§], whereas in the regions on the spiral arms (Regions 2 and 3), the metallicity is 8.83 dex and 8.88 dex ($\sim 1.6\,Z_{\odot}$), respectively.

[§]Solar value for 12+log[O/H] is taken from Asplund et al. (2006) which is 8.66 ± 0.05 dex

3.2.3 Light Curve Properties

Light and color curves evolution

The last non-detection of SN 2020jfo was on UT 2020 May 02.27 (JD 2458971.8) with an AB mag of >19.7 mag in the ZTF$-g$ filter (Nordin et al. 2020). The supernova was discovered on UT 2020 May 06.26 (JD 2458975.7). The mean epoch considering the first detection and the last non-detection is JD 2458973.75. Hence, JD 2458974±2 is taken as the date of explosion and has been used for defining phase throughout this work.

Table 3.5: Peak magnitudes from UV/Optical light curves

Band	**t(m$_{max}$)** (MJD)	**m$_{max}$** (mag)
U	58978.71±0.70	13.83±0.08
B	58979.19±0.28	14.53±0.03
V	58981.54±0.35	14.55±0.03
R	58982.58±0.25	14.38±0.02
I	58981.31±0.56	14.30±0.05
ZTF-g	58980.63±0.21	14.46±0.02
ZTF-r	58982.35±0.37	14.47±0.03
UVU	58979.23±0.28	13.37±0.03
UVB	58980.23±0.31	14.61±0.03
UVV	58981.54±0.58	14.45±0.05

The light curve evolution of SN 2020jfo in Bessell U, B, V, R, I, ZTF$-g, -r$ bands and *Swift* $UVOT$-bands is shown in Figure 3.2. Optical light curves are observed with a relatively swift rise to the peak in all bands. To estimate peak magnitudes and rise times to the peak in various bands, we fitted a cubic spline to the observed photometric data. The estimated peak magnitude and date of maximum in different bands are given in Table 3.5. The rise time ranges from 5.2 d in U to 9.1 d in R band, with a similar trend seen in *Swift*-UVOT bands from 5.7 d in UVU

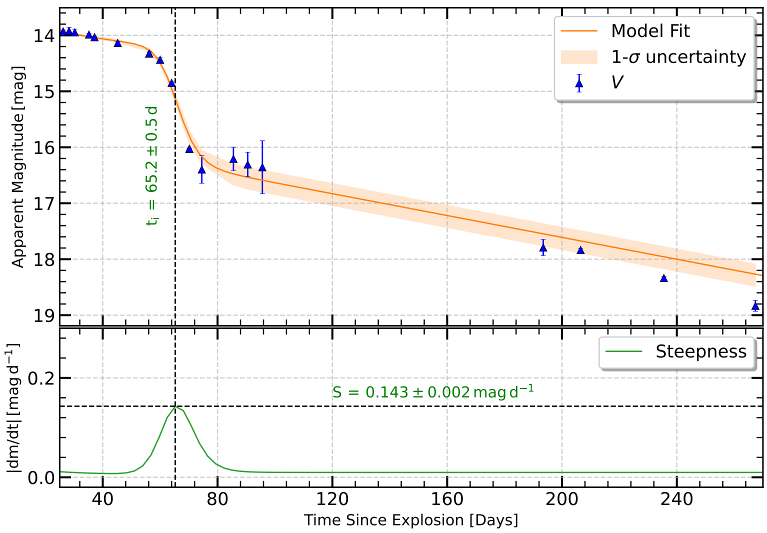

FIGURE 3.3: Estimated Steepness of SN 2020jfo using the functional form from Elmhamdi et al. (2003b).

to 8.0 d in UVV, and 7.1 d and 8.9 d in ZTF$-g$ and r-bands, respectively. Early phase light curves show a bump around the peak light, which is more noticeable in the redder bands (R and ZTF-r). Post peak, the light curves vary very slowly in the redder bands and settle onto a plateau that appears to be short.

To better estimate the plateau length, observations during the transition period, starting from the late plateau to the early radioactive declining phase, are required. Although only one observation could be made during this phase due to observational constraints, we notice a steep decline in ZTF-g band at +60 d. Moreover, observations around +70 d and beyond (in UVV) indicate that the SN has already entered into the radioactive decay tail. This puts an upper limit on the plateau length as 70 d. Also, we do not see any change in slope in the V-band evolution until +56 d. With this, the lower limit of the plateau length is constrained as 56 d. With these limits, the plateau (OPTd, Anderson et al. 2014a) length is estimated as ∼63±7 d.

Another way to estimate the upper limit of the plateau length is by estimating the date of inflection during the transition phase, which is defined as the point of maximum steepness/slope. We use the formulation from Elmhamdi et al. (2003b) to fit the late-plateau and radioactive decay phase in the V-band evolution (Figure 3.3). We could include some more points in V-band during the transition phase covering end-plateau to early nebular phase using ZTF-g and UVV magnitudes. The g-band magnitudes were transformed to V magnitudes by the transformation relations (Jester et al. 2005). Fit to a better sampled time evolution of V-band flux resulted in the steepness parameter 0.143±0.002 mag d^{-1} and 65.2±0.5 d as the day of inflection. This is in concurrence with our plateau length estimate.

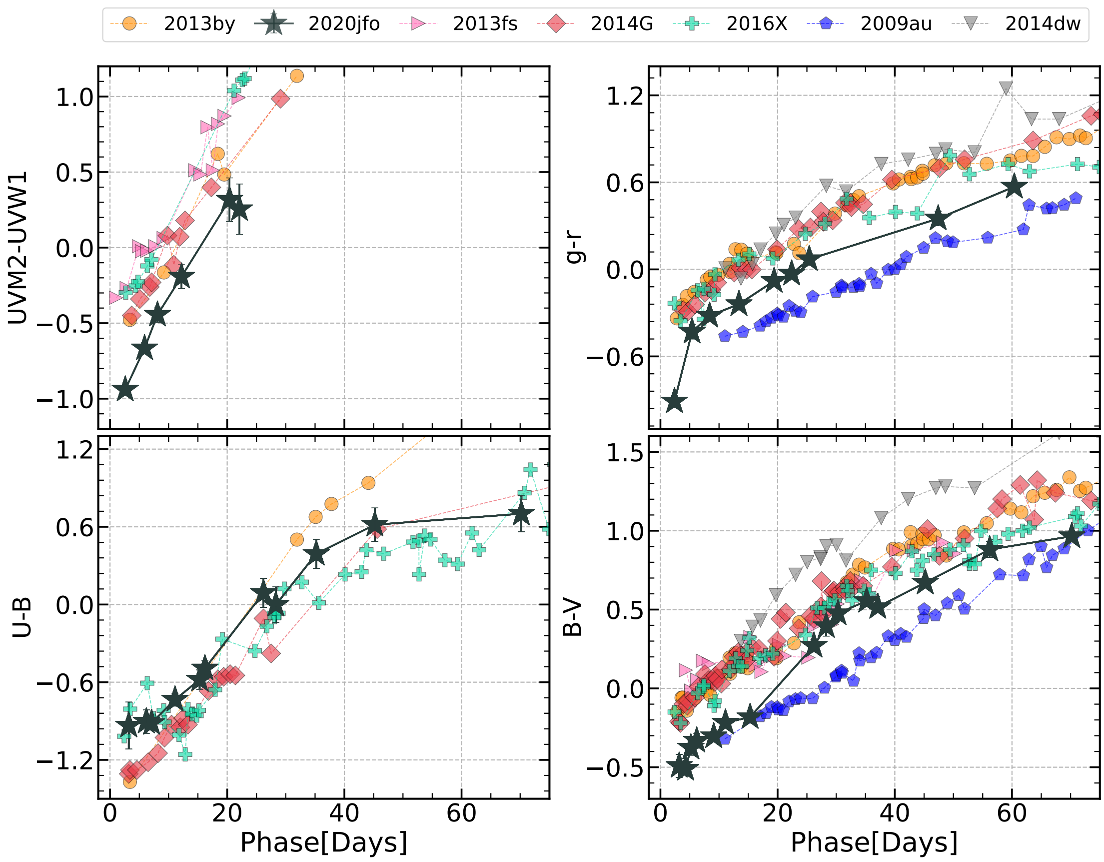

FIGURE 3.4: color evolution of SN 2020jfo from the early rise up to the plateau phase is plotted along with some other Type II SNe.

The mean plateau length for a sample of Type IIP SNe was found to be ∼ 100 d (Anderson et al. 2014a), while the estimated plateau length is much shorter for SN 2020jfo ∼ 63 d. Only a handful of such objects have been discovered till now, namely, SN 2006Y, SN 2006ai, SN 2008bp, SN 2008bu (Anderson et al. 2014a), SN 2014G (Terreran et al. 2016), and SN 2016egz (Hiramatsu et al. 2021a). Temporal evolution for several UV and optical colors for SN 2020jfo during the early phase is given in Figure 3.4. The colors are extinction corrected for reddening estimated in Section 3.2.2. The color evolution of some other well-studied objects is also represented for comparison. The color evolution of SN 2020jfo follows the blue-to-red trend, indicating the cooling of the ejecta as the supernova evolves. SN 2020jfo shows overall bluer color, the $UVM2-UVW1$, $B-V$, and $g-r$ color of SN 2020jfo is observed to be bluer than all other SNe used for comparison, with the exception of SN 2009au.

Absolute V-band light curve

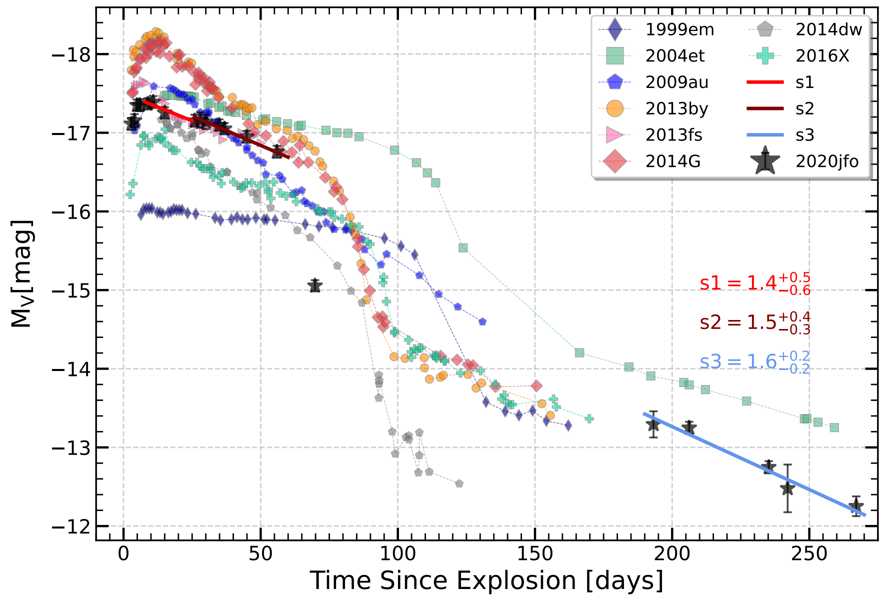

FIGURE 3.5: Absolute V-band light curve of SN 2020jfo is plotted with a few other Type II SNe. Distance and extinction correction for individual objects are obtained from their references as provided in Section 3.2.3. The decline rates during the early plateau (s1), late plateau (s2), and nebular (s3) phases determined using linear fit are also mentioned.

The temporal evolution of absolute V-band magnitudes of SN 2020jfo is obtained after correcting the observed V-band magnitude for extinction with Cardelli extinction law and the estimated distance. The V-band light curve peaked on $\sim 8.0\,$d after the explosion with $M_V = -17.40 \pm 0.37$ mag, putting it under the category of luminous Type IIP events. We estimated the light curve slopes during different phases $s1$, $s2$ and $s3$, (Anderson et al. 2014a) for SN 2020jfo as $1.4^{+0.5}_{-0.6}$, $1.5^{+0.4}_{-0.3}$ and $1.6^{+0.2}_{-0.2}$ mag per 100 days, respectively. Based on a large number of Type II SNe light curves, Anderson et al. (2014a) estimated mean values of 2.65 ($s1$), 1.23 ($s2$), and 1.47 ($s3$) mag per 100 days, indicating a clear switch from the early phase decline to the constant or very slowly declining plateau phase. The estimated values of $s1$ and $s2$ for SN 2020jfo indicate the absence of such a clear transition, although the rise to peak magnitude is similar to other Type II SNe. It thus appears that either the $s1$ phase lasted for a very short period, or is missing entirely.

The comparison of V-band absolute magnitude temporal evolution of SN 2020jfo with other Type II SNe, including short plateau events, is shown in Figure 3.5. As the number of short plateau objects studied in detail so far is small, we compared the light curve of SN 2020jfo with a sample of objects including archetypal Type IIP SNe, SN 1999em (Elmhamdi et al. 2003a) and a nearby well-studied SN 2004et (Sahu et al. 2006), Type II SNe with CSM-signatures, SN 2009au (Rodríguez et al. 2020), SN 2013fs (Bullivant et al. 2018), and SN 2014G (Terreran et al. 2016), and faster declining or short plateau Type II SNe, SN 2013by (Valenti et al. 2015), SN 2014dw (Valenti et al. 2016) and SN 2016X (Huang et al. 2016). Although SN 2014G and SN 2013by are more luminous than SN 2020jfo during the pre-maximum, early decline, and plateau phase, in the nebular phase their light curves are similar to that of SN2020jfo. In the case of SN 2013fs, the early decline after the peak is faster in comparison to SN 2020jfo, but the plateau brightness is similar.

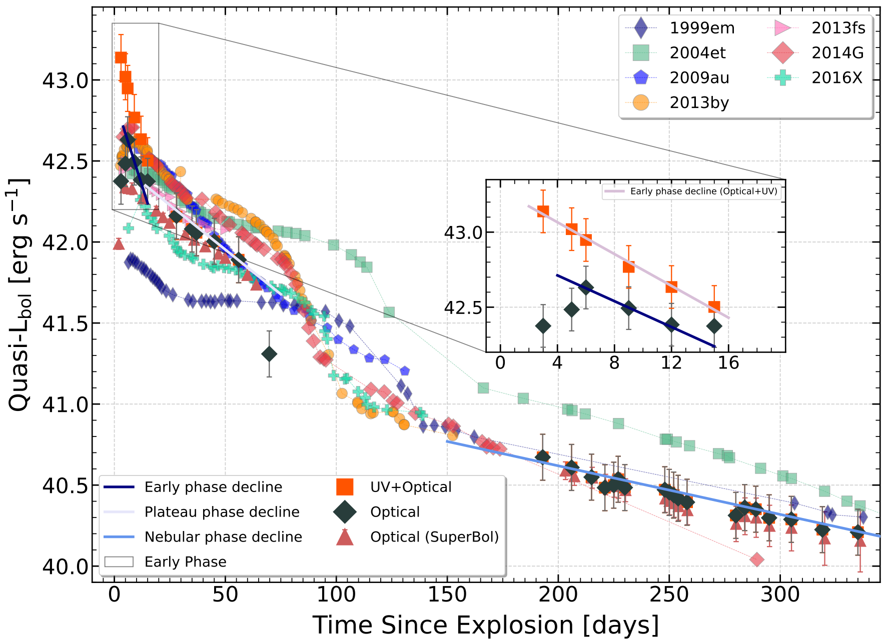

FIGURE 3.6: Quasi-bolometric light curve (Q-bol) of SN 2020jfo along with other Type II SNe. Q-bol with contribution from UV fluxes and from `SuperBol` (without BB-corrections) are also plotted. The inset shows Optical and UV+Optical Q-bol during the early phase.

Pseudo-bolometric Light Curve Evolution

The quasi-bolometric light curve (Q-bol) of 2020jfo is calculated using the observed extinction (MW+host) corrected fluxes in $UVW2, UVM2, UVW1, U, B$, ZTF$-g, V, R$, and I filters. Extinction corrections in individual photometric bands are applied using the relations by Cardelli et al. (1989, $R_V = 3.1$). The extinction-corrected apparent magnitudes were converted to fluxes at the effective filter wavelength, with Bessell-$UBVRI$ zero-points taken from (Bessell et al. 1998). The SVO Filter Profile Service¶ was utilized to obtain zero-point for bands other than 'Bessell' filters. The spectral energy distribution (SED) curve for each epoch was estimated by interpolating the estimated flux in different bands using a spline (cubic) function. Finally, the quasi-bolometric flux was estimated by integrating the SED through the first band's initial wavelength to the last band's upper cut-off

¶SVO FPS: http://svo2.cab.inta-csic.es/theory/fps/

wavelength. On the nights when magnitudes were not available for some bands, we used linear interpolation to estimate them.

The quasi-bolometric luminosity for initial epochs, *i.e.*, up to +28 d, includes UV fluxes obtained from *Swift-UVOT* and, beyond that, the contribution is computed only using $UBgVRI$ filters. Figure 3.6 shows the quasi-bolometric light curve with and without UV contribution. It is evident from Figure 3.6 (and its inset) that during the first $\sim$ 15 days, the contribution from UV bands to the bolometric flux is significant, and beyond this, it becomes very small in comparison to the optical flux. During the late nebular phase, where only ZTF data are available, bolometric correction (BC_g) was derived using the final few observed data in the LC for which the $BgVRI$ quasi-bolometric luminosity could be obtained. The estimated BC_g was applied to ZTF-g magnitudes obtaining bolometric luminosity till the very late phase.

For comparing our bolometric estimates, we also use `SuperBol` (Nicholl 2018), with ZTF-g as the reference band. `SuperBol` fits a polynomial to bands with missing data and integrates those at epochs of the reference band. It seems to slightly underestimate the luminosity at the earlier epochs, where we see some signs of enhanced flux in individual optical light curves. It might be due to the smoothing of the data with a polynomial approximation. At other phases, quasi-bolometric light curve flux estimated in two different ways, match quite well. The contribution from optical flux to the UV+Optical bolometric flux is $\approx$ 20% at +3 d, which increases to $\approx$ 80% at $\sim$ +15 d and almost in entirety at $\sim$ +28 d.

Clearly, discrete decline trends are visible in the Q-bol light curve where the initial decline from +6 d to +15 d is significantly steeper than other supernovae. Each decline phase is linearly fitted using Python's `emcee` routine. For comparison, the slopes for other objects during similar phases are computed and tabulated in Table 3.6.

TABLE 3.6: Best fit slopes of Q-bol light curve during various phases where decline is conspicuous. Slopes for comparison Type II SNe have also been estimated wherever possible.

SNe⇒	2020jfo	1999em	2004et	2009au	2013by	2013fs	2014G	2016X
Phases ⇓	Slopes(dex{log[L(erg s^{-1}]} 100 d^{-1})							
Early	$-4.00^{+1.02}_{-1.09}$	$-1.27^{+0.06}_{-0.05}$	$-1.33^{+0.02}_{-0.02}$	$-1.84^{+0.01}_{-0.01}$	$-1.60^{+0.01}_{-0.01}$	$-1.33^{+0.01}_{-0.01}$	$-1.32^{+0.02}_{-0.02}$	$-1.56^{+0.02}_{-0.02}$
Plateau	$-0.91^{+0.19}_{-0.20}$	$-0.08^{+0.01}_{-0.01}$	$-0.22^{+0.01}_{-0.01}$	-	$-0.89^{+0.01}_{-0.01}$	-	$-0.98^{+0.03}_{-0.04}$	$-0.52^{+0.01}_{-0.01}$
Nebular	$-0.32^{+0.03}_{-0.04}$	$-0.30^{+0.01}_{-0.01}$	$-0.44^{+0.01}_{-0.01}$	-	$-0.45^{+0.05}_{-0.04}$	-	$-0.68^{+0.04}_{-0.03}$	$-0.77^{+0.02}_{-0.02}$
Early UV+Optical	$-5.33^{+0.42}_{-0.41}$	-	-	-	-	-	-	-

Q-bol light curve of SN 2020jfo peaks at $\sim$ $4.3 \pm 1.4 \times 10^{42}$ erg s^{-1} in optical bands around +6 d, whereas we missed the peak in the UV+Optical data. During the very early phase, Q-bol declines at a rate of $4.00^{+1.02}_{-1.09}$ dex 100 d^{-1} and $5.33^{+0.42}_{-0.41}$ dex 100 d^{-1} in Optical and UV+Optical respectively, whereas for the other SNe this early phase decline is less steeper. For SNe 1999em, 2004et, and 2013fs we estimated an early phase decline of 1.27 dex 100 d^{-1}, 1.33 dex 100 d^{-1}, and 1.33 dex 100 d^{-1}, respectively. For some of the SNe SN 2009au (1.84 dex 100 d^{-1}), SN 2013by (1.60 dex 100 d^{-1}) and SN 2016X (1.56 dex 100 d^{-1}), we find the decline to be steeper than normal Type II SNe, but significantly lower than SN 2020jfo (see Table 3.6). During the plateau phase and nebular phase, we find decline rates for SN 2020jfo to be $0.91^{+0.19}_{-0.20}$ dex 100 d^{-1} and $0.32^{+0.03}_{-0.04}$ dex 100 d^{-1}, respectively. Plateau phase decline is found to be similar to SN 2013by (0.89 dex 100 d^{-1}) and SN 2014G (0.98 dex 100 d^{-1}). In terms of magnitude, the slope in the radioactive decay phase is found to be $0.80^{+0.08}_{-0.10}$ mag 100 d^{-1}.

^{56}Ni Mass

To calculate the synthesized mass of ^{56}Ni, we employed two independent methods. Firstly, we used the Equation 2.1. Using the quasi-bolometric luminosity from

$\sim$ 192 d onward as tail luminosity, L_t, the mass of synthesized ^{56}Ni is estimated as $0.019 \pm 0.005\,M_\odot$. In this case, the IR contribution to the pseudo-bolometric luminosity is not included, and hence, terming it to be a lower limit on ^{56}Ni mass.

Subsequently, we conducted a comparative analysis of the late-phase quasi-bolometric luminosity of SN 2020jfo in relation to that of SN 1987A as referred in 2.2. Assuming that the γ-ray deposition in SN 2020jfo is similar to SN 1987A, mass of ^{56}Ni in SN 2020jfo was estimated using Equation 2.2. If a constant fraction of about 35% (as estimated by Patat et al. 2001 and Elmhamdi et al. 2003b) is added to quasi-bolometric flux to account for missing NIR flux, the ^{56}Ni mass synthesized in 2020jfo becomes $0.033 \pm 0.004\,M_\odot$, consistent with our earlier estimate if a similar IR correction is used. This value is also typical of Type II SNe being the average ^{56}Ni mass ($= 0.033\,M_\odot$) obtained by Anderson (2019) for more than 40 SNe of Type II class. Mass of ^{56}Ni estimated using steepness parameters (Equation 2.3) of 0.143 mag d^{-1} (refer Section 3.2.3) is $0.030 \pm 0.002\,M_\odot$, which is similar to earlier estimates.

We also use Equation 2.4 to estimate ^{56}Ni mass. The FWHM of Hα line was measured in the +292 d spectrum by fitting a Gaussian profile. Mass of ^{56}Ni estimated using this method is found to be $0.047^{+0.005}_{-0.004}\,M_\odot$, which is higher than our earlier estimates. It clearly signifies a broadened line emission profile in SN 2020jfo, implying a larger velocity dispersion in the line-forming region, whereas, in a typical Type IIP SN, the dispersion would have been lower due to a massive hydrogen envelope.

3.2.4 Spectroscopic Evolution

The optical spectra of SN 2020jfo spanning about 300 days starting from +3 d to around +292 d is shown in Figure 3.7. The spectral evolution at various phases, also compared with other Type II supernovae, is part of this Section.

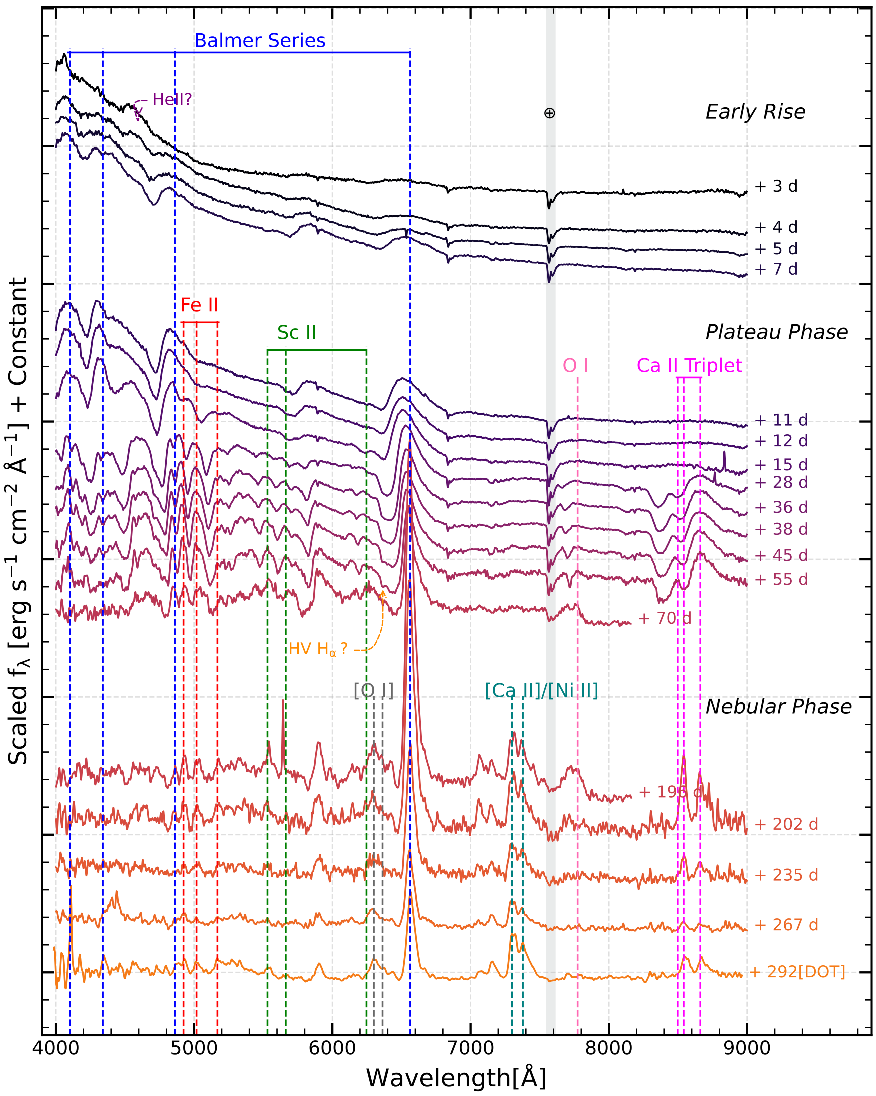

FIGURE 3.7: Time evolution of SN 2020jfo spectra from 3 d until 292 d post explosion. Lines have been identified following Gutiérrez et al. 2017a, with some prominent lines marked. All spectra are flux-calibrated and corrected for reddening and redshift.

.

Pre-Maximum Spectral Evolution

In the first spectrum obtained on +3 d, we detect a broad absorption trough at 6266 Å, likely from Hα and yields a line velocity $\sim$13,500 km s^{-1} (Figure 3.7, 3.8).

If we look for an Hβ counterpart at a similar velocity, we should detect an absorption dip at 4650 Å. Instead, we observe a broad P-Cygni feature with emission at around 4686 Å and its absorption counterpart at roughly 4466 Å. The feature is likely a broad feature of He II 4686 Å at roughly 14,000 km s^{-1}, agreeing with Hα line velocity feature. This feature faded after +4 d, and a feature redward of this started appearing, which was identified as Hβ owing to a similar velocity with the Hα feature. Broad He II 4686 Å was also seen in SN 2013fs (Bullivant et al. 2018; Chugai 2020) and is indicative of the presence of a CDS[‖] above the photosphere. He II feature has a blue-skewed boxy profile, which suggests a geometrically thin and unfragmented CDS (Chugai 2020). The He II presence in the early spectra typically arises from the rapid recombination resulting from the SN ejecta interacting with extended supergiant atmosphere (Bruch et al. 2021). However, these would lead to the existence of narrow emission lines in the spectra. The presence of a broad P-Cygni profile suggests that the spectral line originated in the SN ejecta. This would require that the ejecta and the nearby CSM are highly ionized by the shock passage, it was also observed in SN 2006bp (Quimby et al. 2007).

To ascertain the presence of He II feature observed in the early spectra, we used rapid spectral modeling code TARDIS (Kerzendorf & Sim 2014). Incorporating modifications from Vogl et al. (2019), TARDIS is now capable of synthesizing spectra for Type II events as well. For our initial setup, we used uniform density configuration with a density profile in the form of power law (Vogl et al. 2019). Hydrogen was treated in the non-local thermodynamic equilibrium (NLTE) approximation. We used different compositions for the outer layers, including CNO, H only, He only, H+He only and H+He+CNO. We fixed luminosity parameters for +4 d calculations and used temperature as a free parameter. The observed velocities ($\sim 14000 - 16000$ km s^{-1}) estimated from the spectral features are used as velocities of the envelope layers. The resulting spectral luminosity was scaled with distance to obtain the observed flux values. The synthesised spectra along

[‖]Cold Dense Shell

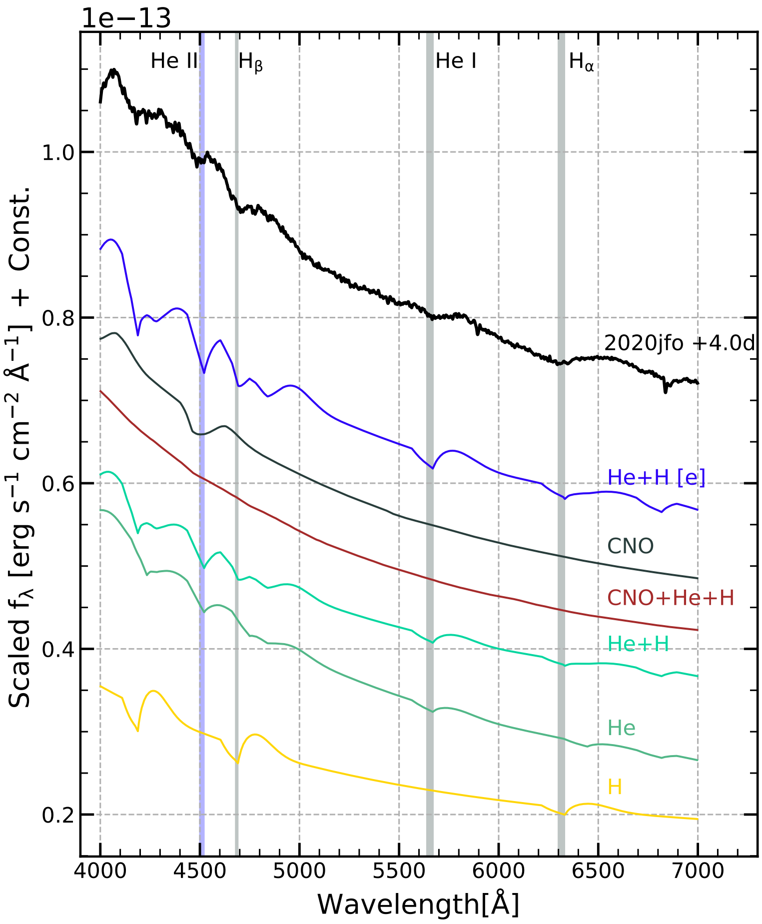

FIGURE 3.8: Early phase (+4.0 d) spectrum of the SN 2020jfo is compared with synthetic spectra generated using TARDIS, indicating the presence of ionized helium. The relative contributions due to different elemental compositions are plotted. In the square brackets, 'e' implies the enhanced abundance of He in the composition.

with the SN 2020jfo spectrum at +4 d are shown in Figure 3.8. It was noticed that reproducing the ionized helium feature required a temperature range of ∼9000 K to ∼18000 K along with a higher helium abundance than Solar values. On the other hand, for this feature to be a blend of Nitrogen and Carbon, the modeling required much higher CNO abundances, which are almost an order of magnitude higher than the Solar values and are rather non-physical. However, some amount of blending along with the helium could not be ruled out altogether. This strengthens the case that the observed broad absorption feature is likely a He II feature.

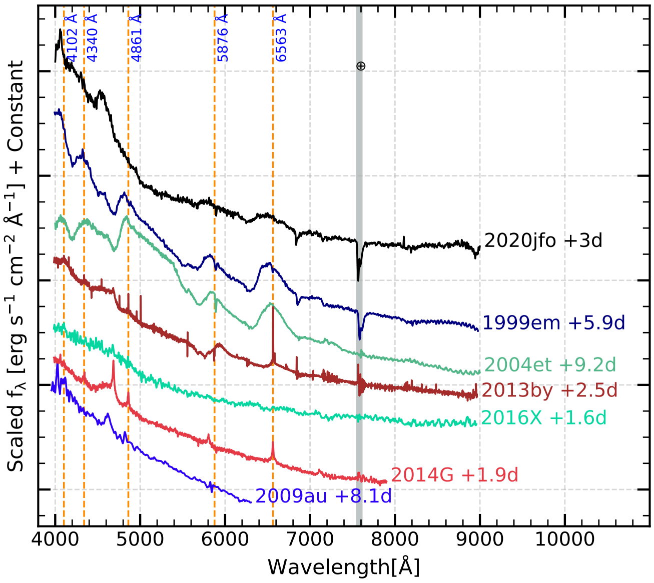

FIGURE 3.9: The pre-maximum (+2.8 d) spectrum of SN 2020jfo compared with the spectra of other Type II SNe around similar epochs.

The spectrum obtained during +4 d to +7 d shows the gradual development of Balmer spectral features. Absorption trough around 5600Å is seen in the spectrum obtained on +4 d which is likely due to He I 5876 Å which evolved into a fully developed P-Cygni profile on +7 d. The continuum becomes redder as the supernova ejecta evolves. We compare SN 2020jfo spectrum obtained on +3 d with some other objects' spectrum at comparable epochs (Figure 3.9). The early phase spectra of SN 1999em and SN 2004et show a broad absorption over blue continuum due to hydrogen Balmer lines, while the early spectra of SNe 2009au, 2013by and 2014G show narrow flash-ionized lines. The spectrum of SN 2020jfo appears different than the other objects with shallow absorption due to Hα and the presence of broad absorption due to He II.

Plateau Phase Spectral Evolution

As SN enters the plateau regime, the photosphere cools to recombination temperature and stays in the hydrogen envelope, leading to the development of various

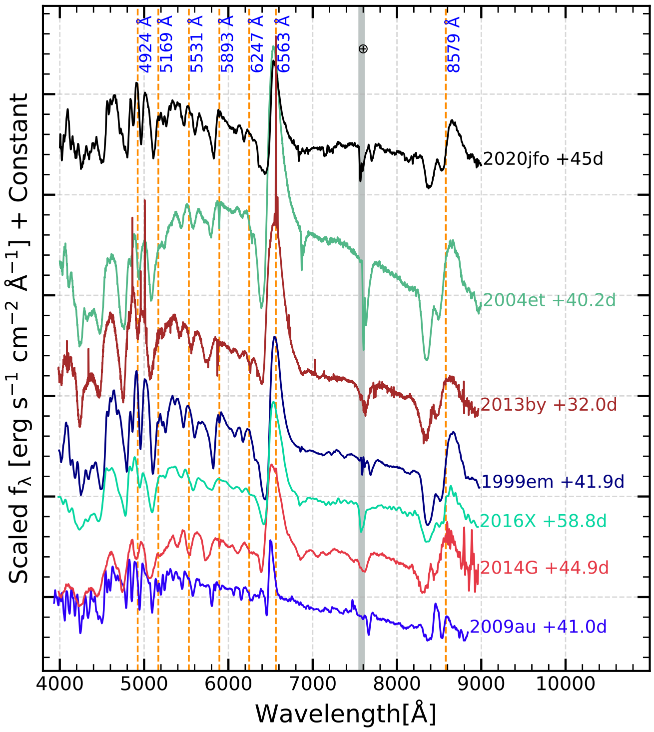

FIGURE 3.10: SN 2020jfo spectrum compared with other Type II SNe during the plateau phase

metallic lines of Iron, Scandium, Oxygen, and Calcium in the spectra. In the early phase, He I feature slowly vanishes by +15 d and the Na I D feature appears at its place. The feeble absorption feature seen around 5000 Å in the +12 d spectrum is due to the Fe II features at 4924 Å, 5018 Å, and 5169 Å). This feature strengthens as the photosphere moves deep inside the hydrogen envelope. Hydrogen Balmer lines become stronger, and several other metal features such as, Sc II (5663 Å), Sc II/Fe II (5531 Å), He I/Na ID, Ba I and Calcium NIR triplet develop in the spectra. We also detect O I 7774 Å absorption feature in the +28 d spectrum.

SN 2020jfo spectrum obtained ∼+45 d is compared with the other well-studied objects' spectra in Figure 3.10. Most spectral features are identical in all the Type II SNe compared. The Hα absorption feature in SN 2020jfo is shallower compared to the typical SNe of Type II class like SNe 1999em and 2004et, whereas it is similar to fast-declining Type II such as SNe 2009au, 2013by, and 2014G. Further, in SN 2020jfo, the Hα absorption trough is broader than other objects. The

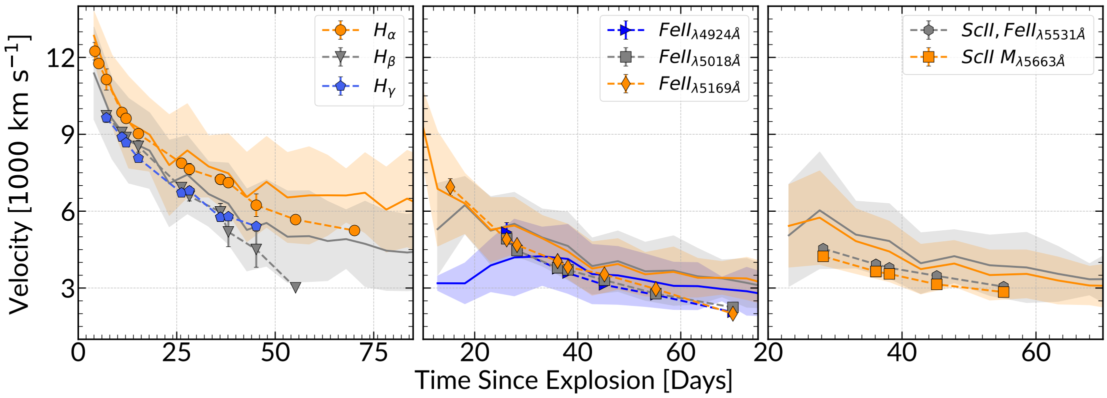

FIGURE 3.11: Line velocity evolution of Balmer, Fe II and Sc II features obtained using their absorption minima are shown here. A comparison with mean Type II SNe velocities from Gutiérrez et al. (2014) is also shown. The solid line represents the mean value, while the shaded region displays the 1-σ scatter from the mean.

velocities inferred from the metallic lines are similar and they fall in the range $\sim 5000\,\mathrm{km\,s^{-1}}$ (+28 d) to $\sim 2000\,\mathrm{km\,s^{-1}}$ (+70 d). Expansion velocities obtained using various species are compared with velocity estimates for large Type II supernovae sample (Gutiérrez et al. 2014) and are shown in Figure 3.11. Except for the early phase ($< +25$ d), where a steep decline in the Hα velocity is observed, the velocities measured using Hα, Hβ and Hγ lines are similar to the average velocity for Type II sample and closely follow the observed trend in Type II supernovae throughout the photospheric phase. The velocities calculated using Fe and Sc lines are found to be marginally slower than the sample average velocities of the Type II SNe. This might probably indicate that SN 2020jfo was an explosion with lower energy, albeit the higher luminosity indicates otherwise. The steep decline observed during the early phase in the Hα velocity could possibly hint towards slowing down of outer layers while encountering circumstellar matter around the progenitor. Nevertheless, if we look at Figure 3.6, we can see that the higher luminosity, in comparison to other Type II events, is only visible initially and reaches a moderate value later achieved through a faster decline, again indicating a short-lived source of secondary radiation, likely CSM.

From +36 d onward, the Hα absorption feature starts to broaden up and a deep and narrow absorption feature (Cachito) starts to develop blue-wards of Hα. This feature is prominently visible on the spectrum of +55 d at a wavelength of 6365 Å. The possibility of this feature arising due to Si II 6355 Å (Valenti et al. 2014) or Ba II 6497 Å was explored. The Cachito absorption lies redwards of Si II rest wavelength and is hence unlikely to be related to it. Assuming the feature originated due to the Ba II line, the expansion velocity inferred is $\sim 6000\,\mathrm{km\,s^{-1}}$ which is almost twice as large as the velocity obtained from other metal lines ($\sim 3000\,\mathrm{km\,s^{-1}}$ for Fe II) at the same epoch.

Chugai et al. (2007) proposed that the formation of high-velocity (HV) hydrogen absorption features is a consequence of the interaction between the RSG wind and the SN ejecta. We also explored the possibility of this feature being a HV feature of Hα. The measured velocity of the observed HV component is $\sim 9000\,\mathrm{km\,s^{-1}}$ similar to the post-maximum expansion velocity of Hα. However, we did not observe a clear Hβ counterpart, likely due to the blending of several metallic lines in that region. This HV feature is similar to the "narrow and deeper" Cachito, seen in Gutiérrez et al. (2017a, e.g. SN 2003hl) Type II SN sample study, and is similar to the case of low-velocity/low-luminosity SNe, where no Hβ counterpart is seen. The likely presence of the HV feature of Hα in the photospheric spectra favors the case of circumstellar interaction (Gutiérrez et al. 2017a).

Spectral Evolution during Nebular Phase

Nebular spectra of 2020jfo during +196 d to +292 d are plotted at the lower panel of Figure 3.7. As the recombination phase ends, the photosphere subsides into the innermost ejecta layers. The luminosity during this phase varies directly to the ^{56}Ni, which was synthesized during explosion (Srinivasaragavan et al. 2021). The light curve flux during this period is mainly due to the radioactive decay of ^{56}Co to ^{56}Fe. Nebular spectra of 2020jfo is filled by prominent emissions from Na ID, Hα,[O I] and [Ca II].

Narrow emission lines from metals are also seen, which become progressively more prominent as the supernova evolves into the late nebular phase. The bluer spectrum side is dominated by lines due to Ba, Sc, Mg, Fe, etc. Hydrogen Balmer lines are seen with decreased absorption strength. As the medium becomes more rarefied forbidden lines of Fe, Ca, and O appear in the spectrum. The prominent lines seen in the nebular phase spectrum are identified and marked in Figure 3.13. The spectra taken during this phase could be used to estimate the progenitor's ZAMS mass when compared with line strengths of model spectra at similar phases. This method has been deployed in many cases to constrain progenitor mass of Type II SNe (e.g., Van Dyk et al. (2019); Szalai et al. (2019); Hiramatsu et al. (2021b).

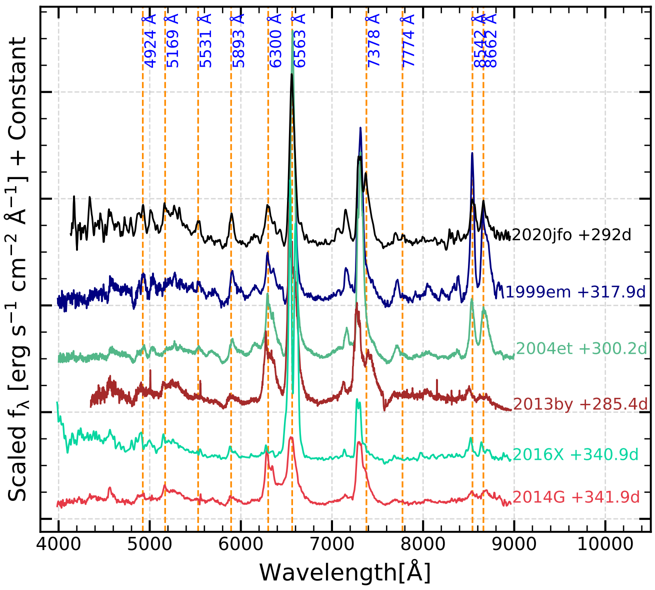

FIGURE 3.12: Spectrum of SN 2020jfo during the nebular phase (+292.2 d) is compared with other Type II SNe at similar epochs.

The SN 2020jfo spectrum at +292 d is compared with nebular phase spectra of several Type II SNe at corresponding epochs (see Figure 3.12). We find that the prominent emission features of [Ca II], Hα, [O I] and Ca II NIR triplet are similar to other normal and even fast-declining Type II SNe. However, if we look closely,

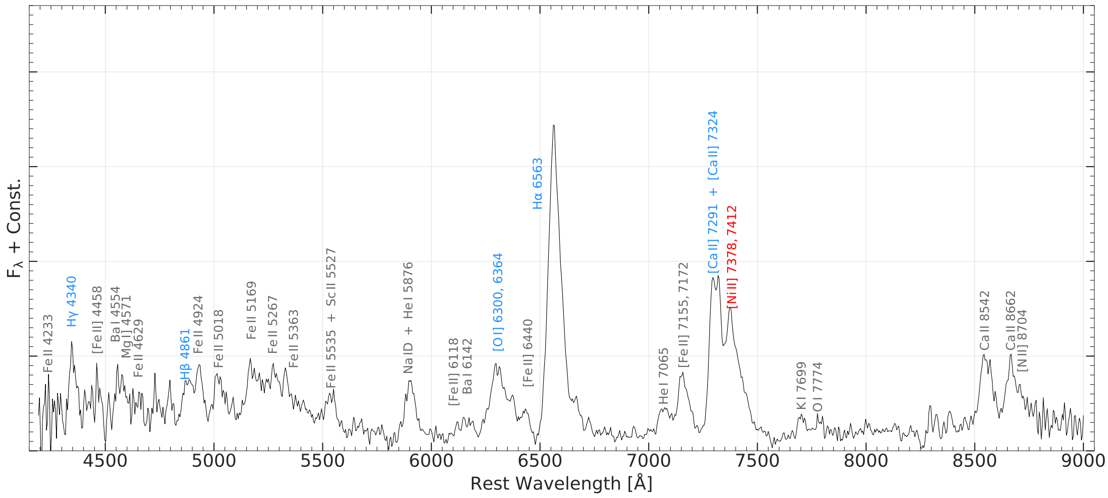

FIGURE 3.13: Identification of lines in the +292 d spectrum of SN 2020jfo.

the spectrum of SN 2020jfo shows a clear blue excess and a forest of features due to lines of [Fe II]/Fe II. Na ID emission line in 2020jfo is similar to features observed in other typical Type II SN 1999em but is more pronounced in comparison to fast-declining events SN 2013by and SN 2014G. The wing on the redder side of [Ca II] shows a clear secondary peak due to [Ni II]. This feature is not observed in normal Type II SNe such as 1999em and 2004et, but seen in Type II SN 2013by (fast-declining).

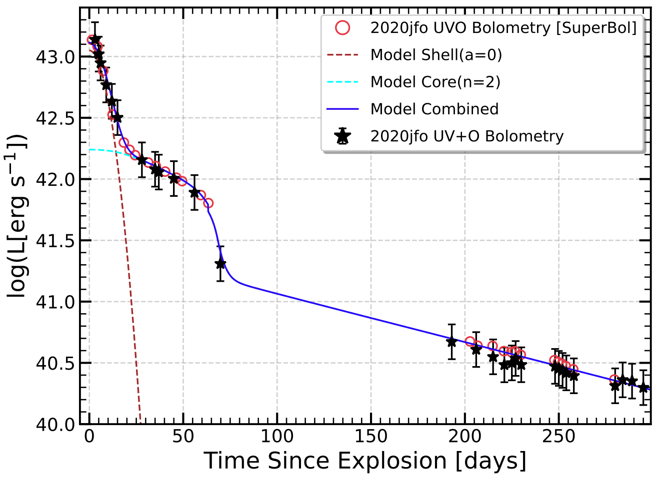

FIGURE 3.14: Best fitting model curves to the bolometric light curve using a two-component model from Nagy & Vinkó (2016). Individual contributions from the shell and core component are shown with the combined bolometric luminosity.

3.2.5 Characteristics of the Possible Progenitor

In this section, we perform observational analysis along with semi-analytical and hydrodynamical modeling to discuss possible progenitor scenarios for SN 2020jfo.

Semi-Analytical modeling

To obtain estimates on progenitor properties, we made use of the semi-analytical modeling approach described in Chapter 2. For ejecta, the core region is assumed with a flat or constant density profile with a constant Thompson-scattering opacity of $\kappa = 0.4\,\mathrm{cm^2\,g^{-1}}$ whereas the shell region has density profile which decreases as a power-law function (n = 2) or as an exponential (a = 0) with an opacity of $\kappa = 0.2\,\mathrm{cm^2\,g^{-1}}$ (Nagy & Vinkó 2016). We obtained an ejecta mass of $\sim 7.5\ \mathrm{M_\odot}$ (core+shell), an RSG radius ranging from 310-340 $\mathrm{R_\odot}$, and a total energy (thermal and kinetic) of $\sim$3 foe based on the closely describing model shown in Figure 3.14. ^{56}Ni mass obtained from this semi-analytical model, with the amount of gamma-leakage added to the model to match the observed light curve time evolution, is $0.03 \pm 0.01\,\mathrm{M_\odot}$, which is in corroboration with our earlier estimates.

Estimate from nebular spectrum

To constrain the progenitor mass, we compared the nebular phase spectrum of +292 d with model spectra from Jerkstrand et al. (2014) (Figure 3.15). The model spectra for different progenitor masses such as 12, 15, 19, and 25 $\mathrm{M_\odot}$ have been scaled with respect to ^{56}Ni mass and the distance of SN 2020jfo (in contrast to 5.5 Mpc for model spectra). To account for the phase dissimilarity between the model spectra and the observed spectrum, the observed spectrum was scaled by

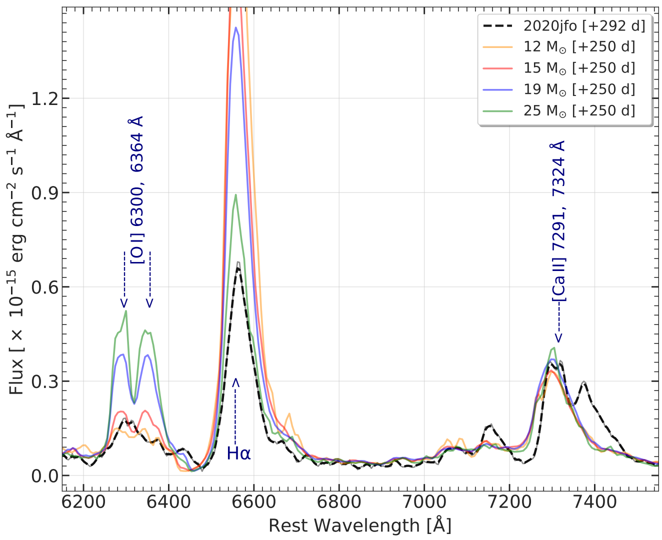

FIGURE 3.15: Nebular spectrum (+292 d) of SN 2020jfo is compared with the model spectra for 12, 15, 19 and 25 $M_{\odot}$ models, at 250 d since explosion. The model spectra obtained from Jerkstrand et al. (2014) are scaled for distance and nickel mass, and corrected for phase mismatch using the characteristic decay time corresponding to SN 2020jfo.

the amount determined from the characteristic time scale of ^{56}Ni-decay chain and the dissimilarity in phases. The comparison of [O I] 6300 Å, 6364 Å line fluxes of the observed spectra with the spectral models suggest a lower mass progenitor of $\sim 12\,M_{\odot}$. However, the flux of Hα is quite weak compared to the $12\,M_{\odot}$ progenitor, indicating a stripped hydrogen envelope in SN 2020jfo. The [Ca II] / [O I] flux ratio was observed to be ~ 1.5 in the ~ 292 d spectrum which is also suggestive of a progenitor with lower initial mass for the case of SN 2020jfo.

SN 2020jfo is one among the few hydrogen-rich SNe where a clear, distinct spectral feature of [Ni II] 7378 Å is seen adjacent to the [Ca II] feature in nebular phase spectral evolution. The feature has its origins from stable ^{58}Ni, synthesized during explosive nucleosynthesis (Jerkstrand et al. 2015a). Utilizing methodology from Jerkstrand et al. (2015b), we computed a Ni/Fe luminosity ratio for SN 2020jfo (see Figure 3.16) as 2.10 ± 0.43 (similar to the value obtained in Sollerman et al. 2021). This translates to a Ni/Fe ratio by mass as 0.18 ± 0.04, which is roughly 3.0 ± 0.6 times the Solar value. This could be achieved either by a neutron excess usually

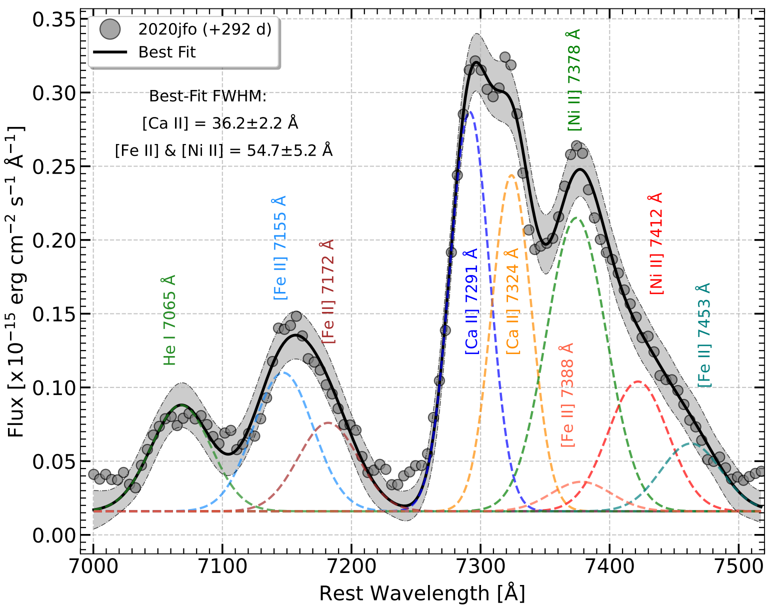

FIGURE 3.16: Multi-component Gaussian fit to the nebular spectrum of SN 2020jfo (+292 d). The fit was performed by having different values of line broadening for [Ca II] and [Fe II]/[Ni II] owing to their differing origins in the ejecta. The FWHM values obtained are mentioned in the figure.

found in the Silicon layer or due to a very high progenitor metallicity ($> 5\,\mathrm{Z}_\odot$) that increases the neutron excess in Oxygen shell (Jerkstrand et al. 2015a). The estimated metallicity close to the SN site is $\sim 1.5\,\mathrm{Z}_\odot$, which is not high enough to produce such a ratio of Ni/Fe in the ejecta. The only plausible scenario for such excess is seen in $\mathrm{M_{ZAMS}} \lesssim 13\,\mathrm{M}_\odot$ models (Jerkstrand et al. 2015a) that house a thick Si layer with a neutron excess. This is concurrent with our estimates of a lower mass progenitor.

Hydrodynamical Modeling

We resort to detailed hydrodynamical modeling for better constraints about the progenitor, its evolution, mass loss history and its environment using `MESA`+`STELLA` as described in Chapter 2. Some important parameters varied are described here. The mixing length parameter (`MLT_option`) is set to *Henyey* with $\alpha_{\mathrm{MLT}} = 1.5$.

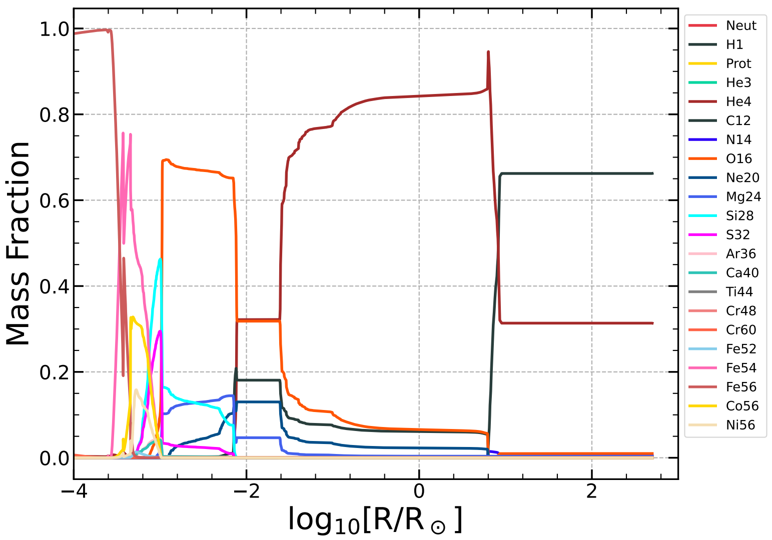

FIGURE 3.17: Pre-supernova mass fractions for an evolved 12 $M_\odot$ model for different species present in the 'approx21_cr60_plus_co56.net' (approx21) network used in `MESA` modeling.

We fixed our metallicity to Z = 0.024 ($Z_\odot$ = 0.016) as estimated in Section 3.2.2 for all the simulations. In our models, we did not vary ^{56}Ni mass ($\sim$0.033 $M_\odot$) obtained earlier to reduce the parameter space.

Recently, Hiramatsu et al. (2021a) discusses possibility of obtaining shorter plateaus in Type II SN light curves from progenitors with ZAMS mass of 18-25 $M_\odot$ with an enhanced or elevated mass loss ($\dot{M} \simeq 10^{-2}\,M_\odot\,yr^{-1}$) in the years, which could be up to decades, prior to collapse. The objects of interest in their study were more luminous events (Peak $M_V < -18$ mag), with a higher ^{56}Ni yield and higher expansion velocities in contrast to SN 2020jfo, which has an average ^{56}Ni mass and lower expansion velocities in comparison to a typical Type II SNe. In addition, a number of other numerical modeling works for example Dessart et al. (2010), and Sukhbold et al. (2016) showed that low mass progenitors of $M \leq 18\,M_\odot$ were not able to produce a shorter plateau duration of around 60 days. In all, none of the simulations for masses $M \leq 15\,M_\odot$ under standard conditions were able to produce light curves with short plateaus. Instead of exploring the parameter space favored by other works for short plateau Type II SNe, we took a different approach, where the inputs were driven from the results of semi-analytical modeling and nebular phase spectra. Hence, we went ahead with the evolution of a ZAMS model of 12 $M_\odot$ and tried variations in the evolution schemes to achieve a shorter plateau.

A 12 $M_\odot$ progenitor was evolved with an initial metallicity slightly higher than Solar and with a finite amount of rotation ($\Omega = 0.1\,\Omega_{\rm critical}$). Figure 3.17 shows the pre-Supernova mass fractions of an evolved model for 'approx21' network. It was found that, for a typical mass loss rate due to winds, a short plateau was not possible as there was not enough stripping of the hydrogen envelope of the progenitor's ejecta. Hence, an enhanced mass loss due to winds was applied during the evolution, which is highly possible in a higher metallicity environment with a rotating progenitor. Mass loss was controlled by MESA's wind scaling factor (wsf). We tried varying this parameter from a default value of 1.0 onwards. At a value of wsf = 5.0, we could get enough material stripped off from its surface in order to achieve a short plateau with a similar period as SN 2020jfo. We also note that the sharp transition could not be produced using physical mass loss schemes. However, a sharp transition is achieved if the mass is removed by hand to leave the final mass as 5.0 $M_\odot$. Some of the models did not converge as the central density was insufficient for the ignition of higher masses during evolution. The simulated light curves obtained for various wind scaling factors along with Q-bol for SN 2020jfo are shown in Figure 3.18, and corresponding pre-SN values for various models are presented in Table 3.7.

TABLE 3.7: Pre-SN parameters for different models

$M_i = 12.0\ M_\odot,\ \Omega = 0.1\Omega_c,\ Z = 0.024$				
M_f ($M_\odot$)	Age (Myr)	$\alpha_{\rm Dutch}$	Radius ($R_\odot$)	E_{tot} (foe)
10.9	18.7	1.0	470	–0.94
8.9	19.2	3.0	780	–1.00
8.7	19.3	3.2	723	–0.93
6.6	**19.7**	**5.0**	**679**	**–0.91**

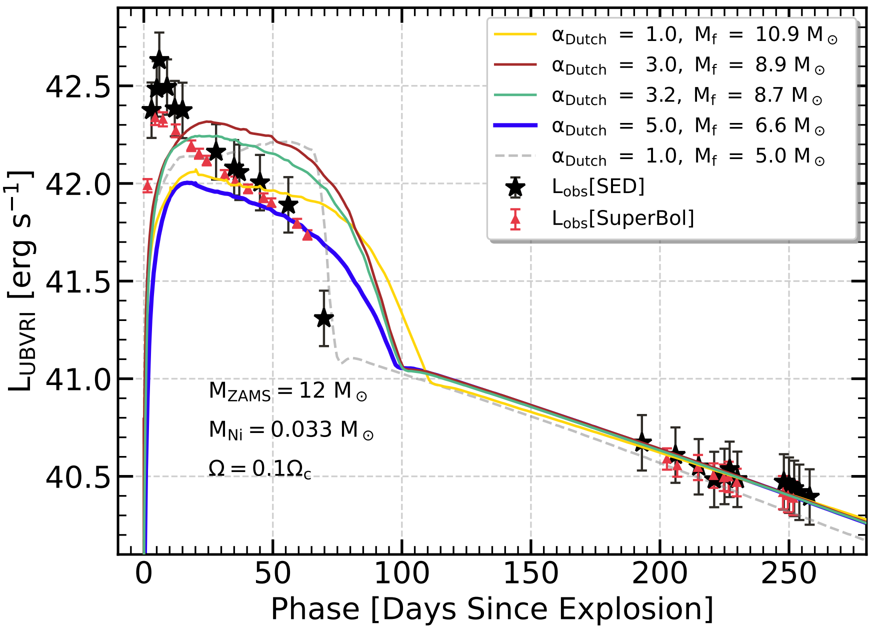

FIGURE 3.18: Quasi-bolometric light curves obtained from `MESA + STELLA` modeling with different values of wsf (1.0, 3.0, 3.2 and 5.0) for the $12\,M_\odot$ ZAMS model. Q-bol of SN 2020jfo is over-plotted for comparison.

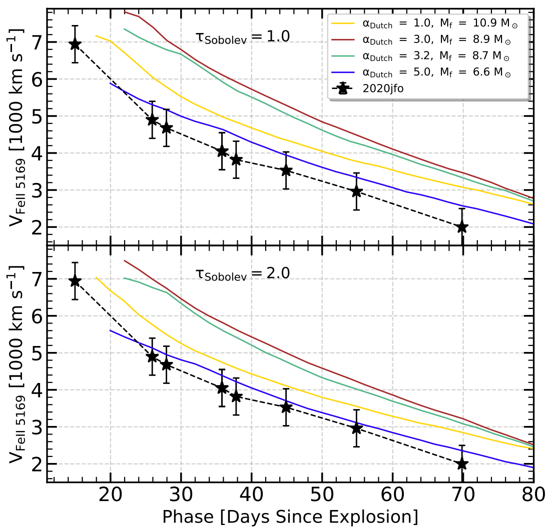

FIGURE 3.19: Photospheric velocity evolution as obtained from `MESA + STELLA` modeling for two different values of optical depth (τ_{Sobolev}=1.0 and 2.0) compared with the observed photospheric velocities.

It was demonstrated by comprehensive modeling that the model of ZAMS with $12\,M_\odot$ and the final mass of the progenitor as $6.6\,M_\odot$, fitted closely the decline to nebular phase and late phase evolution of the observed light curve (Figure 3.18). It had an ejected mass $\sim 5\,M_\odot$ and an excised core of $\approx 1.6\,M_\odot$. The explosion energy for best-fitting models was $E_{exp} = 0.2 - 0.4$ foe. The photospheric velocity evolution for this model is in agreement with the estimates from the observed spectral sequence (see Figure 3.19). Slow velocity evolution could also be attributed to the low energy of the explosion as obtained from hydrodynamic modeling ($0.2-0.4$ foe) along with the low ejecta mass as most of the mass was blown away by winds during evolution. A nickel mass of $0.033\,M_{\odot}$ used in models substantiates our earlier Ni mass estimates. While the modeled light curve matched with the observed plateau duration, decline to the nebular phase, and late phase light curve evolution, it failed to reproduce the early steep rise to a high luminosity observed in the quasi-bolometric light curve. As the calculations are based on normal type IIP SNe, only primary radiation sources viz. shock breakout and cooling, hydrogen recombination, and radioactive decay are considered. The inadequacy of current model to describe the early light curve phase indicates the need to introduce a secondary source of radiation for early times, and the best possible source could be the CSM presence around the progenitor.

Due to the paucity of direct signatures of CSM interaction, we could not calculate the extent and density of the CSM. In order to estimate the same, we used `STELLA`, where it was possible to place the CSM around the progenitor with its configuration defined by the parameters wind velocity, mass loss rate, and its duration. The density profile in `STELLA` is dependent on the radius, r, away from the progenitor's centre as:

$$\rho(r)_w = \frac{\dot{M}_w}{4\pi r^2 v_w}, \tag{3.1}$$

where $\dot{M}_w[M_{\odot}\,yr^{-1}]$ is mass loss rate due to winds and v_w is the wind velocity. We allocated 40 zones out of 400 for CSM configuration and the bolometric flux was obtained at four extents $(2, 10, 20, 40$ AU) with various mass loss rates $(0.001, 0.005, 0.01, 0.05\,M_{\odot}\ yr^{-1})$ and $10^6\ cm\,s^{-1}$ as wind speed. The modeled light curve with $\dot{M} = 0.01\,\mathrm{M_\odot\,yr^{-1}}$, t = 20 yr (implies CSM extent $\sim$ 40 AU) fits the observed quasi-bolometric evolution well (see Figure 3.20). The He II feature considered as proxy for interaction signature is not observed beyond +10 d. This could be due to formation and increasing strength of other lines in the spectra. Furthermore, it could also be due to decrease in CSM-ejecta interaction, giving rise to a steep decline in quasi-bolometric LC evolution. Light curve modeling suggests interaction up to +15 d, which is considered an upper bound. Further, we compare $U - B$ color evolution (Figure 3.20) of models with observed $U - B$ color. We find the color to be flat for initial 8 d and later it evolves towards red. This initial trend is only seen in the models with added CSM.

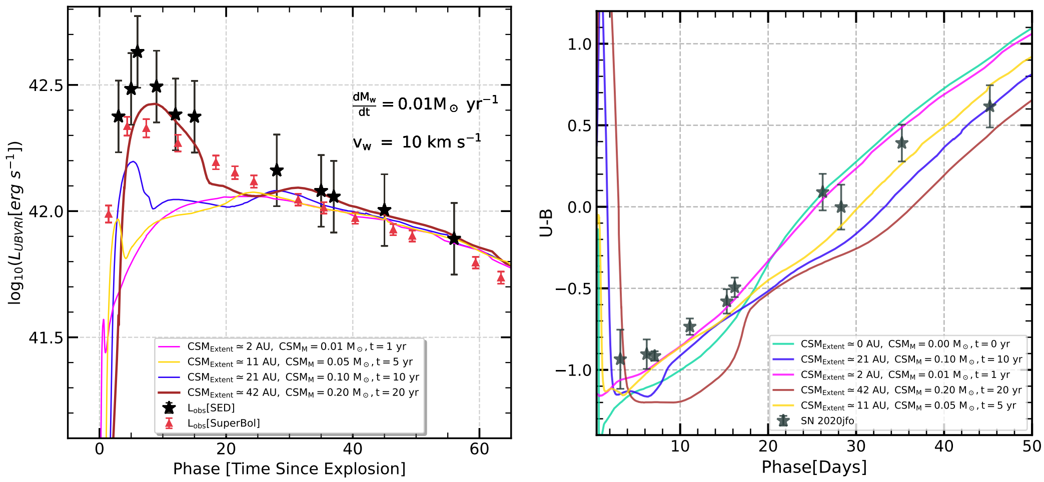

FIGURE 3.20: ***Left:*** Quasi-bolometric light curves as obtained from `MESA + STELLA` modeling for a 12 $\mathrm{M_\odot}$ ZAMS progenitor ($\mathrm{M_f} = 6.6\,\mathrm{M_\odot}$) with different CSM configurations. Q-bol light curve of SN 2020jfo is over-plotted for comparison. ***Right:*** Color evolution as obtained from `MESA + STELLA` modeling for a 12 $\mathrm{M_\odot}$ ZAMS progenitor ($\mathrm{M_f} = 6.6\,\mathrm{M_\odot}$) with different CSM configurations.

3.2.6 Case for a Stripped Low-mass Progenitor

The estimated metallicity was slightly higher than the solar values and might have helped to escalate the progenitor's mass-loss rate. It has been argued in Dessart et al. (2013) that lower envelope mass at higher metallicity ought to produce a

Type II SN with a shorter plateau duration. A direct result of this is seen in the temporal evolution of pseudo-equivalent widths (pEW) of Fe II 5018 Å of 2020jfo when compared to estimates from spectral models from Dessart et al. (2013) (see Figure 3.21). We find that with increasing metallicities, the pEW increases. The higher pEW of 2020jfo in the photospheric period corroborates with an enhanced metallicity environment. However, the implied metallicity is much higher than that estimated for its host (i.e., $\sim$1.5 $Z_\odot$ in Section 3.2.2). Dessart et al. (2013) have shown that the compactness (i.e., radius) of the progenitor affects the pEW of the metal features in plateau phase. This is depicted in Figure 3.21 showing 3 variants of 1 $Z_\odot$ metallicity progenitor, with different final progenitor radii. Observationally, this indicates the presence of a stripped hydrogen envelope, which would make the progenitor more compact and probably explain the lack of a clear early decline ($s1$) phase prior to the beginning of the plateau ($s2$) period.

The semi-analytical modeling of 2020jfo in Section 3.2.5 infers a progenitor of low mass with M_{ej} of $\sim 7.3\,M_\odot$ and RSG radius of $\sim$ 350 $R_\odot$. Considering a typical Neutron Star (NS) remnant core with $\sim 1.5\,M_\odot$, we infer a pre-SN or initial mass of $\sim\ 9\,M_\odot$.

From `MESA+STELLA` modeling, we obtained a stripped progenitor having a pre explosion mass of $\sim 6.6\,M_\odot$ where the initial ZAMS mass was $12, M_\odot$. A similar ZAMS value for the progenitor was also obtained using late nebular spectra (see Section 3.2.5). However, we did not implement any synthetic mass loss scheme (deliberate removal of the H envelope mass) to achieve stripping of progenitor (see Section 3.2.5). Nevertheless, there could be numerous short time windows where enhanced mass loss is possible (Decin et al. 2006), which are hard to predict and hence challenging to include in modeling. The mass loss rate adopted for SN 2020jfo progenitor in `MESA` is five times the typical mass-loss rates for an RSG progenitor but is well within the observed limits. It is difficult to predict what could have caused such a high mass-loss rate, whether it was solely due to the rotation and high metallicity environment, or due to other factors such as interaction with a binary companion or multiple episodes of enhanced mass loss.

It was shown by Eldridge et al. (2018) that the initial progenitor masses around 8-15 $M_\odot$ in the binary scenario possibly give light curves with shorter plateaus of the order of tens of days. However, their physical parameter space was limited, and not much could be said quantitatively about the progenitor properties. Another attempt by Hiramatsu et al. (2021a) showed that the RSG progenitors with initial masses of 18-25 $M_\odot$ with enhanced mass-loss rates could reproduce shorter duration plateaus. However, the observed properties such as nebular spectra, the mass of synthesized radioactive nickel, and velocity evolution of the events (SN 2006Y, SN 2006ai, and SN 2016egz) were also supportive of higher mass progenitors. Both these studies (Eldridge et al.; Hiramatsu et al.) had shown a higher mass progenitor leads to an increased amount of stripping of the hydrogen envelope. However, SN 2020jfo poses a question to the high-mass progenitor scenario. The arguments presented in our analysis and discussion weigh in on a low-mass progenitor with enhanced mass loss that gave birth to the short plateau supernova SN 2020jfo.

3.2.7 CSM Interaction

There have been numerous instances where studies have provided enough evidence for CSM surrounding Type II progenitors both in light curves and spectra. Förster et al. (2018) attributed the steeper light curve rise and delayed shock emergence to the dense CSM from their 26 Type II SNe sample. Another study, combining light curve modeling and observations (Morozova et al. 2018) summarized that $\sim 70\%$ SNe have CSM, and the estimated CSM masses ranged between $0.18 - 0.83\,M_\odot$. Bruch et al. (2021) emphasized the appearance of narrow flash emission features, especially He II 4686 Å, in the very early spectra, ideally taken less than 48 hrs of explosion as CSM signatures in numerous Type II SNe. We do not see such narrow signatures of CSM interaction in our earlier spectra, although we do see broad ionized lines of helium, which were likely formed at the CDS arising due to shock ionization of outer layers or CSM close to the ejecta. Along with this, the presence of HV Hα feature in the mid to late plateau phase spectra is an indication of CSM's presence.

The higher peak luminosity and steeper early phase decline seen in SN 2020jfo also strengthen the case of CSM close to its progenitor. High decline rates in the early epochs of Type II SNe are attributed to the interaction with CSM. The diagnostic in SN 2013by was the presence of asymmetric line profiles with photospheric signatures of HV features of hydrogen (Valenti et al. 2015). In SN 2014G, the presence of highly ionized spectroscopic features was attributed to a metal-rich CSM accumulated from the mass-loss events prior to the explosion (Terreran et al. 2016). It is likely that the increased brightness of SN 2020jfo in the early epochs is due to interaction with the nearby CSM, and its density profile is such that this is not sustained for prolonged periods. We ascertained this possibility with hydro-dynamical modeling using `MESA + STELLA`.

Furthermore, the color evolution trend of SN 2020jfo in the early epochs is slightly bluer in comparison to other SNe, while in the late phase, it flattens out and merges with the normal Type II SN color evolution. The bluer early phase color evolution is almost identical to the CSM-interacting SNe. The Q-bol of 2020jfo during the early phase is comparable to SN 2009au and SN 2014G (see Figure 3.6), which showed clear signs of interaction in their spectra. Though the luminosity is higher during early epochs, a steeper decline in the plateau phase leads to a luminosity comparable to normal Type IIP events such as SN 2016X towards the end of the plateau. The additional source giving rise to the higher luminosity in the initial phase is probably due to CSM interaction, however, CSM itself remains hidden. Nagao et al. (2020) showed that a CSM distributed in the form of a disc, when viewed from a polar angle, would only cause enhancement in flux due to heating effects and would not leave any signatures of interaction in the spectra. Although, as clearly shown in Nagao et al. (2020), overluminous Type IIP SNe might not be powered by such disc interaction, but a slight enhancement is a likely proposition during the early phase.

To have a complete picture, we also looked at the field of SN 2020jfo for any radio detection. The field was observed on October 17, 2021 (JD 2459504.5) in the VLA sky survey (VLASS) (image cut-outs can be found here **). No significant radio emission was detected at the source's position, and a limiting flux density of 309 μJy (3σ upper limit) at 3 GHz was obtained. Unsurprisingly, the SN being $>$ 500 days old at the time of VLASS observations, the radio flux density around this period declined below the sensitivity limits of current radio telescopes, even for radio bright Type IIP SNe. Using the expression for mass-loss rate given in Weiler et al. (1986), we obtained $\dot{M} < 2.5 \times 10^{-5}\,\mathrm{M_{\odot}\ yr^{-1}}$ as an upper limit. This value is somewhat comparable with typical Type IIP SNe but smaller for our case where we estimated a higher mass-loss rate (see Section 3.2.5) from the MESA+STELLA modeling of the early phase bolometric LC evolution. This is likely due to the difference in the epochs of observations of the radio and the modeled light curve with CSM. Sollerman et al. (2021) also looked for X-ray emission post-explosion for SN 2020jfo and could only cite an upper limit based on their estimates. It might be the case that the X-rays from the denser outer material were earlier on and could have been missed as those were absorbed by nearby CSM (similar scenario as pointed out in Jacobson-Galán et al. 2021).

3.2.8 Summary for SN 2020jfo

Using an extensive photometric and spectroscopic study of a short-plateau Type II event, SN 2020jfo. Our findings are as under:-

**http://cutouts.cirada.ca/

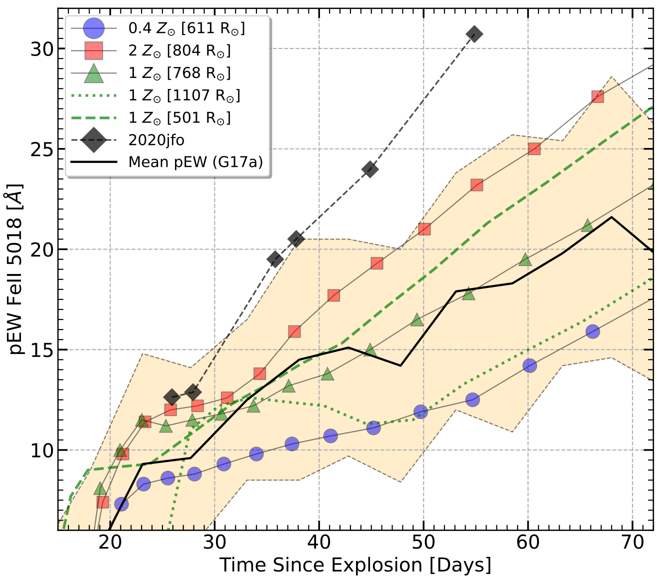

FIGURE 3.21: Temporal evolution of pEW of Fe II 5018 Å in comparison with models from Dessart et al. (2013) having different metallicities (0.4, 1 and 2 $Z_\odot$). The black solid line represents the mean value of the pEW of Fe II 5018 Å and shaded region shows its dispersion from the extensive sample of Gutiérrez et al. (2017a).

1. We estimated a plateau duration of < 65 d for SN 2020jfo, which categorizes it under rare short plateau Type IIP SNe.

2. Observational properties associated with SN 2020jfo are: V-band magnitude during peak, $M_V = -17.4 \pm 0.4$ mag, optical luminosity at peak $4.3 \pm 1.4 \times 10^{42}$ erg s^{-1}, and synthesized ^{56}Ni mass of $0.033 \pm 0.006\,M_\odot$.

3. Using the nebular phase spectrum, we estimated the mass of the progenitor $\sim 12\,M_\odot$.

4. We estimated the progenitor properties for SN 2020jfo from hydrodynamical modeling and concluded that the most plausible progenitor is a Red Super Giant with an initial mass $\sim$12 $M_\odot$, radius $\sim 679\,R_\odot$ and an eventual pre-supernova mass $< 6.6\,M_\odot$. It evolved in a relatively high metallicity environment with a significant amount of mass shredded during its course of evolution.

5. A high Ni/Fe ratio of 0.18±0.04 by mass was estimated for SN 2020jfo that is consistent with a low mass progenitor ($M_{ZAMS} \leq 13\,M_{\odot}$).

6. The pEW evolution for Fe II 5018 Å is much higher than the other observed SNe of Type II class, strengthening the high metallicity environment and a compact progenitor scenario.

7. The presence of ionized He II line, increased brightness in contrast to slower expansion, HV Hα feature, and the sharp decline in luminosity indicated CSM's presence, which was confirmed by `MESA+STELLA` hydrodynamical modeling. It was deduced that a $0.2\,M_{\odot}$ CSM, extended up to $\sim$ 40 AU, was required to explain the early higher luminosity and a faster declining bolometric light curve.

3.3 SN 2018gj: A Type II Supernova with Short Plateau showing Persistent Blue-shifted Hα Emission

In this section, we study a Type IIP supernova SN 2018gj utilizing extensive spectroscopic (low-resolution) and photometric (UV, Optical, and NIR). SN 2018gj discovery in the outskirts of the barred spiral galaxy NGC 6217 (about 122$''$ or $\sim$ 11 kpc away from the host nucleus) (Figure 3.22) was reported on 2018 January 14 (2458132.91 JD) at (J2000), RA, $\alpha = 16°32'02''.40$ and Dec, $\delta = +78°12'41''.13$ (Wiggins 2018). Immediately after the discovery, SN 2018gj was designated Type IIb SN class with the possibility of it being a Type IIP SN (Bertrand 2018). Later on, the classification was reported as a young Type II SN (Kilpatrick 2018).

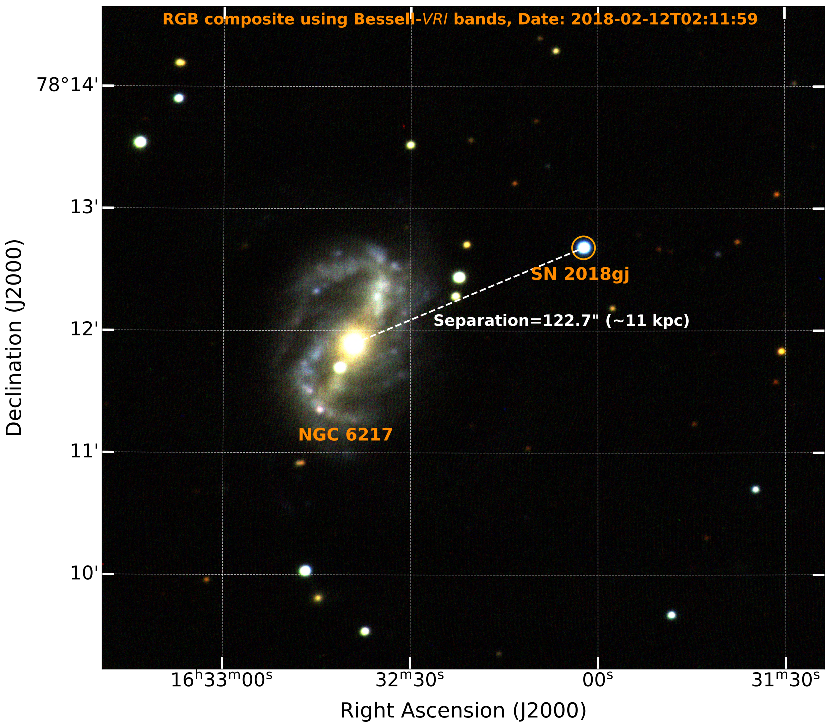

FIGURE 3.22: Location of SN 2018gj in the host NGC 6217. The dashed violet line marks the separation between the host center and SN. The image is an RGB color composite utilizing Bessell's V, R, and I filters.

3.3.1 Observations

We started an extensive follow-up campaign in optical-NIR photometry and spectroscopy, which continued for about 300 d after the discovery. Optical observations were obtained with HFOSC+HCT and NIR observations with HONIR+Kanata. Several standard star fields were observed on four nights under photometric conditions (Landolt 1992). These were utilized for secondary standards calibrations in the SN field. As the SN was relatively isolated in its host galaxy, the supernova magnitude was extracted using PSF photometry. SN 2018gj observations in $UBVRI$ filters are provided in Table 3.8. Table 3.10 provides JHK_s magnitudes observed for SN 2018gj.

Further, our photometry data was supplemented using public archive images from *Swift*/UVOT bands. The final $UVOT$ magnitudes (in Vega system) obtained are

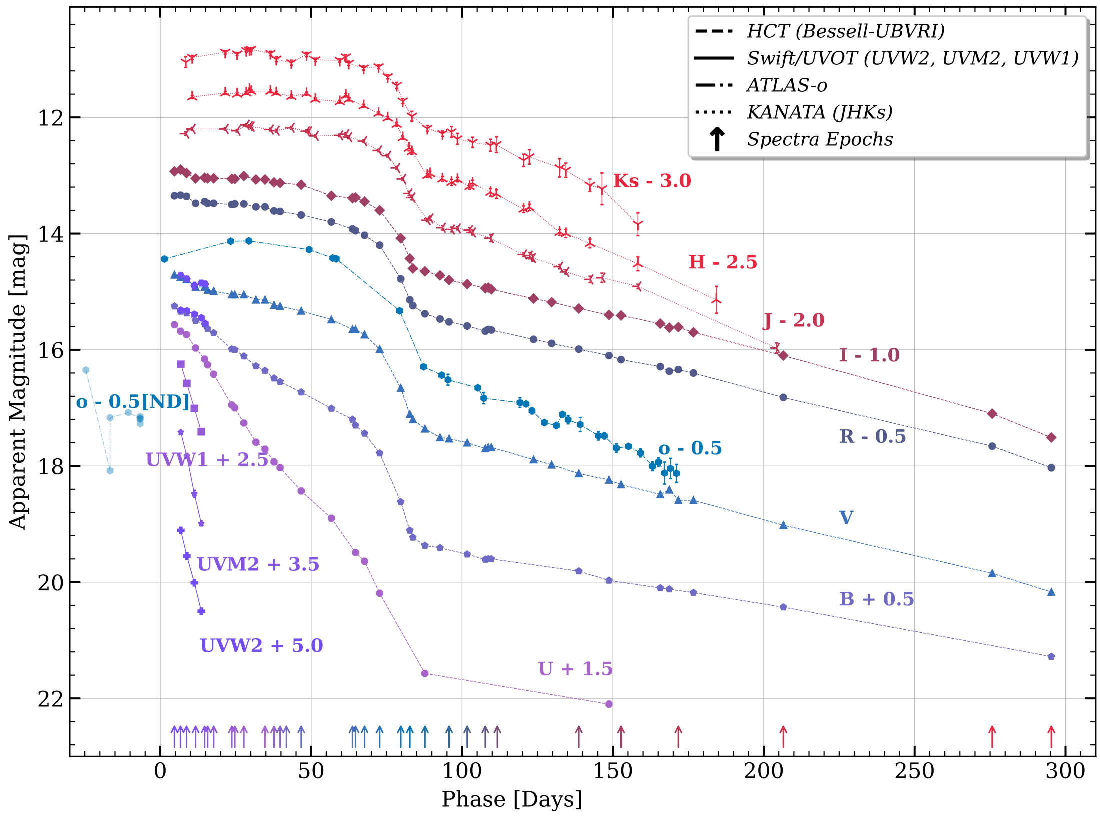

FIGURE 3.23: Photometric data for SN 2018gj spanning ∼300 d post-discovery. Corresponding spectral epochs are marked along the abscissa. [Violet pentagon markers over-plotted on V and B bands are from Swift UVV and UVB bands, respectively]

tabulated in Table 3.9. We also obtained photometry in ATLAS-o band (AB-magnitude) from ATLAS forced photometry server.

The low-resolution spectroscopic (∼ 10 Å) data was obtained with HFOSC from 2018 January 14 (JD 2458132.5) to 2018 October 31 (JD 2458423.1). Spectra log is given in Table 3.11 and spectroscopic observation epochs are also marked in Figure 3.23.

Table 3.8: HCT $UBVRI$ magnitudes for SN 2018gj.

Date (year-mm-dd)	JD 2458000+	Phase* (d)	U (mag)	B (mag)	V (mag)	R (mag)	I (mag)
2018-01-14	132.5	+4.7	14.07 ± 0.01	14.75 ± 0.01	14.71 ± 0.01	14.55 ± 0.01	14.43 ± 0.01
2018-01-16	134.5	+6.7	14.18 ± 0.01	14.84 ± 0.01	14.75 ± 0.01	14.54 ± 0.01	14.40 ± 0.01
2018-01-18	136.5	+8.7	14.24 ± 0.01	14.87 ± 0.01	14.79 ± 0.01	14.56 ± 0.01	14.46 ± 0.01
2018-01-21	139.5	+11.7	14.47 ± 0.01	15.00 ± 0.01	14.92 ± 0.01	14.68 ± 0.01	14.55 ± 0.01
2018-01-24	142.5	+14.7	14.66 ± 0.01	15.06 ± 0.01	14.92 ± 0.01	14.65 ± 0.01	14.54 ± 0.01
2018-01-25	143.5	+15.7	14.76 ± 0.01	15.14 ± 0.01	14.97 ± 0.01	14.68 ± 0.01	14.55 ± 0.01
2018-01-27	145.5	+17.7	14.92 ± 0.02	15.21 ± 0.01	14.99 ± 0.01	14.68 ± 0.01	14.55 ± 0.01
2018-02-02	151.5	+23.7	15.45 ± 0.02	15.49 ± 0.01	15.05 ± 0.01	14.70 ± 0.01	14.56 ± 0.01
2018-02-03	152.5	+24.7	15.50 ± 0.01	15.50 ± 0.01	15.05 ± 0.01	14.69 ± 0.01	14.56 ± 0.01
2018-02-06	155.5	+27.7	15.76 ± 0.02	15.61 ± 0.01	15.05 ± 0.01	14.69 ± 0.01	14.51 ± 0.01
2018-02-10	159.5	+31.7	16.09 ± 0.02	15.78 ± 0.01	15.14 ± 0.01	14.74 ± 0.01	14.57 ± 0.01
2018-02-13	162.5	+34.7	16.21 ± 0.02	15.86 ± 0.01	15.14 ± 0.01	14.74 ± 0.01	14.57 ± 0.01
2018-02-16	165.5	+37.7	16.43 ± 0.02	15.99 ± 0.01	15.23 ± 0.01	14.81 ± 0.01	14.62 ± 0.01
2018-02-18	167.5	+39.7	16.53 ± 0.02	16.05 ± 0.01	15.25 ± 0.01	14.82 ± 0.01	14.63 ± 0.01
2018-02-25	174.5	+46.7	16.93 ± 0.01	16.23 ± 0.01	15.33 ± 0.01	14.88 ± 0.01	14.66 ± 0.01
2018-03-07	184.5	+56.7	17.40 ± 0.01	16.51 ± 0.01	15.48 ± 0.01	15.00 ± 0.01	14.85 ± 0.01
2018-03-14	191.5	+63.7	–	16.70 ± 0.02	15.65 ± 0.01	15.12 ± 0.02	14.89 ± 0.01
2018-03-15	192.5	+64.7	17.99 ± 0.04	16.80 ± 0.01	15.65 ± 0.01	15.15 ± 0.02	14.88 ± 0.01
2018-03-18	195.5	+67.7	18.14 ± 0.03	16.94 ± 0.01	15.74 ± 0.01	15.23 ± 0.01	14.95 ± 0.01
2018-03-23	200.5	+72.7	18.69 ± 0.02	17.28 ± 0.01	15.99 ± 0.01	15.40 ± 0.01	15.10 ± 0.01
2018-03-30	207.5	+79.7	–	18.12 ± 0.02	16.66 ± 0.01	15.98 ± 0.01	15.58 ± 0.01
2018-04-02	210.5	+82.7	–	18.61 ± 0.02	17.11 ± 0.01	16.34 ± 0.01	15.93 ± 0.01
2018-04-03	211.5	+83.7	–	18.73 ± 0.02	17.20 ± 0.01	16.44 ± 0.02	16.10 ± 0.01
2018-04-07	215.5	+87.7	20.07 ± 0.05	18.87 ± 0.02	17.36 ± 0.01	16.58 ± 0.02	16.15 ± 0.02
2018-04-12	220.5	+92.7	–	18.91 ± 0.01	17.51 ± 0.01	16.67 ± 0.01	16.22 ± 0.01
2018-04-15	223.5	+95.7	–	–	17.53 ± 0.01	16.72 ± 0.01	16.30 ± 0.02
2018-04-21	229.5	+101.7	–	19.02 ± 0.01	17.60 ± 0.01	16.79 ± 0.01	16.37 ± 0.02
2018-04-27	235.5	+107.7	–	19.11 ± 0.03	17.70 ± 0.01	16.88 ± 0.01	16.44 ± 0.02
2018-04-28	236.5	+108.7	–	19.10 ± 0.03	17.68 ± 0.02	16.85 ± 0.03	16.43 ± 0.02
2018-04-29	237.5	+109.7	–	19.10 ± 0.02	17.68 ± 0.02	16.86 ± 0.01	16.46 ± 0.02
2018-05-13	251.5	+123.7	–	–	17.89 ± 0.01	17.02 ± 0.02	16.62 ± 0.03
2018-05-19	257.5	+129.7	–	–	17.98 ± 0.01	17.09 ± 0.01	16.68 ± 0.02
2018-05-28	266.5	+138.7	–	19.31 ± 0.03	18.13 ± 0.02	17.19 ± 0.02	16.79 ± 0.02
2018-06-07	276.5	+148.7	20.60 ± 0.05	19.47 ± 0.02	18.24 ± 0.01	17.30 ± 0.01	16.90 ± 0.02
2018-06-11	280.5	+152.7	–	–	18.32 ± 0.01	17.37 ± 0.01	16.91 ± 0.02
2018-06-24	293.5	+165.7	–	19.60 ± 0.02	18.49 ± 0.02	17.49 ± 0.01	17.05 ± 0.02
2018-06-27	296.5	+168.7	–	19.62 ± 0.02	18.41 ± 0.03	17.57 ± 0.01	17.12 ± 0.02
2018-06-30	299.5	+171.7	–	– ± –	18.59 ± 0.01	17.54 ± 0.01	17.11 ± 0.02
2018-07-05	304.5	+176.7	–	19.68 ± 0.03	18.59 ± 0.01	17.60 ± 0.01	17.20 ± 0.02
2018-08-03	334.3	+206.5	–	19.93 ± 0.04	19.02 ± 0.04	18.02 ± 0.02	17.60 ± 0.03
2018-10-12	403.5	+275.7	–	– ± –	19.85 ± 0.03	18.86 ± 0.04	18.60 ± 0.03
2018-10-31	423.1	+295.3	–	20.78 ± 0.03	20.17 ± 0.02	19.23 ± 0.05	19.01 ± 0.04

* With reference to the explosion date (JD 2458127.8).

TABLE 3.9: Swift/UVOT photometry for SN 2018gj

Date (year-mm-dd)	JD 2458000+	Phase* (d)	$UVW2$ (mag)	$UVM2$ (mag)	$UVW1$ (mag)	UVU (mag)	UVB (mag)	UVV (mag)
2018-01-16	134.6	+6.8	14.11 ± 0.03	13.92 ± 0.03	13.75 ± 0.03	13.70 ± 0.03	14.82 ± 0.03	14.72 ± 0.04
2018-01-18	136.6	+8.8	14.55 ± 0.03	14.33 ± 0.04	14.08 ± 0.03	13.81 ± 0.03	14.83 ± 0.03	14.78 ± 0.04
2018-01-20	139.1	+11.3	15.01 ± 0.04	14.98 ± 0.06	14.51 ± 0.04	13.96 ± 0.04	14.89 ± 0.04	14.90 ± 0.06
2018-01-22	141.4	+13.6	15.50 ± 0.03	15.49 ± 0.04	14.91 ± 0.03	14.20 ± 0.03	14.95 ± 0.03	14.85 ± 0.04
2018-01-24	142.7	+14.9	–	–	–	14.34 ± 0.03	15.05 ± 0.03	14.87 ± 0.05

* With reference to the explosion date (JD 2458127.8).

3.3.2 Host and Light Curve Analysis

Host Properties

The preferred redshift (z) and distance (D) of NGC 6217 are 0.00454 ± 0.00001 and 19.61 ± 1.37 Mpc, respectively, and are referenced from NASA/IPAC Extragalactic Database (NED). Other distance estimates exist with a great scatter ranging from 15 Mpc to 35 Mpc (Bottinelli et al. 1984; Tutui & Sofue 1997). The SN was associated with host NGC 6217 ($9'13''.8$ "W" and $47''.4$ "N" implying $\sim 2'$ separation from the host's center). To check the veracity of its association with NGC 6217, an independent distance estimate was made using the Expanding Photosphere Method (EPM) (Kirshner & Kwan 1974; Schmidt et al. 1992; Hamuy et al. 2001). The detailed methodology and calculations are presented in Chapter 2. We found that the distances estimated using constrained explosion epochs and non-constrained explosion epochs varied as much as by 3 Mpc. The average distances using all three dilution factors are 15.7 ± 1.7 Mpc (non-constrained explosion epoch) and 17.5 ± 4.1 Mpc (constrained explosion epoch). Errors quoted are due to the scatter in the different measurements for three filter sets and three dilution factors. The distance of the SN estimated using EPM is in agreement with the distances given in NED for NGC 6217 and establishes the association of SN 2018gj with NGC 6217.

Table 3.10: The JHK_s photometric magnitudes of 2018gj.

Date (year-mm-dd)	JD 2458000+	Phase* (d)	K_s (mag)	H (mag)	J (mag)
2018-01-17	136.3	+8.5	14.05 ± 0.09	–	14.28 ± 0.03
2018-01-19	138.4	+10.6	13.97 ± 0.04	14.15 ± 0.03	14.20 ± 0.03
2018-01-30	149.3	+21.5	13.88 ± 0.03	14.08 ± 0.03	14.20 ± 0.02
2018-02-03	153.3	+25.5	13.91 ± 0.03	14.10 ± 0.02	14.23 ± 0.02
2018-02-06	156.3	+28.5	13.85 ± 0.03	14.08 ± 0.02	14.13 ± 0.02
2018-02-07	157.3	+29.5	13.84 ± 0.02	14.02 ± 0.02	14.15 ± 0.02
2018-02-08	157.9	+30.1	13.83 ± 0.03	14.05 ± 0.02	14.16 ± 0.02
2018-02-14	164.3	+36.5	13.90 ± 0.04	14.05 ± 0.03	14.21 ± 0.02
2018-02-16	166.2	+38.4	14.00 ± 0.04	14.08 ± 0.02	14.23 ± 0.02
2018-02-21	171.2	+43.4	14.06 ± 0.04	14.14 ± 0.03	14.18 ± 0.02
2018-02-26	176.3	+48.5	13.92 ± 0.04	14.09 ± 0.03	14.24 ± 0.02
2018-02-27	177.0	+49.2	–	–	14.24 ± 0.02
2018-03-01	179.2	+51.4	14.01 ± 0.03	14.19 ± 0.02	14.32 ± 0.02
2018-03-09	187.3	+59.5	14.02 ± 0.03	14.23 ± 0.02	14.31 ± 0.02
2018-03-11	189.3	+61.5	13.96 ± 0.04	14.12 ± 0.03	14.29 ± 0.02
2018-03-12	190.3	+62.5	14.07 ± 0.04	14.19 ± 0.03	14.34 ± 0.02
2018-03-17	195.2	+67.4	14.15 ± 0.04	14.30 ± 0.02	14.41 ± 0.02
2018-03-22	200.1	+72.3	14.13 ± 0.03	14.43 ± 0.02	14.57 ± 0.02
2018-03-25	203.2	+75.4	14.30 ± 0.04	14.51 ± 0.03	14.66 ± 0.02
2018-03-28	206.1	+78.4	14.45 ± 0.05	14.62 ± 0.03	14.87 ± 0.02
2018-03-30	208.1	+80.4	14.72 ± 0.04	14.85 ± 0.03	15.06 ± 0.02
2018-04-01	210.2	+82.4	–	15.03 ± 0.04	15.31 ± 0.04
2018-04-02	211.2	+83.4	14.98 ± 0.08	15.09 ± 0.04	15.38 ± 0.04
2018-04-07	216.3	+88.5	15.19 ± 0.05	15.50 ± 0.03	15.77 ± 0.03
2018-04-08	217.2	+89.4	–	15.47 ± 0.04	15.74 ± 0.03
2018-04-12	221.3	+93.5	15.28 ± 0.05	15.56 ± 0.04	15.9 ± 0.04
2018-04-15	224.3	+96.5	15.25 ± 0.09	15.62 ± 0.05	15.93 ± 0.04
2018-04-17	226.3	+98.5	15.37 ± 0.09	15.57 ± 0.04	15.91 ± 0.03
2018-04-21	230.3	+102.5	–	15.69 ± 0.05	15.94 ± 0.04
2018-04-22	231.3	+103.5	15.43 ± 0.09	15.63 ± 0.05	15.98 ± 0.04
2018-04-28	237.2	+109.4	15.48 ± 0.10	15.79 ± 0.07	16.08 ± 0.06
2018-04-30	239.2	+111.4	15.47 ± 0.13	15.82 ± 0.07	–
2018-05-09	248.2	+120.4	15.74 ± 0.11	16.08 ± 0.06	16.36 ± 0.03
2018-05-11	250.1	+122.3	15.68 ± 0.12	16.05 ± 0.05	16.38 ± 0.05
2018-05-12	251.2	+123.4	–	–	16.42 ± 0.05
2018-05-21	260.1	+132.3	15.87 ± 0.16	16.48 ± 0.05	16.57 ± 0.04
2018-05-23	262.2	+134.4	15.91 ± 0.12	16.50 ± 0.07	16.66 ± 0.04
2018-05-31	270.2	+142.4	16.17 ± 0.11	16.67 ± 0.07	16.79 ± 0.06
2018-06-04	274.2	+146.4	16.23 ± 0.27	–	16.76 ± 0.08
2018-06-16	286.1	+158.3	16.84 ± 0.20	17.02 ± 0.12	16.91 ± 0.04
2018-07-12	312.1	+184.3	–	17.64 ± 0.23	–
2018-08-01	332.0	+204.2	–	–	17.97 ± 0.09

* Reference being taken as the explosion date (JD 2458127.8).

From IRSA-Galactic Dust Reddening and Extinction map (Schlafly & Finkbeiner 2011), the Galactic extinction towards the SN direction, $E(B-V)_{MW} = 0.0375 \pm 0.0002$ mag. A feeble absorption feature at the host redshift was detected in the spectra due to Na ID with a pEW of 0.36 Å, averaged over the first five spectra.

TABLE 3.11: Spectra log for SN 2018gj.

Date (year-mm-dd)	JD (2458000+)	Phase* (d)	Range (Å)
2018-01-14	132.5	+4.7	3500–9250
2018-01-16	134.5	+6.7	3500–9250
2018-01-18	136.5	+8.7	3500–9250
2018-01-21	139.5	+11.7	3500–9250
2018-01-24	142.5	+13.7	3500–9250
2018-01-25	143.5	+15.7	3500–9250
2018-01-27	145.5	+17.7	3500–9250
2018-02-02	151.5	+23.7	3500–9250
2018-02-03	152.5	+24.7	3500–9250
2018-02-06	155.5	+27.7	3500–9250
2018-02-13	162.5	+34.7	3500–9250
2018-02-16	165.5	+37.7	3500–9250
2018-02-18	167.5	+39.7	3500–9250
2018-02-20	169.5	+41.7	3500–9250
2018-02-25	174.5	+46.7	3500–9250
2018-03-14	191.5	+63.7	3500–9250
2018-03-15	192.5	+64.7	3500–9250
2018-03-18	195.5	+67.7	3500–9250
2018-03-23	200.5	+72.7	3500–9250
2018-03-30	207.5	+79.7	3500–9250
2018-04-02	210.5	+82.7	3500–9250
2018-04-07	215.5	+87.7	3500–9250
2018-04-15	223.5	+95.7	3500–7800
2018-04-21	229.5	+101.7	3500–9250
2018-04-27	235.5	+107.7	3500–9250
2018-05-01	239.5	+111.7	3500–9250
2018-05-28	266.5	+138.7	3500–9250
2018-06-11	280.5	+152.7	3500–7800
2018-06-29	297.5	+168.7	3500–9250
2018-10-04	396.1	+268.3	5200–9250
2018-10-31	423.1	+295.3	3500–7800

* With reference to the explosion date (JD 2458127.8).

Using Poznanski et al. (2012), we find host reddening, E(B-V) $= 0.04 \pm 0.02$ mag. Hence we adopt E(B-V) $\approx 0.08 \pm 0.02$ mag as total extinction.

Light Curve Analysis

SN 2018gj was last non-detected on 2018 January 7.9 (JD 2458126.4) in the Gaia photometry, up to the limiting magnitude of $\sim$21.5 mag in G-Gaia filter (AB magnitude system), and was discovered on 2018 January 10.7 (JD 2458129.2). Using this last reported non-detection along with the discovery epoch of SN 2018gj, we constrained the explosion time as 2018 January 9.3 ($\sim$JD 2458127.8) $\pm$ 1.4 d. This explosion epoch has been used throughout this work, and all the epochs are reported as per this reference. Panchromatic light curve evolution of SN 2018gj in UV, optical, and NIR bands are presented in Figure 3.23. UV light curves in $UVW2$, $UVM2$ and $UVW1$ bands span a period of $\sim$14 d post-explosion, NIR light curves span up to 180 d whereas the optical light curve extends until $\sim$297 d. In all the light curves, we find a clear transition from the slowly declining (almost constant) plateau period to the nickel-powered tail phase. During this transition, we see a drop of $\geq$ 1.5 mag in visual bands.

During the plateau regime, light curves decline at different rates in different bands. In the U filter, we observe the sharpest decline with 6.44 ± 0.03 mag (100 d)$^{-1}$. As we move towards the redder wavelengths, we find the decline rate slows down to 3.39 ± 0.03 mag (100 d)$^{-1}$ in B, 1.26 ± 0.02 mag (100 d)$^{-1}$ in V, 0.79 ± 0.02 mag (100 d)$^{-1}$ in R and 0.64 ± 0.02 mag (100 d)$^{-1}$ in I band. The decline is even slower in the near-infrared wavelength regime with 0.37 ± 0.02 mag (100 d)$^{-1}$ in J band, but the decline rate increases slightly with 0.42 ± 0.06 mag (100 d)$^{-1}$ and 0.50 ± 0.07 mag (100 d)$^{-1}$ in H and K_s band, respectively. We find the slowest decline to be in the J filter. It is also noteworthy that in the radioactive decay tail phase, the decline rate trend reverses with the slowest decline observed in B band 0.90 ± 0.01 mag (100 d)$^{-1}$ and it is almost the same in V, R and I bands as 1.33 ± 0.01 mag (100 d)$^{-1}$, 1.14 ± 0.02 mag (100 d)$^{-1}$ and 1.26 ± 0.02 mag (100 d)$^{-1}$ respectively. We find the late-phase light curve decline rates to be much higher in the near-infrared bands as 1.86 ± 0.07 mag (100 d)$^{-1}$ in J, 2.58 ± 0.11 mag (100 d)$^{-1}$ in H and 2.12 ± 0.24 mag (100 d)$^{-1}$ in K_s bands. During the late phase, the light curve in the H band declined at the fastest rate.

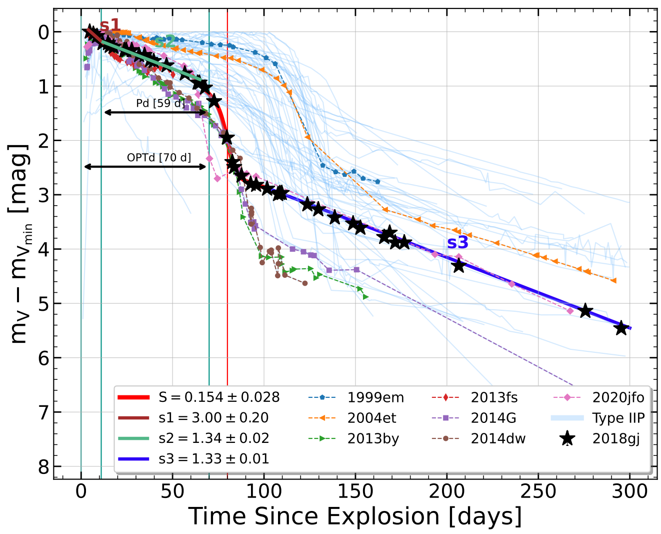

FIGURE 3.24: V-band light curve evolution of SN 2018gj along with other Type II SNe. Continuous light blue lines are representative of a larger Type II sample from Anderson et al. (2014a) and Faran et al. (2014a). Estimated light curve parameters for V-band viz. OPTd, Pd, s1, s2, and s3 are also shown. Supernovae data used in this plot are mentioned in Table 3.12

V-band Light Curve

After correcting for extinction, the apparent V-band magnitudes were transformed to absolute magnitude scale by using distance modulus, $\mu = 31.46 \pm 0.15$ mag (using the preferred distance of 19.61 ± 1.37 Mpc as given in NED). Even though the initial rise in the bluer bands is missed, we see the light curve getting brighter during the first two observations in the I band and, to a similar extent, in the R band. A similar rise is observed in the NIR J and K_s bands.

Due to the lack of V-band flux rising phase, the peak absolute magnitude M_V could not be constrained well (Figure 3.24). However, an upper bound on the peak $M_V \lesssim -17.0 \pm 0.1$ mag can be set. The mean of maximum M_V value for 68 Type II SNe estimated by Anderson et al. (2014a) is -16.74 ± 1.01 mag, which puts SN 2018gj towards the brighter end of Type II SNe. Furthermore, we observe a rapid decline in magnitude after +60 d, corresponding to a sharp transition period starting from end plateau epochs to early nebular epochs. Using the functional form given in Elmhamdi et al. (2003a), we could find the transition time at 79±2 d and a plateau length (OPTd) of ≈ 70±3 d, placing SN 2018gj in the shorter plateau group of Type IIP SNe. Following the definitions given in Anderson et al. (2014a), we estimated light curve parameters for SN 2018gj in V-band. We find $s1$, $s2$, and $s3$ to be 3.00 ± 0.20 mag (100 d)$^{-1}$, 1.34 ± 0.02 mag (100 d)$^{-1}$, and 1.33 ± 0.01 mag (100 d)$^{-1}$, respectively. The $s1$ and $s2$ decline rates are quite similar to the average values obtained from the Type II sample, which are 2.65 ± 1.50 mag (100 d)$^{-1}$, and 1.27 ± 0.93 mag (100 d)$^{-1}$, respectively. However, $s3$ is slower than the average decline rate of 1.47 ± 0.82 mag (100 d)$^{-1}$ for Type II SNe.

Colors

Table 3.12: Type II SN data used in comparison and estimating mean color evolution.

S.No	SN	Reference	S.No.	SN	Reference	S.No.	SN	Reference
1	1992H	Clocchiatti et al. (1996)	16	2006au	Taddia et al. (2012)	31	2013by	†
2	1992af	*	17	2007it	*	32	2013fs	†
3	1992ba	*	18	2007pk	Inserra et al. (2013)	33	LSQ13dpa	†
4	1997D	Hamuy (2003)	19	2008gz	Roy et al. (2011)	34	2013hj	Bose et al. (2016)
5	1999em	*	20	2008in	*	35	2014G	†
6	1999gi	Leonard et al. (2002a)	21	2009E	Pastorello et al. (2012)	36	2014cx	†
7	2000cb	Kleiser et al. (2011)	22	2009N	*	37	2014dw	†
8	2002hx	*	23	2009bw	Inserra et al. (2012)	38	ASASSN-14ha	†
9	2003gd	*	24	2009ib	Takáts et al. (2015)	39	2016X	Huang et al. (2018)
10	2004dj	Zhang et al. (2006)	25	2009md	Fraser et al. (2011)	40	2016bkv	Nakaoka et al. (2018)
11	2004et	Sahu et al. (2006)	26	2012A	Inserra et al. (2012)	41	2017eaw	Tsvetkov et al. (2018)
12	2004fx	*	27	2012aw	Bose et al. (2013)	42	2018ivc	Bostroem et al. (2020)
13	2005af	*	28	2012ec	Barbarino et al. (2015)	43	2018zd	Zhang et al. (2020)
14	2005cs	Pastorello et al. (2006)	29	2013K	Tomasella et al. (2018)	44	2020jfo	Teja et al. (2022)
15	2006V	Taddia et al. (2012)	30	2013ab	†	-	-	-

* Anderson et al. (2014a), †Valenti et al. (2016)

In Figure 3.25, different color evolution and comparison are shown. To compare SN 2018gj colors with other Type IIP SNe, a mean color curve from a sample of 44 Type IIP SNe, available in the literature, is created (For reference, see Table 3.12). We do not consider any epoch on which the number of available data points is less

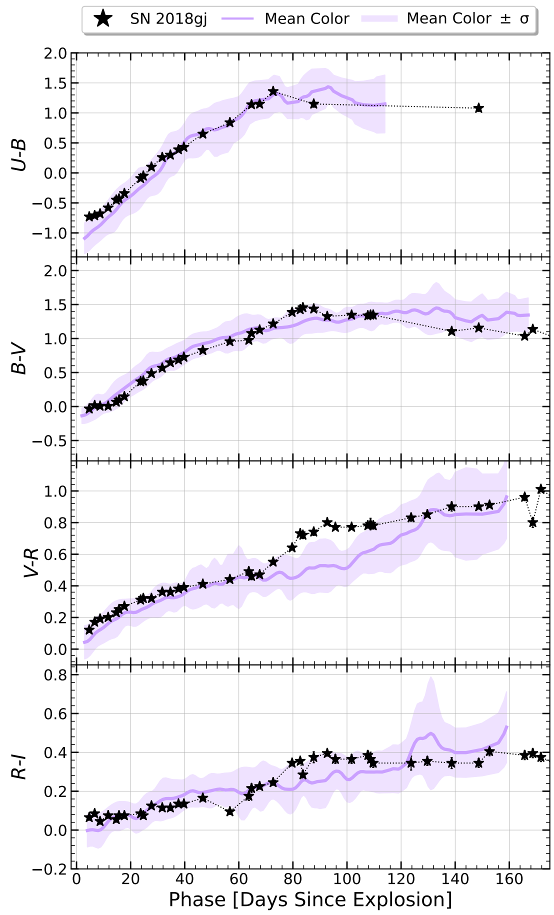

FIGURE 3.25: Mean color evolution of Type II SNe along with the color evolution of SN 2018gj for different bands are shown. The shaded region with a solid line represents the mean colors from a larger Type IIP sample with $1\,\sigma$ scatter from the mean value. Sources of data have been referenced in the Table 3.12.

than five. We apply extinction correction to all the respective individual band photometry using Cardelli et al. (1989) extinction law with $R_V = 3.1$. Further, Gaussian smoothing is applied using `scipy.ndimage.gaussian_filter1d`. The resultant mean colors, from the sample, along with $1\,\sigma$ scatter are over-plotted with that of SN 2018gj (see Figure 3.25). The color evolution of SN 2018gj predominantly follows the typical Type IIP SNe behavior with slight deviations in early $U-B$, late $B-V$, and $V-R$ during the transition phase. The initial $U-B$ color ($<$ 20 d) for SN 2018gj is redder than the average $U-B$ value for Type IIP SNe whereas the $B-V$ color evolution of SN 2018gj starts to deviate after +110 d and becomes bluer than the average sample values. Further, we observe a

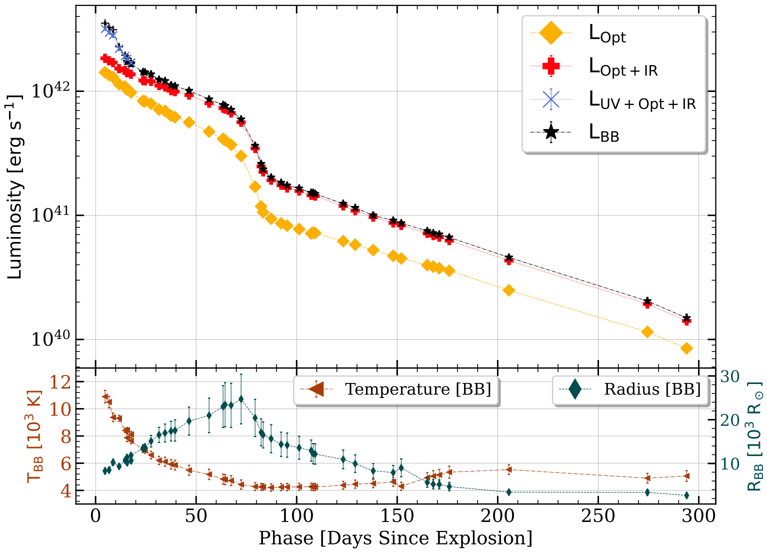

FIGURE 3.26: Pseudo-bolometric and bolometric light curves for SN 2018gj obtained using multiband photometry are shown. The second plot at the bottom shows the temperature and radius evolution obtained using blackbody fits from the SEDs.

slightly redder 'elbow' kind of feature in $V-R$ mean color values around +100 d for the sample, which could signify a mean plateau length duration of 100 d for the sample. In comparison, this break in $V-R$ color evolution is quite significant in SN 2018gj and is observed at +70 d, which later evolves along with the mean color evolution for the sample. The $R-I$ color evolution of SN 2018gj is typical of Type IIP SNe.

Bolometric Light Curve

The multi-broadband photometry is used to obtain the bolometric light curve of SN 2018gj, using the widely employed `SuperBol` (Nicholl 2018) code. The code computes pseudo-bolometric/bolometric curves by integrating the flux over observed bands. Further, a complete bolometric curve is estimated using blackbody extrapolations, additionally providing information about blackbody temperature and radius evolution. Zero points used for conversion between magnitudes and fluxes are obtained from Bessell et al. (1998) for $UBVRIJHK$ of the Johnson-Cousins-Glass system, Tonry et al. (2018b) for the ATLAS filters. Zero points for other filters are obtained from SVO FPS. To accommodate the missing epochs, the light curves were linearly interpolated, and if needed, the extrapolation was achieved using constant color with respect to the well-sampled reference band. These objectives are utilized using various tasks in `scipy`.

We estimate three different pseudo-bolometric/bolometric light curves. With only optical bands a pseudo-bolometric light curve ($L_{\rm Opt}$) is generated. Secondly, we include NIR data with optical and obtain OIR bolometric light curve (see Figure 3.26). As the UV data is not available throughout, we include UV data for the initial few days and estimate the bolometric light curve ($L_{\rm UV+Opt+IR}$). We find that using UVOIR data, the estimated bolometric light curve very closely traces the blackbody corrected estimate to the observed light curve ($L_{\rm BB}$). For further analysis, we use the UVOIR observed bolometric light curve.

We missed the early detection and rise and, therefore, cannot constrain the peak in any of the bands. Hence, we only report the maximum value in the pseudo-bolometric/bolometric light curves. Considering the optical contribution, the peak value obtained is $1.42 \pm 0.06 \times 10^{42}$ erg s^{-1} and if we include the NIR and UV contributions, the values obtained are $1.84 \pm 0.06 \times 10^{42}$ erg s^{-1} and $3.18 \pm 0.08 \times 10^{42}$ erg s^{-1}, respectively. We observe that during the initial phase of $\sim$5-15 d, NIR contributes only $\sim$ 25% to the pseudo-bolometric light curve. It sustains a maximum value of around $\sim$ 50% after the transition phase from 80 d to 110 d. NIR contribution remains significant in the nebular phase as well, with an average value of $\sim 43 \pm 2\%$, which is similar to the values estimated for other SNe (Patat et al. 2001; Elmhamdi et al. 2003a).

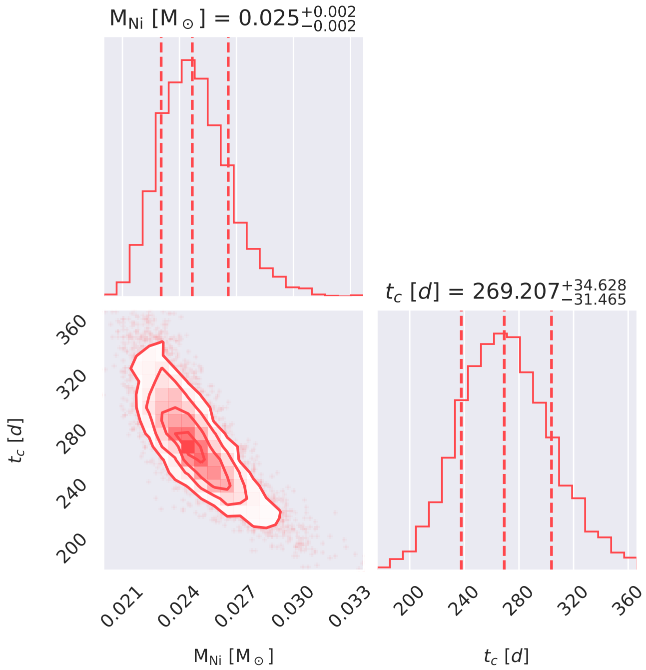

FIGURE 3.27: Posterior plot for nickel mass and characteristic time estimates for SN 2018gj using Equation 2.5.

Radioactive ^{56}Ni

We compared the bolometric luminosity of SN 2018gj in the nebular phase with the bolometric luminosity of SN 1987A. The mass of ^{56}Ni in SN 1987A is very well constrained using multiband photometry and hydrodynamical modeling and can be utilized to estimate mass of ^{56}Ni in SN 2018gj. We compare the bolometric luminosity with the values obtained for SN 1987A at similar epochs and use Equation 2.2 to get an estimate on ^{56}Ni mass.

From the late time light curve (> 110 d) we estimate the mass of ^{56}Ni to be $M_{Ni} = 0.024 \pm 0.004$ $M_\odot$. Mass of ^{56}Ni and characteristic timescale are also estimated using the Equation 2.5 and `scipy.minimize` and `emcee` packages. The posterior distribution for the fits is shown in Figure 3.27. We obtained ^{56}Ni mass and characteristic time of 0.025 ± 0.002 $M_\odot$ and 269 ± 33 d, respectively. The steepness parameter (S) is estimated as $S = 0.154 \pm 0.028$, applying the refined steepness

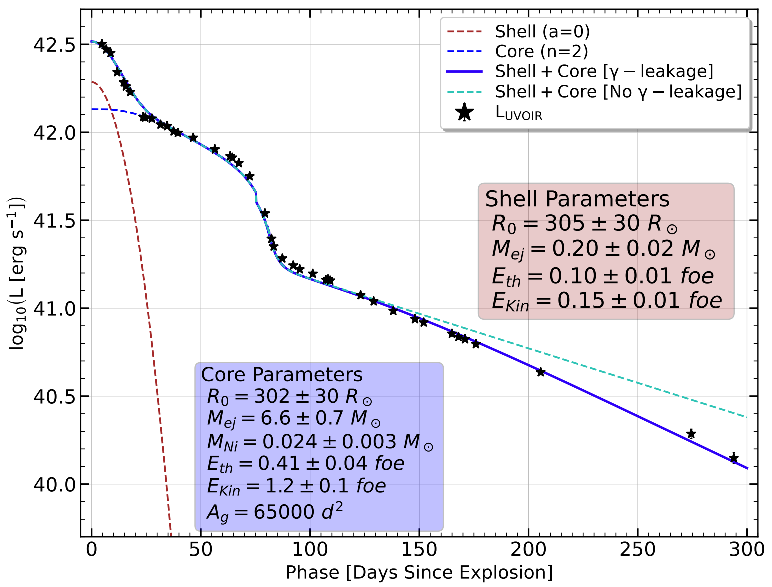

FIGURE 3.28: Semi-Analytical model fitting for SN 2018gj using two-component model as described in Nagy & Vinkó (2016). The contributions from the shell and the core are also shown independently. In the inset, best-fitting parameters are listed for reference. The evolution of the light curve without $\gamma-$ray leakage is shown by the cyan dashed line.

relation from Singh et al. (2018), this translates to $M_{Ni} = 0.026 \pm 0.007\ M_\odot$.

3.3.3 Two-Component Analytical Light Curve Model

We utilize Nagy & Vinkó (2016) analytical model, described in Chapter 2, to fit the observed bolometric luminosity. We use the UVOIR bolometric luminosity to approximate the semi-analytical models. The best fitting model is shown in Figure 3.28, and the obtained parameters are presented in Table 3.13. For the shell component we found, $M_{ej-shell} = 0.2\ M_\odot$ confined within a radius of 2.12×10^{13} cm. We find a similar radius value for the core as well ($\sim 2.10 \times 10^{13}$ cm) with an ejecta mass, $M_{ej-core} = 6.6\ M_\odot$. The outer envelope appears not far-extended, and the density is slightly higher ($\sim 1.0 \times 10^{-8}$ g cm^{-3}) as obtained for other Type IIPs in Nagy & Vinkó (2016). For comparison, the radii obtained are between the values obtained for SN 2005cs ($R_{shell} = 2.0 \times 10^{13}$ cm and $R_{core} = 1.2 \times 10^{13}$ cm) and SN 2012aw ($R_{shell} = 4.5 \times 10^{13}$ cm and $R_{core} = 3.0 \times 10^{13}$ cm). The shell densities obtained for both the cases are 1.8×10^{-8} g cm^{-3} and 5.2×10^{-9} g cm^{-3}, respectively. The values obtained for SN 2018gj are within similar ranges for other Type IIP SNe with a normal plateau duration. From the semi-analytical modeling, we get a total ejecta mass, $M_{ej} \approx 6.8 \pm 0.7$ $M_{\odot}$, radius, R$\approx 305 \pm 30$ $R_{\odot}$, and 1.9 ± 0.2 foe as the total energy released after the explosion.

During nebular period, light curve decline rate of 2018gj (1.34 ± 0.02 mag $100\,d^{-1}$) is much faster than 0.98 ± 0.02 mag $100\,d^{-1}$, the decay rate of ^{56}Co to ^{56}Fe with full $\gamma-$ray trapping. The faster decline of the late-phase light curve indicates that the leakage of γ-rays is significant in SN 2018gj. The effect of $\gamma-$ray leakage on the late time light curve could be introduced using the A_g parameter in the semi-analytical modeling. The late phase light curve, powered by the radioactive decay, is fit by an $A_g = 65000$ days^2 and mass of synthesized ^{56}Ni, (M_{Ni}) = 0.025 $M_{\odot}$. The corresponding T_0 value is 255 d, similar to the value obtained in Section 3.3.2. The M_{Ni} estimated here corroborates our previous estimates in Section 3.3.2. Further, the correlation between ejecta mass and opacity (correlation coefficient, r = 0.984, Nagy & Vinkó 2016) makes it insubstantial to comment on the possible progenitor mass with certainty up to two orders of magnitudes. If we consider a proto-neutron star core of mass ~ 1.5 $M_{\odot}$, nominal mass loss due to winds, and the estimated ejecta mass, we could constrain the lower limit of progenitor mass, which is $\geq 10 - 11$ $M_{\odot}$, an estimate very similar SN 2020jfo (Section 3.2.5), which had a very similar light curve shape, but a shorter plateau by $\sim$10 days.

3.3.4 Spectral Analysis

Apart from SN classification, detailed spectral studies provide insight into the ejecta composition, asymmetries, dust formation, and explosive nucleosynthesis. This section provides a detailed optical spectroscopic analysis of 2018gj. The

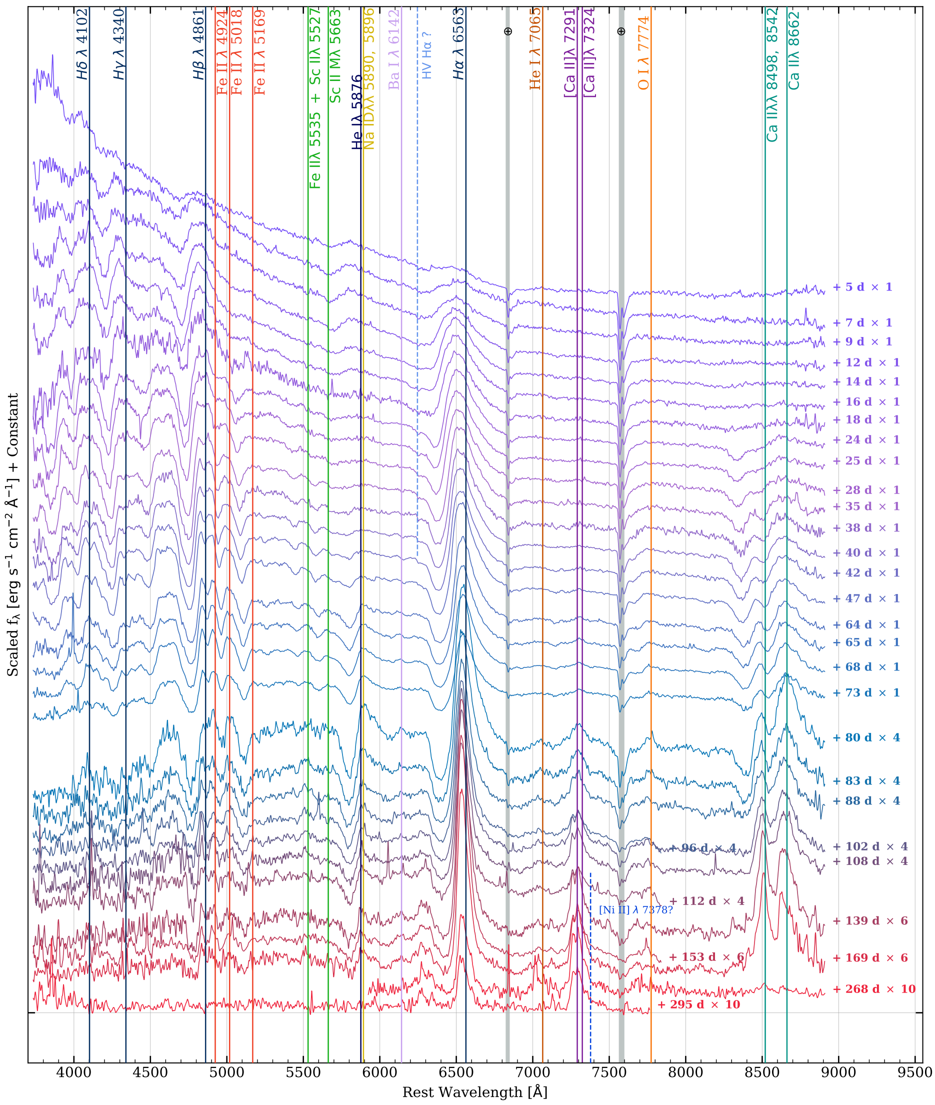

FIGURE 3.29: Spectral time series for SN 2018gj containing 31 epochs spanning 295 d post-explosion. All spectra have been calibrated with photometry for absolute flux and corrected for host redshift. Some of the prominent spectral lines have been marked for clarity. (The data used to create this figure are available.)

TABLE 3.13: Parameters for best-fitting two-component model

Parameters*	Shell	Core
Ejecta Mass, M_{ej} ($M_\odot$)	0.20	6.60
Radius, R (10^{13} cm)	2.12	2.10
Thermal Energy, E_{th} (10^{51} erg)	0.10	0.41
Kinetic Energy, E_{kin} (10^{51} erg)	0.15	1.2
Expansion Velocity, v_{exp} (1000 km s^{-1})	13.0	5.5
Opacity, κ (cm^2 g^{-1})	0.4	0.2

* $T_{rec} \approx 6000$ K, $A_g = 6500$ d^2 and $M_{Ni} = 0.024$ $M_\odot$

temporal evolution of spectra is presented in Figure 3.29, marked with some well-identified hydrogen and metal features. The spectral sequence is not corrected for telluric absorption lines. Further, all the spectra have been scaled with photometry for absolute flux calibration and corrected for the host redshift. We study the spectral evolution spanning 31 epochs over the photospheric phase to the nebular phase beginning +5 d.

Photospheric/Plateau Phase Spectra

The early part of spectra before or around the peak for typical Type II SNe is dominated by a featureless blue continuum along with a hint of formation of broad and discrete hydrogen features, predominantly Balmer series (Hα 6563 Å, Hβ 4861 Å, Hγ 4340 Å and Hδ 4102 Å). The features show a typical P-Cygni profile due to expanding ejecta. Early spectra of 2018gj exhibit these features. The He I 5876 Å appears as early as +5 d and seen till +16 d where it gets blended with the Na ID 5890, 5896 Å. The temperature of the ejecta estimated using SED (Section 3.3.2) around this phase is about $\gtrsim$ 10000 K, as the ejecta expands, it gradually cools down. With the ejecta cooling, metallic lines are seen, dominating the blue region of the spectra. All these metallic features show well-defined P-Cygni profiles. As the SN evolves, the absorption depth increases in strength with Fe II multiplet 4924, 5018, 5169 Å lines conspicuously observed at +24 d.

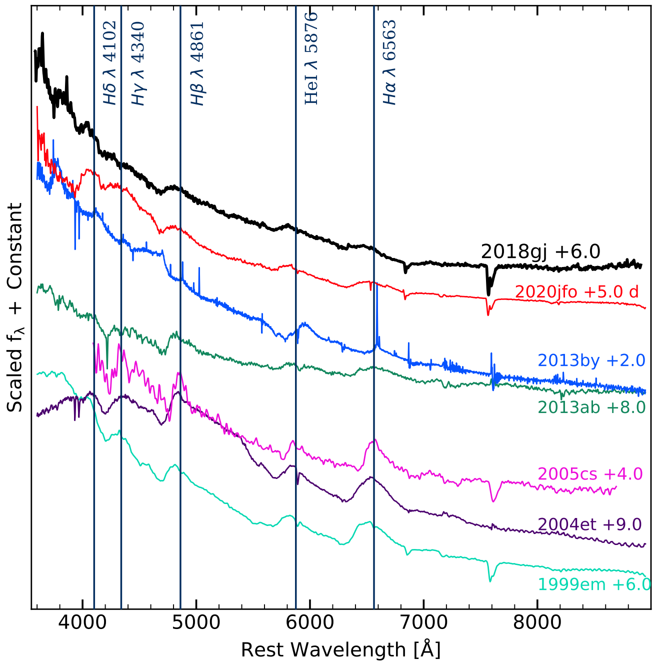

FIGURE 3.30: SN 2018gj spectrum during maximum light. Spectra of other Type II SNe around the maximum is shown for comparison. The comparison sample is drawn from Table 3.12.

The near-infrared region of the spectrum evolves with conspicuous Ca II triplet (8498, 8542, 8662 Å) that is visible during the same phase and becomes prominent as it evolves further. Towards the end of the plateau around $\sim +64$ d, the Na ID line develops prominently.

The spectral evolution covers the transition period very well which includes the late plateau phase to the early nebular phase. We obtained four spectra during the transition period from +72 d to +88 d. We find increased flux in the redder side with the increased strength of Ca II triplet. Similarly, other features become more prominent with an increase in their strengths. Apart from the increasing strength of hydrogen features, other lines, viz. Ba I 6142 Å, He I 7065 Å, and O I 7774 Å develop and are observed clearly (Figure 3.29). This could be either due to the temperature change or because we can probe deep inside the ejecta as the hydrogen layer becomes transparent to the radiation from these parts. Nevertheless, from the SED fitting, we find the temperature fairly consistent within this phase. So this is primarily due to the decreased opacity of the hydrogen layer. We do not find other stark differences during the transition phase.

When we make comparisons of the SN 2018gj spectral features with other Type II SNe, we find that these features are fairly typical and are observed in all sorts of Type II SNe whether they show plateau or decline linearly both in the early phase (Figure 3.30) as well as photospheric phase (Figure 3.31). The primary distinction is broadly the strength and spread of these features. During maximum light, the absorption trough of lines observed in SN 2018gj lies in between other SNe used for comparison. For archetypal Type IIP SNe, SN 1999em (Hamuy et al. 2001; Leonard et al. 2002b; Elmhamdi et al. 2003b) and SN 2004et (Sahu et al. 2006), we find the strength of Balmar features is more prominent around the similar phase. However, even for normal Type IIP SNe, e.g., SN 2005cs (Pastorello et al. 2006; Faran et al. 2014a) and SN 2013ab (Bose et al. 2015) the strength could vary. Although the early spectrum of SN 2020jfo (Teja et al. 2022) appears very similar to the spectrum of SN 2018gj except toward the shorter wavelengths, especially around Hγ, there was the presence of ionized He in the early spectra of SN 2020jfo. Spectral comparison around mid plateau for SN 2018gj reveals the lack of metallic or fully developed features, which are more prominent in other SNe viz. SNe 2020jfo, 2013ej, 2005cs, 2004et, and 1999em. Furthermore, it is observed that the hydrogen and other metallic features in SN 2018gj are weak as compared to normal Type II SNe but similar to SN 2009kr and SN 2013ab. SN 2013ab shows many similarities with SN 2018gj around the same phase.

Ejecta Velocity

In Figure 3.32, we show the expansion velocities estimated using the non-blended absorption minima of various species. The absorption minimum is estimated by fitting a Gaussian profile, and the expansion velocities are measured with respect

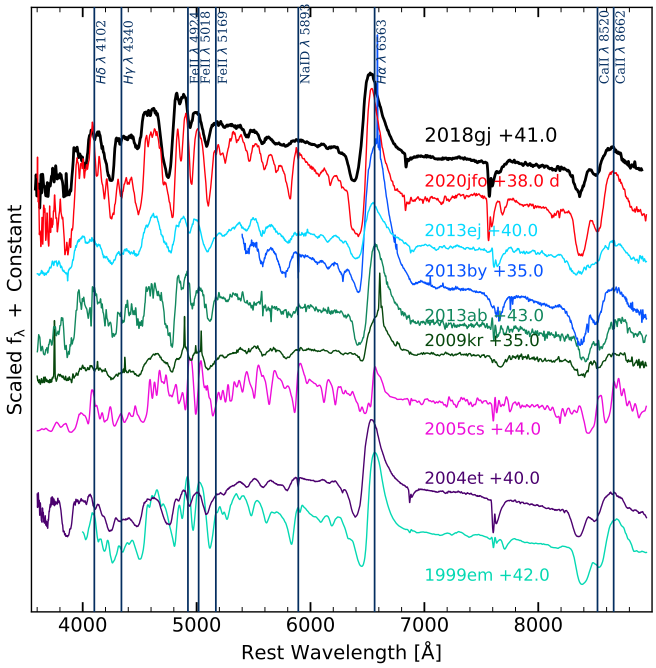

FIGURE 3.31: Spectrum of SN 2018gj during plateau phase is shown in comparison with other Type II SNe. The comparison sample is drawn from Table 3.12.

to the rest frame wavelengths. A peculiar velocity evolution of hydrogen features is seen for the initial few days. It first rises and then declines. The rising part of the ejecta velocity has not been observed for other SNe. While the estimation of an initial lower velocity may indeed be true, the absorption features during this phase are very broad and associated with higher measurement uncertainty. A shallow absorption feature is seen around 6200Å during the early phases (until $\sim$ 40 d). It could be attributed to a high velocity (HV) Hα feature (Dessart & Hillier 2022), at a velocity of $\sim$ 15000 km s^{-1}. Figure 3.32 also shows a comparison of the SN 2018gj velocities with the mean expansion velocities obtained from a large Type II SNe sample. Velocities for SN 2018gj are towards the higher end of $1-\sigma$ scatter from the mean. It continues to follow this higher velocity trend even after transitioning from the plateau phase to the nebular phase. The expansion velocity inferred from Fe II features is found to be higher than the mean value initially; however, later, it follows a trend similar to the mean of the sample.

From various absorption features, we estimate that the layers of the ejecta are

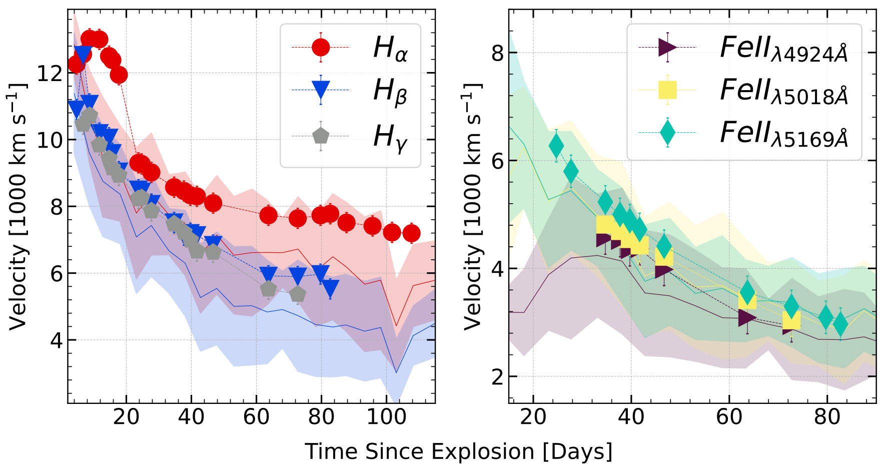

FIGURE 3.32: Temporal velocity evolution of various lines identified in the spectra using the absorption minimum is shown here. The velocities have been compared with the sample from Gutiérrez et al. (2017a) where the solid lines are the mean values from the sample and the shaded area around it in similar color represents the $1-\sigma$ scatter from the mean velocities.

moving with velocities higher than 10000 km s^{-1}. Although the temperature around a similar phase estimated for SN 1999em is similar to SN 2018gj, the Hα velocity inferred was much higher ($\sim$ 16000 km s $^{-1}$) (Elmhamdi et al. 2003b). In the case of SN 2013ej (Valenti et al. 2014) and SN 2020jfo, the expansion velocities are around 13000 km s^{-1} and comparable to that of SN 2018gj. As the ejecta evolves with time, it starts to slow down ($<$ 9000 km s^{-1} around +20 d) and cool to a lower temperature ($\leq$ 8000 K around +20 d).

During the photospheric phase, the expansion velocities continue to follow the declining trend and reach $\sim$8000 km s^{-1} around +40 d. Afterwards, the decline is very slow and does not follow the average trend. The expansion velocities estimated using hydrogen features are on the higher side for the Type II SNe. For SN 1999em around +40 d, typical temperatures are 5000–6000 K and Hα velocity of about 6000 km s^{-1} (Elmhamdi et al. 2003b). In 2005cs, velocities are much lower around +40 d and are estimated as $\leq$ 4000 and 2000 km s^{-1}, respectively for Hα and metal lines (Pastorello et al. 2006). Around similar phase Hα and metal velocities for SN 2004et are 7500 km s^{-1} and 4500 km s^{-1}, respectively. In case of

SN 2009kr, SN 2013by and SN 2020jfo, Hα velocities are $\leq$ 7000 km s^{-1} whereas for SN 2018gj it is close to the velocities estimated for SN 2013ab (8000 km s^{-1}) and SN 2013ej (8500 km s^{-1}).

Similar observations are true for velocities estimated using metal lines. Typical expansion velocities around the plateau phase start at 6000 km s^{-1} while they come down to $\sim$ 3000 km s^{-1} towards the plateau end.

Nebular Phase Spectra

SN in the nebular phase is still optically bright, and the prominent energy source is the radioactive decay chain of ^{56}Ni synthesized in the explosion. The midpoint of transition happens around +80 d, and several metal lines originating from forbidden transitions, e.g. [Ca II] 7291, 7324 Å start appearing. The strength of Na ID 5893 Å and Ca I triplet keeps on increasing as the ejecta evolves with time. Other forbidden lines viz. [Fe II] 6118, 7155, 7172 Å, [O I] 6300, 6364 Å also start to appear in the spectra. Blueward of Ca triplet, we identify the O I 7774 Å. The presence of Hα continues during the nebular phase and is the dominant line in the spectrum, although much narrower.

Figure 3.33 shows the comparison of nebular phase spectra for SN 2018gj with several other Type II SNe. The O I 7774 Å line in SN 2018gj is weakest when compared to other SNe except for SN 2013by. Apart from certain features common in Type II SNe, we find a hint of stable [Ni II] 7378 Å with emission feature having an intrinsic velocity similar to other emission features starting from +112 d (Figure 3.29). This feature was also observed in SN 2020jfo $\sim$ +196 d . However, it is quite possible that in SN 2020jfo, the stable Ni was present from an earlier epoch, but due to its proximity to the Sun, the first nebular spectrum could be

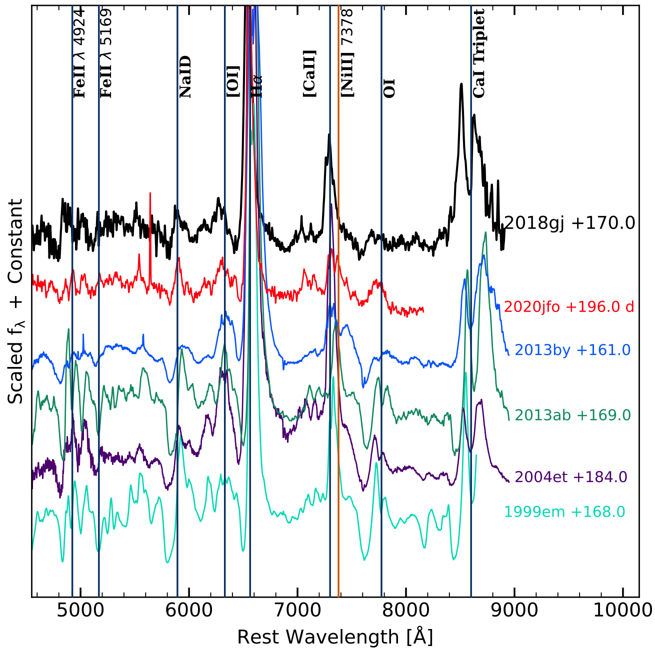

FIGURE 3.33: Spectral comparison of SN2018gj with other Type II SNe around similar epochs during the nebular phase.

obtained $\sim$ +196 d. This feature is very prominent in SN 2020jfo but weak in SN 2018gj.

3.3.5 Prolonged Blue-shifted Emission

We observed blueshift in the emission peaks in the spectral evolution of SN 2018gj. In Figure 3.34, the region around Hα has been plotted, showcasing this persistent blue shift in the Hα emission peak. The Hα emission peak is shifted by $\sim$ 4500 km s^{-1} around +10 d, which decreases monotonically till the end of the plateau around +75 d where it reaches a value $\sim$ 500 km s^{-1} but never reaches rest wavelengths (Figure 3.35). Instead, we observed the shift to increase during the transition phase and settle on a value of 1000 km s^{-1}. The blue shift is seen till the last available spectrum (+295 d). The shift is not only observed in the Hα but is also seen in other lines with similar values.

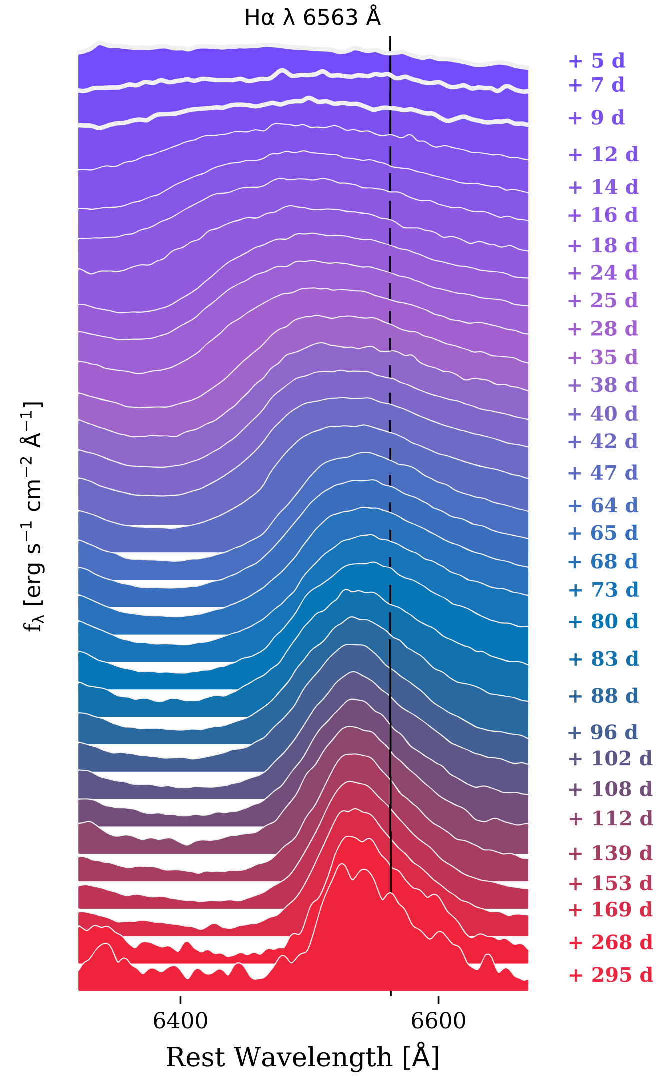

FIGURE 3.34: Focused view of spectral time series for Hα line in SN 2018gj. The black line marked is the rest wavelength for Hα. The spectra are corrected for host redshift, and it is evident that the peak of emission features never reaches the rest wavelength.

3.3.6 Progenitor Mass Estimates Using Nebular Lines

To constrain the progenitor mass of SN 2018gj, we compared the nebular phase spectrum at +295 d with model spectra from Jerkstrand, Anders (2017). The model spectra for 12, 15, 19, and 25 $M_{\odot}$ progenitor have been scaled for the ^{56}Ni mass and the distance of SN 2018gj (in contrast to 5.5 Mpc for the model spectra) (Figure 3.35). To account for the difference in phase between the model spectra

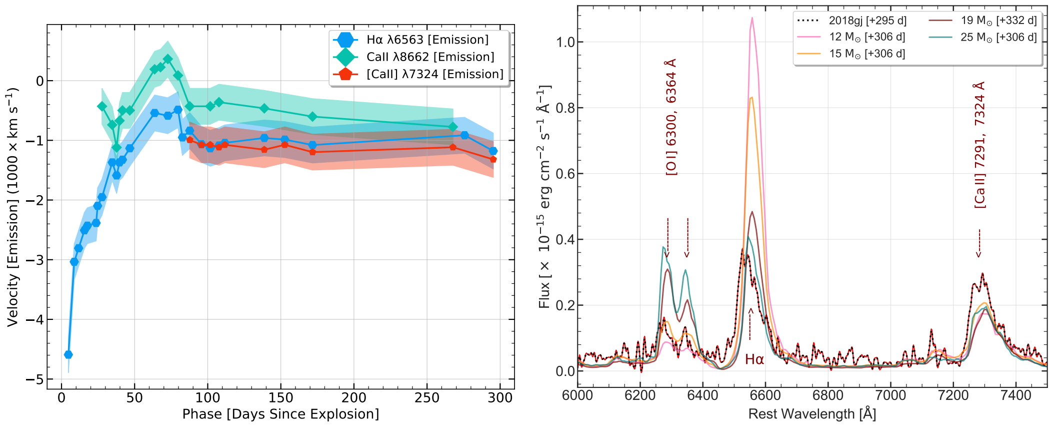

FIGURE 3.35: ***Left:*** Velocity evolution of blue-shifted Hα emission peak. Velocity evolution for emission features obtained using other ions has also been plotted. ***Right:*** Late phase (+295 d) spectrum of SN 2018gj compared with the model spectra around similar phase to estimate the initial mass of the progenitor. The model spectra are obtained from Jerkstrand, Anders (2017).

and the observed spectrum, the observed spectrum was scaled by the brightness difference due to dissimilarity in phases determined from the characteristic time scale (t_c) obtained from the ^{56}Ni-decay powered phase of the light curve using $f_{corr} = f_{obs}/(1 - e^{-(t_c/phase)})$ (Singh et al. 2019a).

The comparison of [O I] 6300 Å, 6364 Å line fluxes of the observed spectra with the spectral models suggests a progenitor of mass $\leq 15\,\mathrm{M}_{\odot}$. However, the observed Hα flux is relatively weak as compared to the $15\,\mathrm{M}_{\odot}$ progenitor, indicating a partially stripped hydrogen envelope in SN 2018gj. The [Ca II] / [O I] flux ratio is a useful indicator of the progenitor mass (Fransson & Chevalier 1989). The lower the value of the ratio, the heavier the progenitor. As seen in the model spectra presented in Figure 3.35, the [Ca II] 7291, 7324 Å line from different mass models have similar line strength whereas it is differentiable in the case of [O I] 6300, 6364 Å and increases with the progenitor masses. In the case of SN 2018gj, the [Ca II] lines are stronger than the model spectra, whereas [O I] lines are much weaker. Therefore, the [Ca II] / [O I] line flux ratio is much larger than one indicating a low mass progenitor.

TABLE 3.14: Parameters for pre-SN/Explosion progenitor models evolved from `MESA` that were used to generate model light curves in `STELLA`

Pre-Supernova Parameters										Explosion Parameters	
M_i ($M_\odot$)	α_{Dutch}	M_f ($M_\odot$)	M_{H-rich} ($M_\odot$)	$M_{He-core}$ ($M_\odot$)	$M_{Fe-core}$ ($M_\odot$)	$\log T_{eff}$ T_{eff}(K)	logL L(erg s^{-1})	Age (Myr)	Radius ($R_\odot$)	E_{Exp} (10^{51} erg)	M_{Ni} ($M_\odot$)
	3.0	9.1	5.35	3.75	1.50	3.57	4.83	16.7	620	0.4	0.025
	4.0	8.2	4.54	3.63	1.53	3.57	4.80	16.7	609	0.4	0.025
13	4.5	7.3	3.66	3.65	1.48	3.51	4.77	16.7	773	0.4	0.030
	5.0	6.9	3.26	3.60	1.52	3.51	4.80	16.8	794	0.2	0.027
	5.0	6.9	3.26	3.60	1.52	3.51	4.80	16.8	794	0.3	0.027
	5.0	**6.9**	**3.26**	**3.60**	**1.52**	**3.51**	**4.80**	**16.8**	**794**	**0.4**	**0.028**
	5.5	6.3	2.69	3.57	1.61	3.52	4.72	16.9	705	0.3	0.025

3.3.7 Hydrodynamical Modeling

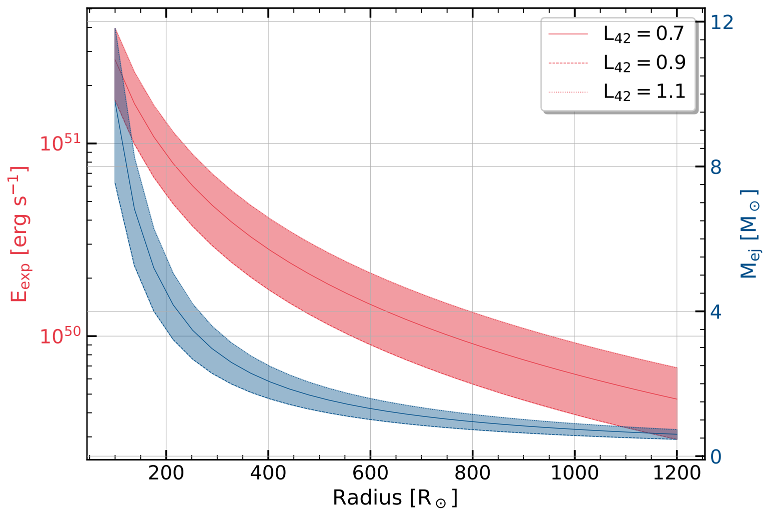

FIGURE 3.36: Scaling relations (Goldberg et al. 2019) in the context of Type IIP SNe as applicable to SN 2018gj.

The lower bound for progenitor mass obtained using the semi-analytical light curve modeling and the independent progenitor mass estimated using the nebular spectrum comparison with model spectra suggest that SN 2018gj resulted from a low-mass RSG progenitor with ZAMS mass ranging from 10-15 $M_\odot$. Model light curves of normal Type IIP SNe have been extensively studied (Dessart et al. 2010; Sukhbold et al. 2016; Eldridge et al. 2018), and in some cases, refined analytical equations are provided to get estimates on the progenitor properties (Goldberg

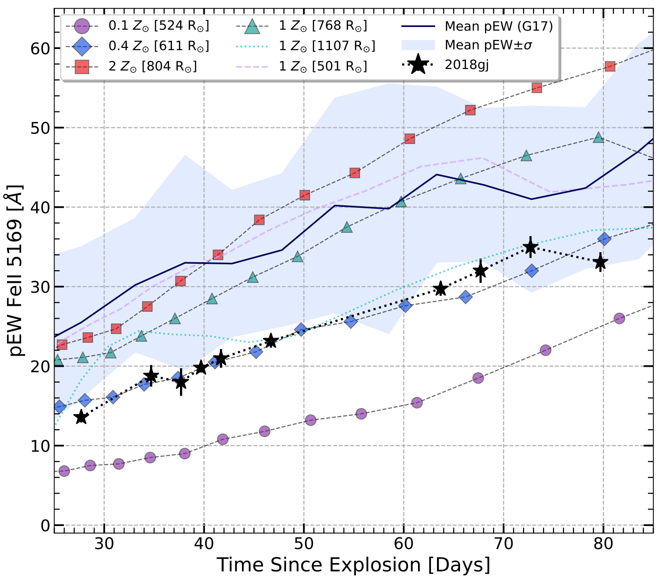

FIGURE 3.37: Temporal evolution of pseudo-equivalent width (pEW) for Fe II 5169 Å line obtained using optical spectra. Other markers represent the pEWs obtained from models given in Dessart et al. (2013). The solid blue line and the shaded region around it represent the mean pEW and the corresponding 1-σ scatter about the mean for a larger sample of Type II SNe given in Gutiérrez et al. (2017a).

et al. 2019). We compare the observables obtained for SN 2018gj with the analytical equations obtained for Type IIP and find that for a specific radius range of RSG ($300 - 1200$ $R_\odot$), the equations hint at a shallow ejecta mass ($0.5 - 2.5$ $M_\odot$) and explosion energy ($0.4 - 0.03$ foe) (see Figure 3.36). These ejecta masses are in disagreement with our previous estimates obtained using semi-analytical modeling and nebular spectra comparisons. Even if we use radii obtained from the semi-analytical modeling in the scaling relation, the values obtained for the ejecta mass and explosion energy are not similar to those obtained from the semi-analytical modeling. But as we go for much smaller radii ($\sim$200 R$\odot$), the ejecta mass (4.5 M$\odot$) and explosion energy (~ 1 foe) increase reaching closer to the values obtained using semi-analytical modeling. However, it is noted here that the analytical equations are calibrated for the SNe IIP that show a normal plateau of ~ 100 days and may not necessarily be valid for short plateaus as also indicated by Hiramatsu et al. (2021a).

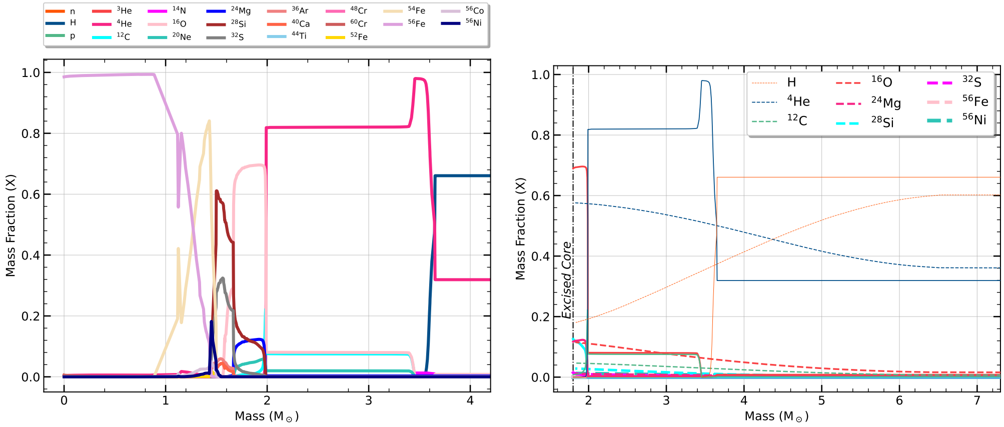

FIGURE 3.38: **Left:** One dimensional representation of mass fractions for 13 $M_\odot$ ZAMS model with final mass 7.3 $M_\odot$. The elements are part of the nuclear reaction rates network used in the model's evolution. The abscissa is shown till 4 $M_\odot$ as the trend followed beyond it is the same for the outer hydrogen envelope. **Right:** Effect of mixing with the implementation of Duffell RTI on the ejecta structure just before the breakout is shown for some of the prominent elements for the same model as in the Left panel.

A more robust way forward is to perform a complete hydrodynamical modeling to better understand the progenitor, its evolution history, and other SN explosion parameters. We perform the modeling using `MESA` version r-15140 and `STELLA` packaged within `MESA`. The modeling setup follows the values prescribed in Farmer et al. (2016). In lower mass models, we had increased the *max_model_number* in each *inlists* to accommodate longer evolution times. We fixed the overshooting values to default settings ($f = 0.01$, $f_0 = 0.005$). We set the *varcontrol_target* $= 10^{-4}$ for the convergence of models with higher mass loss. Some other basic setup parameters are as follows: the nuclear reaction rates network used 'approx21_cr60_plus_co56.net', provided within `MESA`. The mixing length parameter (`MLT_option`) defaults to *Henyey* Henyey et al. (1965), with $\alpha_{\rm MLT} = 1.5 - 2.0$, where $\alpha_{\rm MLT}$ is the ratio of mixing length to the pressure scale height ($= P/g\rho$). Other than the models with 19 $M_\odot$ and 13 $M_\odot$ ($\alpha_{\rm dutch} = 3.0$) where $\alpha_{\rm MLT}$ is set to default value of 1.5, we set it to 2.0 for the remaining models. Cool and hot wind schemes (α_{dutch}) for the Red Giant Branch or Asymptotic Giant Branch phase are considered 'Dutch', combining works by many Dutch authors. The primary combination chosen is based on the work by Glebbeek et al. (2009). Typically, if

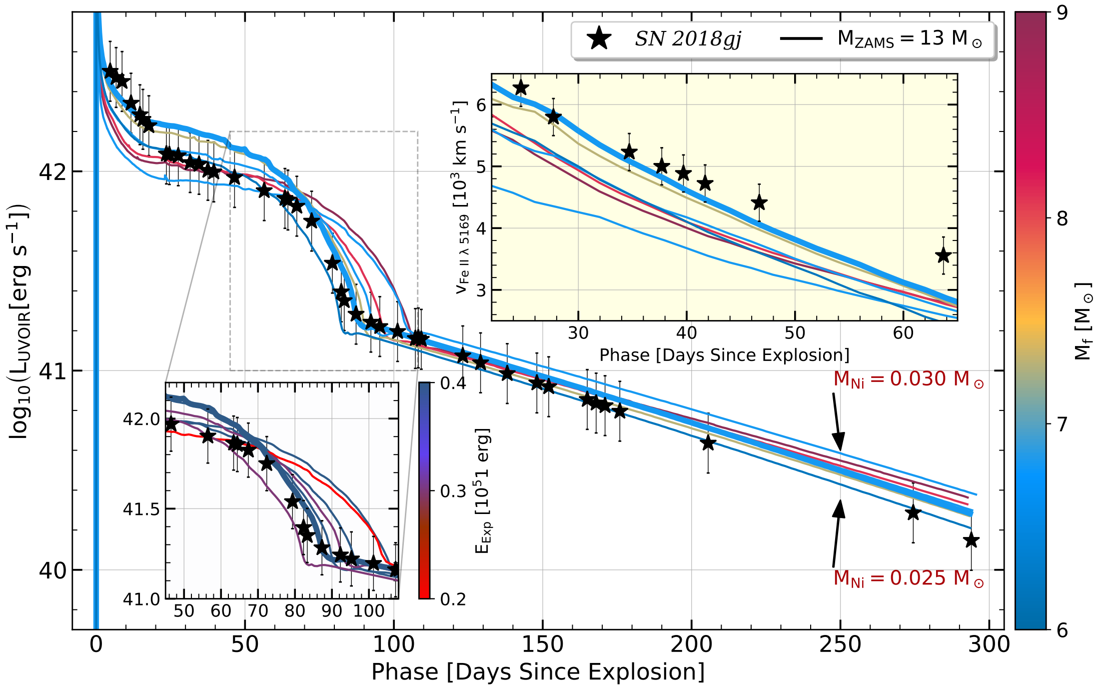

FIGURE 3.39: Variations in 13 $M_\odot$ ZAMS model using different parameters to achieve a shorter plateau length. Zoomed out a plot in the bottom left shows the variation in explosion energy for different model light curves around the plateau transition. The second plot in the right inset shows the corresponding Fe 5169 velocities obtained using models. The thicker line represents the model where the expansion velocity could be matched with the observed velocities.

the surface H has a mass fraction < 0.4 and a $T_{eff} > 10^4$ K, the scheme used is from Vink et al. (2001), otherwise, it is from Nugis & Lamers (2000). The default *Ledoux* criterion is used to determine the position of the convective boundaries.

We used 400 zones for `STELLA` with 40 extra zones in case of CSM. For the case of bolometric light curves, we used 40 frequency bins. However, in the case of UBVRI light curves, we had estimated 13$M_\odot$ cases for 120 frequency bins for better resolution. Another parameter crucial in modeling is the metallicity which could affect wind-driven mass losses, H envelope mass, and the line-profile signatures in Type II SNe (Dessart et al. 2013). Metallicity becomes more significant in the case of short plateaus due to extensive wind mass losses and smaller hydrogen envelopes. Since SN 2018gj is detected significantly far away from its host galaxy center, we tried to image the region around the SN in search of possible nearby

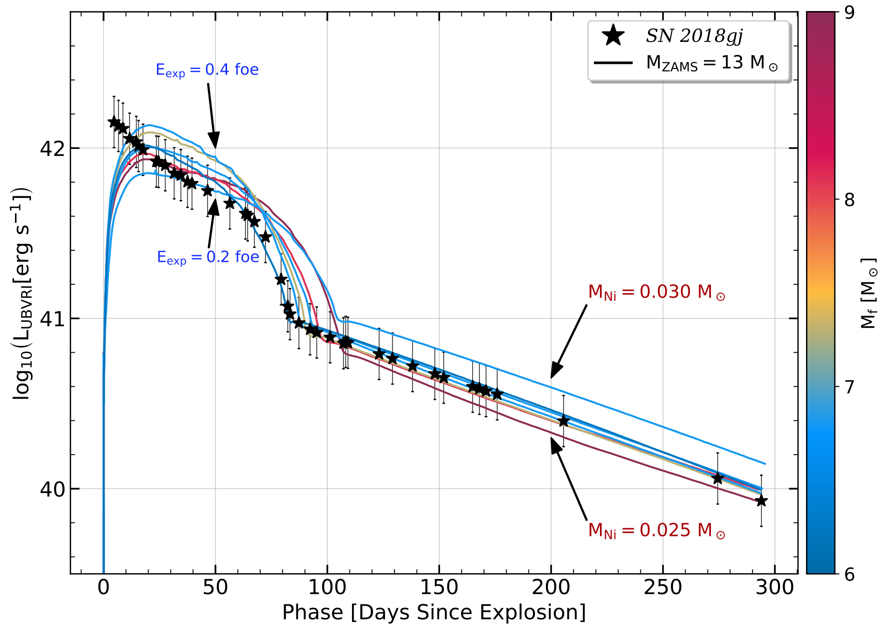

FIGURE 3.40: Optical bolometric luminosities obtained using `MESA+STELLA` are plotted along with the optical bolometric light curve of SN 2018gj. The initial rise is not fitting well in the optical regime.

H II using a narrow band Hα filter. Unfortunately, we could not detect any such region for sufficiently long exposures. To crudely estimate metallicity, we utilized the pEW evolution of Fe II λ 5169 Å. We compared it with the models presented in the Dessart et al. (2013). Figure 3.37 shows the time evolution of pEW of Fe II λ 5169 Å along with the models presented in Dessart et al.. It also shows the mean and $1-\sigma$ scatter in corresponding values for a larger Type II SNe sample. From these models, we found that two models with 0.4 $Z_\odot$ and $Z_\odot$ matched with the pEW obtained in the case of SN 2018gj. Hence, we fix the metallicity of all the models to be of Solar values.

We tried to evolve progenitors with ZAMS masses 13 $M_\odot$ and 14 $M_\odot$ and extracted their pseudo-bolometric/bolometric light curve evolution after they explode. We checked for higher mass models (see Figure 3.41). We found out that with standard mass loss by winds, none of the models were able to reproduce a short plateau. In most cases, the plateau duration was typical of normal Type IIP SNe. However, we could get shorter plateaus as we enhanced the mass loss rate through winds using the *wind scaling factor,* $\alpha_{dutch} = 3.0 - 5.5$. As the plateau duration primarily depends on the hydrogen envelope mass, achieving shorter plateaus from each of these progenitor masses with the correct mass loss was possible, although a simultaneous match to the expansion velocities was not achieved in the models for 14 $M_{\odot}$ progenitor. In the case of 13 $M_{\odot}$ models, we were able to match the light curve and expansion velocities up to the initial 50 days. Figure 3.38 gives the final composition for one of the 13 $M_{\odot}$ models representing the elements used in the progenitor structure. It also shows the mixing effect on the ejecta composition with the implementation of Duffell RTI in MESA (Duffell 2016). The mass fractions beyond 4 $M_{\odot}$ are very similar with no recognizable changes and, therefore, are not shown in Figure 3.38 (Left). Although elements are mixed at different mass coordinates, the core and outer structure fairly consist of iron and hydrogen. From the current understanding of single star evolution, high mass RSG (> 20 $M_{\odot}$), with enough mass loss, could give a smaller plateau as obtained in the works by Dessart et al. (2010); Hiramatsu et al. (2021a). To explore the possibility of a high mass progenitor, we also attempted to generate models using 19 $M_{\odot}$ progenitors, as this is the upper limit for directly detected progenitors. It is possible to obtain smaller plateau lengths with lower mass loss rates, but these models were unable to reproduce ejecta velocity evolution [Figure 3.41].

Properties of some of the pre-SN progenitors based on the models are provided in Table 3.14, giving details of the initial and final masses of the progenitors. Masses of helium and iron core present during evolution are also mentioned in the table. In addition to the used parameters, Table 3.14 also lists the various properties of the pre-SN star, viz. effective temperature, luminosity, age, and radius. We only show those models where we could achieve smaller plateau lengths. As expected from the initial mass of the progenitor models, there are not many differences in the pre-SN structure apart from the mass difference of the hydrogen envelope. All the models with the same initial mass have similar evolution times, effective temperatures, core masses, and luminosities.

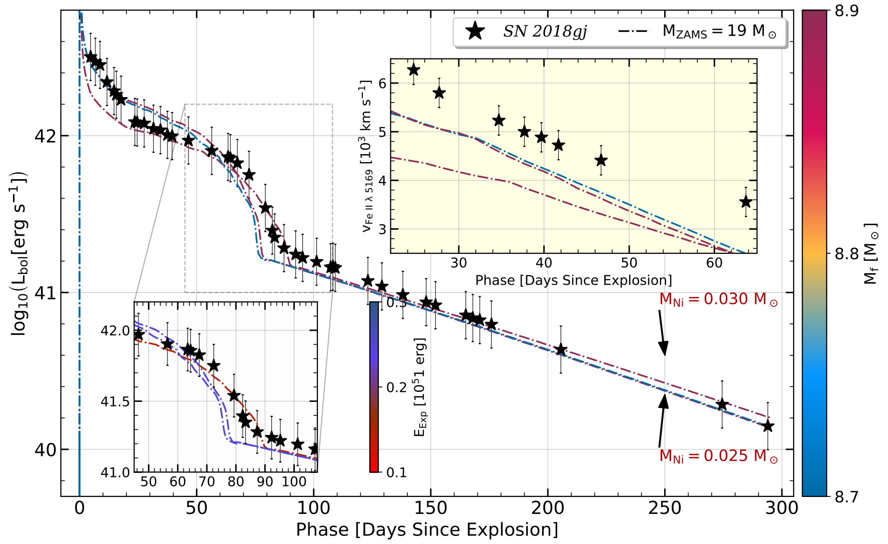

FIGURE 3.41: Variations in 19 $M_\odot$ ZAMS model using different parameters to achieve a shorter plateau length. Zoomed out a plot in the bottom left shows the variation in explosion energy for different model light curves around the plateau transition. The second plot in the right inset shows the corresponding Fe 5169 velocities obtained using models. All the 19 $M_\odot$ models underestimate the velocity evolution.

We attempted to generate the model light curves to match the observed UVOIR bolometric luminosity. After achieving a desired plateau length in the model light curves, the mass of synthesized nickel and explosion energy were constrained by varying the nickel mass (*x_ctrl*(12)) and explosion energy (*inject_until_reach_model_with_total_energy*) parameters during the explosion and shock propagation. Figure 3.39 shows all the models for 13 $M_\odot$ with plateau lengths 80 $\pm$ 10 d. The bolometric luminosity of SN 2018gj is over-plotted. In the model, the explosion energy and nickel mass are well constrained, however, the initial peak (s1) is slightly under-luminous. Instead of comparing the bolometric luminosity, we compare the observed pseudo (optical) bolometric luminosity with modeled pseudo-bolometric luminosity (L_{UBVRI}), which reveals the under-luminous s1 phase more prominently. The nickel mass obtained with the hydrodynamical modeling corroborates the earlier mass estimates through various techniques. The explosion energy obtained is slightly less than the semi-analytical modeling estimates. We discuss the possible presence of CSM interaction in the subsequent Section.

3.3.8 Discussion

Blueshifted Emission

As described earlier in Section 3.3.5, we observed the emission peaks were blueshifted, and these shifts were observed till the late phase. The blue-shifted emission during the photospheric phase has been observed and discussed explicitly in many works (Andrews et al. 2011; Bose et al. 2015). Anderson et al. (2014b) established that this feature is typical to Type IIP SNe during the early/photospheric phase. It was concluded by Chugai (1988) that these blue-shifted emission peaks during the photospheric phase are due to the diffuse reflection of the photosphere's resonance radiation. Primarily in all the cases, the shifts are only present up to the late photospheric phase or early nebular phase except in the case of SN 2007it (Andrews et al. 2011) where it has been observed till 150 d post-explosion. Anderson et al. (2014b) utilizing the Type IIP modeled spectra from Dessart et al. (2013) showed that the shifts in emission peaks vanish after the photospheric phase and the emission peaks are observed at rest wavelengths. Interestingly, the shifted peak is reported for Hα and not in any other lines.

The blue shift in the emission peaks observed in the spectral evolution of SN 2018gj is a typical feature for Type IIP SNe during the photospheric phase. But the intriguing aspect is the presence of these shifts until the late nebular phase and are not just limited to the prominent Hα feature. Observance of such shifts during the late nebular phase is rare in most of the usual Type IIP SNe studied in the literature. The blueward shift might not be physical but apparent and can be explained from the argument presented in Anderson et al. (2014b) regarding ejecta geometry and its composition. One of the critical factors is the changes in the opacity values. Opacity within the photosphere and above depends on various physical processes, viz. density, composition, and ionization degree within the ejecta (Sim 2017). During the photospheric phase, the density structure in Type IIP ejecta is much steeper. It enhances the confinement of the emission/absorption line. Further, it aggravates the concealment of the ejecta's receding portion, hence biasing the blueward line emission for a distant observer during the photospheric phase(Anderson et al. 2014b).

However, the above reasoning might not be valid during the nebular phase when the ejecta behaves like an emission line nebulae. Other radiative transfer effects might come into play, especially due to free electrons, photo-ionization, or the presence of dust (Jerkstrand 2017). During the nebular phase, the amount of electron scattering is relatively low, with an optical depth of $\tau_e \leq 1$. Most photons will not be scattered or will only be scattered once. As a result, the distortions in the line profile are not significant (Jerkstrand 2017). However, the scattering does cause a slight blue shift of the peak. For instance, when $\tau_e = 1$, the shift is approximately $\Delta\lambda/\lambda_0(V_{max}/c) = -0.13$, which corresponds to a velocity shift of 390 kms^{-1} for a line that is 3000kms^{-1} wide Jerkstrand (2017). The blueshift observed in the spectra is much larger than the values obtained for typical opacity. Hence, this might not be the cause of the observed shifts.

The continuous absorptive opacity or the photon destruction (continuous absorption) by dust or photo-ionization could also cause a significant blue shift. For $\tau_e = 1$, the shift is approximately $\Delta\lambda/\lambda_0(V_{max}/c) = -0.31$, which corresponds to a velocity shift of ≈ 900 kms^{-1} (Jerkstrand 2017) which is significant and close to the observed values. But for these effects, the presence of dust or enough optically thick material is required. As a considerable fraction of the hydrogen envelope is removed from the progenitor of SN 2018gj, the presence of optically thick material also does not seem plausible. However, the presence of pre-existing dust or early dust formation in the ejecta could be a possibility. We do not find a convincing signature for the presence of dust in ejecta. During the nebular phase, the light curve in optical bands is found to decline faster than the ^{56}Co decay rate, which could be due to the light absorption by dust. In such a scenario, due to the reprocessing of light by the dust particles, the light curve decline in the redder bands is expected to be slower. However, on the contrary, in SN 2018gj, light curves in the redder bands are found to decline much faster (Section 3.3.2).

Since the supernova occurred in the outskirts of the host galaxy, the intrinsically high velocity of the progenitor star towards the line of sight could also be the possibility. Although it is rare to find such high-mass hyper-velocity stars going rogue but could be possible, as observed in Evans & Massey (2015).

CSM Interaction?

A piece of substantial evidence has been found in favor of early CSM interaction having a signature in the light curves. However, we do not see any interaction feature in the spectral evolution. When we try to fit pseudo bolometric luminosity with UBVRI bolometric luminosity from the models (see Figure 3.40), we could see that the initial part does not fit that well until we introduce CSM interaction (see Figure 3.42).

In Figure 3.42, we introduce three CSM profiles with different wind evolution time and mass loss rates giving total masses 0.1, 0.15, 0.20 $M_\odot$ with different extents. We observe that the initial light curve evolution could be explained with less than 0.15 $M_\odot$ of CSM, which is close to the progenitor. The enhanced pre-SN wind was activated 10-20 years before the explosion.

There is no evidence in spectra to corroborate the presence of CSM around the progenitor. This could be either due to some non-spherical geometry or might be the intrinsic feature of these SNe and warrants a further understanding of these light curve rise times.

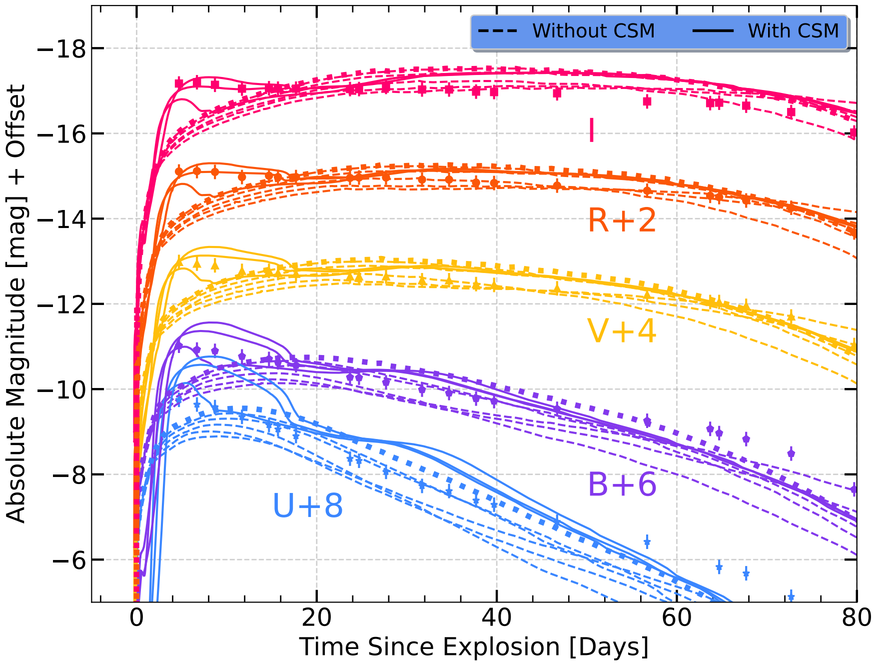

FIGURE 3.42: The effect of adding CSM around the progenitor is prominently seen in the early stage and can explain the initial excess in the individual light curves in redder bands. The thicker dashed lines represent the light curves obtained using 120 frequency bins.

3.3.9 Summary for SN 2018gj

We presented a detailed investigation of a Type IIP supernova SN 2018gj, which exhibited a plateau lasting for $\sim$ 70 d in its light curve. This plateau duration is significantly less than the characteristic plateau length of $\sim$ 100 d for Type IIP SNe. We carried out detailed photometric analysis in UV, optical, and NIR wavelengths and the detailed optical spectroscopic evolution till the nebular phase ($\sim$ 300 d from the explosion). The various light curve parameters were estimated, and the peak V-band magnitude in absolute scale was $-17.0(1)$ mag. Using bolometric flux mass of synthesized radioactive ^{56}Ni is estimated as 0.026 ± 0.007 M$_{\odot}$. Spectroscopic comparison of SN 2018gj with other Type II SNe indicated it to be a normal Type II SN but with high Hα velocities. Further, blueshift in the emission features during the late nebular phase is also reported. We carried out semi-analytical modeling, nebular phase spectral comparisons, and complete 1-D hydrodynamical modeling to ascertain ejecta mass, explosion energy, synthesized nickel mass, and details about the progenitor. The models favored a low mass progenitor of ZAMS mass of < 13 M$_\odot$, contrary to the higher mass RSG channels available in the literature. We found the hydrogen envelope mass to be only $\sim 2.5 - 3.0$ M$_\odot$ and a total pre-SN mass ≤ 7 M$_\odot$.

3.4 Summary

Studying these two events in detail, we find out that even with many similarities in their light curve evolution, plateau duration, and spectral evolution, there are some obvious differences. Each SN has its unique set of properties, for example, the conspicuous presence of stable ^{58}Ni in SN 2020jfo in the late phase and persistent blueshifts in the emission peaks in the SN 2018gj spectra. At the surface level discussing macro properties, these SNe appear to be similar, but probing their individual differences only points to the differences in their progenitors, evolution history, and environment.

Chapter 4

Fast Declining Short-plateau SNe

4.1 Introduction

For ease of this study, in the previous Chapter, the short-plateau IIP SNe were grouped based on their observational properties, and two examples of *"ordinary"* short-plateau events were studied. In this Chapter, we present an example for the *"fast-declining"* short-plateau events. The fast decline implies that the drop from the maximum in optical bands is much faster when compared to the average value for a larger Type II SNe sample (1.27 mag/100 d, Anderson et al. 2014a). Among the short plateau SNe, the fast-declining ones appear to be more natural. Recent work from Hiramatsu et al. (2021a) studied three short plateau objects in detail. All of them exhibited a fast declining plateau. They have shown it to be a distinct class in terms of its observational properties. Here, we carried out a detailed multiwavelength study on the decadal SN 2023ixf, which happens to be another fast-declining short plateau Type IIP supernova. The Chapter comprises of two broad sections; the first part focuses on the initial three weeks of evolution, covering the rising part pervaded by the circumstellar matter interaction. The second part takes it further to the early nebular phase, where we discuss other crucial aspects of this SN.

4.2 SN 2023ixf: From FUV to NIR

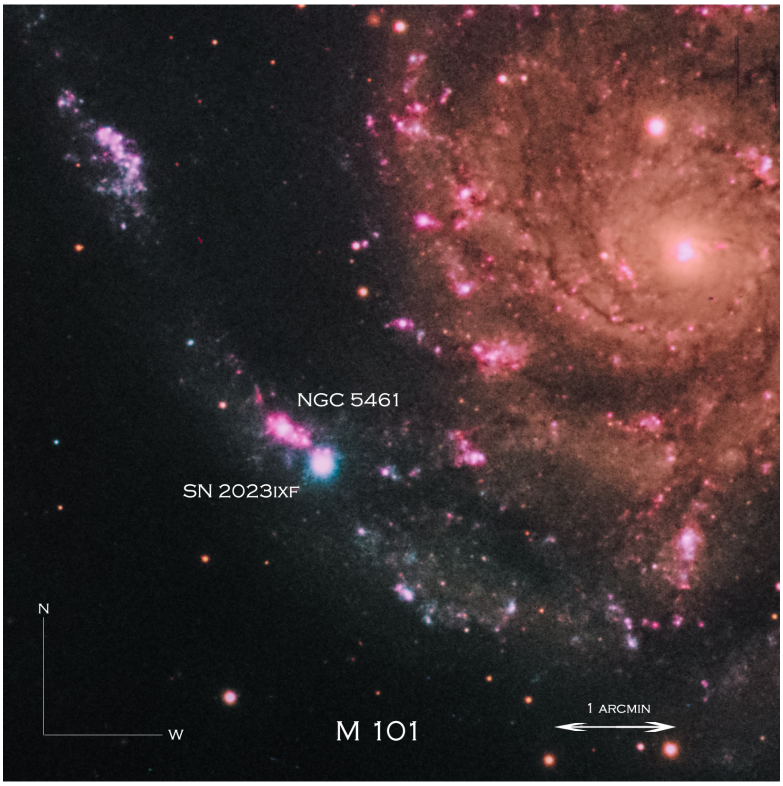

FIGURE 4.1: RGB composite of the host galaxy M 101 using r' (red), g' (green), and u' (blue) images acquired using 2m HCT. SN 2023ixf and the nearby Giant H II region NGC 5461 are labeled.

SN 2023ixf was discovered on 2023 May 19 17:27:15.00 UT in the outer spiral arm of M 101 galaxy at $\sim$ 14.9 mag in 'clear' filter and classified as a Type II SN. SN 2023ixf is the 2nd nearest CCSN in this millennium after SN 2004dj. SN 2023ixf lies proximal to NGC 5461 H II regions in M 101 (see Figure 4.1). Using emission-line diagnostics of the spectra, Van Dyk et al. (2023) estimated an oxygen abundance in range $8.43 \lesssim 12 + \log[\mathrm{O/H}] \lesssim 8.86$, which equates to a metallicity of $0.10 \lesssim \mathrm{Z}[Z_{\odot}] \lesssim 0.020$ close to the site of the SN. The pre-discovery photometry from

Zwicky Transient Facility (ZTF) and other Transient Name Server (TNS) alerts provide tight constraints on the time of explosion. Using the last non-detection (JD 2460083.31) and first detection (JD 2460083.32) (Chufarin et al. 2023), we find the explosion epoch, t_{exp} = JD 2460083.315 ± 0.005 which has been used throughout this chapter. We note that the last non-detection used is not very deep (> 18 mag) and if we consider the deeper non-detection (> 20.5 mag, Mao et al. 2023) on JD 2460083.16, the explosion epoch has a marginal change (of ∼ 0.08 d) to JD 24600083.235.

Several professional and amateur astronomers have followed up on SN 2023ixf. Various time-domain groups across the globe monitored it soon after its discovery. The early phase optical and NIR photometry and optical spectroscopy have been presented by Yamanaka et al. (2023); Hosseinzadeh et al. (2023); Jacobson-Galan et al. (2023). Flash features in the spectra and increased luminosity were interpreted as due to the presence of nitrogen/helium-rich dense CSM and its interaction with SN ejecta (Yamanaka et al. 2023; Jacobson-Galan et al. 2023). By comparing the early phase light curve with the shock cooling emission Hosseinzadeh et al. (2023) suggested that the progenitor of SN 2023ixf could be a red supergiant with radius 410± 10 $R_\odot$. The high-resolution spectroscopy revealed that the confined CSM is asymmetric (Smith et al. 2023). Pre-imaging data at the SN 2023ixf site was analyzed in recent works, constraining the mass of the progenitor between 12 − 17 $M_\odot$ (Jencson et al. 2023; Pledger & Shara 2023; Soraisam et al. 2023). These estimates are well within the mass range of directly detected CCSNe progenitors (Smartt 2009; Van Dyk 2017).

4.3 Observations

SN 2023ixf occured in the outer spiral arm of M 101, a face-on giant spiral galaxy that lies comparatively close to the Local Group. Tikhonov et al. (2015) estimated a mean distance of 6.79 ± 0.14 Mpc ($\mu = 29.15 \pm 0.05$ mag) to M 101 using the tip of the RGB method (Lee et al. 1993) with low-uncertainty. Riess et al. (2022) used Cepheids to estimate a distance of 6.85 ± 0.15 Mpc ($\mu = 29.18 \pm 0.04$ mag). We use mean distance of 6.82 ± 0.14 Mpc ($\mu = 29.17 \pm 0.04$ mag). The gas phase metallicity was computed by Garner et al. (2022) using various H II regions (host) and estimated 12 + log[O/H]$\sim$ 8.7 in the outer spiral arms of the galaxy which is similar to solar value (Asplund et al. 2009).

Galactic reddening towards the SN 2023ixf direction inferred from the dust-extinction map of Schlafly & Finkbeiner (2011) is $E(B-V) = 0.0077 \pm 0.0002$ mag. Using high-resolution spectrum, Lundquist et al. (2023) computed equivalent widths of Na I D1 and D2 lines to be 0.118 Å and 0.169 Å, respectively. Using the relation from Poznanski et al. (2012), we infer average host reddening of $E(B-V) = 0.031$ $\pm$ 0.011 mag. $E(B-V)_{Tot} = 0.039 \pm 0.011$ mag is adopted for SN 2023ixf, consistent with Smith et al. (2023).

Optical and Near-Infrared

We carried out broadband optical photometric observations in SDSS $u'g'r'i'z'$ filters beginning 2023 May 20 UT, using the robotic 0.7-m GIT. We also carried out photometric observations in $BVRI$ using a 0.36-m Schmidt Cassegrain telescope (Celestron EdgeHD 1400) at the Home observatory in Nayoro, Hokkaido, utilizing a CCD FLI ML1001E camera with an IDAS filter (standard system). The data reduction and aperture photometry were carried out using the software MIRA

Pro 64 (Mirametrics, Inc. 2023) with calibrations from APASS catalog (Zacharias et al. 2013). Additionally, optical photometric observations in VRI bands were also carried out using Atik 460 EX Mono CCD mounted on the 0.61-m Vasistha telescope at Ionospheric and Earthquake Research Centre and Optical Observatory, Sitapur, ICSP, Kolkata. Photometric calibrations were done using Tycho software and the ATLAS catalog (Tonry et al. 2018a). $BVRI$-band imaging was also carried out using the 0.51-m telescope at Oku Observatory, Okayama, using the SBIG Camera STXL-6303. Standard data reduction procedures were adopted using `IRAF`.

Optical spectra were obtained using HFOSC+HCT. Optical spectroscopic observations in the photospheric phase were also performed using the "Kyoto Okayama Optical Low-dispersion Spectrograph" with optical-fiber "Integral Field Unit" (KOOLS-IFU, Matsubayashi et al. 2019) mounted at the 3.8-m Seimei Telescope (Kurita et al. 2020) located in Okayama Observatory, Kyoto University, Japan. The KOOLS-IFU observations were carried out using VPH-blue grism (4100-8900 Å, R$\sim$500). The Hydra package in `IRAF` and a reduction software developed for KOOLS-IFU data were used to reduce data. We obtained additional optical spectroscopic data using TriColor CMOS Camera and Spectrograph installed on 3.8-m Seimei telescope having a wavelength coverage of 4000–10500 Å (R$\sim$700). The spectroscopy was also performed from the 0.4-m reflector at the Fujii Kurosaki Observatory (FKO) in Okayama, Japan, with a resolution of R = 1000 and a wavelength coverage of 4000-7800 Å. The spectroscopic data were reduced using standard IRAF tasks. All the spectra have been continuum calibrated with respect to gri photometry and host redshift corrected.

NIR observations were taken from HONIR+Kanata. Near-infrared observations were also carried out using kSIRIUS* attached to the Cassegrain focus of the 1.0-m telescope at the Iriki Observatory in Kagoshima, Japan. The NIR data

*NIR simultaneous $JHKs$-band imager

were reduced using standard procedures in `IRAF`, and the photometric magnitudes were obtained through the PSF photometry utilizing standard `IRAF` tasks. The photometric calibration was performed using secondary standard stars from the 2MASS catalog (Skrutskie et al. 2006).

Ultraviolet

SN 2023ixf was observed by the *UVIT* on board *AstroSat* on 2023 May 25 & 30 UT in both imaging and spectroscopic modes. However, we could only use imaging data from May 30 for photometry since the images from the earlier epoch were saturated. The spectra obtained at all epochs are of good quality and have been used for this study. We also triggered the *UVIT* for several Target of Opportunity (ToO) proposals. However, due to technical constraints, observations against our ToO request could be undertaken only on June 11, 2023. All the *UVIT* observations are listed in Table 4.1.

SN 2023ixf was also monitored extensively by the *Swift*/UVOT beginning May 21, 2023. We utilize the publicly available data obtained from *Swift* Archives[†]. Being a very bright SN, most photometric data points were saturated. We checked the `saturate` and `sss_factor` flags from the output and discarded all the saturated and unusable data points based on those flags. We used the archival data for the host M101 obtained on Aug 29, 2006, under OBSID 00035892001, available in the *Swift* archive, as template images for removing the host contribution. The flux obtained at the SN site in the template images is comparable to the late-phase fluxes in all the *Swift* bands. We employed `Swift_host_subtraction`[‡] code (Brown et al. 2009, 2014) to remove any contribution form the host.

[†] Swift Archive Download Portal
[‡] https://github.com/gterreran/Swift_host_subtraction

Spectroscopic data reduction for *Swift* UV-grism data was performed using the standard `UVOTPY` package as described in Chapter 2. Further, multiple spectra captured intra-night were summed using `uvotspec.sum_PHAfiles` program in `UVOTPY` to increase the overall SNR. The first two spectra separated by just 0.1 d showed intranight flux variability due to the rapid rise; hence, these two spectra were not summed. Around 1800 Å, a few spectra were contaminated by a strong source, therefore, we have considered the UVOT spectra beyond 1900 Å only.

TABLE 4.1: Log of AstroSat observations.

ObsID	Date (yyyy-mm-dd)	Phase (d)	Instrument	Time (ks)
T05_108T01_9000005664	2023-05-25	+6.9	UVIT FUV	7.32
T05_110T01_9000005672	2023-05-30	+11.9	UVIT FUV	4.32
T05_116T01_9000005682[a]	2023-06-11	+23.4	UVIT FUV	3.48

[a] Observation against our ToO

Other Data Sources

Being a nearby SN in one of the most well-observed host galaxies, M 101, many amateur astronomers and professional observatories have monitored the SN. We supplemented our photometric dataset with various detections and non-detections of SN 2023ixf from ATELs and TNS Astronotes, and include the magnitudes reported by Filippenko et al. (2023); Zhang et al. (2023); Limeburner (2023); Kendurkar & Balam (2023); Fulton et al. (2023); Mao et al. (2023); González-Carballo et al. (2023); Perley & Irani (2023); Desrosiers et al. (2023); Fowler et al. (2023); Koltenbah (2023); Chufarin et al. (2023); D'Avanzo et al. (2023); Vannini (2023); Balam & Kendurkar (2023); Vannini & Julio (2023a,b); Singh et al. (2023). We further supplemented our multi-wavelength light curve data with early phase photometry ($< 10\,$d) in *griz* from Jacobson-Galan et al. (2023). We also utilized the streak photometry performed on the saturated *Swift*/UVOT UV bands from Zimmerman et al. (2023).

4.4 Flash Phase and CSM Characteristics

Optical Spectra

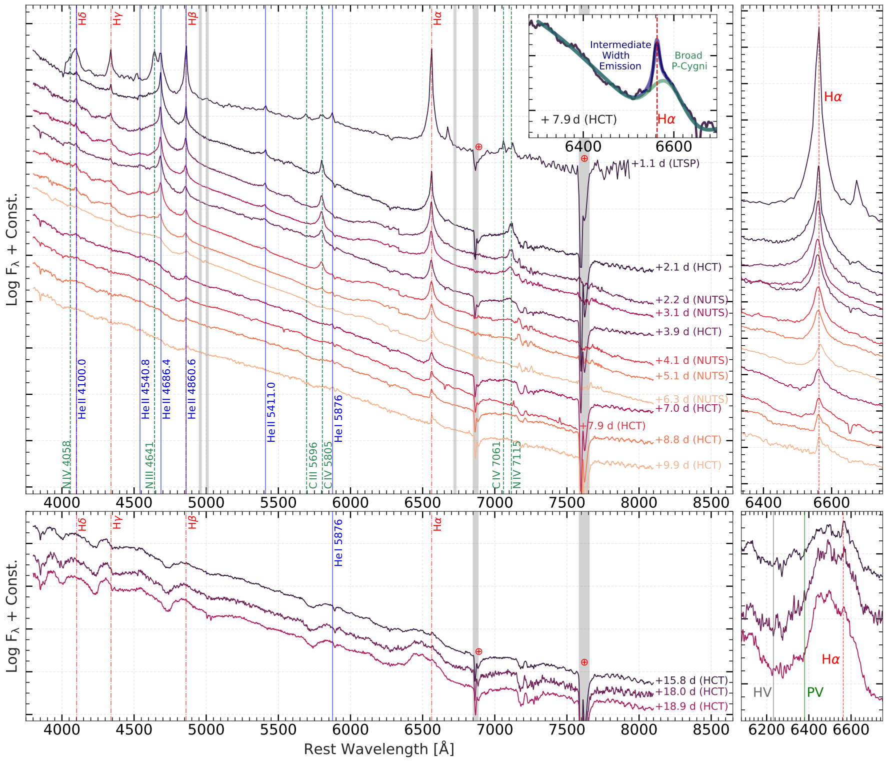

FIGURE 4.2: Optical spectral evolution for SN 2023ixf from HCT, Perley & Gal-Yam (2023) and Stritzinger et al. (2023). The spectra are corrected for the redshift of the host galaxy M 101, and the epochs are labeled with respect to our adopted explosion epoch. **Top:** *Left:* Early time spectral sequence of flash features in SN 2023ixf with line identification of high-ionization features and Balmer lines. The inset depicts the H α profile on +7.9 d having a broad P-Cygni feature and an Intermediate-width Lorentzian emission. *Right:* Evolution of line-profile of H alpha during the flash phase. **Bottom:** *Left:* Spectral sequence of SN 2023ixf during the photospheric phase. *Right:* Evolution of multi-peaked emission profile of H alpha during the photospheric phase. HV and PV refer to the high-velocity and photospheric velocity components in the blue-shifted absorption wing of H α.

The first spectrum of 2023ixf in optical was obtained just after the discovery (within 5 hrs) by the Liverpool Telescope (Perley & Gal-Yam 2023). Our spectroscopic follow-up with HCT began ~ 2 days after the explosion. In the first part of this work, we present the spectral data obtained from HCT until ~ 19 days after the explosion. The spectral evolution is given in Figure 4.2. The early spectra, until $\sim$10 d, show a prominent blue continuum with strong high-ionization emission features due to C IV, N IV and He II, specifically, C IV 5805 Å, C IV 7061 Å, N IV 7115 Å, He II 4540 Å, He II 4686 Å and He II 5411 Å along with the Balmer lines Hα, Hβ, Hγ, and Hδ. Weak signatures of C III 5696 Å, N III 4641 Å and He I 5876 Å are also seen in the spectra. The highly ionized emission features at $\sim$2.1 d are well reproduced by a combination of a narrow Lorentzian (limited by the resolution) and an intermediate-width Lorentzian of 2500 km s^{-1}. Our findings during the flash-ionization phase are similar to those reported in Smith et al. (2023); Jacobson-Galan et al. (2023); Bostroem et al. (2023a); Yamanaka et al. (2023).

The strength of the narrow component fades gradually, in contrast to the intermediate width component, as the SN flux rises in the optical wavelengths. Most of the flash features in our spectral sequence disappear after +7 d. In the spectrum of 7.9 d, we observe an intermediate-width Hα emission at $\sim$ 1,000 km s^{-1} in addition to the emergence of a broad P-Cygni feature with absorption trough. This could possibly be due to residual of ongoing interaction with the dense CSM responsible for the flash-ionized phase. A similar profile is also seen for the Hβ line. Beginning $\sim$16 d (bottom-right panel in Figure 4.2), we observe a blue-shifted multi-peaked emission profile of Hα with a broad absorption feature, which mimics the profile of a detached atmosphere (Jeffery & Branch 1990), and is an indication of the fast-moving SN shock encountering a low-density shell-shaped CSM (Pooley et al. 2002). The multi-peaked emission profile seen here is similar to the boxy-emission profile seen during the photospheric phase in SN 2007od (Andrews et al. 2010), SN 2016gfy (Singh et al. 2019a) and SN 2016esw (de Jaeger et al. 2018).

We observe two absorption troughs blue-ward of Hα at 8,000 km s^{-1} (PV; Photospheric velocity) and 15,000 km s^{-1} (HV; High-Velocity) in the spectrum of $\sim$16 d. The HV feature, labeled "Cachito" in the literature, could instead be due to the presence of Si II 6355 Å (Gutiérrez et al. 2017a) in the blue-wing of Hα. The estimated velocity ($\sim$ 5000 km s^{-1}) is lower than the photospheric velocity if the feature is from Si II. We also detect an analogous profile bluewards of Hβ with a similar velocity as seen in the Hα profile, indicating that the feature plausibly attributes to hydrogen only. However, the possibility of Si II blended with the HV feature of hydrogen can not be ruled out altogether.

We estimated the photospheric velocity using the minima of the absorption trough of Hβ, Hγ and He I 5876 Å. Although velocities estimated from Fe II act as a reliable tracer of photospheric velocities (Dessart & Hillier 2005b), we used H and He line velocities as they fairly resemble the photospheric velocities early in the photospheric phase (Faran et al. 2014a). Using the ejecta velocities (PV and HV) estimated above, we compute an inner radius of $\sim$75 AU and an outer radius of $\sim$ 140 AU for the shell-shaped CSM encountered by the SN ejecta. Assuming a standard RSG wind velocity of 10 km s^{-1} (Smith 2014), the progenitor of SN 2023ixf likely experienced this enhanced mass-loss $\sim$35 - 65 years before the explosion. If we consider the wind velocity of $\sim$ 115 km s^{-1} inferred by Smith et al. (2023) using high-resolution optical spectra, we estimate that mass loss episode likely occurred $\sim 3-6$ years before the explosion.

UV Spectra

We discuss FUV (1250 - 1800 Å) and NUV (1900 - 3400 Å) spectral evolution of SN 2023ixf obtained with *AstroSat* and *Swift*, respectively. Predominantly, the UV lines arise due to re-emitted UV emission from highly ionized species created from the shock wave expanding into the ambient material (Williams 1967; Chevalier

1981; Fransson 1984; Chevalier & Fransson 1994). Along with the emission lines, the UV spectra are dominated by many absorption features from the interstellar matter (ISM) in the Milky Way and the host galaxy due to high ionized states of C, N, O, Si, etc. (Fransson 1984). Further, the UV spectra are not a simple continuum with isolated emissions and absorptions but a continuous set of features having both emission and absorption features which at times are hard to identify (Pun et al. 1995; Dessart & Hillier 2010; Bostroem et al. 2023b). The UV spectra of Type II SNe are scarcely studied, particularly the FUV domain is largely unexplored with SN 1979C (Panagia et al. 1980) to be the first one observed extensively in FUV, and SN 2022acko (Bostroem et al. 2023b) was the most recent one. For the present work, we restrict ourselves to describing the UV spectra qualitatively.

FUV spectra

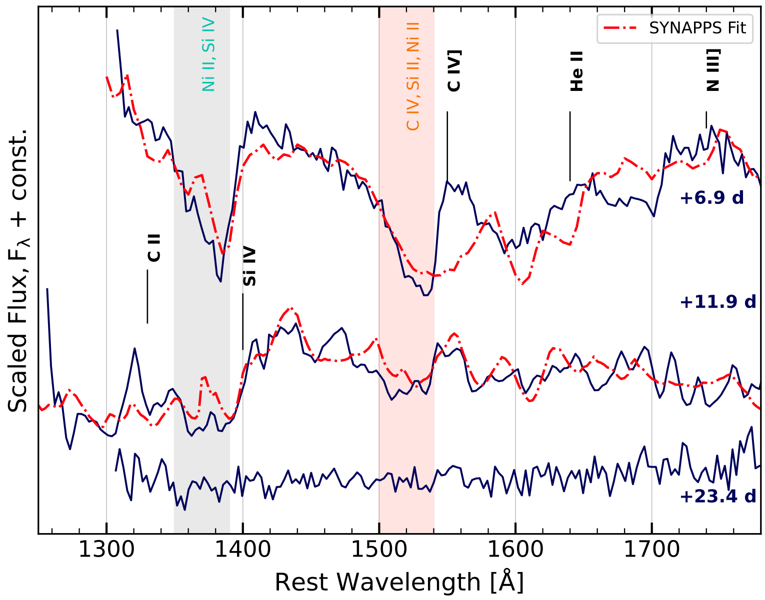

FIGURE 4.3: FUV spectral evolution obtained using Astrosat/UVIT and the SYNAPPS fit to the spectrum of ~ 7 d and ~ 12 d.

The FUV spectra of SN 2023ixf were obtained at three epochs ~ 7 d, ~ 12 d, and $\sim$ 23 d (see Table 4.1). The first spectrum for SN 2023ixf in FUV is around the optical maximum (Section 4.5). In the spectrum of ~ 7 d, we observe two strong absorption bands in the wavelength regions 1340-1400 Å and 1500-1560 Å , which can be attributed to a blend of all or potentially a subset of following species Ni II 1370-1399 Å, Si IV 1394-1403 Å lines and C IV, Si II 1527 Å, Ni II 1511 Å lines, respectively (Figure 4.3). Due to the low redshift of SN 2023ixf and with the available spectral resolution, it is difficult to discern whether the interstellar absorptions are either Galactic or due to the host galaxy. We further identify Doppler broadened emission features originating from C IV 1550 Å, He II 1640 Å, and N III] 1750 Å marked in Figure 4.3 similar to SN 1979C (Fransson 1984) and SN 2022acko (Bostroem et al. 2023b).

In the spectrum obtained at $\sim$ 12 d, we continue to observe the two absorption bands but with diminishing depth. Other than the emission features observed in the spectrum of $\sim$7 d, we find emission from C II 1335 Å, which could earlier be blended with strong absorption. Si IV and N IV] could also be observed in the wavelength region 1400-1500 Å. As the flux continues to reduce in the FUV region, we see the disappearance of He II and N III] emission features. We confirm the presence of these features by modeling the FUV spectrum at $\sim$7 d and $\sim$12 d using the synthetic spectra generation code `SYNAPPS` (Thomas et al. 2011). Many of the features in the spectra could be reproduced in the synthetic spectrum using the high-ionization (up to IV) species of He, C, N, O, S, Si, and Ni. More detailed spectral modeling with multiple elements is required to study these features extensively (Dessart & Hillier 2010; Bostroem et al. 2023b). As the SN evolves further, the high density of low-ionization lines of iron-group elements (especially Fe II and Fe III) (Mazzali 2000) amplify the line blanketing in the UV regime as is evident in the FUV spectrum of $\sim$ 23 d, which is noisy and featureless owing to the completely extinguished continuum flux. The complete extinction in FUV flux around +20 d is also evident in other Type II objects such as SN 2021yja (Vasylyev et al. 2022), SN 2022wsp (Vasylyev et al. 2023), and SN 2022acko (Bostroem et al. 2023b).

NUV spectra

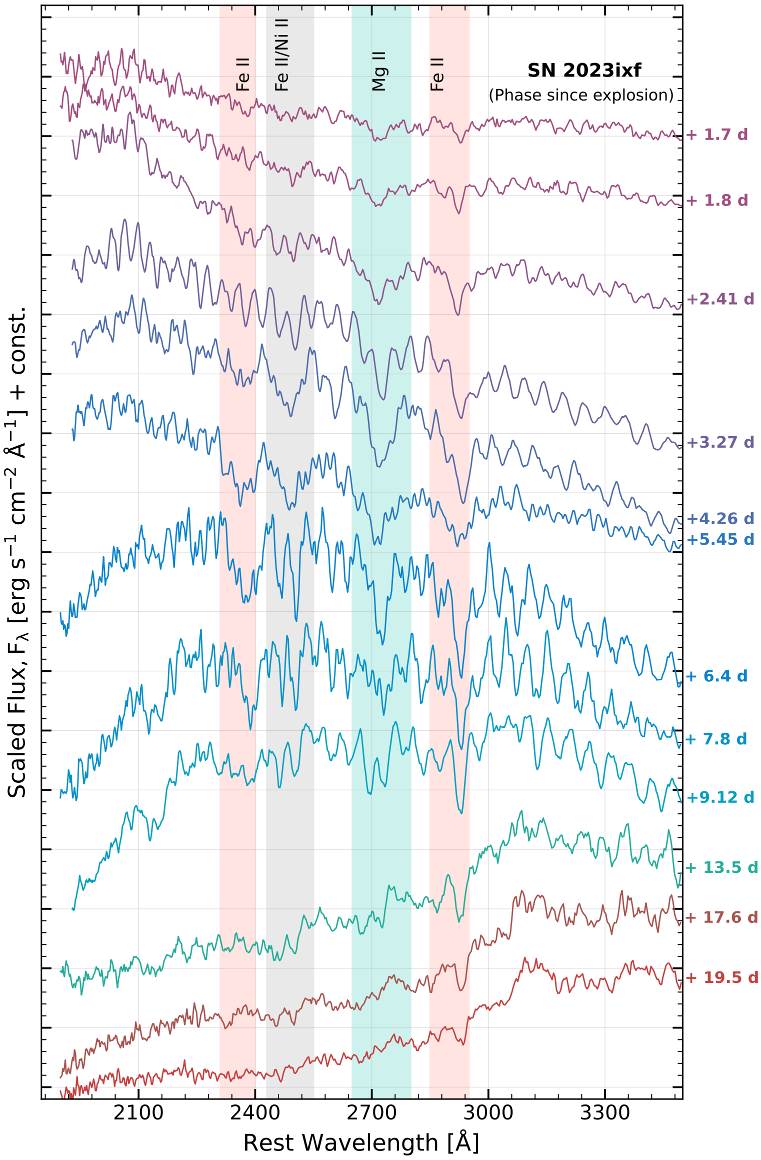

FIGURE 4.4: NUV spectral evolution for SN 2023ixf obtained using Swift/UVOT.

The first NUV spectrum obtained at + 1.7 d is the earliest-ever NUV spectrum for any CCSN observed after SN 1987A. Contrary to the FUV, many Type II SNe have been observed in NUV at multiple epochs. The NUV spectral coverage of SN 2023ixf is the most comprehensive ever up to + 20 d after the explosion, with 12 spectra.

We observe weak and blended absorption features in the first spectrum in the wavelength range 2300-3000 Å. These absorption features continue to grow in strength and width and fully dominate the SN spectra at + 6.4 d. The features arise particularly due to Fe II, Ni II and Mg II species (Brown et al. 2007; Bostroem et al. 2023b; Vasylyev et al. 2023). The prominence of these absorption features weakens along with increased line blanketing except for the feature present around 2900 Å, which is observed even in the last spectrum presented here, at +19.5 d.

The flux in NUV started rising from the first epoch and reached a maximum at $\sim$ 5 d after the explosion as the SED transitioned to NUV. In the subsequent epochs, the NUV flux starts declining and drops to the level of the first epoch at around $\sim$ 14 d. There is a significant drop in the flux between +5.5 d and +6.4 d in the region $<$ 2200 Å, observed with the change in the shape of SED as apparent in Figure 4.4. Plausibly, the rapid ejecta cooling coupled with increased line blanketing in the UV wavelengths due to metal lines cause this (Bufano et al. 2009). The effect of line blanketing in the region $<$ 3000 Å is much more prominent after + 13.5 d, and it continues to dominate, with fluxes declining in this region.

The NUV spectrum of SN 2023ixf is compared with a few Type II SNe such as ASASSN-15oz (Bostroem et al. 2019), SN 2017eaw (Szalai et al. 2019), and SN 2021yja (Vasylyev et al. 2022) at similar epochs in Figure 4.5. Two spectra of SN 2021yja (+ 9 d and + 14 d) are from HST. All other spectra used for comparisons are from Swift/UVOT. Initially, the UV spectra of Type IIP SNe were thought to be homogeneous (Gal-Yam et al. 2008), but as the number grew, the dissimilarities became more evident (Bostroem et al. 2023b; Vasylyev et al. 2023). The absorption feature around 2700 Å arising from Mg II is observed in all the SNe. The feature around 2900 Å was observed in SN 2023ixf, SN 2017eaw (IIL) (Szalai et al. 2019), SN 2022wsp (IIP) (Vasylyev et al. 2023) and SN 2022acko (IIP) (Bostroem et al. 2023b). Detailed modeling for SN 2022acko revealed it to be an absorption window from the close-by Fe II, Cr II, and Ti II absorption complexes (Bostroem et al. 2023b). This absorption feature is also observed in the spectrum of SN 2021yja.

The shape of the continuum is very similar prior to + 10 d for SN 2021yja and SN 2023ixf. As the spectra evolve, a sharp cutoff in flux below 3000 Å could be observed beyond + 10 d in all the SNe compared, indicating a significant line blanketing. Around + 14 d, the differences in spectra are very apparent, especially in ASASSN-15oz, where in the spectrum below 2700 Å, we find strong emissions/absorptions, whereas other SNe are devoid of flux comparable to regions beyond 2700 Å. Slightly higher flux beyond 3000 Å could indicate ongoing interaction (Vasylyev et al. 2022). More SNe need to be observed in the UV, specifically within the first three weeks of the explosion. This will be crucial in understanding the progenitor characteristics, its environment, and its effects on the early evolution and will aid in testing homogeneity in their spectra (Kulkarni et al. 2021; Bostroem et al. 2023b).

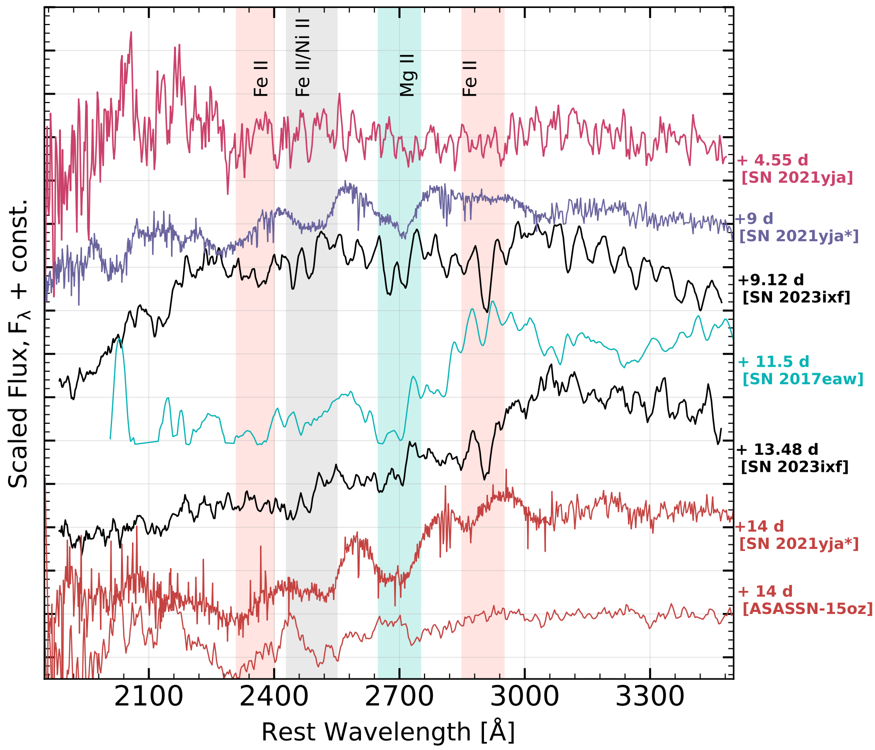

FIGURE 4.5: Spectral comparison of NUV spectra with other Type II SNe.

4.5 Early Phase Light Curve Analysis

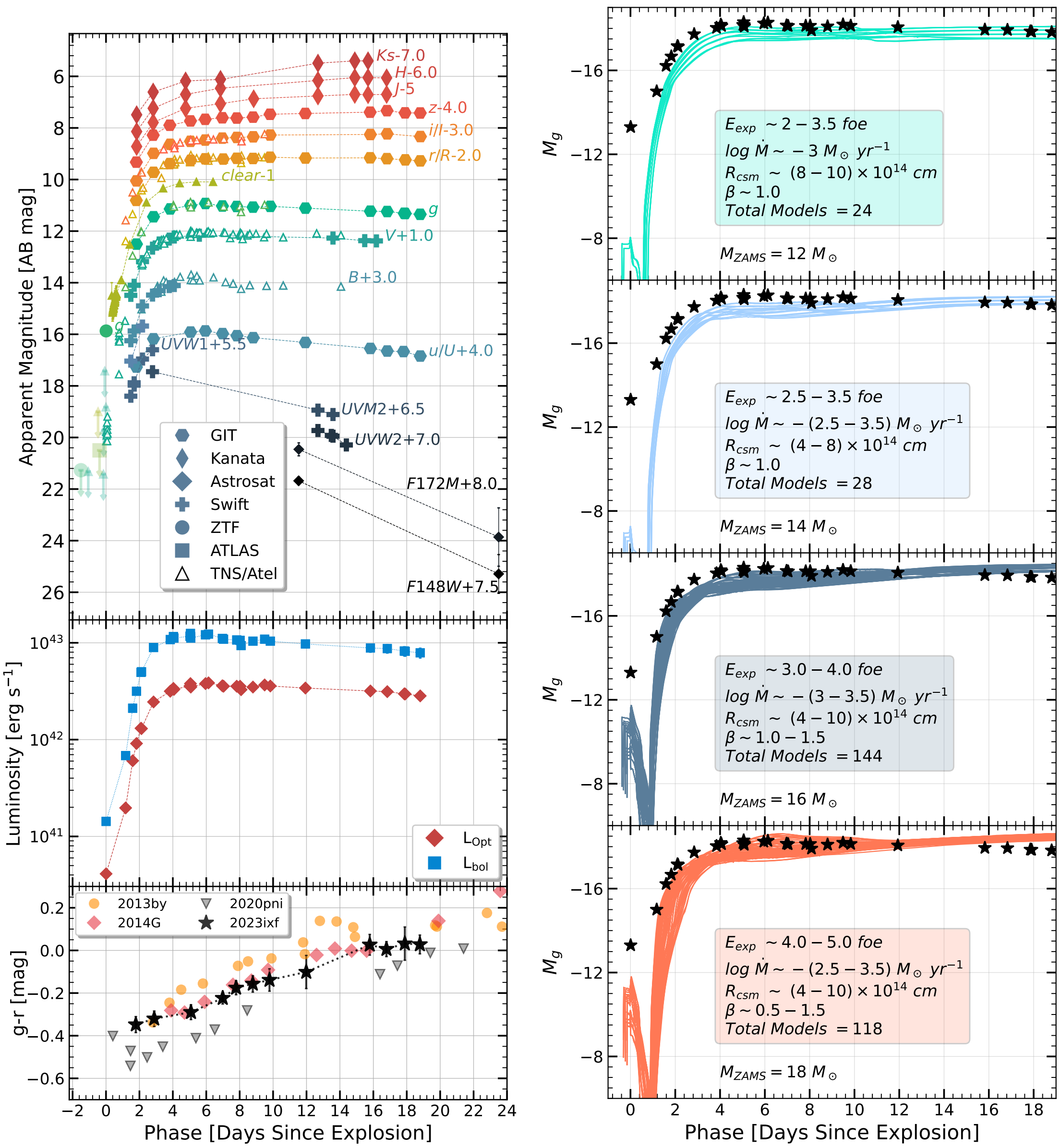

FIGURE 4.6: *Left*: (Top to Bottom) Multiband photometry is shown along with the data compiled from public sources. The second plot shows the bolometric light curve evolution. The bottom plot shows the color evolution of SN 2023ixf along with the other SNe with observed flash features. *Right:* Best model light curves that could represent the g-band light curve evolution of SN 2023ixf obtained out from a large sample of >170,000 models presented in Moriya et al. (2023) for different progenitor masses.

The multiband light curves based on observations from the various facilities are given in Figure 4.6. All pre- and post-discovery public data were converted to

AB magnitude scale and included it with our dataset using the transformations described in Blanton & Roweis (2007). The public dataset reported is very helpful in the explosion epoch estimation (Hosseinzadeh et al. 2023).

SN 2023ixf reached a peak $V-$band magnitude of -18.06 ± 0.07 mag around ~ 5 d after explosion. The peak magnitude falls at the brighter end of Type II SNe. The peak $V-$band brightness is comparable with SN 2013by (Valenti et al. 2015) and SN 2014G (Terreran et al. 2016), which were classified as Type IIL, although with many similarities to the Type IIP sub-class. SN 2014G also showed flash ionization features in early spectral evolution. While the initial decline of SN 2023ixf is inconsistent with that of Type IIL, its evolution at later phases is probed in subsequent sections. Although the early spectra indicate interaction with a nearby dense CSM, SN 2023ixf is not extremely bright in the UV bands like Type IIn SNe.

The observed rise time of $\sim 4-5$ d is shorter than other normal Type II SNe, which, on average, take ~ 10 days to reach the peak (Valenti et al. 2016). We compare $g-r$ color (Figure 4.6) with similar events that showed flash features, for example SN 2013by (Black et al. 2017; Valenti et al. 2015), SN 2014G (Terreran et al. 2016), and the bluest Type II SN 2020pni (Terreran et al. 2022). The color evolution is similar to these events for the initial $\sim$20 d but slightly redder than SN 2020pni. The NIR light curves are also presented in Yamanaka et al. (2023) up to a week post-explosion. We show the evolution beyond that and observe that the flux increases in the NIR, possibly due to pre-existing dust around the ejecta. The presence of pre-SN dust is also described in Neustadt et al. (2023).

The early prolonged flash features indicated the presence of a dense CSM near the progenitor. Moriya et al. (2023) provided a comprehensive set of grids for model light curves that could shed light on the structure of CSM and its effects on the early light curve of interacting Type II SNe. In their work, a confined CSM is attached over radius, R_0, for five progenitors with mass ranging from 10 to 18 $M_\odot$. The CSM density structure follows from Moriya et al. (2018), whereas the wind velocity, v_{wind} at a distance r was taken to be in the form as given below:

$$v_{wind}(r) = v_0 + (v_\infty - v_0)\left(1 - \frac{R_0}{r}\right)^\beta, \tag{4.1}$$

where v_0 and v_∞ are the initial wind velocity at the surface of the progenitor and terminal velocity, respectively, and β is a wind structure parameter that determines the efficiency of wind acceleration.

These model light curves can be used to constrain the very early light curve behavior of Type II SNe. Our work utilizes the well-sampled g-band light curve of SN 2023ixf to compare with the model grid of interacting Type II SNe generated by Moriya et al. (2023). We used the models with ^{56}Ni mass in the typical range of 0.01 to 0.04 $M_\odot$ (Anderson et al. 2014a). Furthermore, we found that the initial light curves are insensitive to the ^{56}Ni mass. We iterated over each parameter (E_{exp}, β, R_{CSM}, and $\dot{M}$) in succession, keeping others fixed with their full range for a single run. This procedure is repeated for 12, 14, 16, and 18 $M_\odot$ progenitor models. We categorically reject models which show significant deviations from the observed light curves based on their peak luminosities and rise times. Subsequently, we do this for other parameters constraining the values for previous parameters. Most closely describing models for each progenitor are presented in Figure 4.6 (right panels). We note that the slow early rise till day 2 is not captured by any of the models, and the later evolution is such that either the rise or plateau could be matched but not the entire light curve. Since we are concerned about the initial rise, we do not probe it further; detailed hydrodynamical modeling specific to this particular event will be required to understand the entire light curve evolution. Further, the degeneracy in the progenitor masses could not be lifted by these models, but these models give a very tight constraint on the radius of the outer CSM utilizing the rise times of the model light curves. The dense CSM is confined to $4.0 - 10.0 \times 10^{14}$ cm. Further, β varies from 0.5 to 1.5 depending on the progenitor mass, which is close to the typical values for RSGs ($\beta > 1$). The $\beta < 1$ value obtained for $M_{\rm ZAMS}$ would accelerate winds slightly faster and cause less dense CSM in the vicinity, which is not the case for SN 2023ixf. The mass loss rate is also slightly on the higher end ($10^{-3.0\pm0.5}$ $M_\odot$ yr^{-1}). The average density of the CSM comes out to be $\sim 10^{-14}$ g cm^{-3} which is in line with the values obtained in Bostroem et al. (2023a) but below the values inferred in Jacobson-Galan et al. (2023) obtained from the detailed spectral modeling. The mass-loss rates align with the density limits of CSM derived from the non-detection of radio emission (230 GHz) at early times (Berger et al. 2023). For a typical RSG (~ 500 $M_\odot$), the above would translate to a mass loss $\sim 14 - 18$ years before the explosion. But as seen in Smith et al. (2023), wind speeds measured using high-resolution early spectra are one order higher than what is assumed in the model parameters, which would give an eruptive mass loss timeline to be around 2 years before the explosion. However, wind acceleration cannot be ruled out. Another parameter that is tightly constrained by the models is the explosion energy. Only the models with explosion energies more than 2.0 foe could match the observed g-band flux. The explosion energy increases as the progenitor mass is increased. The explosion energy obtained is higher than for the usual Type II SNe.

In a recent work, Khatami & Kasen (2023) presented various light curves of transients arising from interacting SN. These include SN ejecta interacting with no CSM to a very heavy CSM. Considering the latent space of luminosity and rise-time presented in that work, we find that the light curve evolution of SN 2023ixf (for the period presented in this work) appears to be similar to the model light curves for shock-breakout in a light-CSM scenario. Comparing the rise-times and peak luminosity of SN 2023ixf with the shock-breakout happening inside the CSM, we find that it falls within $0.01 < M_{CSM}$ [$M_\odot$] < 0.1. Using the parameters obtained from light curve analysis, we get a CSM mass ranging from 0.001-0.03 $M_\odot$ (assuming $v_{\rm wind} = 10$ km s^{-1}), where the upper limit is well within the range obtained

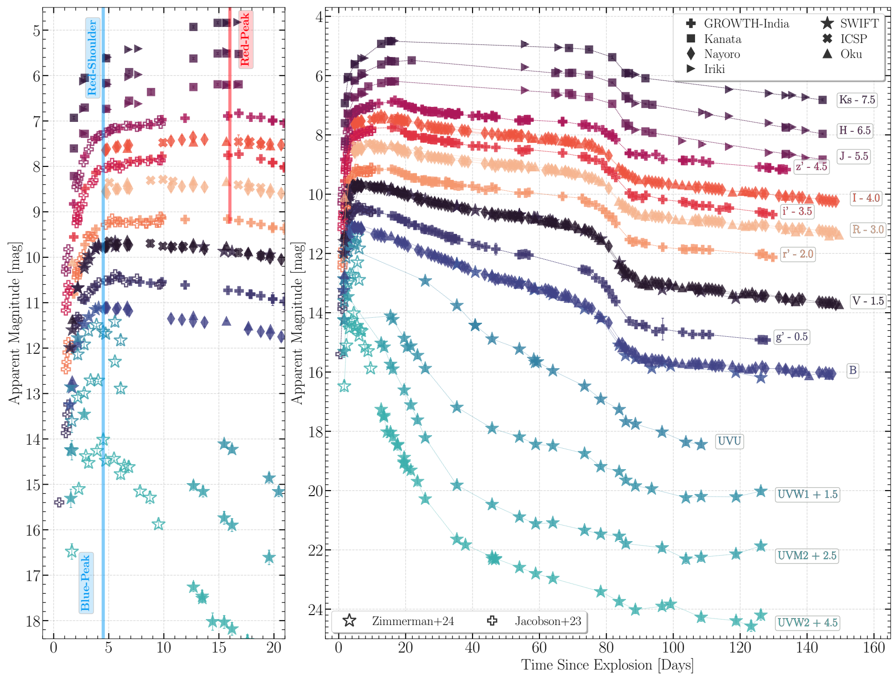

FIGURE 4.7: Multi-wavelength photometry of SN 2023ixf spanning ultraviolet, optical, and near-infrared wavelengths. Template subtraction was performed only in the UV bands ($UVW2$, $UVM2$, and $UVW1$) due to non-negligible contamination. The left panel provides a close-up of the initial rise across all bands, annotated as *blue peak & red shoulder*, and the subsequent *red peak*.

from Khatami & Kasen (2023). It indicates the mass loss rate could have been even higher than $10^{-2.5}$ M$_\odot$ yr^{-1}, as also being reported in Jacobson-Galan et al. (2023); Hiramatsu et al. (2023).

4.6 Photometric Evolution Till Early Nebular Phase

Panchromatic light curves covering ultraviolet, optical, and near-infrared wavelengths from various facilities are shown in Figure 4.7, displaying the well-sampled SN evolution spanning 1.4 d – 180 d after the explosion. All the magnitudes were calibrated to the AB system using the transformations described in Blanton & Roweis (2007).

Rise times, decline rates, and plateau length

The light curve peaks were measured by fitting the light curves with a smooth spline, calculating the gradient (dm/dt) of the fit, and identifying the zero-crossing points to determine the peaks. SN 2023ixf shows a sharp rise to the peak in the ultraviolet bands - $UVW2$ and $UVW1$ (i.e. *blue peak*) with a rise time of $\sim$4.5 d. The rise time is $\sim$6 d in V filter, faster than the prototypical Type II SN 1999em (with minimal signatures of interaction), which displayed a rise time of $\sim$10 d in V-band (Leonard et al. 2002b). The steepening of the light curve (and faster rise) is more pronounced in the bluer bands ($<0.5\,\mu$m) due to heating as discussed by Morozova et al. (2017); Moriya et al. (2018). The light curves in the redder bands ($r'i'z'$) seem to show a steep rise to a distinct shoulder, i.e., *red shoulder* post $\sim$5 d and a gradual ascent to the maximum, i.e., *red peak* at $\sim$16 d. The *red shoulder* is seen as an abrupt change of slope in the gradient of the early light curve. The presence of *red shoulder* is driven by the flux excess due to SN 2023ixf's ejecta interacting with some confined material since it coincides with the timing of the peak in the UV wavelengths (i.e., *blue peak*). A similar shoulder and peak are visible in the simulated SNe II red-band light curves (Dessart et al. 2017) with strong wind models ($> 10^{-3}$ M$_\odot$ yr^{-1}) . Additionally, rise to the *red peak* seems to stem from the adiabatic cooling of shock-heated SN ejecta, which results from the migration of the spectral energy distribution (SED) into the redder bands, despite a declining net bolometric luminosity (Singh et al. 2019b). The rise time for the *red peak* is higher than that of SNe IIP (7.0 ± 0.3 d) and in the ballpark of SNe IIL (13.3 ± 0.6 d) (Gall et al. 2015). This is suggestive of the higher energy/mass ratio in SNe IIL as seen in SN 2023ixf (see Section 4.8).

Post-maximum, the multiband light curves of SN 2023ixf settle onto a plateau of roughly $\sim$75 d in V and other redder bands before transitioning to the radioactively-powered tail phase at $\sim$90 d. The plateau length is at the shorter end of the typical plateau length of 100 d for SNe II, hence putting SN 2023ixf amongst some of the rarely observed short plateau SNe (Hiramatsu et al. 2021a; Teja et al. 2023b). We estimated the plateau decline rates of SN 2023ixf following the prescription of Anderson et al. (2014a). The V-band light curve of SN 2023ixf showed an early plateau decline rate (s1) of $2.70^{+0.48}_{-0.49}$ mag $(100\,\mathrm{d})^{-1}$ and a late-plateau decline rate (s2) of $1.85^{+0.13}_{-0.14}$ mag $(100\,\mathrm{d})^{-1}$. The late-plateau decline rate of SN 2023ixf is much higher than the mean decline rate of 1.3 mag $(100\,\mathrm{d})^{-1}$ inferred for SNe II (Anderson et al. 2014a). The tail phase decline rate (s3) of SN 2023ixf is $1.33^{+0.09}_{-0.09}$ mag $(100\,\mathrm{d})^{-1}$ which is faster than the characteristic decline rate of ^{56}Co to ^{56}Fe (i.e., 0.98 mag $(100\,\mathrm{d})^{-1}$) indicating an incomplete trapping of e^{+} and γ-rays.

Light curve comparisons

The comparison of V-band absolute magnitude light curve of SN 2023ixf is shown in the top panel (A) of Figure 4.8. Owing to the short plateau length and fast declining nature of SN 2023ixf, the comparison sample consists of normal Type IIP SNe: 2006bp (Quimby et al. 2007), 2007od (Andrews et al. 2010), 2013fs (Bullivant et al. 2018), 2016gfy (Singh et al. 2019a), 2017eaw (Szalai et al. 2019) and 2020tlf (Jacobson-Galán et al. 2022); short-plateau Type IIP SNe: 2018gj, 2020jfo (Chapter 3), and Type IIL SNe: 2013by (Valenti et al. 2015), 2014G (Terreran et al. 2016), 2017ahn (Tartaglia et al. 2021) and 2020pni (Terreran et al. 2022). The peak V-band luminosity of SN 2023ixf is –18.2 mag, significantly brighter than the average peak luminosity of SNe II (i.e., –16.74 mag) inferred by Anderson et al. (2014a), which is dominated by the population of slow-declining SNe II. The peak luminosity of SN 2023ixf is similar to the SNe IIL, namely SN 2013by, SN 2014G, and SN 2017ahn, but slightly fainter than that of SN 2020pni; however, it is brighter than the majority of normal and short-plateau SNe IIP. The plateau-decline rate of SN 2023ixf is similar to that of SN 2014G (~ 1.7 mag $(100\,\mathrm{d})^{-1}$) and SN 2013by (~ 1.5 mag $(100\,\mathrm{d})^{-1}$). The ~ 75 d plateau length of SN 2023ixf is similar to that of SNe 2014G, 2013by and 2013fs. We infer a $\sim 1.8 \pm 0.1$ mag drop

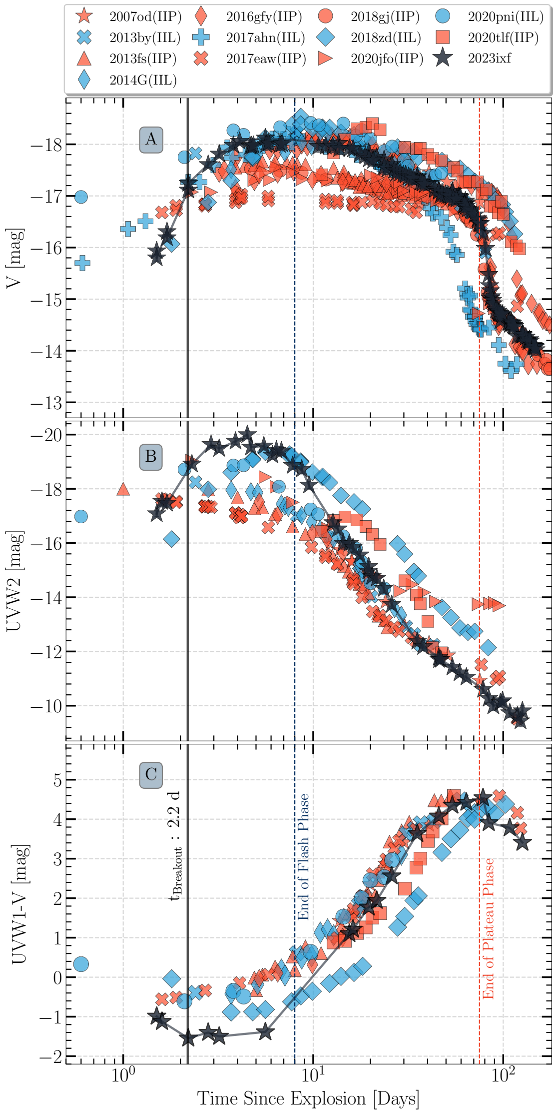

FIGURE 4.8: Comparison of absolute magnitude light curves of SN 2023ixf in $UVW2$ and V bands along with the $UVW1 - V$ color evolution compared to other SNe II showing CSM interaction signatures.

from the plateau phase to the tail phase for SN 2023ixf, similar to that of SNe 2014G ($\sim$2.0 mag) and 2013by ($\sim$1.8 mag). Overall, SN 2023ixf shows remarkable photometric resemblance in peak-luminosity, plateau decline rates, plateau length, and plateau drop to SN 2013by and SN 2014G.

We further compare SN 2023ixf to SNe II with CSM interaction, followed up extensively in UV by *Swift* over the last two decades in panel (B) of Figure 4.8.

The data were downloaded from SOUSA[§], and Vega-mag was transformed to AB-mag for consistency. SN 2023ixf shows a steep rise in the UV fluxes in $UVW2$ and $UVW1$ bands, which has been seen only in SN 2013fs, SN 2020pni and SN 2020tlf. In the exhaustive sample of SNe II observed by *Swift*, even though SN 2023ixf is not the earliest followed-up Type IIP/L SN, the $UVW2$ and $UVW1$ bands exhibit a rapid surge in the flux, brightening by over $\sim$3 mags in 3 days, before reaching a peak magnitude of $\sim$ –20 mag at $\sim$4.5 d. This prolonged brightening observed in the early UV light curve indicates a shock breakout within a compact and dense CSM, leading to a more luminous and elongated shock breakout event (Ofek et al. 2010). Such a distinct signature in the early UV light curves has been observed in only a limited number of SNe II. The detection of a UV burst extending over 1-day in PS1-13arp by Gezari et al. (2015) was the first observation hinting at the possibility of the shock breaking out into a confined CSM. In our comparison sample, SN 2020pni (Terreran et al. 2022) and SN 2020tlf (Jacobson-Galán et al. 2022) showed a similar intensification of the early phase UV light curve. $UVW1 - V$ color evolution for the sample is also shown Figure 4.8 (Panel C).

The *Swift* UV light curves of SNe II typically decline rapidly due to the rapid cooling of the SN ejecta and the prevalence of metal absorption features, which eats away at the UV flux as the ejecta cools. We discern this in the FUV spectrum of SN 2023ixf at $\sim$23 d, which shows an entirely featureless spectrum owing to the line-blanketing from the iron-group elements (Bufano et al. 2009). However, even with severe line blanketing during the early plateau phase, we still infer a decent contribution ($\sim$10%, see Panel B in Figure 4.9) of UV flux to the overall bolometric light curve (i.e., a UV excess) during the late-plateau phase ($>$50 d). This likely suggests continued interaction with CSM despite the absence of discernible signatures in the spectral sequence outlined in Section 4.7. This aligns with the inference from the theoretical models of interacting SNe II by Dessart

[§]Swift Optical/Ultraviolet Supernova Archive (Brown et al. 2014)

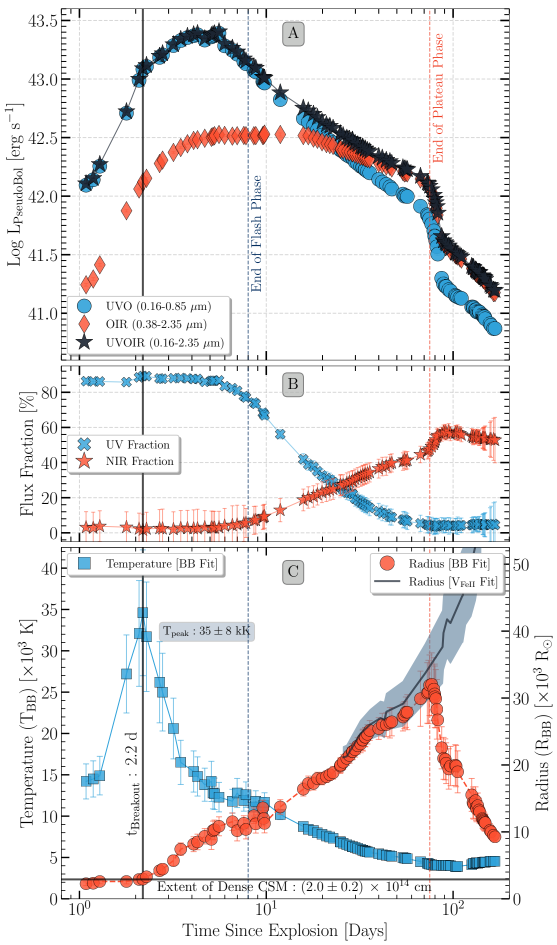

FIGURE 4.9: `Panel A`: Pseudo-bolometric light curves of SN 2023ixf computed in multiple wavelength bins. `Panel B`: Temporal evolution of UV and NIR flux of SN 2023ixf. `Panel C`: Temperature and radius evolution of SN 2023ixf estimated from blackbody fits to the FUV-Optical-NIR data ($0.16-2.35\,\mu$m). The radius of the line-forming region, i.e., the photospheric radius estimated from Fe II, is overplotted. The steep rise in temperature and the flat evolution in radius exemplify the shock breakout inside a dense CSM (shaded in grey).

et al. (2022) that display early interaction frequently display a surplus of UV radiation during late phases.

Bolometric Light Curve and ^{56}Ni Mass

We computed the pseudo-bolometric light curves of SN 2023ixf using data from GIT, Kanata, Iriki, Nayoro, and *Swift*/UVOT using `SuperBol` (Nicholl 2018). The bolometric luminosity, color temperature (T_{col}), and radius (R_{BB}) evolution of the layer of thermalization were estimated using the blackbody fits to the SED of the SN at each epoch. The missing data in certain filters over the intermediate epochs was interpolated using a low-order spline. We computed the bolometric light curve in 3 wavelength bins, i.e., UVOIR ($0.16-2.35\,\mu$m), UVO ($0.16-0.85\,\mu$m) and OIR ($0.38-2.35\,\mu$m) (Figure 4.9; Panel A).

Henceforth, we refer to the UVOIR pseudo-bolometric light curve as the bolometric light curve in our discussion. In an RSG, the shock breakout from the surface of the progenitor happens within an hour of the core collapse, followed by a rapid cooling due to the rapid expansion driven by the shock (Falk & Arnett 1977). This would result in a rapid expansion of the photospheric radius and a decrease in the temperature of the supernova ejecta within a few hours following the explosion. However, examining the color temperature and radius evolution shown in Panel C of Figure 4.9, shows a steep increase in the temperature from around 14,000 K to 35,000 K over a duration of 2.2 ± 0.1 d and a relatively-flat radius evolution at $(2.0 \pm 0.2) \times 10^{14}$ cm (13 ± 1 AU). The extended heating at a near-flat radius, in addition to the prolonged brightening in the UV flux, as discussed in Section 4.6, further strengthens that in SN 2023ixf, the shock broke out inside a compact and dense CSM surrounding the progenitor.

From the photometric observations at 1.1 d, the bolometric luminosity, $L_{BOL} = (1.28 \pm 0.11) \times 10^{42}$ erg s^{-1}, and effective temperature of $(14 \pm 2) \times 10^{3}$ K rises ten folds and two folds, respectively, in a span of just ~ 1 d. However, due to the ensued heating, the bolometric light curve of SN 2023ixf flux peaked later on

$\sim 4.5\,\mathrm{d}$ with a luminosity of $2.5 \pm 0.3 \times 10^{43}$ erg s^{-1}. The temporal evolution of UV and NIR fraction of the pseudo-bolometric luminosity is shown in Panel B of Figure 4.9. The contribution of the UV flux ($0.16 - 0.38\,\mu$m) to the bolometric flux stays at roughly about 85% even beyond the epoch of shock breakout until the bolometric maximum (and the UV peak) is reached indicating an ongoing source of heating. The UV flux falls gradually until the end of the plateau phase. If we ignore the early UV data for SN 2023ixf, the OIR bolometric light curve (see Panel A in Figure 4.9) underestimates the bolometric luminosity by an order of magnitude, emphasizing the importance of UV observations of infant CCSNe and its importance to detailed hydrodynamical modeling.

^{56}Ni Mass

We computed the ^{56}Ni-mass using Equation 2.1. The mean tail luminosity of SN 2023ixf around ~ 145 d yields a ^{56}Ni mass of 0.054 ± 0.006 M$_\odot$. Upon comparison with SN 1987A at a similar phase, a ^{56}Ni-mass of 0.054 ± 0.005 M$_\odot$ is estimated for SN 2023ixf. The above techniques assumed complete trapping of γ-rays by the SN ejecta. However, that is not always true, especially for short-plateau SNe due to a thinner hydrogen envelope and may lead to underestimation of the yield of the ^{56}Ni. Hence, we modeled the late-phase UVOIR bolometric light curve of SN 2023ixf until 150 d using the analytical formulation from Valenti et al. (2008). We derived a total ^{56}Ni-mass of 0.059 ± 0.001 M$_\odot$ and a characteristic γ-ray trapping timescale of $\sim 220 \pm 3\,\mathrm{d}$, indicating a short-lived trapping and a shallower envelope. We derive this as the upper limit of ^{56}Ni yield since there might be an additional contribution to the tail phase from CSM interaction as mentioned in Section 4.6.

4.7 Spectroscopic Evolution Post Flash Phase

Photospheric Phase: 8 - 80 d

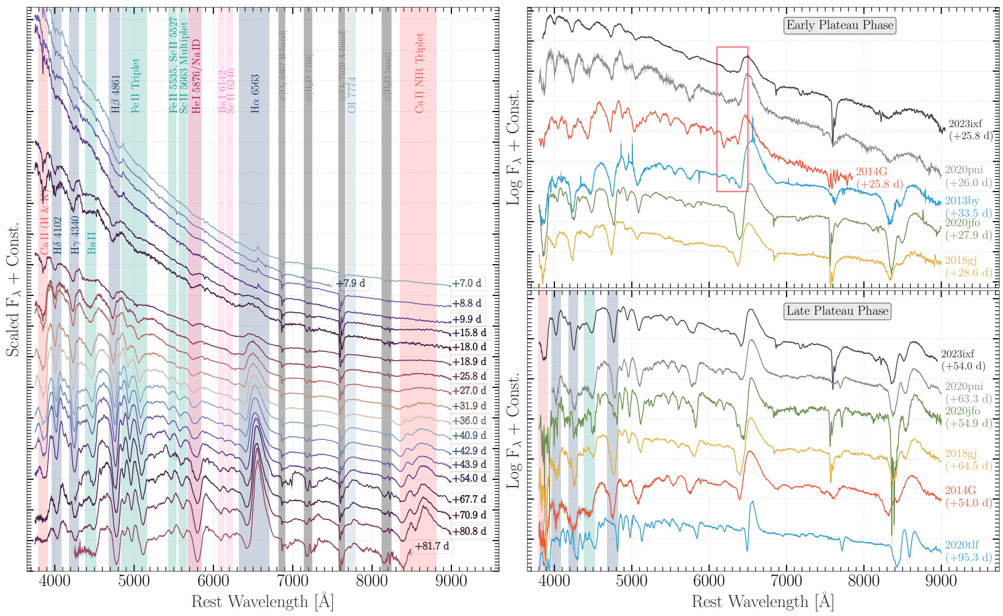

FIGURE 4.10: **Left Panel:** Photospheric phase spectral evolution of SN 2023ixf. Prominent spectral features are labeled and depicted using colored shaded areas. **Right Panels:** Comparison of the early and late plateau phase spectrum of SN 2023ixf with other SNe II from the literature with signatures of CSM interaction in the top and bottom panels, respectively.

The complete photospheric phase spectroscopic evolution of SN 2023ixf from 7 d to 82 d is presented in Figure 4.10 (Left Panel). During the transition from the flash phase to the photospheric phase, we see the reminiscence of interaction with the dense CSM in the form of intermediate-width Lorentzian emission along with the emergence of broad P-Cygni features of Hα and Hβ (Teja et al. 2023b). This spans until $\sim$10 d, beyond which the Lorentzian emission profile vanishes.

Beginning $\sim$16 d, we observe a more intricate and complex multi-peaked profile of Hα with a persistent high-velocity absorption feature, which we extensively discuss in Section 4.7. In addition to the distinguishable Balmer lines in the early spectra, several distinct features start to appear $\sim$16 d onwards, particularly Ca II H&K

and He I 5876 Å. As the photosphere recedes further into the ejecta, we detect the appearance of various lines of Fe II, Sc II and Ba II, and the Ca II Triplet beginning ~ 25 d. These metal features are visibly developed around ~ 36 d. The broad Na ID starts to emerge at the location of He I λ 5876, evident from the slightly broadened absorption trough at around ~ 40 d (continuing up to ~ 54 d). This is further indicative of the cooling of the ejecta and is suggestive of an ejecta that is cooling a lot slower than typical SNe II as the appearance of Na ID, is usually observed around ~ 30 d (Gutiérrez et al. 2017a). Towards the end of the plateau drop, i.e. around 70 d, we also begin to observe O I λ 7774.

In the right panel of Figure 4.10, we compare the spectrum of SN 2023ixf with the spectra of other SNe II encompassing a sample of SNe IIL and short plateau SNe i.e. SN 2013by (Valenti et al. 2015); SN 2014G (Terreran et al. 2016); SN 2018gj (Teja et al. 2023a); SN 2020jfo (Teja et al. 2023b); SN 2020pni (Terreran et al. 2022); SN 2020tlf (Jacobson-Galán et al. 2022). Photospheric features develop pretty late in SN 2023ixf compared to other Type IIL and short-plateau SNe II, significantly later than normal SNe II. In the early plateau phase (~ 25 d), the spectra blueward of Hα is generally dominated by metallic features as in the case for SN 2014G, SN 2020jfo and SN 2020pni; however, the features are relatively underdeveloped in SN 2023ixf and SN 2018gj. The line strengths appear much weaker in SN 2023ixf than in spectral lines of other SNe. This also plausibly hints at the ejecta being still hot and/or metal-poor compared to normal SNe II. In addition, the Hα P-Cygni absorption during the early photospheric phase in SN 2023ixf is a lot weaker than short-plateau SNe 2018gj and 2020jfo; however, it is similar to SNe 2014G and 2020pni. The spectral features are likely less prominent due to the luminosity from interaction enhancing the ejecta's temperature (and ionization), leading to an ionization wave penetrating the ejecta inwards from the cold, dense shell (CDS, Chevalier & Fransson 1994). CDS arises from the higher density of the inner CSM ($> 10^{-14}$ g cm^{-3}, see Section 4.8) resulting from the cooling of shocked areas during the early phases.

This is also in concordance with Type IIL SNe, which tend to show weaker P-Cygni absorption troughs since these SNe likely have more significant interaction with CSM than typical Type IIP SNe (Gutiérrez et al. 2014). Upon examination of spectra comparison during the late-plateau phase, we observe higher line blending in SN 2023ixf due to its higher photospheric velocity (see Section 4.7) during the late-plateau phase in comparison to all other SNe II in our comparison except that of SN 2014G.

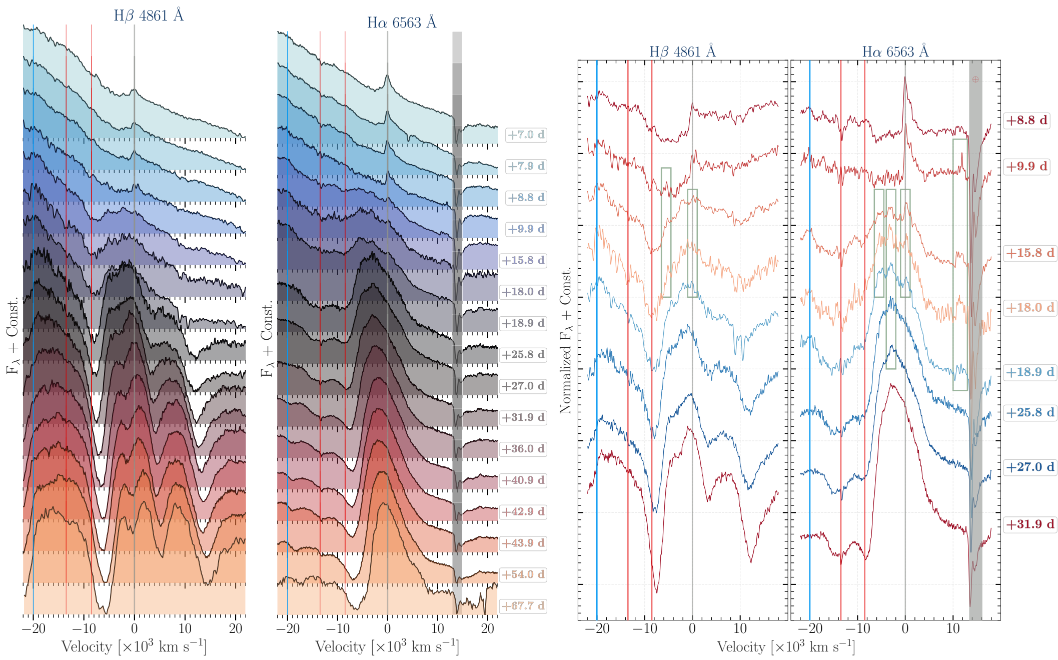

FIGURE 4.11: Temporal evolution of Hβ and Hα profile of SN 2023ixf from the decline of the flash-ionization phase until the late plateau phase. The rest-frame zero-velocity is marked with a grey line. The red lines mark the absorption-minima of the P-Cygni absorption (8,500 km s^{-1}) and the high-velocity absorption (13,500 km s^{-1}) when they first appear simultaneously in the spectra on $\sim$16 d. The blue edge of the high-velocity feature (20,000 km s^{-1}) is shown with a blue line. The clumpy features that appear over several epochs are indicated by green boxes in right panels.

Evolution of Hα : High-Velocity Absorption and Clumpy CSM

We show the temporal evolution of the Hβ and Hα covering the photospheric phase of SN 2023ixf in Figure 4.11. We observe the emergence of the broad P-Cygni feature of Hα by 7 d in our spectral sequence with a blue edge of $\sim$8,500 km s^{-1}. A similar broad P Cygni absorption manifests around Hβ, confirming the emergence of the SN ejecta. A few epochs later, the Hα absorption further broadens, possibly due to the emergence of a high velocity (HV) component of Hα. The broad Hα profile is seen to be clearly developing in two distinct components in the $\sim$27 d spectrum. The appearance of HV absorption in Hα is in sync with the *red peak* in light curves of SN 2023ixf. The absorption minima of the HV absorption lies roughly at 13,500 km s^{-1} whereas the blue edge of the absorption profile extends up to 20,000 kms^{-1} at $\sim$16 d. We confirm its association with hydrogen since we see an analogous profile in Hβ, although its effect is not as pronounced due to the low optical depth of these lines. This HV feature was also reported by Teja et al. (2023b), who dismissed its association with Si II as it would lead to line velocities lower than the photospheric velocity.

In the case of an expanding SN ejecta, we tend to observe an absorption component forming from the inner layers of the ejecta moving towards our line-of-sight, leading to a P-Cygni profile of Hα during the plateau phase. The outer recombined ejecta does not contribute towards the absorption profile (Chugai et al. 2007). However, the collision between the SN ejecta and CSM creates a dual-shock structure, where forward shock moves through CSM while reverse shock travels within the SN ejecta (Chevalier 1982). This results in the ionization of the outer layers of the unshocked ejecta by Lyman-α photons, causing the emergence of HV absorption features blueward of P-Cygni absorption (Chugai et al. 2007). Such an HV feature of hydrogen arising due to interaction is generally narrow and doesn't show a considerable evolution in velocity, and starts appearing about a month after the explosion (Gutiérrez et al. 2017a). In contrast, the HV absorption feature seen in SN 2023ixf is broad (FWHM $\gtrsim$ 7,000 km s^{-1}), starts appearing ∼16 d and shows considerable evolution in velocity from ∼ 13,500 km s^{-1} at 16 d to ∼ 9,500 km s^{-1} at 70 d. Hence, it is unlikely that the feature arose due to the interaction with the dense CSM.

The P-Cygni profile of Hα from ∼ 10 – 32 d also shows many intricate structures indicating the presence of clumpy matter in the interaction region. We spot many distinct clumpy features at similar velocities in Hα and Hβ, and they disappear as the SN evolves into the mid-plateau phase (> 40 d), indicating that the SN ejecta overcomes most of the clumps beyond the mid-plateau phase.

The emission peak of Hα has a blueshifted offset by as much as ∼ 3,000 kms^{-1} at ∼ 32 d but evolves towards zero rest velocity by the end of the plateau. The blueshifted offset of the emission peak of Hα (at 30 d) typically correlates with the decline rate during the plateau phase and the peak luminosity of SNe II (Anderson et al. 2014b). The steep decline rate of SN 2023ixf *(*$s_2 \sim 1.9$ mag (100 d)$^{-1}$*)* is in agreement with its large offset of ∼ 3,000 km s^{-1} indicating that the ejecta mass could be smaller in SN 2023ixf leading to its shorter plateau. Although this effect is commonly seen in SNe II, this effect is more pronounced in only a handful of events, e.g., SN 2014G (Terreran et al. 2016) and SN 2018gj (Teja et al. 2023a), where the emission peak stays blue-shifted till the nebular phase.

Line velocity Evolution

We compare Fe II λ 5169 velocity evolution for SN 2023ixf with other SNe II in Figure 4.12. We estimated the line velocity evolution from the blue-shifted absorption trough of their line profiles in the redshift-corrected spectral sequence of SN 2023ixf. We adopt the Fe II λ 5169 velocities as the photospheric velocity

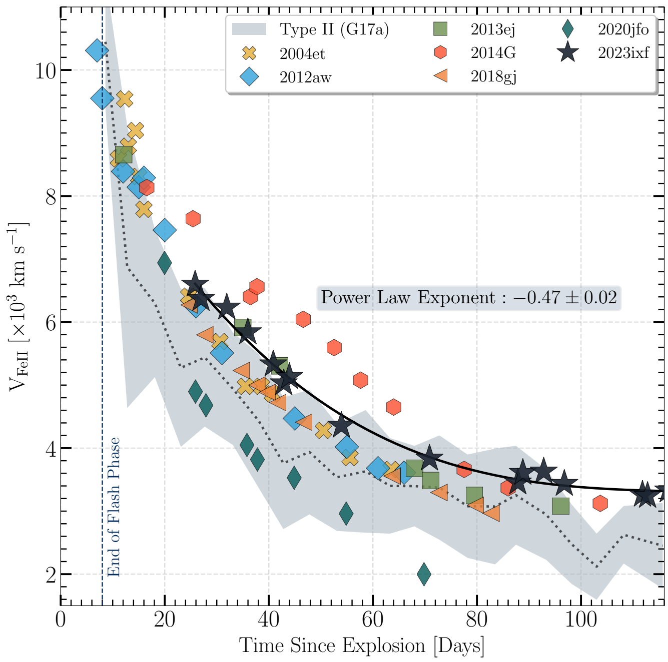

FIGURE 4.12: Comparison of Fe II λ 5169 line velocity evolution of SN 2023ixf with SNe II from the literature and the mean photospheric velocity evolution for SNe II computed by Gutiérrez et al. (2017a).

since it forms closest to the photosphere (Dessart & Hillier 2005a) and is the least blended among the iron lines seen in the spectral sequence. The photospheric radius estimated from Fe II absorption trough closely mirrors the blackbody radius as shown in Figure 4.9. During the mid-plateau phase ($\sim$53 d), the Fe II λ 5169 velocity inferred for SN 2023ixf is 4350 km s^{-1}. This positions it at the higher end of the 1-σ range when compared with the mean velocity of Fe II λ 5169 for an extensive collection of SNe II by Gutiérrez et al. (2017a, 3537 ± 851 km/s). This is evident in the spectral comparison during the late-plateau phase, since we observe higher line blending in SN 2023ixf due to its higher photospheric velocity in comparison to all other SNe II in our comparison except that of SN 2014G. The trend continues onto the early nebular phase ($\sim$116 d), where SN 2023ixf displays a Fe II λ 5169 velocity of 3330 km s^{-1} compared to the mean value of 2451 ± 679 km s^{-1} from Gutiérrez et al. (2017a). The higher photospheric velocity is in agreement with the luminosity-velocity correlation of homologously expanding recombination front of hydrogen (Kasen & Woosley 2009) since SN 2023ixf is brighter during the mid-plateau phase compared to a normal Type II SN (Anderson et al. 2014a). Additionally, the CSM interaction in SN 2023ixf could also drive the elements at outer/faster regions of the ejecta to be reionized and recombined, leading to a higher estimate of photospheric velocity (Andrews et al. 2019).

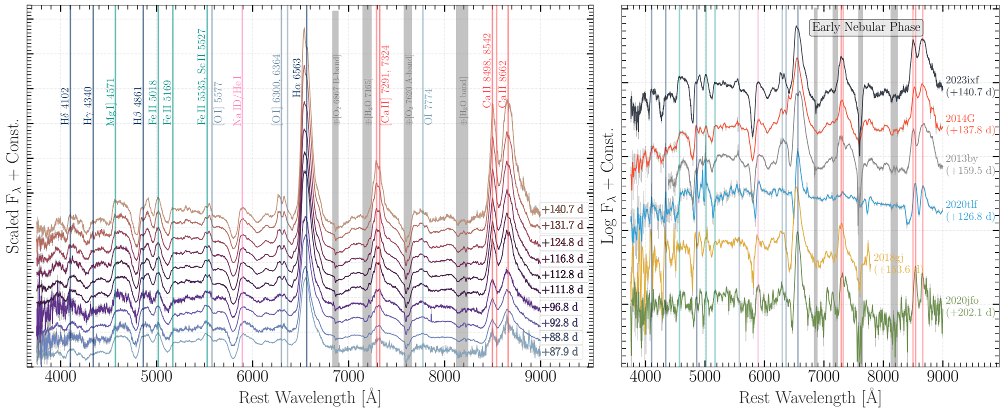

FIGURE 4.13: `Left Panel`: Nebular spectroscopic evolution of SN 2023ixf from HCT. The marked vertical lines indicate the rest wavelength of the labeled spectral features. `Right Panel`: Comparison of the early nebular phase spectrum of SN 2023ixf with other SNe II from the literature with signatures of CSM interaction.

Early Nebular Phase (90–150 d)

The nebular-phase spectral sequence of SN 2023ixf is shown in the left panel of Figure 4.13. The nebular spectra of SN 2023ixf display prominent emission features of H γ, Mg I] λ 4571, H β, O I λ 5577, Na I D / He I, [O I] $\lambda\lambda 6300, 6364$, H α, [Ca II] $\lambda\lambda 7291, 7324$ and the Ca II NIR triplet with a flat continuum, typical of SNe II. We observe an asymmetry in the line profile of certain emission features during the nebular phase. We observe a dual-peaked axisymmetric *(the separation between the two components is less than that of the two components of the O I doublet)* profile of the [O I] doublet in SN 2023ixf during the early nebular phase in Figure 4.14. We also observe an apparent redshifted excess in H α and [Ca II] $\lambda\lambda 7291, 7324$ at around +5,000 km s^{-1} possibly indicating asymmetries in the

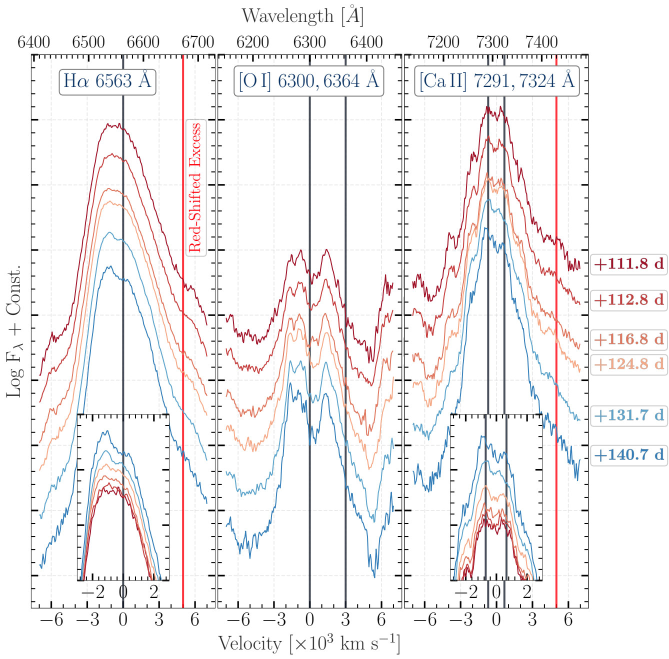

FIGURE 4.14: Evolution of Hα 6563 Å, [O I] 6300, 6364 Å, and [Ca II] 7291, 7324 Å during the early nebular phase of SN 2023ixf. The redshifted excess in Hα and [Ca II] $\lambda\lambda$7291, 7324 is labelled at +5,000 km s^{-1}. The insets show a zoomed view of the peak of the Hα and [Ca II], showing redward attenuation as the SN progressed onto the nebular phase.

ejecta. However, the Hα and [Ca II] showed a single peak symmetric profile with visible signs of redward attenuation as the SN progressed into the nebular phase.

The emergence of an asymmetric emission profile of Hα and [Ca II] arising due to the attenuation of the red-ward emission from the receding portions of the ejecta is first noticed in our spectral sequence beginning $\sim$125 d in Figure 4.14. This indicates the onset of dust formation and was first noticed in SN 1987A (Lucy et al. 1989). We also observe an increase in red-blue asymmetry as the SN evolves into the nebular phase, indicating an increased dust formation with time (Bevan et al. 2019). The early signatures of dust suggest its formation inside the CDS since the SN ejecta during the 125 – 140 d is too warm for the condensation of molecules (Kozasa et al. 1991). The flash-ionization features in the early spectral sequence and the steep rise in early UV light curves of SN 2023ixf conclusively indicated the presence of a dense CSM. As the shockwave from the SN encountered the denser

CSM, it decelerated, compressing the material and increasing the density within the shocked CSM. Radiative cooling then facilitated the emission of photons, aiding in its cooling and forming a distinctive CDS (Chugai 2009) in the denser CSM. The CDS enables an additional pathway for dust formation in interacting SNe II (Rho et al. 2018). In addition, the clumpiness within the extended CSM encompassing SN 2023ixf facilitates the formation of additional CDS (in addition to its formation in the dense CSM), consequently enhancing molecule formation and eventually forming dust (Inserra et al. 2011). Since nebular phase Hα arises from the inner ejecta, it wouldn't show wavelength-dependent attenuation if the dust is formed in the outer CDS. This suggests that the regions where Balmer lines form and dust formation occurs essentially overlap, indicating thorough mixing of the CDS into the inner ejecta following a significant episode of CSM interaction (Bevan et al. 2019).

We also see evidence of flattening in the Ks-band light curve of SN 2023ixf beyond 125 d in Figure 4.7 evolving at 1.3 ± 0.1 mag $100\,\mathrm{d}^{-1}$ against the relatively consistent decline of 1.8 ± 0.1 mag $100\,\mathrm{d}^{-1}$ in the J and H bands. This indicates that the continuum luminosity in NIR is evolving steadily; however, the Ks-band light curve is evolving rather slowly due to the emission from CO overtone around 2.3μm. Type II SN 2017eaw (Rho et al. 2018) showed the presence of the first overtone of CO as early as 124 d and also showed flattening in their Ks-band light curves. Although we do not have NIR spectra of SN 2023ixf to investigate the CO overtone, flattening of the Ks-band light curve around the similar epoch strengthens our inference for indirect conformation of molecular CO and eventually dust in the case of SN 2023ixf.

4.8 Progenitor and Explosion Parameters

Building upon the similar models used in the early phase modeling to estimate CSM parameters, we further use those models to constrain the progenitor properties (Singh et al. 2024). Using the pre-computed model grid, we first looked for the best matching models considering the g- and r-filters by searching models with minimum χ^2. We found that the models from a low-mass progenitor (10 $M_\odot$) best fit the light curves of SN 2023ixf. The best fitting models have the explosion energy of around 2×10^{51} erg, the ^{56}Ni mass of around 0.06 $M_\odot$, the mass-loss rate of around 10^{-2} $M_\odot$ yr^{-1}, the CSM radius of around 6×10^{14} cm, and β of around 3. We performed extra numerical light curve calculations and found that the model with the CSM radius of 5×10^{14} cm matches the observed dataset, including the photospheric velocity. The mass of the confined CSM below 5×10^{14} cm in this model is 0.67 $M_\odot$. This extra model assumes that ^{56}Ni is uniformly mixed in the entire ejecta. We found that the fully mixed model better fits the transition from the plateau phase to the tail phase. However, they also lead to an excess emission in the redder bands during the late plateau phase as ^{56}Ni starts diffusing out earlier than in the case of a centrally concentrated ^{56}Ni. A much more prominent effect of ^{56}Ni-mixing was seen in the case of SN 2009ib (Takáts et al. 2015) and SN 2016gfy (Singh et al. 2019a). Since the ^{56}Ni synthesized in SN 2023ixf is high in comparison to normal SNe II (0.03 $M_\odot$, Anderson et al. 2014a), the late-plateau luminosity bump is apparently stronger in the redder bands.

Finally, we estimated a progenitor mass of 10 $M_\odot$ with a radius of 470 $R_\odot$ and an explosion energy of 2×10^{51} erg and 0.059 $M_\odot$ of ^{56}Ni. The early UV excess was best modeled by a confined dense CSM spanning from the tip of the progenitor to 5×10^{14} cm arising from a mass-loss rate of 10^{-2} $M_\odot$ yr^{-1} and a r^{-2} density structure. The late-plateau UV excess was modeled by an extended CSM spanning 5×10^{14} cm to 10^{16} cm with a mass-loss rate of 10^{-4} $M_\odot$ yr^{-1} and a r^{-3} density structure.

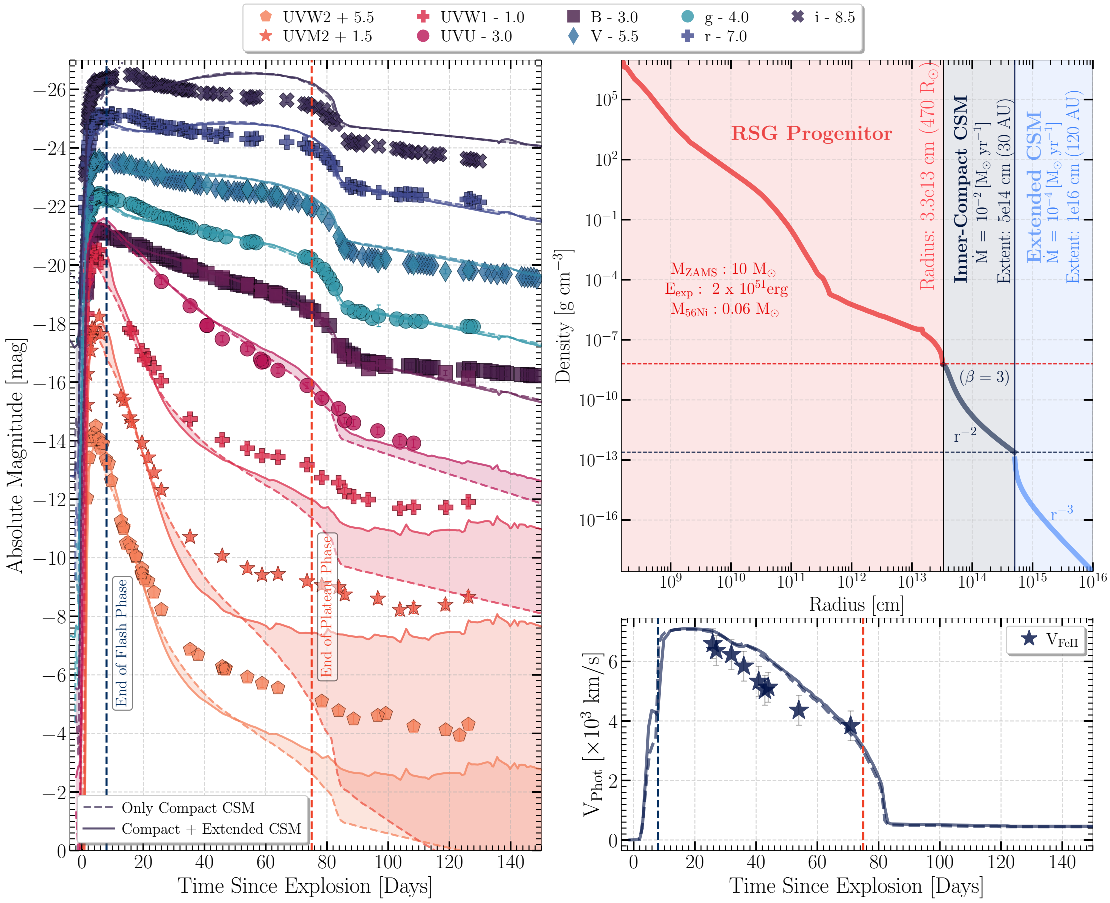

FIGURE 4.15: *Left Panel*: Hydrodynamical modeling of the light curves of SN 2023ixf with only a compact CSM (dashed line) and including an extended CSM (solid line). The shaded region shows the UV excess from the interaction due to the extended CSM. *Top-right panel*: The density structure of the RSG progenitor, the inner-compact CSM, and the extended CSM. The inner-compact CSM extended to 5×10^{14} cm and the extended CSM extends to 1×10^{16} cm. *Bottom-right panel*: The photospheric velocity estimates from both the hydrodynamic models are compared with the observed evolution of photospheric velocity. (Red vertical dotted line marks the plateau end)

SN 2023ixf has a higher peak luminosity, higher ^{56}Ni-mass, and a higher photospheric velocity than a typical Type II SN. The peak V-band luminosity of SN 2023ixf is ∼-18.2 mag, which is 4 times brighter than compared to the luminosity of a typical Type II SN, i.e., ∼-16.7 mag (Anderson et al. 2014a). The ^{56}Ni-mass of SN 2023ixf is 0.059 ± 0.001 M$_\odot$ which is 80% higher than the ^{56}Ni-mass estimate of a typical Type II SN, i.e., 0.033 M$_\odot$. Previous studies on SNe II (Hamuy 2003; Pejcha & Prieto 2015; Gutiérrez et al. 2017b) have shown that more energetic explosions lead to higher photospheric velocities and a higher ^{56}Ni-yield in the SN. The estimated ^{56}Ni-mass does indicate that SN 2023ixf is a highly energetic event and is in concordance with the high explosion energy of 2×10^{51} erg estimated from the light curve modeling. Other works on numerical modeling of SN 2023ixf also suggest high explosion energies. Bersten et al. (2024) estimate 1.2 foe as explosion energy for a 12 $M_\odot$ RSG with 10.9 $M_\odot$ as the final progenitor mass. Hiramatsu et al. (2023) estimated 1 foe as explosion energy while exploring 2 foe as well for a 12 $M_\odot$ progenitor with 11 $M_\odot$ as the final progenitor mass.

In our case, where we have the best match with a lower mass progenitor, slightly higher explosion energies must be required to match the observed light curves. Although we fit both photospheric velocities and light curves simultaneously, our mass and radius of the progenitors are fixed since we adopt progenitor models from Sukhbold et al. (2016). We cannot lift degeneracies between the ejecta mass, radius, and explosion energy (Goldberg et al. 2019). However, the high-explosion energy cannot entirely explain the peak luminosity of SN 2023ixf. It is enhanced further by early interaction with CSM. The photospheric velocity of SN 2023ixf is 20% faster than a proto-typical Type II SN at 50 d (see Section 4.7), and a power-law fit to photospheric velocity evolution returned exponent -0.47 ± 0.04, which is slower than the average value derived from a large sample of SNe IIP (-0.581 ± 0.034) (Faran et al. 2014a). However, since SN 2023ixf is a short-plateau SN, the slightly low-ejecta mass could be one reason for its higher photospheric velocity (Teja et al. 2023b).

4.9 Discussion

Timeline of significant epochs during evolution

In its infancy, SN 2023ixf showed a rapid evolution spearheaded by the appearance of an increase in ionization in the early flash-ionization phase, accompanied by a rapid ascent in the early UV flux. Additionally, the increase in the color temperature to approximately 35,000 K until around 2.2 days signifies that the shock breakout occurred within a confined, dense CSM. The epoch of peak UV luminosity (and the bolometric peak) at 4.5 d is synonymous with the peak of the He II line flux of Zimmerman et al. (2023), which traces the strength/flux of the flash-ionization features. The change in the line profile of the narrow Hα feature and the drop in its strength seen in the high-resolution spectroscopy of SN 2023ixf (Smith et al. 2023) also happens around 4.4 d, and is synonymous with UV peak. This indicates that the thermal heating and ionization continued beyond the shock breakout (2.2 d). The emergence of a CDS (Chugai 2009) within the post-shock CSM and the decelerated SN ejecta is probably contributing to the photo-ionization and prolonged heating observed in the flash-ionized features of SN 2023ixf. During the breakout phase, the radius of thermal emission remained relatively constant at $(2.0 \pm 0.2) \times 10^{14}$ cm (or 13 ± 1 AU), indicating the location where thermal radiation originates from within the dense CSM (Chevalier & Irwin 2011). This radius, derived from blackbody fits to UV-Optical-NIR data, is typically smaller (as it generally forms deeper) than the radius of photospheric emission ($\tau \sim 2/3$) (Moriya et al. 2011) and the surface of last scattering of the dense CSM.

The first detection of SN 2023ixf in X-rays from *NuSTAR* on ~ 4 d showed a large column density of absorption, consistent with arising from a shocked dense CSM (Grefenstette et al. 2023). However, the next epoch of X-ray observations at 11 d and 13 d (Grefenstette et al. 2023; Chandra et al. 2023) exhibited a substantial decline in the column density of absorption. SN 2023ixf showed the emergence of broad P-Cygni of Hα at 7 d, and flash-ionized phase end lasted $\sim$8 d. We see the appearance of the broad HV absorption of Hα at 16 d in synonymity with the *red peak* in our multiband light curves in Section 4.6. The intermediate-width Lorentzian features from CSM interaction disappeared in the spectra around 16 – 18 d (Smith et al. 2023). SN 2023ixf was not detected at millimeter wavelengths from 2.6 – 18.6 d (Berger et al. 2023). SN 2023ixf was eventually detected in radio wavelengths rather feebly after 29.2 d (Matthews et al. 2023).

Progenitor of SN 2023ixf

Numerous works on SN 2023ixf have estimated progenitor mass, mass-loss rate, and CSM extent around the progenitor. Pre-explosion imaging through *HST* and *Spitzer* revealed a point source similar to an RSG star surrounded by a large amount of dust (Soraisam et al. 2023; Jencson et al. 2023; Neustadt et al. 2024). However, no counterpart was discovered in UV or X-rays (Basu et al. 2023; Matsunaga et al. 2023; Kong 2023; Panjkov et al. 2023). However, there is a disparity in the estimates of progenitor mass from the pre-explosion imaging revealing estimates in 2 broad ranges, i.e. 9 – 14 $M_\odot$, (Kilpatrick et al. 2023a; Pledger & Shara 2023; Van Dyk et al. 2023; Neustadt et al. 2024), and 17 – 22 $M_\odot$, (Qin et al. 2023; Niu et al. 2023; Jencson et al. 2023; Soraisam et al. 2023). Our numerical hydrodynamical modeling best matched a ZAMS progenitor mass of 10 $M_\odot$ for SN 2023ixf having a radius of 470 $R_\odot$. Only other work that performed hydrodynamical modeling of the complete light curve until the nebular phase also indicated a low-mass progenitor (i.e., 12 $M_\odot$, Bersten et al. 2024). The short-plateau nature of SN 2023ixf indicates a relatively lower ejecta mass, which is also reflected in its steep plateau decline rate. Furthermore, the considerable blueshifted offset observed in Hα ($\sim$3,000 km s^{-1}) during the early phase reinforces this deduction, indicating an escalated degree of stripping undergone by the 10 $M_\odot$ progenitor of SN 2023ixf.

Pre-explosion observations of the progenitor of SN 2023ixf revealed variability in the mid-IR and near-IR observations from *Spitzer* and ground-based telescopes (Kilpatrick et al. 2023a; Soraisam et al. 2023; Jencson et al. 2023). However, despite this variability, there is no indication of pre-SN outbursts in the pre-explosion imaging conducted by Jencson et al. (2023), nor any signs of variability in the optical spectrum (Dong et al. 2023; Neustadt et al. 2024), which likely denies the existence of episodic mass loss in SN 2023ixf. This lack of pre-explosion outbursts suggests that the progenitor of SN 2023ixf likely had a rapid rotation and/or underwent a pre-SN interaction with a binary companion (Smith 2014; Matsuoka & Sawada 2023). Such an interaction would have led to an enhanced mass loss in the lead-up to the explosion and drive a significant asymmetry in the observed CSM. SN 2023ixf is thus a low-mass RSG progenitor showcasing a multi-faceted CSM geometry arising from enhanced mass loss during its twilight years.

Characteristics of CSM around SN 2023ixf

SN 2023ixf showed several signs of interaction with CSM both photometrically and spectroscopically. The hydrodynamical modeling in Section 4.8 emphasized confined dense CSM presence was responsible for the origin of flash-ionization features, steep rise in UV flux, bolometric luminosity and temperature, and an extended low-density CSM, which led to the late-phase UV excess and the clumpy features around Hα. This brings forward the argument that the progenitor of SN 2023ixf had an enhanced wind that developed before the explosion, leading to the delayed shock breakout.

The modeling also revealed that the true extent of the confined CSM is roughly

5×10^{14} cm (33 AU), more significant than the nearly-flat radius of thermal emission during the early SN evolution in Section 4.6. Our estimates align well with the estimates from comparison with CMFGEN models (Jacobson-Galan et al. 2023), high-cadence early spectroscopy (Bostroem et al. 2023a), early light curve modeling (Hiramatsu et al. 2023) and pre-discovery photometry close to the explosion (Li et al. 2023). The confined CSM is characterized by a wind-like structure with a mass-loss rate of $\sim 10^{-2}$ $M_{\odot}$ yr^{-1} which is consistent with other works (Jacobson-Galan et al. 2023; Zimmerman et al. 2023). The mass-loss rate indicates a progenitor star in the eruptive phase, which could lie anywhere between $10^{-2} - 0.1$ $M_{\odot}$ yr^{-1} (Smith 2017).

4.10 Summary

SNe II are the most common type of CCSNe and yet harbor several mysteries regarding the late-stage evolution of its massive star progenitors, resulting in considerable observational heterogeneity. This Chapter presents an extensive set of observations for the closest CCSN in the last 25 years, SN 2023ixf, that exploded in M 101. The panchromatic observations covered wavelengths from the FUV to NIR regime using both ground and space-based observatories. We highlight the major results below:

- **Early Phase Spectra:** Detailed spectral coverage in FUV, NUV, and optical during the first $\sim$ 25 days since the explosion is presented, beginning within 2 days from the explosion. The lines due to Mg II, Fe II in the NUV, and C III, C II, Si IV, He II in the FUV were identified. The early (<7 d) spectral sequence of SN 2023ixf indicates the presence of a dense CSM. There are no significant signatures subsequently, except for an intermediate-width emission feature of H α after +7 d. The high-resolution spectra presented by Smith et al. (2023) show the presence of an intermediate-width P-Cygni profile during this phase, lasting for about a week, arising in the post-shock, swept-up CSM shell. The line profile during the photospheric phase beginning $\sim$16 d shows a multi-peaked/boxy profile of H alpha, indicating an ongoing CSM interaction with a shell-shaped CSM with an inner radius of $\sim$75 AU and an outer radius of $\sim$ 140 AU. Considering a standard RSG wind velocity, the progenitor likely experienced enhanced mass-loss $\sim$35 - 65 years before the explosion. All the above inferences from our multi-wavelength observations indicate a multi-faceted circumstellar matter around the progenitor of SN 2023ixf.

- **Confined CSM**: The early discovery and classification allowed for the coverage of the SN just after 1 d wherein we observe an initial rise in the blackbody temperature evolution, blueward rise of UV colors, and an order-of-magnitude rise in UV flux at a nearly constant radius of evolution asserting the delayed shock breakout due to a confined dense CSM in SN 2023ixf.

- **Photometric evolution:** The early phase light curve of SN 2023ixf is influenced by the presence of dense nearby CSM, which was likely accumulated due to enhanced mass loss(es) during the later stages of the progenitor's evolution. SN 2023ixf was found to have a very bright peak luminosity ($M_V \approx -18.1$ mag), much brighter than the average luminosity for Type II SNe ($M_V \approx -16.7$ mag). Light curves were compared with a large model grid of interacting SNe with varied progenitor masses and CSM properties to infer the properties of the dense CSM in SN 2023ixf. Based on our comparison with light curve models, the high luminosity is likely a mix of interaction with a confined CSM and an inherently energetic explosion. SN 2023ixf showed rise times of 4.5 d (*blue peak*) arising due to CSM interaction and 16 d (*red peak*) arising from the SN ejecta. SN 2023ixf shows an early plateau decline rate (s1) of $2.70^{+0.48}_{-0.49}$ mag $(100\,\mathrm{d})^{-1}$ and a late-plateau decline rate (s2) of $1.85^{+0.13}_{-0.14}$ mag $(100\,\mathrm{d})^{-1}$, resembling fast-declining SNe II. The plateau length of SN 2023ixf is 75 d, towards the shorter end of SNe II. SN 2023ixf is one of the brightest SN IIP/L ever observed in UV with a peak UVW1 magnitude of ∼–20 mag.

- **Slow photospheric evolution and Distinctive** Hα **profile:** We infer a delayed development of metal features in the spectral sequence of SN 2023ixf, hinting at the ejecta cooling slower than a normal SNe II, possibly due to CSM interaction. The weaker absorption in the P-Cygni profile of Hα suggests ongoing interaction during the plateau phase, reminiscent of Type IIL SNe. Post 16 d, the Hα and Hβ are characterized by a high-velocity broad absorption feature at 13,500 km s^{-1} in addition to the clumpy P-Cygni profile with an absorption minimum at 8,500 km s^{-1}.

- **Signs of Molecular CO formation:** The flattening in the K_s-band light curve and the attenuation of the red-edge of Hα post 125 d indicates early onset of molecular CO and hence dust formation in SN 2023ixf similar to SN 2017eaw and SN 1987A.

Chapter 5

Faint Short-plateau SNe

From a natural perspective, majority of short-plateau SNe studied are on the brighter end of luminosities. Here, we present a rare, one-of-a-kind supernova SN 2021wvw. As we move towards the fainter end of Type IIP SNe, the general trend is prolonged plateau lengths for both low and intermediate brightness. In this Chapter, we study SN 2021wvw, which is a short plateau object with many characteristics resembling an intermediate luminosity, normal plateau Type II class. Thus, it appears to be not falling in any of the known sub-classes of Type II SNe.

5.1 SN 2021wvw: A CCSN at the sub-luminous, slower & shorter end of Type IIPs

SN 2021wvw (other names: PS21jnb, ZTF21abvcxel, ATLAS21bgtz, Gaia21eqm) was discovered on August 24, 2021 14:32.6UT (JD=2459451.1) in UGC 02605 (Jones et al. 2021) with 17.93 ABMag in the $i - P1$ filter. Subsequently, it was classified as an SN from the Type II class with a strong blue continuum having Balmer (Hα, Hβ) emissions (Hinkle 2021). The first detection in ZTF-g filter (19.34 mag) was on JD 2459449.95 and the last non-detection in ZTF-r filter (19.15 mag) was on JD 2459449.91. Using this, we obtain JD 2459449.93 ± 0.02 as the explosion epoch. A similar epoch, shifted by +0.2 d, is obtained using data from ATLAS forced photometry server with 5-σ last non-detection (>18.89 mag) on JD 2459449.1 and first detection (18.10±0.08 mag) on JD 2459451.1 both in ATLAS-o filter. The non-detections in both ZTF-r and ATLAS-o are at a similar epoch, hence we consider this as the last non-detection, and the first detection in ZTF-g band. Using this, we obtain $t_{exp} = 2459449.9 \pm 0.3$ as the explosion epoch and use this throughout. SN 2021wvw's location in its host galaxy is marked in Figure 5.1.

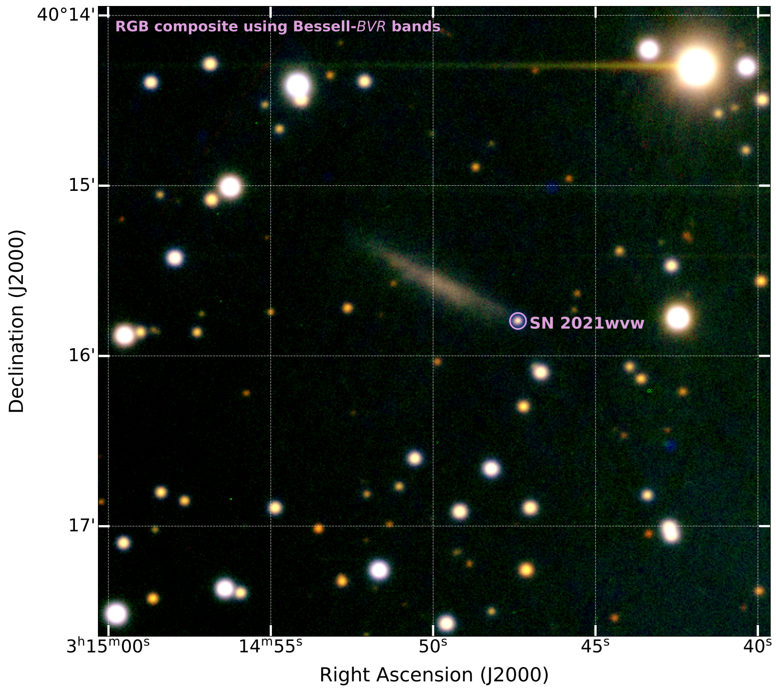

FIGURE 5.1: RGB color composite finder chart for SN2021wvw utilizing images in Bessell-BVR filters from HCT.

TABLE 5.1: Spectra log of SN 2021wvw obtained from HCT.

Date (year-mm-dd)	JD (2459000+)	Phase† (d)	Range (Å)
2021-08-28	455.4	5.5	4000-7700
2021-09-13	471.3	21.4	4000-8900
2021-09-18	476.3	26.3	4000-8900
2021-09-19	477.4	27.4	4000-7700
2021-09-29	487.3	37.3	4000-8900
2021-10-02	490.2	40.3	4000-8900
2021-10-09	497.2	47.3	4000-8900
2021-10-10	498.2	48.3	4000-8900
2021-10-14	502.2	52.2	4000-8900
2021-10-19	507.2	57.3	4000-8900
2021-10-21	509.1	59.2	4000-8900
2021-10-22	510.2	60.3	5300-8900
2021-10-26	514.2	64.2	4000-8900
2021-10-30	518.2	68.3	4000-8900
2021-11-08	527.1	77.2	4000-8900
2021-11-15	534.3	84.4	4000-8900
2021-11-26	545.1	95.1	4000-7700

†Phase given for t_{exp} = 2459449.9 JD

5.2 Photometry and Spectroscopy: Data sources

We began photometry of SN 2021wvw in the optical since +8.4 d past explosion using GIT and HCT. GIT covered dense multi-band photometry in SDSS-$g'r'i'z'$ filters, and HCT covered in Bessell-V and -R filters. We supplemented our observations with photometry from the ATLAS forced photometry server in c and o filters. We also obtained ZTF-g and -r filter apparent magnitudes from ALeRCE (Förster et al. 2021). The ATLAS photometry, being noisy, has been binned for 2 d intervals in the late phase using `python` script from Young (2020). During the late phase, we took multiple exposures using GIT and HCT and summed them for a better signal-to-noise ratio in respective filters. The SN being far away from the host nucleus ($\sim 31''$) and at the periphery, we do not perform any template subtraction. The last detected photometric points are significantly brighter (1.5-3 mag) than the SDSS photometry* in the regions near the SN position. Standard photometric data reduction procedures have been adopted utilizing `IRAF` and `pyraf`. The photometric data are given in Table 5.2. The spectra observed with grisms Gr7 and Gr8 were combined to obtain spectra covering a wavelength range of 4000 to 9000 Å. The optical spectra were obtained during 5 - 95 d post-explosion. Beyond 95 d, the SN faded considerably, and spectroscopy with HCT was not feasible.

The host redshift (z=0.0099, Schneider et al. (1992)) and line of sight extinction ($E(B-V) = 0.24$ mag) are taken from NED and IRSA, respectively. This redshift converts to a distance of 41.51 ± 2.91 Mpc or $\mu = 33.09 \pm 0.15$ mag, assuming the ΛCDM cosmology†. Galactic reddening was corrected using Cardelli et al. (1989) law. We do not find any discernible Na ID features at host redshift in SN spectra and hence assume no extinction due to the host galaxy.

5.3 Light Curve Analysis

We present the panchromatic light curve evolution of SN 2021wvw in Figure 5.2. The light curve evolution spans roughly 220 d post-explosion. Other than the bluer bands such as g-band, the light curves evolution in different filters show a very flat evolution up to 70 to 80 d before transitioning sharply into the tail phase. The plateau and transition phases are very densely sampled in most filters. In R and V filters, the tail phase is sampled up to 220 d. We estimate a plateau length of around 75 d (OPTd, Anderson et al. 2014a) and a sharp transition period of about 10 d.

*https://skyserver.sdss.org/dr18/
†$H_0 = 72.5$ km s^{-1} Mpc^{-1} (Riess et al. 2022)

Table 5.2: Photometric observations of SN 2021wvw from GIT and HCT.

JD (2459000+)	Phase† (d)	g (mag)	V (mag)	r (mag)	R (mag)	i (mag)	z (mag)
458.3	8.4	18.07 ± 0.18	-	17.68 ± 0.09	-	17.72 ± 0.11	-
459.3	9.4	18.10 ± 0.12	-	17.68 ± 0.08	-	17.65 ± 0.11	17.45 ± 0.11
460.2	10.3	18.11 ± 0.15	-	17.65 ± 0.10	-	17.64 ± 0.14	-
462.3	12.4	-	-	17.66 ± 0.05	-	17.63 ± 0.06	-
463.3	13.4	18.12 ± 0.10	-	17.67 ± 0.05	-	-	17.36 ± 0.13
465.3	15.4	18.17 ± 0.10	-	-	-	-	-
471.3	21.4	-	-	-	-	-	17.40 ± 0.18
474.3	24.4	18.30 ± 0.16	-	17.69 ± 0.08	-	17.66 ± 0.07	17.44 ± 0.10
476.3	26.4	18.40 ± 0.12	18.06 ± 0.01	17.81 ± 0.05	17.56 ± 0.01	17.64 ± 0.06	-
477.3	27.4	-	18.05 ± 0.01	17.79 ± 0.06	17.55 ± 0.02	17.64 ± 0.07	17.49 ± 0.09
478.2	28.3	-	-	-	-	17.62 ± 0.12	-
479.3	29.4	-	-	17.80 ± 0.06	-	17.70 ± 0.08	-
485.3	35.4	-	-	17.76 ± 0.05	-	17.66 ± 0.06	-
486.3	36.4	18.49 ± 0.11	-	17.65 ± 0.05	-	17.63 ± 0.08	17.56 ± 0.12
487.3	37.4	-	-	17.75 ± 0.06	-	17.69 ± 0.07	17.51 ± 0.11
488.4	38.5	18.53 ± 0.15	-	17.75 ± 0.09	-	17.67 ± 0.08	-
489.2	39.3	18.51 ± 0.14	-	17.76 ± 0.09	-	17.61 ± 0.11	-
490.2	40.3	18.55 ± 0.14	18.07 ± 0.01	17.78 ± 0.06	17.56 ± 0.01	17.66 ± 0.09	-
491.3	41.4	18.58 ± 0.16	-	17.79 ± 0.08	-	17.61 ± 0.09	17.52 ± 0.11
492.2	42.3	18.62 ± 0.14	-	17.81 ± 0.11	-	17.68 ± 0.10	17.46 ± 0.11
493.3	43.4	18.62 ± 0.15	-	17.78 ± 0.09	-	17.72 ± 0.09	17.55 ± 0.12
494.2	44.3	18.54 ± 0.14	-	17.78 ± 0.09	-	17.66 ± 0.14	-
495.4	45.5	18.57 ± 0.15	-	17.81 ± 0.09	-	17.64 ± 0.11	17.56 ± 0.14
497.3	47.4	18.60 ± 0.15	-	17.83 ± 0.12	-	17.67 ± 0.13	17.53 ± 0.16
498.2	48.3	18.58 ± 0.12	-	17.81 ± 0.12	-	17.72 ± 0.09	-
501.3	51.4	18.72 ± 0.20	-	17.77 ± 0.12	-	-	17.61 ± 0.14
502.2	52.3	18.60 ± 0.14	-	17.84 ± 0.07	-	17.67 ± 0.08	-
503.2	53.3	18.51 ± 0.24	-	-	-	-	-
504.1	54.2	18.75 ± 0.13	-	17.92 ± 0.06	-	17.66 ± 0.07	17.56 ± 0.08
507.1	57.2	-	-	17.89 ± 0.08	-	17.63 ± 0.10	17.60 ± 0.12
508.3	58.4	-	-	17.75 ± 0.08	-	17.73 ± 0.10	17.66 ± 0.15
514.4	64.5	-	-	17.94 ± 0.13	-	-	17.69 ± 0.14
515.4	65.5	18.83 ± 0.16	-	18.05 ± 0.10	-	17.83 ± 0.11	-
516.3	66.4	-	-	17.93 ± 0.14	-	-	17.65 ± 0.21
517.2	67.3	-	-	18.04 ± 0.07	-	17.87 ± 0.08	-
518.3	68.4	18.89 ± 0.23	-	18.01 ± 0.16	-	-	-
519.1	69.2	-	-	18.06 ± 0.08	-	17.89 ± 0.08	-
521.2	71.3	18.85 ± 0.19	-	18.13 ± 0.11	-	-	-

> − >Continued on next page

†Phase given for t_{exp} = 2459449.9 JD

Continued from previous page > − >

JD (2459000+)	Phase† (d)	g (mag)	V (mag)	r (mag)	R (mag)	i (mag)	z (mag)
521.2	71.3	18.85 ± 0.19	-	18.13 ± 0.11	-	-	-
522.2	72.3	18.94 ± 0.20	-	18.13 ± 0.11	-	17.98 ± 0.11	17.72 ± 0.13
523.2	73.3	-	-	18.21 ± 0.13	-	-	-
524.2	74.3	18.99 ± 0.16	-	18.12 ± 0.07	-	17.99 ± 0.10	17.81 ± 0.12
525.1	75.2	19.02 ± 0.18	-	18.13 ± 0.08	-	18.00 ± 0.09	-
526.2	76.3	19.03 ± 0.22	-	18.21 ± 0.13	-	-	17.84 ± 0.16
527.1	77.2	19.28 ± 0.19	-	18.29 ± 0.10	-	-	-
528.2	78.3	19.38 ± 0.24	-	18.29 ± 0.13	-	18.12 ± 0.14	17.94 ± 0.16
529.2	79.3	-	-	18.45 ± 0.14	-	18.18 ± 0.14	18.33 ± 0.20
530.1	80.2	19.70 ± 0.16	-	18.57 ± 0.09	-	18.35 ± 0.08	-
531.1	81.2	19.90 ± 0.11	-	18.79 ± 0.04	-	18.68 ± 0.06	-
532.1	82.2	-	-	19.04 ± 0.05	-	-	-
533.1	83.2	-	-	-	-	18.86 ± 0.07	-
534.1	84.2	-	-	19.38 ± 0.14	-	19.31 ± 0.11	-
535.1	85.2	-	-	19.52 ± 0.05	-	19.42 ± 0.08	-
536.1	86.2	-	-	19.73 ± 0.06	-	-	-
541.1	91.2	-	-	19.69 ± 0.08	-	-	-
542.1	92.2	-	-	19.85 ± 0.08	-	-	-
543.1	93.2	-	-	19.75 ± 0.07	-	19.50 ± 0.07	-
544.1	94.2	-	-	19.77 ± 0.07	-	-	-
548.2	98.3	-	-	19.78 ± 0.15	-	-	-
555.1	105.2	-	-	-	-	19.59 ± 0.17	-
563.1	113.2	-	-	-	-	19.64 ± 0.12	-
568.2	118.3	-	-	19.67 ± 0.08	-	-	-
575.0	125.1	-	20.95 ± 0.10	-	19.81 ± 0.05	-	-
580.0	130.1	-	21.17 ± 0.28	-	-	-	-
597.3	147.4	-	-	19.91 ± 0.10	-	-	-
600.2	150.3	-	-	20.21 ± 0.19	-	-	-
605.0	155.1	-	21.15 ± 0.26	-	20.19 ± 0.12	-	-
610.2	160.3	-	-	20.01 ± 0.24	-	-	-
625.0	175.1	-	21.19 ± 0.27	-	20.08 ± 0.10	-	-
626.2	176.3	20.97 ± 0.19	-	-	-	-	-
628.0	178.1	-	21.09 ± 0.12	-	20.44 ± 0.06	-	-
629.2	179.3	-	-	-	-	20.50 ± 0.23	-
636.0	186.1	-	21.03 ± 0.15	-	-	-	-
650.1	200.2	-	-	20.63 ± 0.12	-	-	-
665.0	215.1	-	21.65 ± 0.11	-	20.91 ± 0.10	-	-

†Phase given for t_{exp} = 2459449.9 JD

The mid-plateau brightness is $\approx -16.0 \pm 0.1$ mag (absolute magnitude) in r-band. It puts SN 2021wvw in intermediate luminosity regime of Type IIP SNe. The plateau duration is also shorter ($\sim$ 75 d), whereas the typical plateau length for Type IIP SNe is $\sim$100 d and even longer in the case of under-luminous SNe (SN 2005cs, SN 2016bkv, SN 2021gmj). In Figure 5.3, r-band light curve of

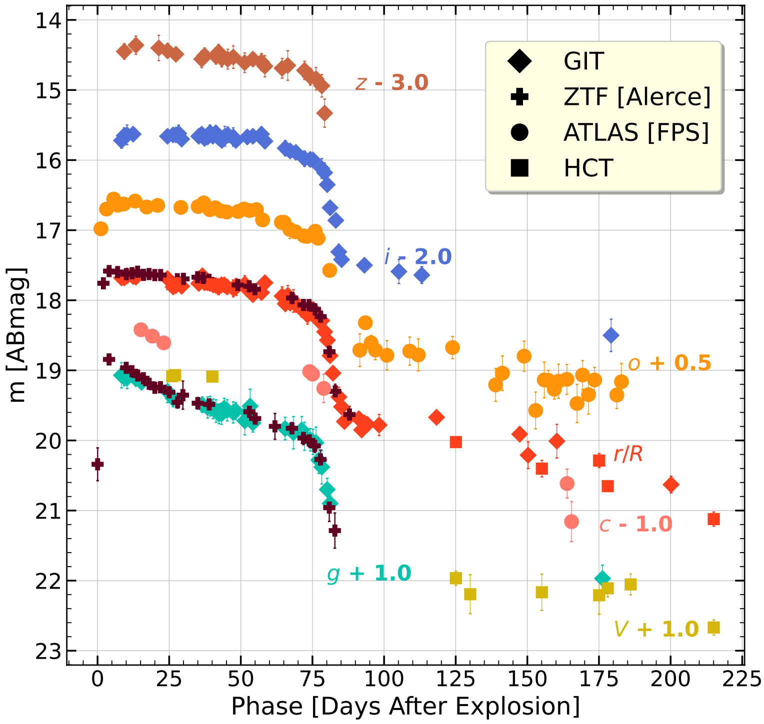

FIGURE 5.2: Light curve evolution of SN 2021wvw for various filters from GIT and HCT is shown. The light curves also include data from ZTF and ATLAS surveys. The constants added to the individual light curves are for visual clarity.

2021wvw is compared with other intermediate/low luminosity and short plateau SNe r/R-band light curves. We compare with the archetypal SNe 2005cs (Pastorello et al. 2006) and 2021gmj (Murai et al. 2024) low luminosity SNe. Although short plateaus are very rare considering overall Type II SNe, we compare with other well-studied short plateau SNe in literature such as SNe 2006Y, 2006ai, 2016egz (Hiramatsu et al. 2021a), 2018gj (Teja et al. 2023a), 2020jfo (Teja et al. 2022) and 2023ixf (Teja et al. 2023b; Singh et al. 2024).

The photospheric phase light curve evolution of SN 2021wvw, particularly for r- and i-bands, is gradual, which is atypical for short plateau SNe, for which the decline is generally rapid (Hiramatsu et al. 2021a). Although the early decline ($s1$) phase after maximum is not evident in the multi-band light curves, upon closer inspection, the g- and r-bands show a gradual decline in the post-peak evolution.

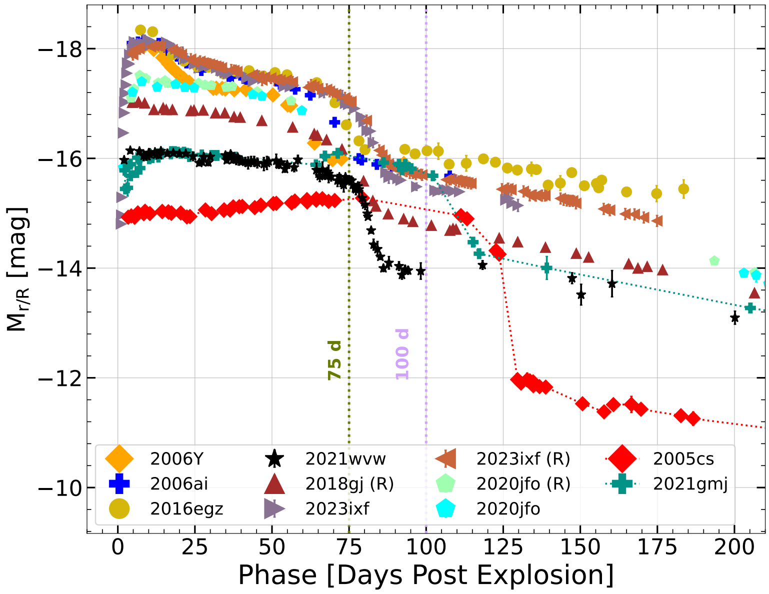

FIGURE 5.3: SN 2021wvw r band light curve evolution is compared with the r/R band light curves of other short plateau SNe. We also show the archetypal low-luminosity SN 2005cs and an intermediate-luminosity SN 2021gmj.

We find this to be $2.52^{+0.52}_{-0.53}$ mag 100 d^{-1} (g-band) and $0.34^{+0.19}_{-0.19}$ mag 100 d^{-1} (r-band), whereas decline is much steeper in other objects: for example, SN 2006Y and SN 2006ai have $4.62^{+0.51}_{-0.52}$ mag 100 d^{-1} and $4.44^{+0.05}_{-0.05}$ mag 100 d^{-1} respectively in g-band. We also estimated decline rates of the plateau ($s2$) and tail ($s3$) phases. The estimated values of various slopes and the mid-plateau absolute magnitudes are shown in Table 5.3. Interestingly, plateau phase in the $i-$ band for SN 2021wvw is almost non-declining with $s2 = 0.10 \pm 0.13$ mag 100 d^{-1}, whereas for other SNe, both with lower luminosity and shorter-plateau SNe, it is around an order of magnitude higher. Evidently, the tail phase decline ($s3 = 0.64 \pm 0.28$mag 100 d^{-1}) of SN 2021wvw in the r-band is close to the values obtained for other lower luminosity SNe (SN 2021gmj, SN 2005cs). At a similar phase, slope s3 in the i-band is non-differentiable for both low-luminosity and short-plateau SNe with values ranging from 1.1 to 1.5 mag 100 d^{-1}.

Comparing mid-plateau luminosity ($M_{\mathrm{tp1/2}}$) of SN 2021wvw in r/R-band with other SNe, we find 2021wvw shows similar absolute magnitude as of SN 2021gmj

TABLE 5.3: Various slopes obtained for different phases of light curves are presented. Slopes and absolute magnitude for other SNe are also compared. The absolute magnitudes ($M_{r/R}$) are reported from the middle of the plateau.

SN	g [mag (100 d)$^{-1}$]		r/R [mag (100 d)$^{-1}$]			i [mag (100 d)$^{-1}$]		$M_{r/R}$
	s1	s2	s1	s2	s3	s2	s3	[mag]
2021wvw	2.52 ± 0.53	1.25 ± 0.16	0.34 ± 0.19	0.78 ± 0.17	0.64 ± 0.28	0.10 ± 0.13	1.09 ± 0.25	-16.0
2005cs	-	-	-	-0.53 ± 0.01	0.60 ± 0.02	-	-	-15.2
2006Y	4.62 ± 0.51	3.28 ± 0.10	4.75 ± 0.13	0.29 ± 0.20	-	1.22 ± 0.10	-	-17.3
2006ai	4.44 ± 0.05	2.86 ± 0.06	4.01 ± 0.10	0.96 ± 0.04	1.03 ± 0.13	1.01 ± 0.04	1.53 ± 0.19	-17.5
2016egz	-	2.83 ± 0.19	-	0.89 ± 0.13	1.11 ± 0.04	1.51 ± 0.17	1.10 ± 0.10	-17.6
2021gmj	-	-	-	0.25 ± 0.01	0.51 ± 0.11	1.28 ± 0.02	1.27 ± 0.03	-15.9

(-15.9 mag), and is about 1 mag brighter than the $M_{tp1/2}$ of SN 2005cs (-15.2 mag). $M_{tp1/2}$ of a majority of other short-plateau SNe is brighter than -17 mag except for SN 2018gj (-16.7 mag) as shown in Figure 5.3.

Radioactive ^{56}Ni

`SuperBol` is used to estimate the pseudo-bolometric/bolometric evolution from observations. Extrapolated blackbody estimates were used to obtain full bolometric luminosity. The extinction-corrected multi-band light curves were used as input, taking well-sampled r-band as the reference light curve. The filters utilized for the pseudo-bolometric curves were $groiz$. We estimate the ^{56}Ni using the Equation 2.5 considering the $\gamma-$ray leakage in case of a stripped envelope:

We use `scipy` and `emcee` packages to fit and estimate errors in the values. Using the pseudo-bolometry, we obtained $M_{Ni} = 0.011 \pm 0.001$ $M_\odot$ providing a lower limit on the ^{56}Ni mass. In addition, considering the blackbody fitted luminosity as bolometric luminosity, we obtain $M_{^{56}Ni} = 0.023 \pm 0.003$ $M_\odot$, which we consider as an upper limit for the estimated values. The latter value is more than twice what was obtained using the pseudo-bolometry but synonymous with a $\sim 50\%$

NIR contribution seen in SN 2023ixf's nebular phase (Singh et al. 2024). We lack NIR data to provide more information about the accuracy of the contribution in the late phase. Nevertheless, the ^{56}Ni mass estimated implies a significant NIR flux contribution at late phases. Hence, NIR observations for such objects in the nebular phase are crucial for a better understanding. In subsequent sections, we perform light curve modeling to constrain the nickel mass and other parameters more robustly.

5.4 Spectra

We present a complete spectral evolution of SN 2021wvw covering the plateau and transition phases in Figure 5.4. The spectra have been calibrated with the corresponding multi-band fluxes, corrected for the host redshift, and de-reddened with the estimated extinction. The phases mentioned start from the estimated explosion epoch. All well-identified lines are marked for clarity in the Figure.

Evolution and comparisons

The first spectrum was observed at +5.5 d. It comprises a blue continuum with broad Balmer features and He I 5876Å superposed on it. After that, there is a gap of around 15 d; the following spectrum is on +21 d. Thereafter, the spectral evolution is densely sampled until the supernova enters the nebular phase. Qualitatively, absorption features appear relatively narrow at first glance compared to typical IIP SNe, indicating relatively low velocities, and they become narrower with time. Although there are some hints of Fe II in the bluer region at +21 d, these features do not evolve much till +37 d, after which we start to see Fe II lines conspicuously. Around +21 d, we also observe the appearance of Ca NIR triplet

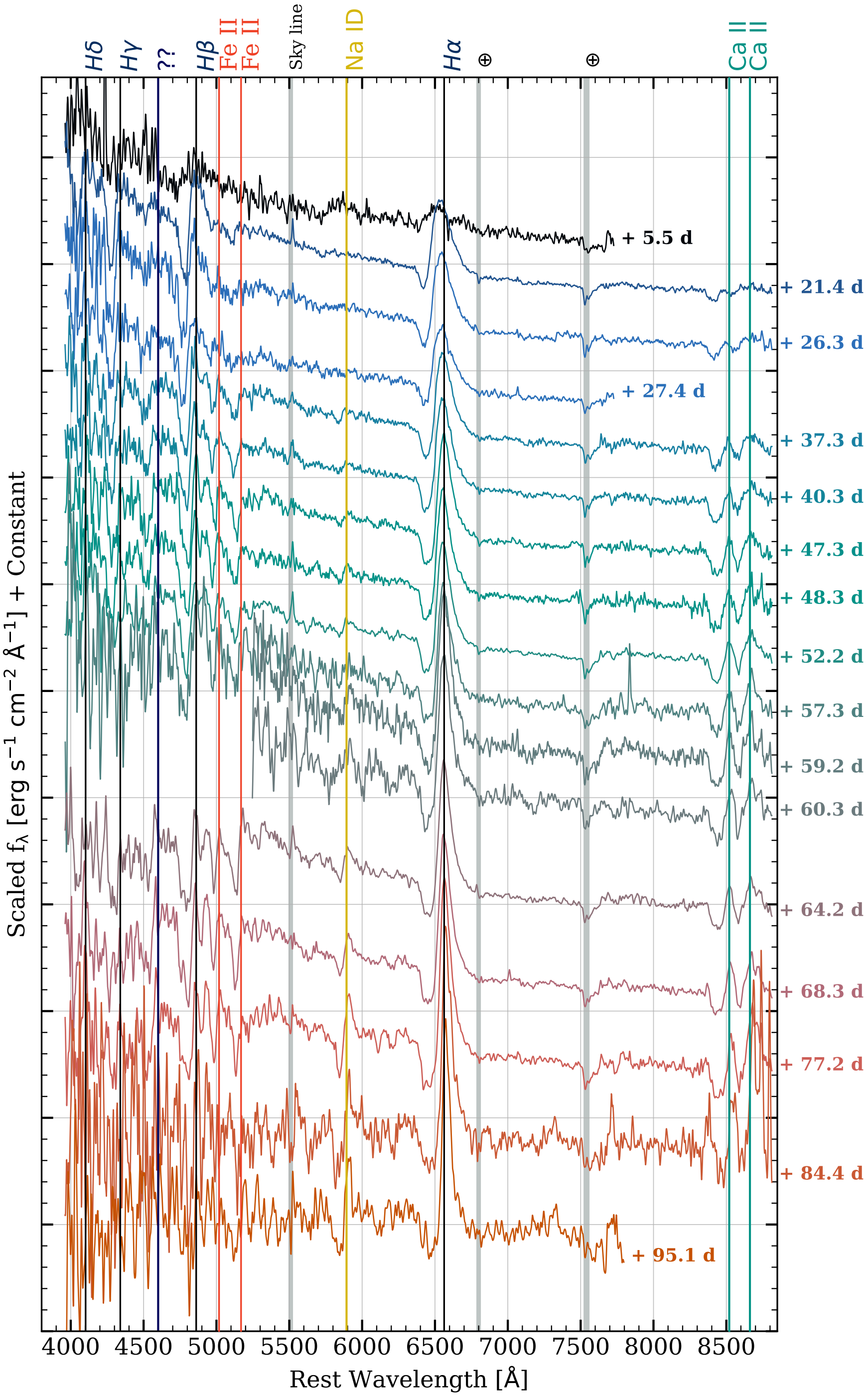

FIGURE 5.4: Spectral sequence for SN 2021wvw. The spectra have been corrected for absolute flux using corresponding photometry and also de-reddened using Milky Way line-of-sight extinction.

feature in the red-ward region, which strengthens as SN ejecta evolves further in the photospheric regime. Interestingly, the region between Fe II lines and Hα is

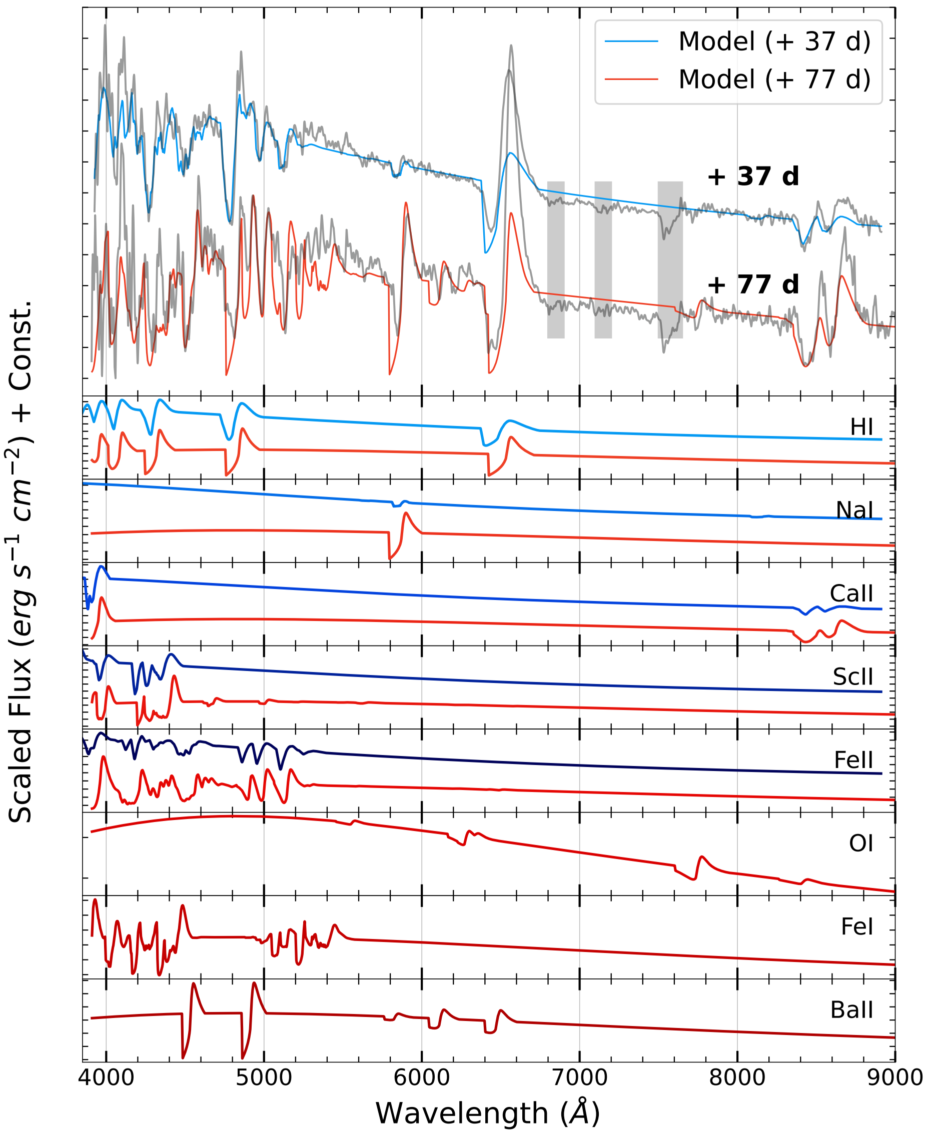

FIGURE 5.5: SYNAPPS model fitting to the observed spectra around the mid and end plateau phases. The lower small panels show the model spectra of individual species when the contribution from the rest of the species is turned off. Tellurics marked with grey bands are not considered while fitting.

devoid of any lines except a weak appearance of Na ID from +37 d onward. Similarly, the region between Hα and Ca triplet lacks any discernible features until the end of the observed evolution. We observe a band of emission lines between Hβ and Hγ throughout, usually attributed to Fe lines.

The mid-plateau and end-plateau spectra are modeled using `SYNAPPS/Syn++` to better ascertain the minimum number of species required to explain the observed spectra.

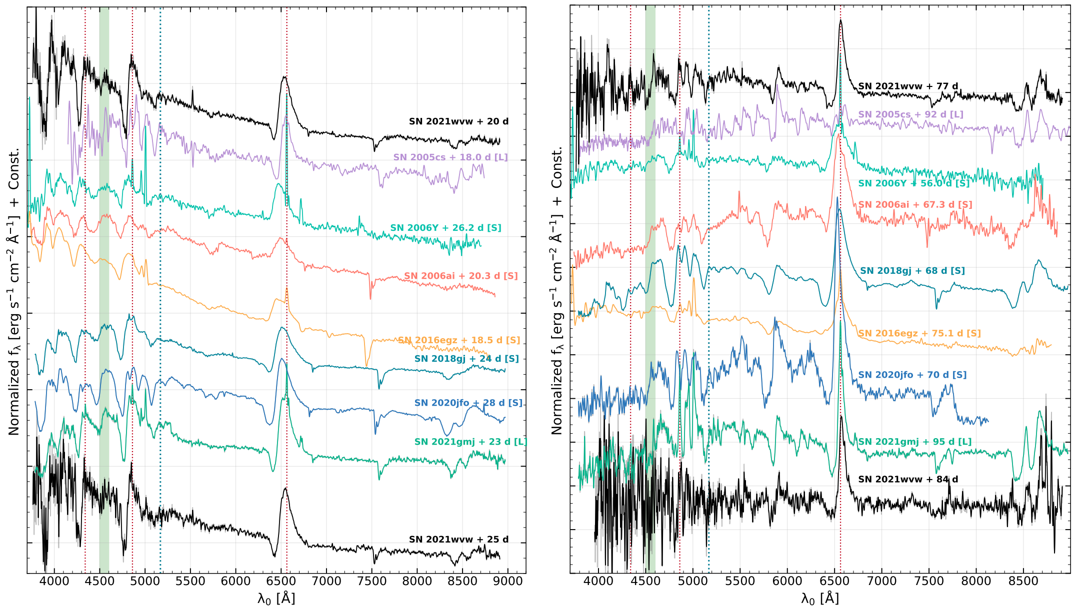

FIGURE 5.6: Spectral comparisons at the early and late plateau phase with short-plateau SNe and with other sub-luminous SNe.

For the first setup to model the +37 d spectrum, we include only five species namely H I, Ca II, Na I, Sc II and Fe II. The overall best-fit spectra and various species contributions are presented in Figure 5.5. The individual species contributions are obtained by utilizing the best-fit output as input in `Syn++` by turning on one species at a time in the input file. No warping function is applied, i.e., a1=a2=0. Only a0 is varied, which signifies the flux level. Photospheric velocity obtained on the day +37 d is 3830 km s^{-1}.

For the end-plateau spectrum at +77 d, in addition to the previously included species, we add three more metal species, namely Ba II, Fe I, and O I. Further, we find that the broad emission band around 4800 Å is a blend of multiple metal lines originating from neutral Fe, Sc II, and Ba II. The photospheric velocity obtained from these fits around +77 d is 2170 km s^{-1}.

In Figure 5.6, we compare SN 2021wvw spectra with a few other short-plateau SNe along with the low-luminosity SN 2005cs and intermediate luminosity SN 2021gmj. Firstly, in Figure 5.6 (left), we compare the spectra around 20 d when the metal features are well developed. We clearly observe that there are similarities as well as dissimilarities in the spectral features. At first glance, the features appear similar to SN 2005cs and SN 2021gmj, i.e., narrow and strong absorption. The Hα absorption appears shallow, which seems to be the general trend for the short-plateau SNe and is completely indiscernible in some of the brighter and fast-declining short-plateau SNe, for example, SN 2006Y, SN 2006ai, and SN 2016egz. At similar epochs, other SNe have well-developed metal features such as Fe II lines toward the blue end, whereas we only see a hint of these lines in SN 2021wvw. In the same figure (right), we compare SN 2021wvw spectra during the end plateau phase, where we find the appearance of the strongest metallic features. The SN 2021wvw spectra show similar features to other sub-luminous SNe, but the absorption depths are shallow. However, SN 2021wvw has well-developed P-Cygni (more representative of a typical Type IIP) profiles compared to much shallower absorption depths in short-plateau SNe 2006Y, 2006ai, and 2016egz.

Velocities

We utilize some of the well-resolved absorption features to estimate ejecta velocities. We iteratively measure the minimum of these lines using `IRAF` by fitting an inverted Gaussian assuming a multitude of continuum points. The absorption minima are corrected for redshift and eventually converted to the expansion velocities using the central rest wavelengths of the corresponding features. We have estimated these velocities for six lines as shown in Figure 5.7. The errors in velocity estimates are much smaller than the instrumental resolution; hence, the latter has been quoted as the errors in the velocities.

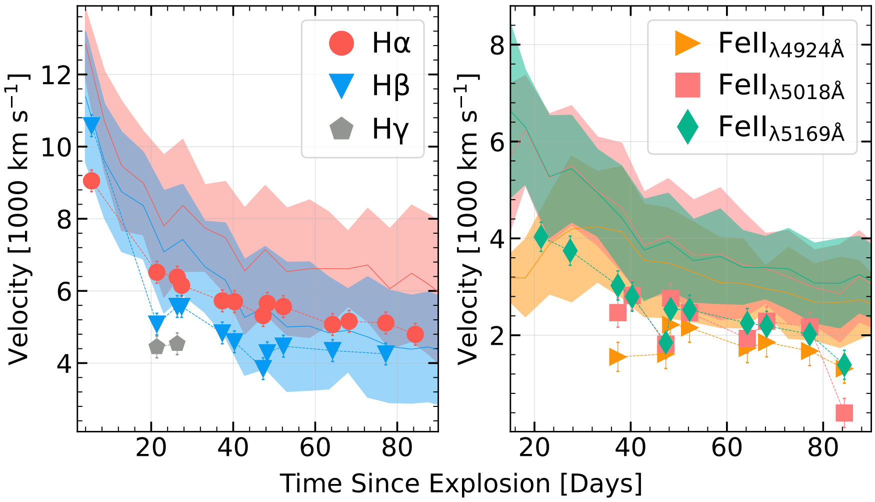

FIGURE 5.7: Expansion velocity evolution estimated from several prominent metallic features (including Balmer lines) observed in the spectra. The velocities have been compared with a large sample taken from Gutiérrez et al. (2017a). The shaded region gives the corresponding 1-σ scatter around the sample mean.

For the first epoch (+5.5 d), we could identify the absorption dips blueward of Hα and Hβ rest wavelengths corresponding to $\sim 9,100$ km s^{-1} and $\sim 10,600$ km s^{-1} line velocity respectively. At +21 d, apart from Balmer features, we could measure Fe II 5169 Å velocity. Up to +85 d, the velocities are measured, and their time evolution is shown in Figure 5.7. Around +40 d, which is proximal to the mid-plateau mark, we measure the Hα and Fe II 5169 Å velocities as $\sim 5,700$ km s^{-1} and $\sim 2,800$ km s^{-1}, respectively. The `SYNAPPS` modeling around similar phase gives a value which is between these two values (~ 3830 km s^{-1}). As ejecta evolves, expansion velocities keep decreasing until we can confidently resolve the absorption minimum. Towards the end of plateau period, around +75 d, we find the expansion velocities to be $\sim 2,000$ km s^{-1} from Fe lines and $\sim 5,100$ km s^{-1} from Hα. The `SYNAPPS` model spectrum around a similar phase gives $\sim 2,170$ km s^{-1} as the photospheric velocity, which closely follows the values obtained from the metallic features.

We further compare these velocities with the mean expansion velocities obtained from a larger sample of Type II SNe (Gutiérrez et al. 2017a). The mean velocities and 1-σ scatter in these are overplotted in Figure 5.7. We see that the SN 2021wvw velocities lie at the lower 1-σ end of the sample, implying that this is a slowly evolving ejecta. For metal lines, the velocities are even smaller than the lower 1-σ edge from the sample. Around mid-plateau, the difference between the mean velocities of the sample and SN 2021wvw observed velocities is $\sim 1,500$ km s^{-1}.

5.5 Plausible Progenitor

5.5.1 Semi-analytical models

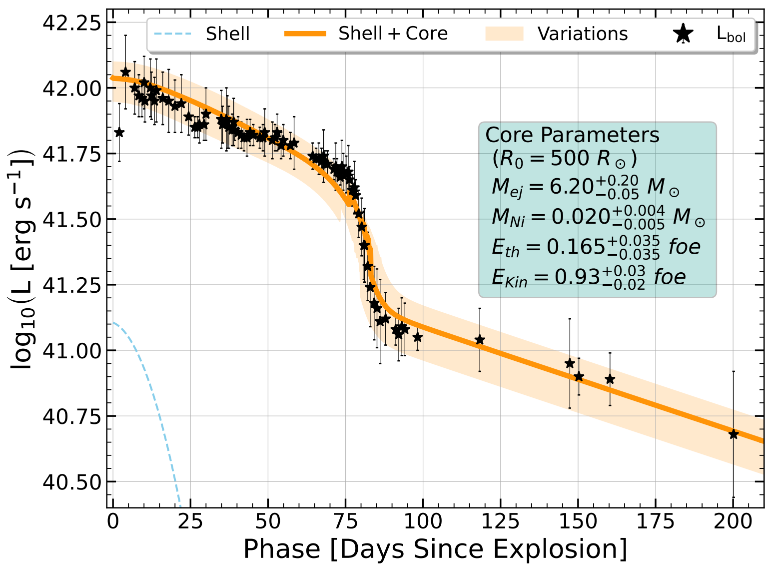

FIGURE 5.8: Semi-analytical fit for fixed radii of 500 $R_\odot$. The values provided in the inset are for the best-matching models.

We attempt to model the bolometric light curve of SN 2021wvw using a two-component progenitor model to roughly constrain a few parameters and motivate detailed modeling. There is a degeneracy among various parameters (Nagy & Vinkó 2016). In a similar analysis for two other short plateau SNe, SN 2018gj and SN 2020jfo, the progenitor radii did not match well with the results obtained using detailed hydrodynamical modeling (Chapter 3). So, in this work, we do not attempt to constrain the progenitor radius; instead, we fix the radius to multiple values beforehand. We take three cases: a fairly compact progenitor (300 $R_\odot$), a typical RSG radius (700 $R_\odot$), and a radius in between (500 $R_\odot$). We vary other parameters to get a light curve matching the observed light curve. Another caveat to consider is the lack of early UV and U-band data, which, in models, is usually governed by the shell part. This outer envelope could also act as proximal CSM around the RSG progenitor. Due to lack of data, no attempts were made to estimate CSM related parameters.. Instead, we fixed the shell values (to a negligible contribution) so that they do not affect the early light curve. Since the models are analytical, the errors are estimated by first obtaining a match to the observed light curve data, followed by varying the parameters to fit the upper and lower error bars associated with the observed light curve. The best parameters obtained for the fixed radii values are presented in Table 5.4. We could find that the model fits equally well with very similar parameters within error bars for each radii value. The case for 500 $R_\odot$ is presented in Figure 5.8.

Parameters M_{ej} and M_{Ni} do not vary much for the different radii considered here in the best-fit cases. The only considerable changes are in the energy values. From these models, we find the M_{ej} to be ~ 6.5 $M_\odot$, $M_{Ni} = 0.020 \pm 0.005$ $M_\odot$, and a total energy between 1.1 to 1.3 foe. The M_{ej} values for SN 2021wvw are similar to those obtained in other short plateau cases (for example, SN 2018gj, SN 2020jfo) but with lower explosion energy. The lower energy values are expected for SN 2021wvw, considering its sub-luminous nature. The total energy contribution from the core in the case of low-luminosity SN 2005cs is ~ 0.5 foe (Nagy & Vinkó 2016) with $M_{ej} = 8.0$ $M_\odot$. Considering the intermediate brightness of SN 2021wvw and a shorter plateau length, the estimated parameters are reasonably well constrained with tight bounds on the ^{56}Ni mass. Using these values as our reference point, we delve into more details about the progenitor and its origins using complete hydrodynamical modeling.

TABLE 5.4: Core parameters for best matching semi-analytical models

Parameters*	R=300 $M_\odot$	R=500 $M_\odot$	R=700 $M_\odot$
M_{ej} ($M_\odot$)	$6.50^{+0.20}_{-0.20}$	$6.20^{+0.20}_{-0.05}$	$6.60^{+0.10}_{-0.10}$
E_{th} (10^{51} erg)	$0.27^{+0.13}_{-0.05}$	$0.17^{+0.04}_{-0.04}$	$0.12^{+0.03}_{-0.02}$
E_{kin} (10^{51} erg)	$1.00^{+0.20}_{-0.12}$	$0.93^{+0.03}_{-0.02}$	$1.05^{+0.01}_{-0.01}$
M_{Ni} ($M_\odot$)	$0.020^{+0.004}_{-0.006}$	$0.020^{+0.004}_{-0.005}$	$0.020^{+0.004}_{-0.005}$

* $T_{rec} \approx 6000$ K, $A_g = 6.5 \times 10^{10}$ d^2

5.5.2 Hydrodynamical Modeling

In the previous section, we obtained rough estimates of the progenitor parameters. Unfortunately, we lack the nebular phase spectra, which could also be utilized to constrain the progenitor's C/O core mass. Initially, we looked for models representative of SN 2021wvw evolution in other previous studies. However, none of the grids of model light curves or individual models available in the literature could provide a short plateau length with low luminosity (Dessart et al. 2010; Eldridge et al. 2018; Moriya et al. 2023). For short-plateau SNe case, it has been noticed that a wide range of plausible RSG masses ranging from $8-12$ $M_\odot$ (Sollerman et al. 2021; Teja et al. 2022; Utrobin & Chugai 2024a) and reaching up to $20-30$ $M_\odot$ (Dessart et al. 2010; Hiramatsu et al. 2021a) could give rise to these SNe. Therefore, to ascertain the properties of the plausible progenitor of SN 2021wvw, its evolutionary scenario, mass loss before SN, explosion energy, and ejecta mass, we perform hydrodynamical modeling by evolving progenitors for both the lower and higher end of RSGs, allowing arbitrarily enhanced winds to mimic the impact of prior mass loss (because of binary interaction e.g. Laplace et al. 2021; Ercolino et al. 2024 or eruptive mass loss during the star's life e.g. Cheng et al. 2024) on H-rich ejecta mass.

We use the binding-energy fallback scheme introduced in Paxton et al. (2019); Goldberg et al. (2019) to quantify late-time fallback during shock propagation phase. In this work, we mainly focus on the following parameters in `MESA`: ZAMS mass, metallicity (Z), wind scaling factor (α_{wsf}), mixing length (α_{MLT}), E_{exp}, Ni mass, and explosive mixing via Duffell Rayleigh Taylor Instability (RTI) (Duffell 2016) 1D implementation by varying the ratio of RTI parameter $\eta_{R,e}$ and diffusion parameter η_R (Paxton et al. 2018). Before evolving a new set of progenitors, we first try the short-plateau models from previous works, namely SN 2020jfo and SN 2018gj. Exploding these with lower energies to match the plateau luminosities makes the plateau length longer, leaving these models infructuous. We then proceed to evolve additional models.

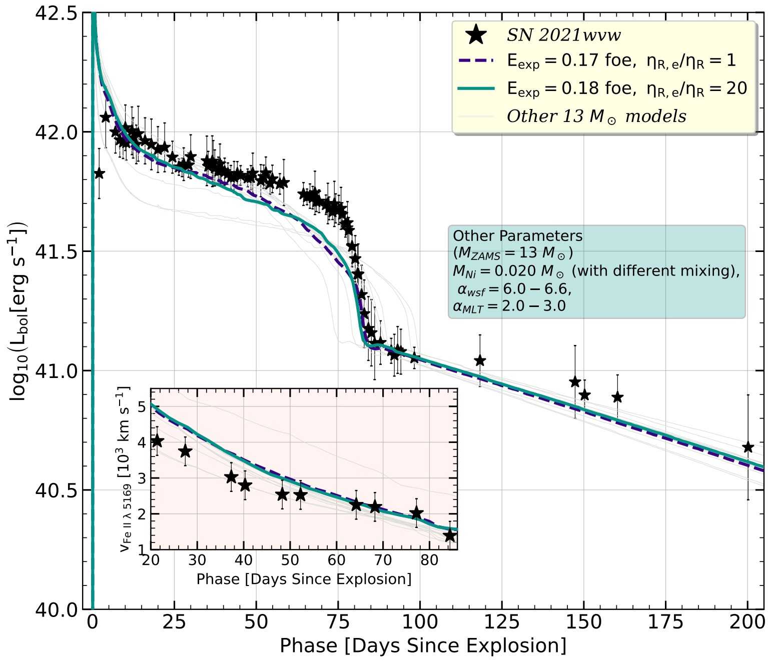

FIGURE 5.9: Observed and modeled bolometric evolution of SN 2021wvw for 13 $M_\odot$ ZAMS models with different sets of parameters. The inset in the left bottom shows the corresponding modeled and observed Fe II 5169 velocities.

Firstly, we evolve 13 $M_\odot$ ZAMS mass models with solar metallicity for the lower mass end. We change the wind scaling (α_{wsf}) in steps and explode each progenitor with various explosion energies until we match the plateau luminosity and its duration. Some of the resulting bolometric light curves and corresponding Fe II 5169 velocities are presented in Figure 5.9, which are compared with the observed values. As stated earlier, we do not attempt to match the initial 10-20

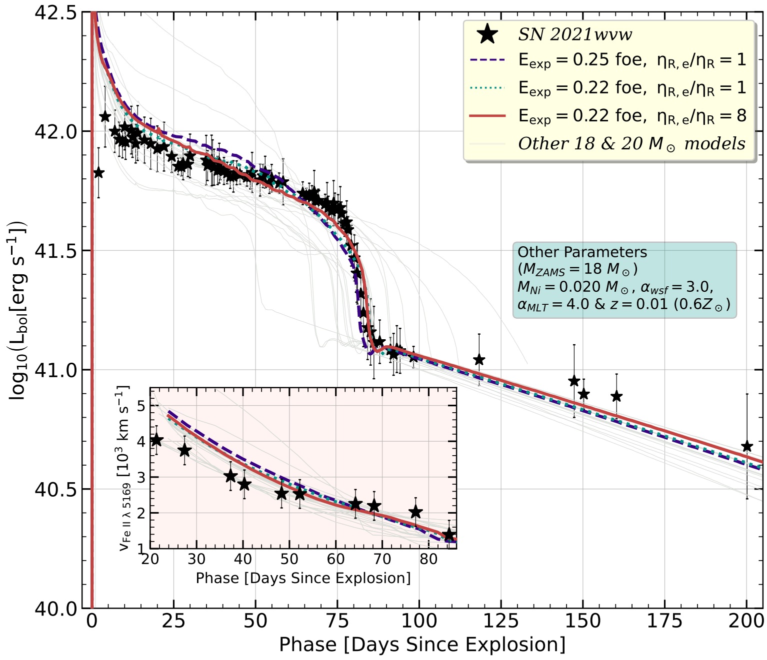

FIGURE 5.10: Observed and modeled bolometric evolution of SN 2021wvw for 18 M$_\odot$ ZAMS models with different sets of parameters. The solid red curve gives the best description of the model. The inset in the bottom left shows the corresponding modeled and observed Fe II 5169 velocities.

days of observations exactly with models due to lack of relevant observations. We find that the velocities, plateau luminosity, and nickel tail match reasonably well for low-mass RSG models. However, these models could not replicate the observed slow decline during the plateau period and the sharp plateau-to-tail phase transition. A sharp decline for SN 2005cs was obtained by increasing the strength of RTI mixing, as shown in (Paxton et al. 2018). As a more thoroughly mixed ejecta is expected to cause a steeper plateau drop due to a more even distribution of H throughout the entire ejecta, we also attempt to vary the RTI mixing via $\eta_{R,e}/\eta_R$, which directly changes the density structure as well as the abundance structure of the progenitor and the varied degree of mixing of species. Even for a value as high as $\eta_{R,e}/\eta_R = 20$, we only observe minor changes in the model light curves, but insignificant to satisfy the observed transition (refer Figure 5.9).

We proceed further to explore and explode the higher ZAMS mass models in the range 18-20 M$_\odot$ which plausibly lie on the upper mass limit for the directly detected progenitors of Type II SNe (Smartt et al. 2009; Davies & Beasor 2020b). The resulting models are shown in Figure 5.10 with colored lines representing the best match to the observed values (the remaining models are in gray color). Owing to their large progenitor radii ($\sim$ 1000 $R_\odot$) at the mixing length α_{MLT} = 2, the initial models were too bright to fit the plateau luminosities even with very low explosion energies. Hence, we evolved slightly compact progenitors to match the plateau decline and luminosities by varying the α_{MLT} and metallicity z. For $\alpha_{\mathrm{MLT}} = 4.0$ & z = $0.6Z_\odot$, we could obtain a considerable match with the observed light curves for explosion energies of $\approx$ 0.22 to 0.25 foe with M_{ej} = 4.7 $M_\odot$. This value of α_{MLT} is on the higher end of typically-considered values (see, e.g. Goldberg & Bildsten 2020), and is consistent with 3D simulations of convective RSG envelopes (Goldberg et al. 2022). The transition to the end of the plateau obtained for these models is inherently sharp, which is further matched well by varying the RTI parameter. We could replicate the observed transition profile for $\eta_{R,e}/\eta_R = 8$. ^{56}Ni mass required to fit the observations is similar to earlier estimates with $M_{\mathrm{Ni}} \approx 0.020$ $M_\odot$. The ejecta mass and explosion energies obtained through hydrodynamical modeling are lower than those obtained from the semi-analytical approach. However, such discrepancies between semi-analytic and detailed modeling are fairly common (see for example, Szalai et al. (2019); Teja et al. (2023a)). This could be due to various simplified approximations in the semi-analytical work, including the assumed density and velocity profile of the ejecta, as well as the assumption of a simple two-zone ejecta with a grey opacity treatment independent of metallicity (Nagy & Vinkó 2016).

We show the structural differences in the various models considering the effect of the RTI parameter in Figure 5.11 using a few species out of the 22 species network used in the modeling. Solid lines represent the mass fraction just after we inject the explosion energy. The other two dashed lines show the final ejecta structure before the shock breakout (SB) for different $\eta_{R,e}/\eta_R$ values. The figure shows that the higher η ratio weakens the RTI mixing with increasing species concentration

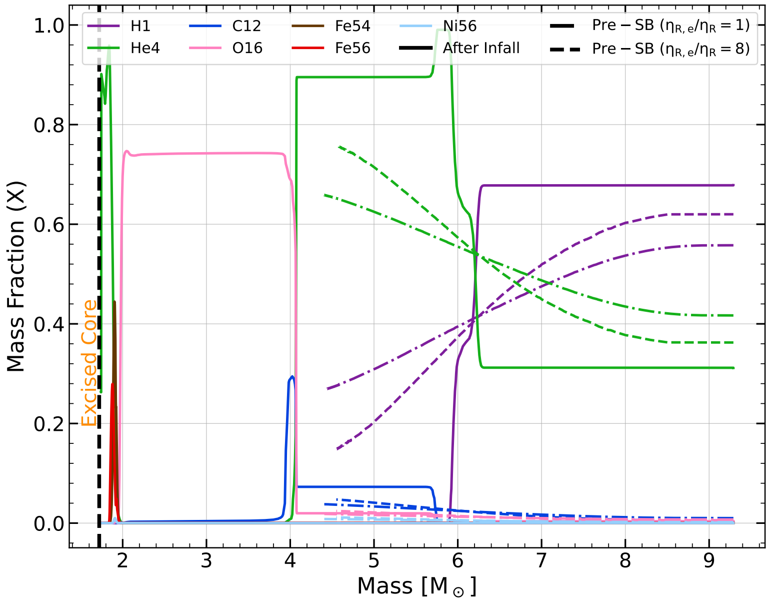

FIGURE 5.11: MESA+STELLA structures for different cases of 18 M$_\odot$ ZAMS models with different RTI parameter. A few species out of the 22 species network used in the modeling are shown here. Solid lines present the mass fraction just after we inject the explosion energy. The other two dashed lines show the final ejecta structure before the shock breakout (SB) for different $\eta_{R,e}/\eta_R$ values. The final ejecta profiles suffer from significant fallback during the shock-propagation phase, which we discuss in Section 5.6.2.

towards the inner layers. At the boundary interface, the gradient is steeper for a higher η ratio. Due to the small explosion energies, the models experience significant fallback during the shock-propagation phase as reverse shocks off the steep density gradients at various compositional boundaries sweep marginally-unbound material back onto the inner boundary. This is also evident in Figure 5.11, where the inner boundary of the final pre-SB structure is at a significantly higher mass co-ordinate ($\approx$ 4.5 M$_\odot$) than what was initially excised as a core remnant mass ($\approx$ 1.7 M$_\odot$). The detailed fallback treatment in `MESA` is described in Goldberg et al. (2019). Due to the relatively low core binding energy in the suite of 13M$_\odot$ progenitors, we find only 0.2 to 0.4 M$_\odot$ of material is falling onto the core, whereas it is much larger for high mass scenarios reaching up to 2-3 M$_\odot$ (owing to the larger core binding energy of the high-mass progenitors). Approximately 1 M$_\odot$ of fallback was also present in the SN 2005cs models (Paxton et al. 2018) even for an initial low mass progenitor (13 M$_\odot$).

5.6 Discussion

5.6.1 Scaling relation degeneracies and model differences for short-plateau SNe

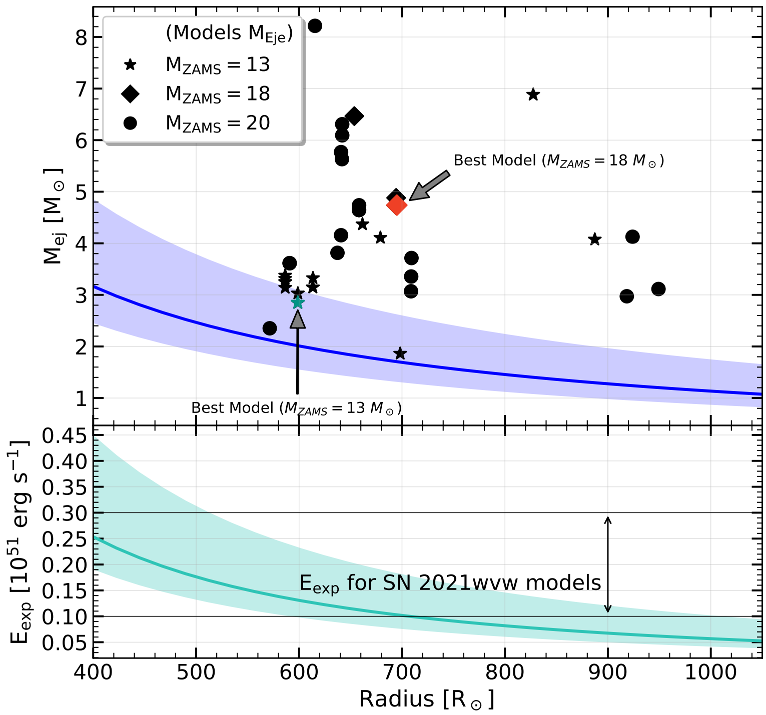

FIGURE 5.12: Plausible E_{exp} and M_{ej} ranges plotted for the scaling relations from Goldberg et al. (2019). The scatter points represent the ejecta masses obtained for various models utilized in this work. The energy values for all the evolved models are between 0.1 to 0.3 foe. The shaded regions include the values obtained considering the errors in the observables.

Many works have highlighted the non-uniqueness of hydrodynamical modeling of SN-IIP lightcurves and plateau velocities (Martinez & Bersten 2019; Dessart & Hillier 2019; Goldberg et al. 2019; Goldberg & Bildsten 2020). Semi-analytical scalings between luminosity and plateau duration with progenitor properties thus entail families of explosions which may produce qualitatively similar lightcurves, with higher M_{ej} and E_{exp} at lower R being comparable to smaller M_{ej} and E_{exp} at higher R (Popov 1993; Kasen & Woosley 2009; Sukhbold et al. 2016; Goldberg et al. 2019; Goldberg & Bildsten 2020). We compare a selection of our `MESA` models (from Section 5.5) to the scaling relations obtained by Goldberg et al. (2019) to estimate a comprehensive set of ejecta mass and explosion energies, shown in Fig 5.12. We note that these scaling relations were calibrated to higher Ni masses and more typical (i.e., less-stripped) events. We do not take these scaling relations as the absolute truth in this regime, but rather, show them as representative of the degeneracies characteristic of SNe IIP (Goldberg et al. 2019; Dessart & Hillier 2019; Goldberg & Bildsten 2020), and use them to motivate and contextualize our hydrodynamical modeling efforts. For radii between 400-1000 $R_{\odot}$, we find the explosion energy varies from $\approx 2.5 \times 10^{50}$ erg s^{-1} to much lower 5×10^{49} erg s^{-1}.

For the given radii range, the predicted ejecta masses are less than 3 $M_{\odot}$. The modeled ejecta masses lie somewhat above the values obtained utilizing scaling relations for all the progenitors, possibly due to the smaller ratio of core mass to envelope mass in the sample used to calibrate the scalings compared to the models presented here. The explosion energy provides good matching values. These relations tend to give similar values obtained by semi-analytical modeling for the much more compact radii (< 400 $R_{\odot}$), also seen in case of SN 2018gj.

In both the low and high mass cases for SN 2021wvw, we find apparent differences in the early phase (< 40 d) modeled and observed velocities. The differences are significant in the 13 $M_{\odot}$ models. This tension is further increased in low-mass models when we try to match the observed plateau luminosity by increasing their progenitor radius. In other modeling works, it has been noted that the `MESA+STELLA` models provide an excellent velocity match with typical Type IIP SNe observed velocities from early phase until photospheric phase, which is not the case for the short plateau events.

5.6.2 Fallback during the shock propagation phase

In a majority of the modeled sub-luminous SNe that are the result of low-energy explosions, whether they come from low to moderate mass (8-18 $M_{\odot}$) RSGs (Chugai & Utrobin 2000; Pumo et al. 2017; Lisakov et al. 2018; Valerin et al. 2022) or high-mass RSG explosions ($>$ 20 $M_{\odot}$ Zampieri et al. 2003), there are discussions related to fallback material onto the core. Namely, when E_{Exp} is positive but only comparable in magnitude to the total binding energy of the progenitor star, late-time fallback from reverse shocks during the pre-SBO phase may sweep marginally unbound material back onto the central remnant (Colgate see, e.g. 1971; Perna et al. see, e.g. 2014. In some cases, the central remnant has been speculated to turn into a black hole post-accretion, but with no observational evidence (Zampieri et al. 2003). In other cases, very late-time enhanced luminosity is associated with the accretion of material to the central remnant (Gutiérrez et al. 2020). For many of these objects, the ^{56}Ni mass obtained is an order of magnitude or even much lesser than the ^{56}Ni mass obtained for SN 2021wvw. Further, the velocity obtained for these cases is much less than the usual Type II expansion velocities.

Interestingly, the short plateau and a sharp transition from plateau to tail phase are remarkable features for SN 2021wvw, which are unusual for low to intermediate luminosity SNe. Given the low inferred E_{exp}, the short plateau length requires a low H-rich ejecta mass for both low-mass and high-mass progenitors, which could be the result of a higher mass loss during evolution. Such high mass loss might be consistent with the notion that the sharp drop from the plateau is actually *excess* luminosity during the plateau drop driven by late-time interaction with previously ejected material. But, as observed in the spectral evolution (Section 5.4), there are no discernible CSM signatures in the spectra. On the other hand, if there is an actual fallback (as occurs during hydrodynamical modeling in Section 5.5) of the inner layers onto the core, the inward receding photosphere may reach earlier to the base of the H-rich ejecta, giving a short plateau with a sharp transition.

This may manifest in late-time signatures of accretion if such accretion persists (see, e.g. Dexter & Kasen 2013; Moriya et al. 2019). However, the lack of late time light curve (beyond 300 d) and spectral information restricts us from saying anything about further observational signatures of fallback accretion.

While the short plateau and its sharp transition could be due to fallback, further discussion of the physical consequences of this fallback and ascertaining its influence on the sharp transition from plateau requires further detailed modeling. We nonetheless encourage follow-up observations searching for any signatures of continued accretion or very late-time circumstellar interaction from this unique event.

5.6.3 SN 2021wvw in the Type II domain

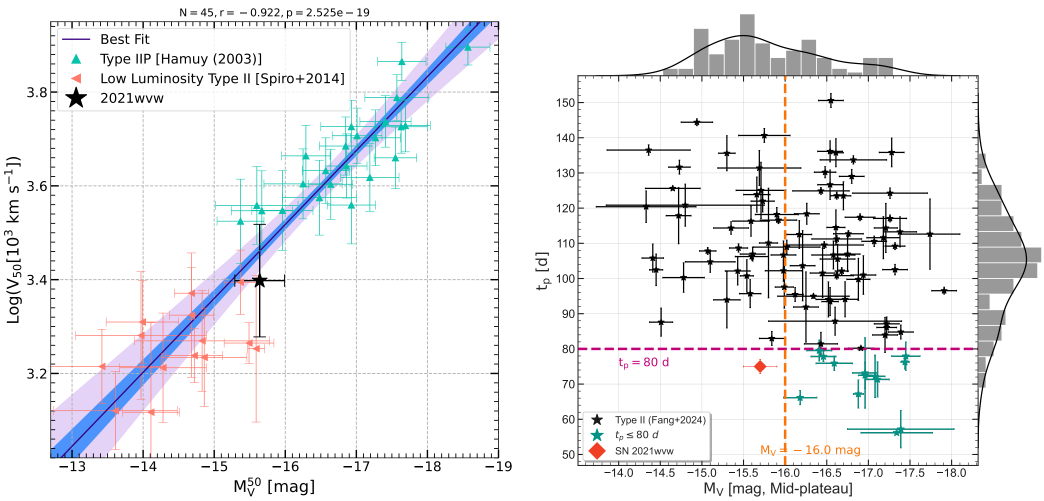

FIGURE 5.13: *Left:* Correlation between plateau brightness at 50 d, M_V^{50} and expansion velocities at 50 d after explosion. *Right:* Mid-plateau brightness, M_V versus plateau duration (t_p) for a large sample including a wide range of Type II SNe obtained from Fang et al. (2024).

We compare SN 2021wvw with a large sample of normal Type IIP SNe (Hamuy 2003) and low-luminosity Type II SNe (Spiro et al. 2014) as shown in Fig 5.13.

SN 2021wvw fits well in the established tight correlation between expansion velocity and luminosity for Type II SNe at 50 d. Moreover, we find it bifurcating the two populations in both luminosity and expansion velocities. In this space, it is a bridging object between the normal Type IIP SNe and under luminous ones. Apart from this expected behavior, SN 2021wvw is unique due to its short plateau and low luminosity. Considering existing works (e.g., refer Fig 17 in Valenti et al. 2016) showing a correlation between plateau luminosity and plateau duration, SN 2021wvw clearly is an outlier. Even for a larger sample for all Type II subclasses (Fang et al. 2024), SN 2021wvw stands apart, as is evident in the right panel of Fig 5.13. SN 2021wvw has the shortest plateau among all the intermediate and low-luminosity SNe. In contrast, it is the faintest SN among all the short plateau subclass of Type IIP SNe presented in the sample and, presumably, in the literature.

5.7 Summary

This work provides photometric and spectroscopic observations of an under-luminous, short-plateau supernova SN 2021wvw. We have presented detailed light curves and spectral comparisons with other short-plateau SNe. The spectra and light cueves are modeled to obtain the physical parameters of the explosion. Some of the key findings are summarized as follows:

- SN 2021wvw is fainter (at $M_r \approx -16$ mag) compared with other short-plateau SNe and shows the shortest plateau (≈ 75 d) among the intermediate luminosity SNe, with a sharp transition period of ~ 10 d from plateau to tail phase.
- The ejecta expansion velocities are slowly evolving and lie below the 1-σ lower bound in comparison to the Type II SNe sample.

- Early spectra show fewer metallic features as compared to other short-plateau and sub-luminous SNe. The lack of metal features is evident till the last spectrum (+95 d) presented here.

- Detailed `MESA+STELLA` hydrodynamical modeling disfavors the lower mass RSG models and is more inclined towards the higher mass end of RSGs. A compact progenitor with 18 $M_\odot$ ZAMS mass, a radius of 650-700 $R_\odot$ and a final H-rich ejecta mass of $\approx$ 5 $M_\odot$ is seen to provide a good fit to the observed properties.

- Modeling also suggests a low explosion energy ($\approx 0.23 \times 10^{51}$erg) with an estimated 0.020 $M_\odot$ of radioactive ^{56}Ni.

Chapter 6

Short-plateau SNe: A separate class?

We have studied several short-plateau Type II SNe, which were almost non-existent in previous studies. This half-decade has turned out to be crucial for studying these short-plateau events. In the earlier studies, these SNe only cropped up in a handful of modeling works without a detailed understanding. Even a significant number of analytical relations that are used to estimate various Type II SNe properties are not able to provide satisfactory results in the case of short-plateau events. In the preceding Chapters, we have noticed that apart from their common characteristic of a shorter plateau in the light curves, they exhibit diverse observational properties. With the growing number of these events fueled by other detailed works, the diversity among these is ever-increasing. Hence, apart from their short plateau as a distinctive property, we find diversity similar to typical Type II SNe based on their other properties, such as spectra and velocity evolution. In this Chapter, we try to understand these differences and study these SNe as a collective object type. We further discuss rising inhomogeneities amidst these SNe and where these lie in a large Type II sample space.

6.1 Short-plateau SNe within Type II Class

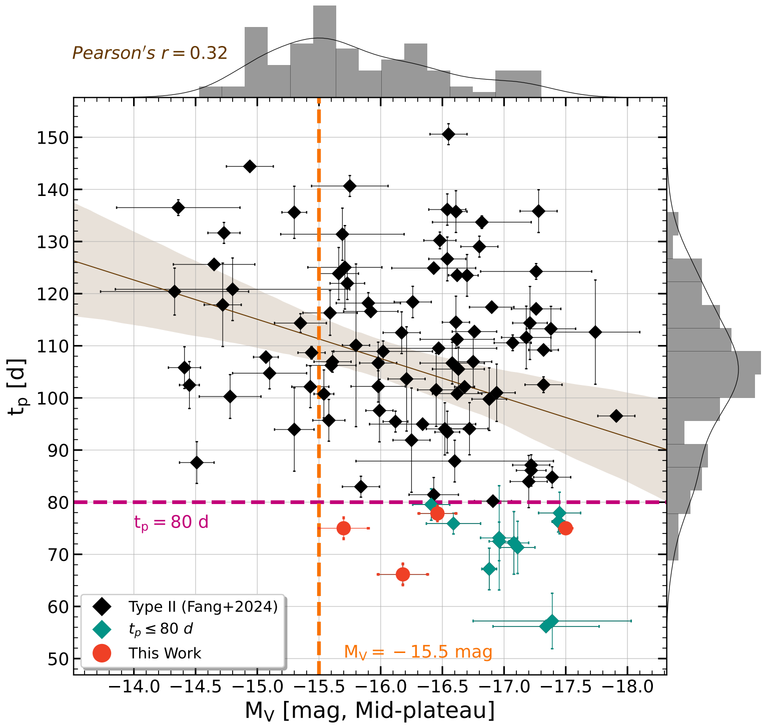

FIGURE 6.1: Plot showing mid-plateau absolute V-band magnitude (M_V) vs the plateau duration (t_p). The sample points are obtained from Fang et al. (2024).

Several recent studies have focused on individual short plateau objects. The short plateau objects studied so far are not limited to luminous short-plateau events but show diverse properties. It ranges from very fast declining (s2 > 2 mag 100 d^{-1}) plateaus to gradually evolving plateaus. There are apparent differences in their brightness at the peak and around mid-plateau, with the latter varying from −15.5 mag to −18 mag in V-band. Recent work by Fang et al. (2024) performed detailed light curve modeling for a wide range of SNe in Type II class utilizing mid-plateau (instead of widely used definitions at t = 50 d) statistics to find various analytical relations. It thus incorporates the influence of short-plateau SNe in a large sample as well. Figure 6.1 shows a plot of the plateau duration and mid-plateau brightness in the V-band for the SNe sample from Fang et al. (2024) and SNe studied in this work. For an overall sample, a weak correlation (Pearson′s r = 0.32, and p = 0.001) is established with increasing brightness leading to shorter plateaus when the short plateau SNe are included in the sample. However, the scatter in the sample makes it insignificant. Even if we consider these two populations as separate classes, we do not find any significant correlation in either of the populations. The short-plateau SNe have $\mathrm{Pearson's\ r} = 0.29,\ \&\ \mathrm{p-value} = 0.32$ while the other Type II SNe excluding short-plateaus have $\mathrm{r} = 0.17,\ \mathrm{and\ p-value} = 0.12.$

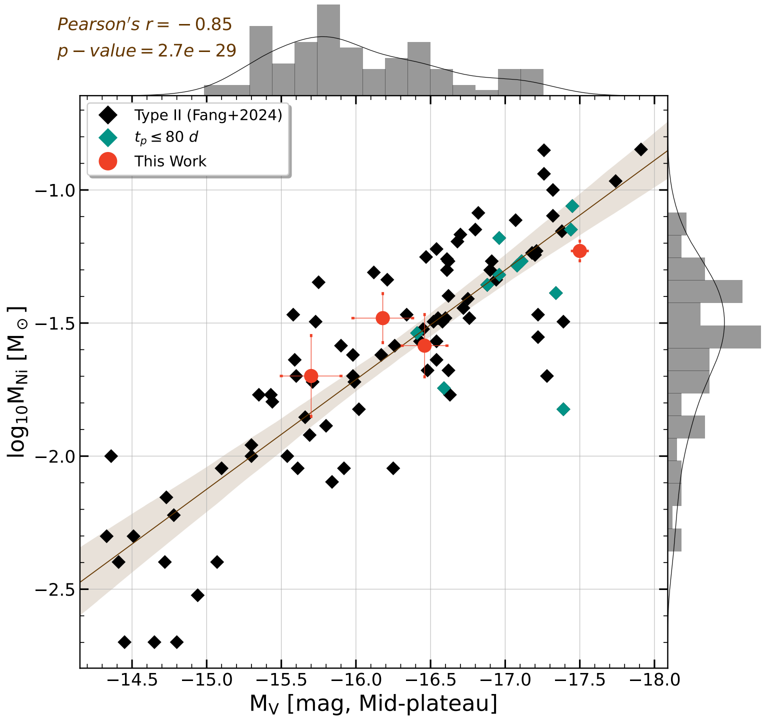

FIGURE 6.2: Position of short-plateau Type II SNe shown with other large Type II sample closely following the already established tight correlation between M_{Ni} and mid-plateau luminosity.

It has been well-established that ^{56}Ni mass correlates strongly with the plateau brightness (Hamuy 2003). This is also shown in Figure 6.2, for the sample of SNe from Fang et al. (2024) and this study. A strong linear correlation is obtained with $\mathrm{Pearson's\ r} = -0.85\ \&$ a corresponding $\mathrm{p-value} = 2.7\mathrm{e}-29$ (the negative r value is due to the absolute values being negative). It implies that the brighter the mid-plateau luminosity, the higher the ^{56}Ni obtained. The short-plateau events spread evenly in this sample space. However, if we try to find correlation in short-plateau events only, we find it weak with Pearson‘s $\mathrm{r} = -0.56$ and a corresponding p − value = 0.03. This could possibly be due to a small sample size as of now. Nevertheless, short-plateau events do not deviate significantly when studied with a large Type II SNe sample size.

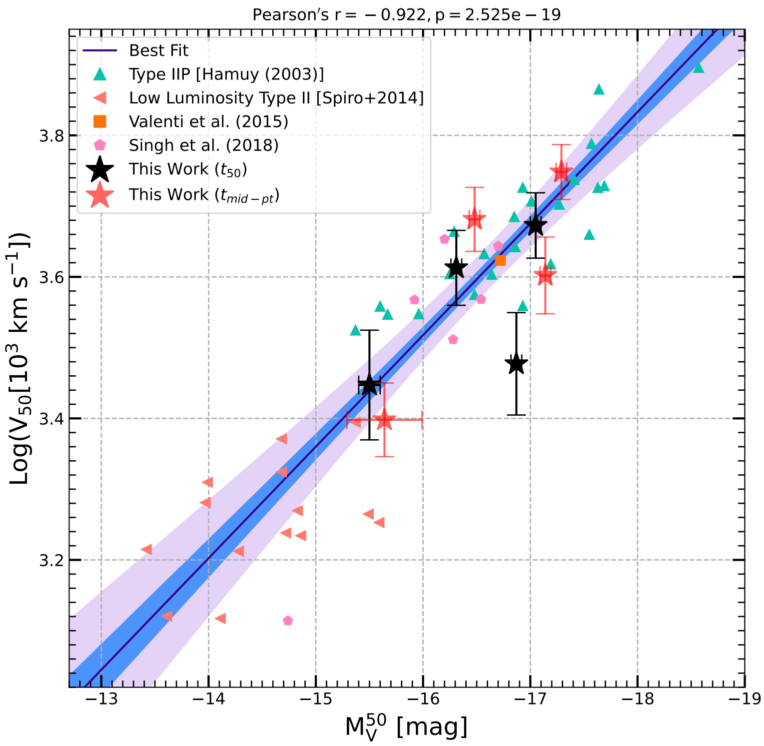

FIGURE 6.3: Position of short-plateau Type II SNe in the well-established correlation between plateau brightness and expansion velocity (estimated from Fe II 5018) at 50 days. The red 'star' markers show the values obtained by taking measurements at the mid-plateau epoch rather than at 50 days.

Another well-defined correlation between expansion velocity and plateau brightness at 50 days or rather classical mid-plateau epoch is presented in Figure 6.3. The majority of SNe studied in this work closely follow this correlation. However, there are outliers to this relation, plausibly due to the measurement epoch defined at the midpoint of typical plateau lengths (100 d). If we ease out this restriction and define measurements at the actual mid-point of the respective plateau lengths, we get an improvement in the outlier case while leaving others more or less still following the relation (Figure 6.3). As seen in Fang et al. (2024) and here as well, with the increasing number of varied plateau lengths, it is more imperative to

TABLE 6.1: Some of the estimated parameters of well-studied short-plateau Type II SNe from literature and this work. *(The values are quoted as mentioned in the respective works.)*

SN ⇓	**Progenitor**		**Other Parameters**		**Ref.**
	M_{ZAMS} ($M_\odot$)	**Methodology**	^{56}Ni Mass ($M_\odot$)	M_{ejecta} ($M_\odot$)	
2006Y	$\sim 18-22$	Hydrodynamical	$\sim 0.06-0.09$	7.1	1
	$10.28^{+0.72}_{-0.20}$	Hydrodynamical+MCMC	0.075 ± 0.004	$5.49^{+0.27}_{-0.62}$	2
2006ai	$\sim 18-22$	Hydrodynamical	0.062 ± 0.002	$7.1-8.5$	1
	$10.60^{+0.68}_{-0.42}$	Hydrodynamical+MCMC	0.047 ± 0.005	$7.36^{+0.09}_{-0.04}$	2
2016egz	$\sim 18-22$	Hydrodynamical+Nebular	0.090 ± 0.005	$7.1-8.5$	1
2017ahn	$\sim 15-25$	Numerical Modeling	0.041 ± 0.006	≤ 10	3
2018gj	≤ 13	Hydrodynamical+Nebular	0.026 ± 0.007		‡
	~ 29	Hydrodynamical	0.031 ± 0.005	≈ 23	4
2018hfm	–	–	< 0.015	~ 1.3	5
2020jfo	≤ 12	Hydrodynamical+Nebular	0.033 ± 0.006	~ 5	‡
	12 or less	Nebular + Direct	~ 0.025	~ 5	6
	$12-15$	Semi-Anaytical+Nebular	0.03 ± 0.01	$13.6^{+0.2}_{-2.5}$	7
	$8-12$	Nebular+Direct	0.018 ± 0.007	–	8
	≈ 8	Hydrodynamical	$\sim$0.013	~ 6	9
2021wvw	≥ 18	Hydrodynamical	0.020 ± 0.006	~ 4.7	‡
2023ixf	~ 10	Hydrodynamical	≈ 0.06	–	‡
	~ 10	Hydrodynamical	$\sim 0.04-0.06$	–	10
	$12-15$	Hydrodynamical	≈ 0.05		11
	$10-20$	Direct	–	–	12

‡**This Work**, (1) Hiramatsu et al. (2021a), (2) Martinez et al. (2022), (3) Tartaglia et al. (2021), (4) Utrobin & Chugai (2024b), (5) Zhang et al. (2022), (6) Sollerman et al. (2021), Ailawadhi et al. (2023), (7) Ailawadhi et al. (2023), (8) Kilpatrick et al. (2023b), (9) Utrobin & Chugai (2024a), (10) Moriya & Singh (2024), (11) Bersten et al. (2024), and (12) Multiple Works (See Figure 6.5)

define observable at the mid-point plateau epochs rather than at a fixed epoch of 50 d.

6.2 Progenitors

Ultimately, we turn our attention toward one of the most sought-after questions in terms of any SNe, which is about their origins and possible progenitors, as discussed in this work, where multiple attempts have been made to ascertain the progenitors of these short-plateau events utilizing several methods. Apart from this work, several other attempts have been made to constrain the progenitor mass of these events. There are a handful of other short plateau events for which explosion parameters and progenitor properties have been estimated; they are listed in Table 6.1. It shows the estimated ZAMS for the progenitors of a few short-plateau events. Also provided in the same table are the estimates for other explosion parameters, such as ejecta mass (M_{ej}) and ^{56}Ni mass.

The properties of the progenitor stars of the short plateau supernovae are highly debated, and there is no consensus about their mass. In most of the cases, both the massive ($\geq 18\ M_{\odot}$) and less massive ($\leq 15\ M_{\odot}$) RSG stars are proposed as their progenitors. From Table 6.1, it can be seen that, except for SN 2016egz and SN 2021wvw, where a high mass RSG is preferred, in all other cases, there is at least one study for each SNe which attributes their progenitor to be a low-mass ($\leq 15\ M_{\odot}$) RSG star. With the RSG progenitors, to obtain short plateau supernovae a significant amount of hydrogen envelope needs to be removed. This is possible only if the mass loss rate in these progenitors is significantly higher (maybe 2 - 3 orders of magnitude) than the mass loss rate observed for RSG stars (Mauerhan et al. 2013). The exact mass loss mechanism in these progenitors is not well understood, both theoretically and observationally. However, there is evidence of elevated mass loss before the explosion in Type IIP SNe, the consequences of which have been observed in terms of early flash features (Bruch et al. 2023). Short-plateau events are no exception to that, where we have seen signatures of early CSM interaction in light curves and flash features in their spectra. So far, there is no evidence of elevated mass loss during the RSG phase or main sequence until the companion scenario is evoked. However, progenitors in a binary scenario are primarily associated with more stripped Type IIb, Type Ib/c SNe.

Nevertheless, the lower ejecta mass estimated for most of the short plateau SNe studied here indicate towards stripped envelope which could result from the binary interaction of the progenitor. While modeling the short plateau objects, various schemes are employed to obtain the required mass loss rate during the evolution of the progenitor. In addition to single RSGs, population synthesis works involving a range of binaries have also resulted in short-plateau SNe (Eldridge et al. 2018).

Additionally, the elevated mass loss years to decades before SN has been predicted in many cases. Although, the physical reason behind this is not yet fully established. Several works mention eruptive mass loss due to giant eruptions, pulsations, and super Eddington winds (Smith (2014) and references therein). It has been observed in many cases that the typical matter density close to progenitor follows r^{-2} dependence, but there are cases where the density profile is different and requires different treatment of wind mass-loss (Moriya et al. 2023). Another important aspect that influences the mass loss is metallicity, depending on the temperature and phase during evolution, mass loss rate through steady wind can vary significantly (Smith 2014).

The critical question about the properties of the progenitors of these supernovae is still unanswered. Various methods have been employed to estimate the progenitor properties of short plateau SNe. For estimating their progenitor mass, direct imaging, nebular spectroscopy, detailed hydrodynamical modeling, etc., have led to different progenitor masses for even a single object. However, in most of the cases, it is seen that the mass of the ejecta is less than 8 $M_{\odot}$ (except for SN 2018gj, in which Utrobin & Chugai (2024b) have suggested higher mass). Currently, the only SN that the community agrees on its progenitor is SN 2020jfo, which originated from a low mass RSG. Otherwise, the scenario is somewhat mixed for all other

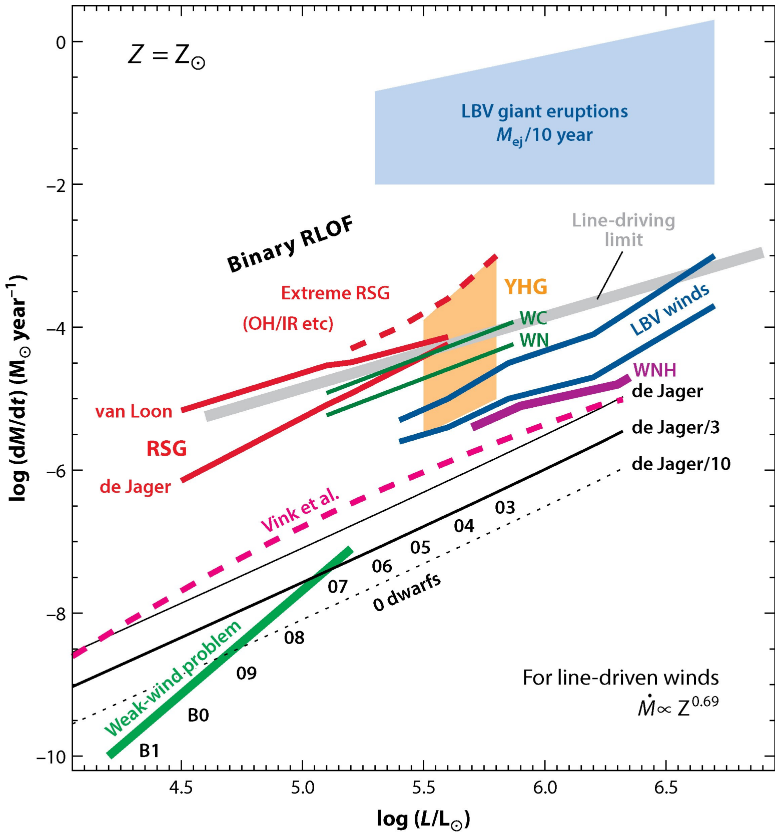

FIGURE 6.4: Various wind mass-loss schemes used in different models are shown with observational ranges for various stellar types. For typical RSGs the observational wind mass-loss limits are $< 10^{-4}$ $M_\odot$ yr^{-1}. [*Source:* *Smith (2014) and references therein*]

objects marred by the lack of direct detection. Even for SN 2023ixf, which had clear direct detection in multiple bands, the progenitor mass is still filled with uncertainties (see Figure 6.5). This is plausibly due to several techniques employed to get final photometry from archival images. Further, the different stellar tracks utilized in estimating the progenitor's mass could also lead to differences in the calculations. 1-D stellar tracks have their own caveats and shortcomings as well.

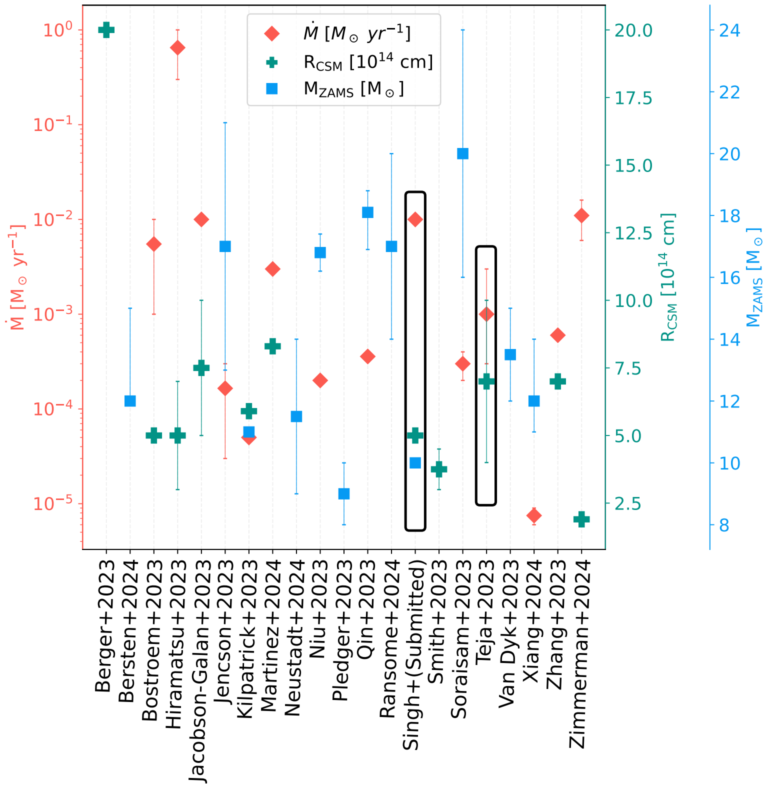

FIGURE 6.5: Values for CSM parameters and progenitor mass obtained from various works on SN 2023ixf.

6.3 A Separate Class ?

Studies of short-plateau Type IIP events based on detailed, long-term, multiwavelength monitoring, as presented in this study, have revealed many new insights about these SNe. It is now evident that the plateau phase period depends not only on the mass of the hydrogen envelope but also on many other factors. Other crucial factors dictating the plateau length could be the explosion energy, the amount of ^{56}Ni synthesized in the SN, the presence of a binary component, and other factors playing a role during evolution, such as rotation and environment. Consequently, we have obtained a range of ejecta masses, progenitors masses, expansion velocities, explosion energies, synthesized nickles masses, etc., for these short-plateau Type II SNe.

So far, with a wide range of progenitor masses, ejecta masses, luminosities, nickel mass, and other observable, it is difficult to conclude that these SNe form a separate class of supernovae. They are more likely a consequence of a more comprehensive Type II class but with a rare occurrence. This rarity plausibly arises from a combination of several factors, including progenitor evolution, environment, and others that dictate the observed properties. More detailed studies are required to deepen the understanding of these SNe further.

Chapter 7

Summary and Future Work

7.1 Summary

Type II-P supernovae were canonically established with a typical plateau length of 100 d, which is still a kind of 'magic number' for most of these SNe observed in nature. However, time and again, theoretical works have shown a great diversity in plateau lengths ranging from tens of days to more than 150 d. Yet, the short-plateau SNe were missing from the observational scenario. Through this work, we have presented detailed studies on four such rare short-plateau SNe, namely SN 2018gj, SN 2020jfo, SN 2021wvw, and the decadal SN 2023ixf. The plateau lengths of these SNe vary from 65 d to 75 d. We have attempted to constrain various observational and physical properties associated with these events. Before we summarize various key aspects of this work, a chapter-wise summary is presented as follows:

- Chapter 1 describes the stellar pathways focusing on various phases in the massive star evolution until they end up as SNe. A brief overview of different types of SNe is also presented, along with their classification. A significant part of this Chapter covers Type II SNe, their diversity, powering mechanisms, and progenitors. The short-plateau SNe have also been introduced, and our understanding of them is also provided.

- Chapter 2 briefly describes various multiwavelength observational facilities along with their key instruments utilized in this work. Some of the data processing techniques related to the data obtained using these instruments are also mentioned. It further gives the methodology, various analysis tools, and techniques such as analytical tools, empirical relations, hydrodynamical modeling, and others that are required to understand SNe and estimate their several explosion parameters and progenitor properties and finally to understand the supernovae.

- Chapters 3, 4, and 5 study various short-plateau supernovae in detail. These SNe comes with different traits and are subsequently put under various subcategories namely SN 2018gj and SN 2020jfo in *'ordinary'* short-plateau SNe, SN 2023ixf in *'fast-declining'* short-plateau SNe and SN 2021wvw in *'faint'* short-plateau SNe. These Chapters provide detailed multiwavelength observations, covering far-UV to near-IR in some cases. A thorough analysis is done to estimate various observables such as plateau duration, peak magnitudes, decline rates, etc., and several other explosion parameters. The progenitor characteristics and explosion parameters are deduced using semi-analytical and hydrodynamical modeling. A comprehensive list of some of the key parameters obtained for all the SNe studied is presented in Table 7.1.

- Chapter 6 attempts to understand the short-plateau SNe as a class and tries to answer whether they really form a separate class utilizing various well-established correlations. It also discusses the plausible progenitor scenario for short-plateau SNe and the challenges ahead.

TABLE 7.1: Summary of various observed/estimated parameters for all short-plateau Type II SNe studied in this work.

SN ⇓	**Various Observed/Estimated Parameters**						
	M_{ZAMS} ($M_{\odot}$)	t_p (days)	^{56}Ni Mass ($M_{\odot}$)	M_{ejecta} ($M_{\odot}$)	$M_V^{\ddagger}$ (mag)	E_{exp} (10^{51} erg	CSM Sign
2018gj	≤ 13	70 ± 3	0.026 ± 0.007	~ 6.9	-16.48 ± 0.09	$\sim$0.4	✓
2020jfo	≤ 12	63 ± 7	0.033 ± 0.006	~ 5	-17.14 ± 0.06	$0.20 - 0.40$	✓
2021wvw	≥ 18	~ 75	0.020 ± 0.006	~ 4.7	$- -15.64 \pm 0.35$	$0.22 - 0.25$	✗
2023ixf	~ 10	~ 75	≈ 0.06	$7 - 8$	-17.29 ± 0.05	$\gtrsim 2.0$	✓

‡Estimation at mid-plateau epoch

As has been observed for the Type II class in general, these SNe come with great diversity in their properties. The significant observational differences are in their peak and plateau brightness, decline rates, absorption depths in spectral features, and expansion velocities. These differences are also reflected in various estimated properties such as synthesized radioactive Nickel mass, ejecta mass, progenitor mass, and explosion energy. Consequently, the short-plateau SNe follows similar diversity in their properties. This could easily be deduced even from a limited sample. It was observed in this work that short-plateau SNe have diverse plateau and peak brightness, with the faintest to date being SN 2021wvw and the brightest being SN 2023ixf. Their expansion velocities are shown to deviate at least by 1-σ, both lower and higher than the mean expansion velocities of a large Type II sample. The synthesized ^{56}Ni masses also show great diversity, although correlating strongly with the intrinsic brightnesses of the SNe.

The progenitors of short plateau SNe were thought to be high-mass red supergiant stars, going through an evolutionary process with standard mass loss prescription. However, through this work we have clearly established that it is not true. Using various analytical and hydrodynamical modeling, it is shown that these SNe could originate from RSG progenitor with mass ranging from 8 $M_{\odot}$ to 18 $M_{\odot}$, even a much higher mass limit considering other recent works. Although no straightforward progenitor mass, whether low or high, could be genuinely associated with these SNe, the ejecta mass obtained for all SNe is well constrained.

Other than the plateau length shorter than the Type IIP supernovae, each SN studied here showed some remarkable and rare aspects. For example, the emission peak of the line profiles was blue-shifted till the very late nebular phase in SN 2018gj. We found the strong signature of stable ^{58}Ni in the nebular phase spectral evolution of SN 2020jfo. A very sharp drop during the transition from plateau phase to nebular was observed in SN 2021wvw, which was eventually fitted with models that experienced significant fallback during shock propagation. Lastly, SN 2023ixf showed evidence of multiple CSM layers around it and signatures of an asymmetric explosion. Such events in the future must pose more questions to us, which warrants special attention.

Apart from understanding the details of short-plateau SNe, the implications of this work extend to our understanding of stellar evolution, mass loss mechanism in RSG progenitors, properties of the CSM, and finally, the SN explosion mechanism. This work also highlights the importance of very early detection and rapid multi-wavelength follow-up in deciphering the progenitor properties and understanding their environment. Some of these features included "flash ionization" and other observable characteristics of Type II SNe, such as the enhanced optical luminosity and the CSM interaction signatures in late spectra. This makes more qualitative contributions to our understanding of Type II SNe's tremendous diversity and the roles of their progenitors in its evolution.

7.2 Future Work

The past five years have been remarkable in terms of advancement in the understanding of rarely occurring short-plateau SNe. This has happened both with the aid of extensive multiband observations and detailed modeling. Yet, many challenges remain to fully explore these phenomena and core-collapse SNe in general. The community is engaged in understanding SNe in detail utilizing more advanced 3-D modeling techniques, understanding the effect of binarity on progenitor evolution, and the resultant pre-SN structure. Comprehensive works are being carried out to constrain the observational mass losses and implement those in modeling. Though attempts have been made to understand these SNe, a lot more remains to be explored. With the increasing number of short-plateau SNe, we find that these events have varied luminosities, synthesized ^{56}Ni masses, and expansion velocities. It is evident that these are not restricted to moderate to luminous events, as seen previously. With the upcoming extensive surveys such as LSST, this number would only increase, possibly making the Type IIP class or subclasses more homogenous in different parameter spaces.

As mentioned earlier and also evident from the work being done in the direction of short-plateau CCSNe, there is still a lot of scope to understand these much better. This also applies to the CCSNe in general. It may seem implausible to plan work for a future much far ahead, but certainly, a few of the studies could still be carried out in the near future with the existing set of resources. This could be realized both in the observational and modeling domains. We list some potential works that could be materialized in the upcoming years.

7.2.1 Long-term Multiwavelength Monitoring Campaigns:

Majority of SNe are primarily followed-up in optical wavelengths whereas much of the crucial information is also contained in other wavelength domains, especially the very early and late phases. Nascent phases of SNe are highly dynamic in nature and require UV to X-ray observation to constraint better about the progenitor and its surroundings. At the other end, during late phases, we have observed increase in NIR flux in many CCSNe, and if there is prior mass loss during evolution it could also give signatures in late-time radio follow-up of these events. Hence, to obtain a comprehensive picture SNe should be followed in all possible wavelengths and that too for longer phases. The advent of JWST has already opened new horizons in transient astronomy, with several monitoring campaigns in place to study the formation and accumulation of dust from SNe, which exploded a few to tens of years ago. More such campaigns will reveal new insights.

Multiband observations for a longer duration until the very late nebular phase should be continued for the maximum events possible. Some of the targeted campaigns could focus on the RSG stars in the Galaxy to better understand mass losses at various phases of evolution. Observing more SNe, especially short-plateau ones, and studying their host properties will aid in associating these with their host and constrain the environment parameters much more reliably. More discoveries and extensive follow-up would significantly enhance the rare short-plateau SNe population and eventually reveal their true nature as part of the Type II class.

7.2.2 Type II SNe Light Curves Models including Short-plateau SNe

During this work, it was realized that the available model light curves for short plateau supernovae, which could be utilized to constrain various explosion parameters and progenitor properties, are limited. Though light curves with short plateau lengths popped up in several modeling works, these model grids are not comprehensive in nature as to involve a variety of progenitors. Further, the available light curve grids are heavily biased toward the high-mass RSG progenitors. Hence, we have attempted to create a grid of several progenitors with different evolution and explosion properties. Most of the parameters are chosen from the typical values obtained for a large Type II SNe sample. Along with this, other parameters are varied so that each ZAMS model results in normal SNe and, in addition to that, in a short-plateau Type II SN. The parameter space explored in this grid is as follows:

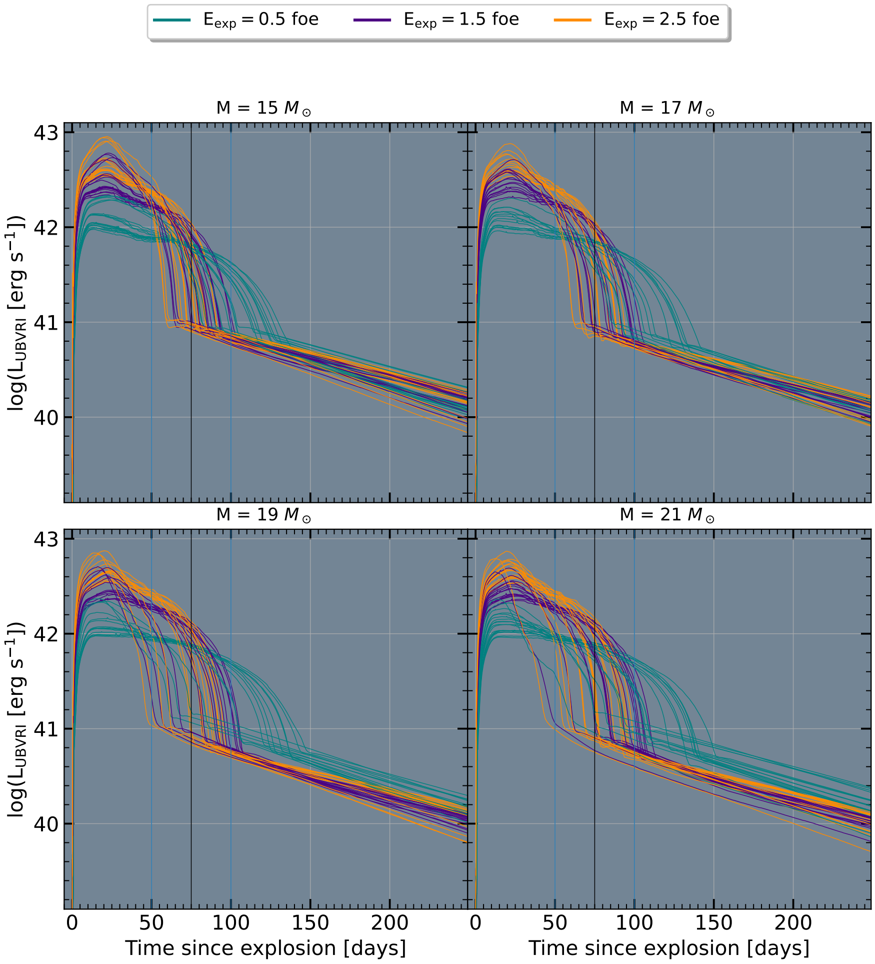

FIGURE 7.1: Pseudo-bolometric light curves obtained from a part of a larger grid showing variations due to differences in explosion energies for various ZAMS masses. (Multiple light curves in the same colors are due to variations in other parameters that are not explored/shown here.)

- **Initial Progenitor Masses,** $M_{ZAMS} \in \{11, 13, 15, 17, 19, 21, 23, 25, 27\}$ $M_\odot$
- **Metallicity,** $Z \in \{0.008, 0.016, 0.024\}$ $Z_\odot$, implying sub-solar, solar and above-solar metallicties.

- **Wind Scaling for Mass Loss,** $\alpha_{\mathrm{wsf}} \in \{1.0, 2.0, 3.0, 4.0, 5.0\}$, these values allow high wind mass loss even in less massive progenitors.

- **Stellar Rotation,** $\mathrm{v/v_c} \in \{0.0, 0.1\}$, implying non-rotating and slightly rotating progenitors.

- **Explosion Energy,** $\mathrm{E_{exp}} \in \{0.5, 1.5, 2.5\}$ foe

- **Nickel Mass,** $\mathrm{M_{Ni}}$ is kept fixed at 0.03 $\mathrm{M_\odot}$ (which is a mean value from a large Type II sample) but can be varied in later few steps.

- Mixing Length, $\alpha_{\mathrm{MLT}} \in \{1.5, 3.0\}$, eventually creating two sets of progenitors: typical radii and slightly compact radii.

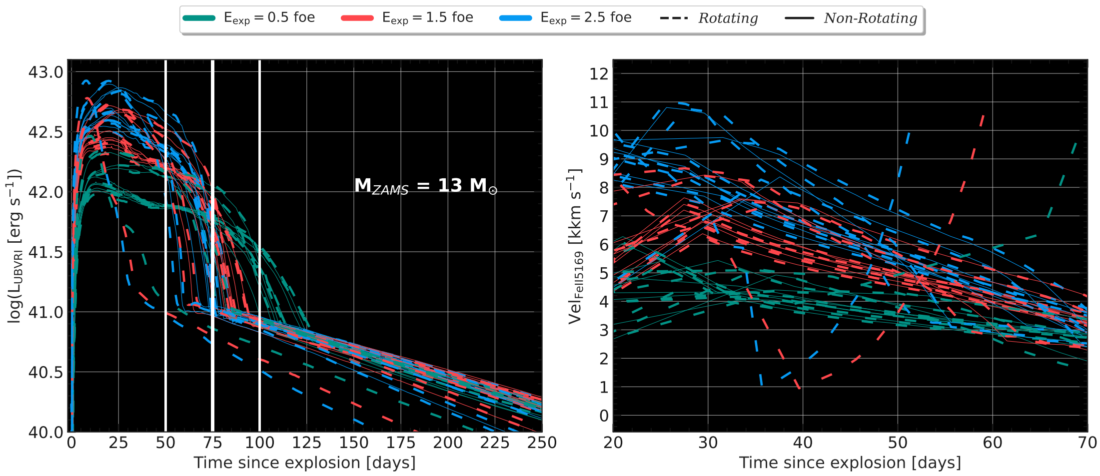

FIGURE 7.2: Pseudo-bolometric light curves and velocity evolution shown here for $\mathrm{M_{ZAMS}}$ = 13 $\mathrm{M_\odot}$ models with differences obtained for rotating and non-rotating models with different explosion energies. ((Multiple light curves in the same colors are due to variation in other parameters that are not explored/shown here.))

The work related to this grid is in progress. This progenitor grid, along with light curves and expansion velocity evolution, would be helpful in understanding these SNe. These progenitors can be analyzed in great detail to see the various structural differences between different metallicities, rotations, and other parameters. Light curves obtained can be directly implemented for new observations, and in many

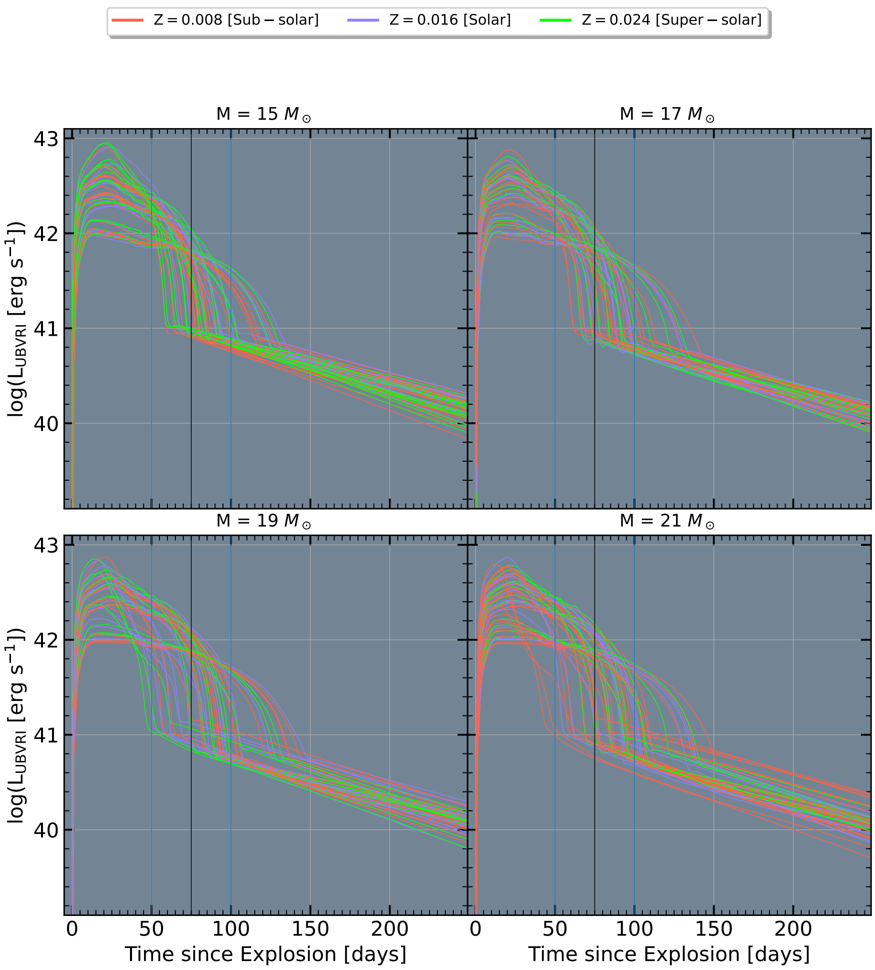

FIGURE 7.3: Pseudo-bolometric light curves obtained from a part of a larger grid showing variations due to differences in metallicity for various ZAMS masses.

cases, it can provide a good starting point for further detailed modeling. Some of the preliminary results are provided here.

Figure 7.1 shows the final pseudo-bolometric light curves for some of the progenitors that exploded with different energies. Clearly, at first glance, a high energy value shortens the plateau length in most of the cases. The detailed consequences of each parameter will be studied at a later point in time. Figure 7.2 and 7.3 also show light curve evolution for different parameters. It would be interesting to study the effects of these parameters on the progenitor structure and to see if there are any fundamental changes in a normal Type II SNe progenitor and short-plateau Type II SNe progenitors. Quantifying these differences and obtaining some analytical relations for short plateau events will be a crucial extension of this work.

The advent of night sky surveys, instant ease of access to public data, and advancement in modern tools and techniques have spearheaded transient science to a whole new domain. Extensive panchromatic observation covering radio waves to infrared aided by detailed theoretical works has increased our understanding of transients. We are discovering tens of thousands of such events yearly, and some turn out to be 'exotic' or out-of-the-ordinary events. Although only a tiny fraction of these transients, specifically SNe, get much attention, a majority are left unclassified. Another exciting domain still in the nascent stage and has been dormant for decades is the UV astronomy of transients, which explains the very early phases of these SNe and the late phase of the progenitor. Upcoming missions, such as UVEX and ULTRASAT, will help advance our understanding of this early phase and, eventually, our knowledge of these transients. In the era of JWST, where we are advancing transient astronomy to much greater redshifts and the initiation of the upcoming Vera C. Rubin Observatory, this number will explode. We will require more 4-10 m class telescopes to be able to follow up on these exciting transients.

✣ ✣ ✣ ✣

Bibliography

Ailawadhi, B., Dastidar, R., Misra, K., et al. 2023, *Mon. Not. Roy. Astron. Soc.*, 519, 248, doi: 10.1093/mnras/stac3234

Akitaya, H., Moritani, Y., Ui, T., et al. 2014, in procspie, Vol. 9147, Ground-based and Airborne Instrumentation for Astronomy V, 91474O, doi: 10.1117/12.2054577

Anderson, J. P. 2019, *Astron. Astrophys.*, 628, A7, doi: 10.1051/0004-6361/201935027

Anderson, J. P., González-Gaitán, S., Hamuy, M., et al. 2014a, *Astrophys. J.*, 786, 67, doi: 10.1088/0004-637X/786/1/67

Anderson, J. P., Dessart, L., Gutierrez, C. P., et al. 2014b, *Mon. Not. Roy. Astron. Soc.*, 441, 671, doi: 10.1093/mnras/stu610

Andrews, J. E., Gallagher, J. S., Clayton, G. C., et al. 2010, *Astrophys. J.*, 715, 541, doi: 10.1088/0004-637X/715/1/541

Andrews, J. E., Sugerman, B. E. K., Clayton, G. C., et al. 2011, *Astrophys. J.*, 731, 47, doi: 10.1088/0004-637X/731/1/47

Andrews, J. E., Sand, D. J., Valenti, S., et al. 2019, *Astrophys. J.*, 885, 43, doi: 10.3847/1538-4357/ab43e3

Angulo, C. 1999, in American Institute of Physics Conference Series, Vol. 495, Experimental Nuclear Physics in europe: Facing the next millennium, 365–366, doi: 10.1063/1.1301821

Arcavi, I. 2017, in Handbook of Supernovae, ed. A. W. Alsabti & P. Murdin (Springer International Publishing AG 2017), 239, doi: 10.1007/978-3-319-21846-5_39

Arnett, W. D. 1980, *Astrophys. J.*, 237, 541, doi: 10.1086/157898

—. 1982, *Astrophys. J. Lett.*, 263, L55, doi: 10.1086/183923

Arnett, W. D., & Fu, A. 1989, *Astrophys. J.*, 340, 396, doi: 10.1086/167402

Asplund, M., Grevesse, N., & Jacques Sauval, A. 2006, *Nuclear Physics A*, 777, 1, doi: 10.1016/j.nuclphysa.2005.06.010

Asplund, M., Grevesse, N., Sauval, A. J., & Scott, P. 2009, *Ann. Rev. Astron. Astrophys.*, 47, 481, doi: 10.1146/annurev.astro.46.060407.145222

Astropy Collaboration, Robitaille, T. P., Tollerud, E. J., et al. 2013, *Astron. Astrophys.*, 558, A33, doi: 10.1051/0004-6361/201322068

Astropy Collaboration, Price-Whelan, A. M., Sipőcz, B. M., et al. 2018, *Astron. J.*, 156, 123, doi: 10.3847/1538-3881/aabc4f

Astropy Collaboration, Price-Whelan, A. M., Lim, P. L., et al. 2022, apj, 935, 167, doi: 10.3847/1538-4357/ac7c74

Baklanov, P. V., Blinnikov, S. I., & Pavlyuk, N. N. 2005, Astronomy Letters, 31, 429, doi: 10.1134/1.1958107

Balam, D. D., & Kendurkar, M. 2023, Transient Name Server AstroNote, 154, 1

Barbarino, C., Dall'Ora, M., Botticella, M. T., et al. 2015, *Mon. Not. Roy. Astron. Soc.*, 448, 2312, doi: 10.1093/mnras/stv106

Barbon, R., Benetti, S., Cappellaro, E., Rosino, L., & Turatto, M. 1990, *Astron. Astrophys.*, 237, 79

Basu, J., Barway, S., Anupama, G. C., Teja, R. S., & Dutta, A. 2023, The Astronomer's Telegram, 16064, 1

Beasor, E. R., Davies, B., Smith, N., et al. 2020, *Mon. Not. Roy. Astron. Soc.*, 492, 5994, doi: 10.1093/mnras/staa255

Berger, E., Keating, G. K., Margutti, R., et al. 2023, Millimeter Observations of the Type II SN2023ixf: Constraints on the Proximate Circumstellar Medium. https://arxiv.org/abs/2306.09311

Berger, E., Keating, G. K., Margutti, R., et al. 2023, *Astrophys. J. Lett.*, 951, L31, doi: 10.3847/2041-8213/ace0c4

Bersten, M. C., Orellana, M., Folatelli, G., et al. 2024, *Astron. Astrophys.*, 681, L18, doi: 10.1051/0004-6361/202348183

Bertrand, E. 2018, Transient Name Server Classification Report, 2018-56, 1

Bessell, M. S., Castelli, F., & Plez, B. 1998, *Astron. Astrophys.*, 333, 231

Bevan, A., Wesson, R., Barlow, M. J., et al. 2019, *Mon. Not. Roy. Astron. Soc.*, 485, 5192, doi: 10.1093/mnras/stz679

Black, C. S., Milisavljevic, D., Margutti, R., et al. 2017, *Astrophys. J.*, 848, 5, doi: 10.3847/1538-4357/aa8999

Blanton, M. R., & Roweis, S. 2007, *Astron. J.*, 133, 734, doi: 10.1086/510127

Blinnikov, S., & Sorokina, E. 2004, *Astrophys. Space Sci.*, 290, 13, doi: 10.1023/B:ASTR.0000022161.03559.42

Blinnikov, S. I., & Popov, D. V. 1993, *Astron. Astrophys.*, 274, 775

Blinnikov, S. I., Röpke, F. K., Sorokina, E. I., et al. 2006, *Astron. Astrophys.*, 453, 229, doi: 10.1051/0004-6361:20054594

Blondin, S., & Tonry, J. L. 2007, *Astrophys. J.*, 666, 1024, doi: 10.1086/520494

Bose, S., & Kumar, B. 2014, *Astrophys. J.*, 782, 98, doi: 10.1088/0004-637X/782/2/98

Bose, S., Kumar, B., Misra, K., et al. 2016, *Mon. Not. Roy. Astron. Soc.*, 455, 2712, doi: 10.1093/mnras/stv2351

Bose, S., Kumar, B., Sutaria, F., et al. 2013, *Mon. Not. Roy. Astron. Soc.*, 433, 1871, doi: 10.1093/mnras/stt864

Bose, S., Valenti, S., Misra, K., et al. 2015, *Mon. Not. Roy. Astron. Soc.*, 450, 2373, doi: 10.1093/mnras/stv759

Bostroem, K. A., Valenti, S., Horesh, A., et al. 2019, *Mon. Not. Roy. Astron. Soc.*, 485, 5120, doi: 10.1093/mnras/stz570

Bostroem, K. A., Valenti, S., Sand, D. J., et al. 2020, *Astrophys. J.*, 895, 31, doi: 10.3847/1538-4357/ab8945

Bostroem, K. A., Pearson, J., Shrestha, M., et al. 2023a, arXiv e-prints, arXiv:2306.10119, doi: 10.48550/arXiv.2306.10119

Bostroem, K. A., Dessart, L., Hillier, D. J., et al. 2023b, arXiv e-prints, arXiv:2305.01654, doi: 10.48550/arXiv.2305.01654

Bottinelli, L., Gouguenheim, L., Paturel, G., & de Vaucouleurs, G. 1984, *Astron. Astrophys. Suppl.*, 56, 381

Brown, P. J., Breeveld, A. A., Holland, S., Kuin, P., & Pritchard, T. 2014, A&SS, 354, 89, doi: 10.1007/s10509-014-2059-8

Brown, P. J., Dessart, L., Holland, S. T., et al. 2007, *Astrophys. J.*, 659, 1488, doi: 10.1086/511968

Brown, P. J., Holland, S. T., Immler, S., et al. 2009, *Astron. J.*, 137, 4517, doi: 10.1088/0004-6256/137/5/4517

Bruch, R. J., Gal-Yam, A., Schulze, S., et al. 2021, *Astrophys. J.*, 912, 46, doi: 10.3847/1538-4357/abef05

Bruch, R. J., Gal-Yam, A., Yaron, O., et al. 2022, arXiv e-prints, arXiv:2212.03313. https://arxiv.org/abs/2212.03313

—. 2023, *Astrophys. J.*, 952, 119, doi: 10.3847/1538-4357/acd8be

Bufano, F., Immler, S., Turatto, M., et al. 2009, *Astrophys. J.*, 700, 1456, doi: 10.1088/0004-637X/700/2/1456

Bullivant, C., Smith, N., Williams, G. G., et al. 2018, *Mon. Not. Roy. Astron. Soc.*, 476, 1497, doi: 10.1093/mnras/sty045

Burrows, A., & Vartanyan, D. 2021, *Nature*, 589, 29, doi: 10.1038/s41586-020-03059-w

Cardelli, J. A., Clayton, G. C., & Mathis, J. S. 1989, *Astrophys. J.*, 345, 245, doi: 10.1086/167900

Chandra, P., Chevalier, R. A., Maeda, K., Ray, A. K., & Nayana, A. J. 2023, arXiv e-prints, arXiv:2311.04384, doi: 10.48550/arXiv.2311.04384

Chatzopoulos, E., Wheeler, J. C., & Vinko, J. 2012, *Astrophys. J.*, 746, 121, doi: 10.1088/0004-637X/746/2/121

Cheng, S. J., Goldberg, J. A., Cantiello, M., et al. 2024, arXiv e-prints, arXiv:2405.12274, doi: 10.48550/arXiv.2405.12274

Chevalier, R. A. 1981, *Astrophys. J.*, 251, 259, doi: 10.1086/159460

—. 1982, *Astrophys. J.*, 258, 790, doi: 10.1086/160126

Chevalier, R. A., & Fransson, C. 1994, *Astrophys. J.*, 420, 268, doi: 10.1086/173557

Chevalier, R. A., & Irwin, C. M. 2011, *Astrophys. J. Lett.*, 729, L6, doi: 10.1088/2041-8205/729/1/L6

Chufarin, V., Potapov, N., Ionov, I., et al. 2023, Transient Name Server AstroNote, 150, 1

Chugai, N. N. 1988, Soviet Astronomy Letters, 14, 334

—. 2009, *Mon. Not. Roy. Astron. Soc.*, 400, 866, doi: 10.1111/j.1365-2966.2009.15506.x

—. 2020, *Mon. Not. Roy. Astron. Soc.*, 494, L86, doi: 10.1093/mnrasl/slaa042

Chugai, N. N., Chevalier, R. A., & Utrobin, V. P. 2007, *Astrophys. J.*, 662, 1136, doi: 10.1086/518160

Chugai, N. N., & Utrobin, V. P. 2000, *Astron. Astrophys.*, 354, 557, doi: 10.48550/arXiv.astro-ph/9906190

Clocchiatti, A., Benetti, S., Wheeler, J. C., et al. 1996, *Astron. J.*, 111, 1286, doi: 10.1086/117874

Colgate, S. A. 1971, *Astrophys. J.*, 163, 221, doi: 10.1086/150760

Cowen, D. F., Franckowiak, A., & Kowalski, M. 2010, Astroparticle Physics, 33, 19, doi: 10.1016//j.astropartphys.2009.10.007

Curtis, S., Wolfe, N., Fröhlich, C., et al. 2021, *Astrophys. J.*, 921, 143, doi: 10.3847/1538-4357/ac0dc5

Cyburt, R. H., Amthor, A. M., Ferguson, R., et al. 2010, *Astrophys. J. Suppl.*, 189, 240, doi: 10.1088/0067-0049/189/1/240

Dastidar, R., Misra, K., Singh, M., et al. 2021, *Mon. Not. Roy. Astron. Soc.*, 504, 1009, doi: 10.1093/mnras/stab831

D'Avanzo, P., Bianchetti, N., Bianchessi, M., et al. 2023, Transient Name Server AstroNote, 153, 1

Davies, B., & Beasor, E. R. 2020a, *Mon. Not. Roy. Astron. Soc.*, 493, 468, doi: 10.1093/mnras/staa174

—. 2020b, *Mon. Not. Roy. Astron. Soc.*, 496, L142, doi: 10.1093/mnrasl/slaa102

de Jaeger, T., Galbany, L., Gutiérrez, C. P., et al. 2018, *Mon. Not. Roy. Astron. Soc.*, 478, 3776, doi: 10.1093/mnras/sty1218

de Jaeger, T., Zheng, W., Stahl, B. E., et al. 2019, *Mon. Not. Roy. Astron. Soc.*, 490, 2799, doi: 10.1093/mnras/stz2714

Decin, L., Hony, S., de Koter, A., et al. 2006, *Astron. Astrophys.*, 456, 549, doi: 10.1051/0004-6361:20065230

Desrosiers, J. B., Kendurkar, M. R., & Balam, D. D. 2023, Transient Name Server AstroNote, 142, 1

Dessart, L., & Hillier, D. J. 2005a, *Astron. Astrophys.*, 439, 671, doi: 10.1051/0004-6361:20053217

—. 2005b, *Astron. Astrophys.*, 437, 667, doi: 10.1051/0004-6361:20042525

—. 2010, *Mon. Not. Roy. Astron. Soc.*, 405, 2141, doi: 10.1111/j.1365-2966.2010.16611.x

—. 2019, *Astron. Astrophys.*, 625, A9, doi: 10.1051/0004-6361/201834732

—. 2022, *Astron. Astrophys.*, 660, L9, doi: 10.1051/0004-6361/202243372

Dessart, L., Hillier, D. J., & Audit, E. 2017, *Astron. Astrophys.*, 605, A83, doi: 10.1051/0004-6361/201730942

Dessart, L., Hillier, D. J., Waldman, R., & Livne, E. 2013, *Mon. Not. Roy. Astron. Soc.*, 433, 1745, doi: 10.1093/mnras/stt861

Dessart, L., Livne, E., & Waldman, R. 2010, *Mon. Not. Roy. Astron. Soc.*, 408, 827, doi: 10.1111/j.1365-2966.2010.17190.x

Dessart, L., Prieto, J. L., Hillier, D. J., Kuncarayakti, H., & Hueichapan, E. D. 2022, *Astron. Astrophys.*, 666, L14, doi: 10.1051/0004-6361/202244413

Dewangan, G. C. 2021, Journal of Astrophysics and Astronomy, 42, 49, doi: 10.1007/s12036-021-09691-w

Dexter, J., & Kasen, D. 2013, *Astrophys. J.*, 772, 30, doi: 10.1088/0004-637X/772/1/30

Domínguez, A., Siana, B., Henry, A. L., et al. 2013, *Astrophys. J.*, 763, 145, doi: 10.1088/0004-637X/763/2/145

Dong, Y., Valenti, S., Bostroem, K. A., et al. 2021, *Astrophys. J.*, 906, 56, doi: 10.3847/1538-4357/abc417

Dong, Y., Sand, D. J., Valenti, S., et al. 2023, *Astrophys. J.*, 957, 28, doi: 10.3847/1538-4357/acef18

Duffell, P. C. 2016, *Astrophys. J.*, 821, 76, doi: 10.3847/0004-637X/821/2/76

Ekström, S. 2021, Frontiers in Astronomy and Space Sciences, 8, 53, doi: 10.3389/fspas.2021.617765

Eldridge, J. J., Fraser, M., Smartt, S. J., Maund, J. R., & Crockett, R. M. 2013, *Mon. Not. Roy. Astron. Soc.*, 436, 774, doi: 10.1093/mnras/stt1612

Eldridge, J. J., Xiao, L., Stanway, E. R., Rodrigues, N., & Guo, N. Y. 2018, *Publications of the Astronomical Society of Australia*, 35, e049, doi: 10.1017/pasa.2018.47

Elmhamdi, A., Chugai, N. N., & Danziger, I. J. 2003a, *Astron. Astrophys.*, 404, 1077, doi: 10.1051/0004-6361:20030522

Elmhamdi, A., Danziger, I. J., Chugai, N., et al. 2003b, *Mon. Not. Roy. Astron. Soc.*, 338, 939, doi: 10.1046/j.1365-8711.2003.06150.x

Ercolino, A., Jin, H., Langer, N., & Dessart, L. 2024, *Astron. Astrophys.*, 685, A58, doi: 10.1051/0004-6361/202347646

Evans, K. A., & Massey, P. 2015, *Astron. J.*, 150, 149, doi: 10.1088/0004-6256/150/5/149

Falk, S. W., & Arnett, W. D. 1977, *Astrophys. J. Suppl.*, 33, 515, doi: 10.1086/190440

Fang, Q., Maeda, K., Ye, H., Moriya, T., & Matsumoto, T. 2024, arXiv e-prints, arXiv:2404.01776, doi: 10.48550/arXiv.2404.01776

Faran, T., Poznanski, D., Filippenko, A. V., et al. 2014a, *Mon. Not. Roy. Astron. Soc.*, 442, 844, doi: 10.1093/mnras/stu955

—. 2014b, *Mon. Not. Roy. Astron. Soc.*, 445, 554, doi: 10.1093/mnras/stu1760

Farmer, R., Fields, C. E., Petermann, I., et al. 2016, *Astrophys. J. Suppl.*, 227, 22, doi: 10.3847/1538-4365/227/2/22

Filippenko, A. V. 1997, *Ann. Rev. Astron. Astrophys.*, 35, 309, doi: 10.1146/annurev.astro.35.1.309

Filippenko, A. V., Zheng, W., & Yang, Y. 2023, Transient Name Server AstroNote, 123, 1

Foreman-Mackey, D., Hogg, D. W., Lang, D., & Goodman, J. 2013, *Pub. Astron. Soc. Pac.*, 125, 306, doi: 10.1086/670067

Förster, F., Moriya, T. J., Maureira, J. C., et al. 2018, Nature Astronomy, 2, 808, doi: 10.1038/s41550-018-0563-4

Förster, F., Cabrera-Vives, G., Castillo-Navarrete, E., et al. 2021, *Astron. J.*, 161, 242, doi: 10.3847/1538-3881/abe9bc

Fowler, M., Sienkiewicz, F., & Dussault, M. 2023, Transient Name Server AstroNote, 143, 1

Fransson, C. 1984, *Astron. Astrophys.*, 133, 264

Fransson, C., & Chevalier, R. A. 1989, *Astrophys. J.*, 343, 323, doi: 10.1086/167707

Fraser, M., Ergon, M., Eldridge, J. J., et al. 2011, *Mon. Not. Roy. Astron. Soc.*, 417, 1417, doi: 10.1111/j.1365-2966.2011.19370.x

Fulton, M. D., Nicholl, M., Smith, K. W., et al. 2023, Transient Name Server AstroNote, 124, 1

Gal-Yam, A., Bufano, F., Barlow, T. A., et al. 2008, *Astrophys. J. Lett.*, 685, L117, doi: 10.1086/592744

Gall, E. E. E., Polshaw, J., Kotak, R., et al. 2015, *Astron. Astrophys.*, 582, A3, doi: 10.1051/0004-6361/201525868

Garner, R., Mihos, J. C., Harding, P., Watkins, A. E., & McGaugh, S. S. 2022, *Astrophys. J.*, 941, 182, doi: 10.3847/1538-4357/aca27a

Gehrels, N., Chincarini, G., Giommi, P., et al. 2004, *Astrophys. J.*, 611, 1005, doi: 10.1086/422091

Gerling-Dunsmore, H. J., & Ott, C. D. 2015, in APS Meeting Abstracts, Vol. 2015, APS April Meeting Abstracts, L1.010

Gezari, S., Jones, D. O., Sanders, N. E., et al. 2015, *Astrophys. J.*, 804, 28, doi: 10.1088/0004-637X/804/1/28

Glebbeek, E., Gaburov, E., de Mink, S. E., Pols, O. R., & Portegies Zwart, S. F. 2009, *Astron. Astrophys.*, 497, 255, doi: 10.1051/0004-6361/200810425

Goldberg, J. A., & Bildsten, L. 2020, *Astrophys. J. Lett.*, 895, L45, doi: 10.3847/2041-8213/ab9300

Goldberg, J. A., Bildsten, L., & Paxton, B. 2019, *Astrophys. J.*, 879, 3, doi: 10.3847/1538-4357/ab22b6

Goldberg, J. A., Jiang, Y.-F., & Bildsten, L. 2022, *Astrophys. J.*, 933, 164, doi: 10.3847/1538-4357/ac75e3

González-Carballo, J., Farfán, R. G., Limón, F., et al. 2023, Transient Name Server AstroNote, 136, 1

Grefenstette, B. W., Brightman, M., Earnshaw, H. P., Harrison, F. A., & Margutti, R. 2023, *Astrophys. J. Lett.*, 952, L3, doi: 10.3847/2041-8213/acdf4e

Guillochon, J., Parrent, J., Kelley, L. Z., & Margutti, R. 2017, *Astrophys. J.*, 835, 64, doi: 10.3847/1538-4357/835/1/64

Gutiérrez, C. P., Anderson, J. P., Hamuy, M., et al. 2014, The Astrophysical Journal, 786, L15, doi: 10.1088/2041-8205/786/2/l15

Gutiérrez, C. P., Anderson, J. P., Hamuy, M., et al. 2014, *Astrophys. J. Lett.*, 786, L15, doi: 10.1088/2041-8205/786/2/L15

—. 2017a, *Astrophys. J.*, 850, 89, doi: 10.3847/1538-4357/aa8f52

—. 2017b, *Astrophys. J.*, 850, 90, doi: 10.3847/1538-4357/aa8f42

Gutiérrez, C. P., Sullivan, M., Martinez, L., et al. 2020, *Mon. Not. Roy. Astron. Soc.*, 496, 95, doi: 10.1093/mnras/staa1452

Hamuy, M. 2003, *Astrophys. J.*, 582, 905, doi: 10.1086/344689

Hamuy, M., Pinto, P. A., Maza, J., et al. 2001, *Astrophys. J.*, 558, 615, doi: 10.1086/322450

Harris, C. R., Millman, K. J., van der Walt, S. J., et al. 2020, Nature, 585, 357, doi: 10.1038/s41586-020-2649-2

Henyey, L., Vardya, M. S., & Bodenheimer, P. 1965, *Astrophys. J.*, 142, 841, doi: 10.1086/148357

Hinkle, J. 2021, Transient Name Server Classification Report, 2021-2941, 1

Hiramatsu, D., Howell, D. A., Moriya, T. J., et al. 2021a, *Astrophys. J.*, 913, 55, doi: 10.3847/1538-4357/abf6d6

Hiramatsu, D., Howell, D. A., Van Dyk, S. D., et al. 2021b, Nature Astronomy, 5, 903, doi: 10.1038/s41550-021-01384-2

Hiramatsu, D., Tsuna, D., Berger, E., et al. 2023, *Astrophys. J. Lett.*, 955, L8, doi: 10.3847/2041-8213/acf299

Horne, K. 1986, *Pub. Astron. Soc. Pac.*, 98, 609, doi: 10.1086/131801

Hosseinzadeh, G., Farah, J., Shrestha, M., et al. 2023, arXiv e-prints, arXiv:2306.06097, doi: 10.48550/arXiv.2306.06097

Huang, F., Wang, X., Zampieri, L., et al. 2016, *Astrophys. J.*, 832, 139, doi: 10.3847/0004-637X/832/2/139

Huang, F., Wang, X. F., Hosseinzadeh, G., et al. 2018, *Mon. Not. Roy. Astron. Soc.*, 475, 3959, doi: 10.1093/mnras/sty066

Hunter, J. D. 2007, Computing in Science & Engineering, 9, 90, doi: 10.1109/MCSE.2007.55

Inserra, C., Turatto, M., Pastorello, A., et al. 2011, *Mon. Not. Roy. Astron. Soc.*, 417, 261, doi: 10.1111/j.1365-2966.2011.19128.x

—. 2012, *Mon. Not. Roy. Astron. Soc.*, 422, 1122, doi: 10.1111/j.1365-2966.2012.20685.x

Inserra, C., Pastorello, A., Turatto, M., et al. 2013, *Astron. Astrophys.*, 555, A142, doi: 10.1051/0004-6361/201220496

Jacobson-Galán, W., Dessart, L., Jones, D., et al. 2021, arXiv e-prints, arXiv:2109.12136. https://arxiv.org/abs/2109.12136

Jacobson-Galán, W. V., Dessart, L., Jones, D. O., et al. 2022, *Astrophys. J.*, 924, 15, doi: 10.3847/1538-4357/ac3f3a

Jacobson-Galan, W. V., Dessart, L., Margutti, R., et al. 2023, arXiv e-prints, arXiv:2306.04721, doi: 10.48550/arXiv.2306.04721

Janka, H.-T. 2012, Annual Review of Nuclear and Particle Science, 62, 407, doi: 10.1146/annurev-nucl-102711-094901

Jeffery, D. J., & Branch, D. 1990, in Supernovae, Jerusalem Winter School for Theoretical Physics, ed. J. C. Wheeler, T. Piran, & S. Weinberg, Vol. 6, 149

Jencson, J. E., Pearson, J., Beasor, E. R., et al. 2023, *Astrophys. J. Lett.*, 952, L30, doi: 10.3847/2041-8213/ace618

Jerkstrand, A. 2017, in Handbook of Supernovae, ed. A. W. Alsabti & P. Murdin (Springer International Publishing AG 2017), 795, doi: 10.1007/978-3-319-21846-5_29

Jerkstrand, A., Smartt, S. J., Fraser, M., et al. 2014, *Mon. Not. Roy. Astron. Soc.*, 439, 3694, doi: 10.1093/mnras/stu221

Jerkstrand, A., Timmes, F. X., Magkotsios, G., et al. 2015a, *Astrophys. J.*, 807, 110, doi: 10.1088/0004-637X/807/1/110

Jerkstrand, A., Smartt, S. J., Sollerman, J., et al. 2015b, *Mon. Not. Roy. Astron. Soc.*, 448, 2482, doi: 10.1093/mnras/stv087

Jerkstrand, Anders. 2017, in Handbook of Supernovae, ed. A. W. Alsabti & P. Murdin (Cham: Springer International Publishing), 1–48, doi: 10.1007/978-3-319-20794-0_29-1

Jester, S., Schneider, D. P., Richards, G. T., et al. 2005, *Astron. J.*, 130, 873, doi: 10.1086/432466

Jones, D. O., French, K. D., Agnello, A., et al. 2021, Transient Name Server Discovery Report, 2021-2917, 1

Kasen, D., & Woosley, S. E. 2009, *Astrophys. J.*, 703, 2205, doi: 10.1088/0004-637X/703/2/2205

Kendurkar, M. R., & Balam, D. D. 2023, Transient Name Server AstroNote, 129, 1

Kerzendorf, W. E., & Sim, S. A. 2014, *Mon. Not. Roy. Astron. Soc.*, 440, 387, doi: 10.1093/mnras/stu055

Khatami, D., & Kasen, D. 2023, arXiv e-prints, arXiv:2304.03360, doi: 10.48550/arXiv.2304.03360

Kilpatrick, C. 2018, Transient Name Server Classification Report, 2018-2075, 1

Kilpatrick, C. D., Foley, R. J., Jacobson-Galán, W. V., et al. 2023a, arXiv e-prints, arXiv:2306.04722, doi: 10.48550/arXiv.2306.04722

Kilpatrick, C. D., Izzo, L., Bentley, R. O., et al. 2023b, *Mon. Not. Roy. Astron. Soc.*, 524, 2161, doi: 10.1093/mnras/stad1954

Kirshner, R. P., & Kwan, J. 1974, *Astrophys. J.*, 193, 27, doi: 10.1086/153123

Kleiser, I. K. W., Poznanski, D., Kasen, D., et al. 2011, *Mon. Not. Roy. Astron. Soc.*, 415, 372, doi: 10.1111/j.1365-2966.2011.18708.x

Kluyver, T., Ragan-Kelley, B., Pérez, F., et al. 2016, in Positioning and Power in Academic Publishing: Players, Agents and Agendas, ed. F. Loizides & B. Scmidt (Netherlands: IOS Press), 87–90. https://eprints.soton.ac.uk/403913/

Kochanek, C. S. 2020, *Mon. Not. Roy. Astron. Soc.*, 493, 4945, doi: 10.1093/mnras/staa605

Koltenbah, B. 2023, Transient Name Server AstroNote, 144, 1

Kong, A. K. H. 2023, The Astronomer's Telegram, 16051, 1

Kozasa, T., Hasegawa, H., & Nomoto, K. 1991, *Astron. Astrophys.*, 249, 474

Kuin, P. 2014, UVOTPY: Swift UVOT grism data reduction, Astrophysics Source Code Library, record ascl:1410.004. http://ascl.net/1410.004

Kulkarni, S. R., Harrison, F. A., Grefenstette, B. W., et al. 2021, arXiv e-prints, arXiv:2111.15608, doi: 10.48550/arXiv.2111.15608

Kumar, A., Ghosh, S. K., Hutchings, J., et al. 2012, in *SPIE conference proceedings*, Vol. 8443, Space Telescopes and Instrumentation 2012: Ultraviolet to Gamma Ray, 84431N, doi: 10.1117/12.924507

Kumar, H., Bhalerao, V., Anupama, G. C., et al. 2022, *Astron. J.*, 164, 90, doi: 10.3847/1538-3881/ac7bea

Kurita, M., Kino, M., Iwamuro, F., et al. 2020, *Pub. Astron. Soc. Japan*, 72, 48, doi: 10.1093/pasj/psaa036

Landolt, A. U. 1992, *Astron. J.*, 104, 340, doi: 10.1086/116242

Laplace, E., Justham, S., Renzo, M., et al. 2021, *Astron. Astrophys.*, 656, A58, doi: 10.1051/0004-6361/202140506

Lee, M. G., Freedman, W. L., & Madore, B. F. 1993, *Astrophys. J.*, 417, 553, doi: 10.1086/173334

Leonard, D. C., Filippenko, A. V., Li, W., et al. 2002a, *Astron. J.*, 124, 2490, doi: 10.1086/343771

Leonard, D. C., Filippenko, A. V., Gates, E. L., et al. 2002b, *Pub. Astron. Soc. Pac.*, 114, 35, doi: 10.1086/324785

Li, G., Hu, M., Li, W., et al. 2023, arXiv e-prints, arXiv:2311.14409, doi: 10.48550/arXiv.2311.14409

Li, W., Leaman, J., Chornock, R., et al. 2011, *Mon. Not. Roy. Astron. Soc.*, 412, 1441, doi: 10.1111/j.1365-2966.2011.18160.x

Limeburner, S. 2023, Transient Name Server AstroNote, 128, 1

Limongi, M. 2017, in Handbook of Supernovae, ed. A. W. Alsabti & P. Murdin, 513, doi: 10.1007/978-3-319-21846-5_119

Lisakov, S. M., Dessart, L., Hillier, D. J., Waldman, R., & Livne, E. 2018, *Mon. Not. Roy. Astron. Soc.*, 473, 3863, doi: 10.1093/mnras/stx2521

Lucy, L. B., Danziger, I. J., Gouiffes, C., & Bouchet, P. 1989, in IAU Colloq. 120: Structure and Dynamics of the Interstellar Medium, ed. G. Tenorio-Tagle, M. Moles, & J. Melnick, Vol. 350, 164, doi: 10.1007/BFb0114861

Lundquist, M., O'Meara, J., & Walawender, J. 2023, Transient Name Server AstroNote, 160, 1

Maguire, K., Jerkstrand, A., Smartt, S. J., et al. 2012, *Mon. Not. Roy. Astron. Soc.*, 420, 3451, doi: 10.1111/j.1365-2966.2011.20276.x

Mao, Y., Zhang, M., Cai, G., et al. 2023, Transient Name Server AstroNote, 130, 1

Martinez, L., & Bersten, M. C. 2019, *Astron. Astrophys.*, 629, A124, doi: 10.1051/0004-6361/201834818

Martinez, L., Anderson, J. P., Bersten, M. C., et al. 2022, *Astron. Astrophys.*, 660, A42, doi: 10.1051/0004-6361/202142555

Matsubayashi, K., Ohta, K., Iwamuro, F., et al. 2019, arXiv e-prints, arXiv:1905.05430. https://arxiv.org/abs/1905.05430

Matsunaga, K., Uchida, H., Enoto, T., Tsuru, T., & Sato, T. 2023, The Astronomer's Telegram, 16060, 1

Matsuoka, T., & Sawada, R. 2023, arXiv e-prints, arXiv:2307.00727, doi: 10.48550/arXiv.2307.00727

Matthews, D., Margutti, R., AJ, N., et al. 2023, Transient Name Server AstroNote, 180, 1

Mauerhan, J. C., Smith, N., Silverman, J. M., et al. 2013, *Mon. Not. Roy. Astron. Soc.*, 431, 2599, doi: 10.1093/mnras/stt360

Mazzali, P. A. 2000, *Astron. Astrophys.*, 363, 705

Mazzali, P. A., Röpke, F. K., Benetti, S., & Hillebrandt, W. 2007, Science, 315, 825, doi: 10.1126/science.1136259

Minkowski, R. 1941, *Pub. Astron. Soc. Pac.*, 53, 224, doi: 10.1086/125315

Mirametrics, Inc. 2023, Mira Pro x64, 8.62. https://www.mirametrics.com/mira_pro.php

Moriya, T., Tominaga, N., Blinnikov, S. I., Baklanov, P. V., & Sorokina, E. I. 2011, *Mon. Not. Roy. Astron. Soc.*, 415, 199, doi: 10.1111/j.1365-2966.2011.18689.x

Moriya, T. J., Förster, F., Yoon, S.-C., Gräfener, G., & Blinnikov, S. I. 2018, *Mon. Not. Roy. Astron. Soc.*, 476, 2840, doi: 10.1093/mnras/sty475

Moriya, T. J., Müller, B., Chan, C., Heger, A., & Blinnikov, S. I. 2019, *Astrophys. J.*, 880, 21, doi: 10.3847/1538-4357/ab2643

Moriya, T. J., & Singh, A. 2024, arXiv e-prints, arXiv:2406.00928, doi: 10.48550/arXiv.2406.00928

Moriya, T. J., Subrayan, B. M., Milisavljevic, D., & Blinnikov, S. I. 2023, *Pub. Astron. Soc. Japan*, 75, 634, doi: 10.1093/pasj/psad024

Morozova, V., Piro, A. L., & Valenti, S. 2017, *Astrophys. J.*, 838, 28, doi: 10.3847/1538-4357/aa6251

—. 2018, *Astrophys. J.*, 858, 15, doi: 10.3847/1538-4357/aab9a6

Murai, Y., Tanaka, M., Kawabata, M., et al. 2024, *Mon. Not. Roy. Astron. Soc.*, 528, 4209, doi: 10.1093/mnras/stae170

Nagao, T., Maeda, K., & Ouchi, R. 2020, *Mon. Not. Roy. Astron. Soc.*, 497, 5395, doi: 10.1093/mnras/staa2360

Nagy, A. P., Ordasi, A., Vinkó, J., & Wheeler, J. C. 2014, *Astron. Astrophys.*, 571, A77, doi: 10.1051/0004-6361/201424237

Nagy, A. P., & Vinkó, J. 2016, *Astron. Astrophys.*, 589, A53, doi: 10.1051/0004-6361/201527931

Nakaoka, T., Kawabata, K. S., Maeda, K., et al. 2018, *Astrophys. J.*, 859, 78, doi: 10.3847/1538-4357/aabee7

Nasa High Energy Astrophysics Science Archive Research Center (Heasarc). 2014, HEAsoft: Unified Release of FTOOLS and XANADU, Astrophysics Source Code Library, record ascl:1408.004. http://ascl.net/1408.004

Neustadt, J. M. M., Kochanek, C. S., & Rizzo Smith, M. 2023, arXiv e-prints, arXiv:2306.06162, doi: 10.48550/arXiv.2306.06162

Neustadt, J. M. M., Kochanek, C. S., & Smith, M. R. 2024, *Mon. Not. Roy. Astron. Soc.*, 527, 5366, doi: 10.1093/mnras/stad3073

Nicholl, M. 2018, Research Notes of the American Astronomical Society, 2, 230, doi: 10.3847/2515-5172/aaf799

Niu, Z., Sun, N.-C., Maund, J. R., et al. 2023, *Astrophys. J. Lett.*, 955, L15, doi: 10.3847/2041-8213/acf4e3

Nordin, J., Brinnel, V., Giomi, M., et al. 2020, Transient Name Server Discovery Report, 2020-1248, 1

Nugis, T., & Lamers, H. J. G. L. M. 2000, *Astron. Astrophys.*, 360, 227

Ofek, E. O., Rabinak, I., Neill, J. D., et al. 2010, *Astrophys. J.*, 724, 1396, doi: 10.1088/0004-637X/724/2/1396

Omar, A., Kumar, T. S., Krishna Reddy, B., Pant, J., & Mahto, M. 2019, arXiv e-prints, arXiv:1902.05857. https://arxiv.org/abs/1902.05857

Panagia, N., Vettolani, G., Boksenberg, A., et al. 1980, *Mon. Not. Roy. Astron. Soc.*, 192, 861, doi: 10.1093/mnras/192.4.861

pandas development team, T. 2020, pandas-dev/pandas: Pandas, latest, Zenodo, doi: 10.5281/zenodo.3509134

Panjkov, S., Auchettl, K., Shappee, B. J., et al. 2023, arXiv e-prints, arXiv:2308.13101, doi: 10.48550/arXiv.2308.13101

Parrent, J., Branch, D., & Jeffery, D. 2010, SYNOW: A Highly Parameterized Spectrum Synthesis Code for Direct Analysis of SN Spectra, Astrophysics Source Code Library, record ascl:1010.055

Pastorello, A., Sauer, D., Taubenberger, S., et al. 2006, *Mon. Not. Roy. Astron. Soc.*, 370, 1752, doi: 10.1111/j.1365-2966.2006.10587.x

Pastorello, A., Pumo, M. L., Navasardyan, H., et al. 2012, *Astron. Astrophys.*, 537, A141, doi: 10.1051/0004-6361/201118112

Patat, F., Cappellaro, E., Danziger, J., et al. 2001, *Astrophys. J.*, 555, 900, doi: 10.1086/321526

Paxton, B., Bildsten, L., Dotter, A., et al. 2011, *Astrophys. J. Suppl.*, 192, 3, doi: 10.1088/0067-0049/192/1/3

Paxton, B., Cantiello, M., Arras, P., et al. 2013, *Astrophys. J. Suppl.*, 208, 4, doi: 10.1088/0067-0049/208/1/4

Paxton, B., Marchant, P., Schwab, J., et al. 2015, *Astrophys. J. Suppl.*, 220, 15, doi: 10.1088/0067-0049/220/1/15

Paxton, B., Schwab, J., Bauer, E. B., et al. 2018, *Astrophys. J. Suppl.*, 234, 34, doi: 10.3847/1538-4365/aaa5a8

Paxton, B., Smolec, R., Schwab, J., et al. 2019, *Astrophys. J. Suppl.*, 243, 10, doi: 10.3847/1538-4365/ab2241

Pejcha, O., & Prieto, J. L. 2015, *Astrophys. J.*, 799, 215, doi: 10.1088/0004-637X/799/2/215

Perley, D., Barbarino, C., Sollerman, J., et al. 2020, Transient Name Server Classification Report, 2020-1259, 1

Perley, D., & Gal-Yam, A. 2023, Transient Name Server Classification Report, 2023-1164, 1

Perley, D. A., & Irani, I. 2023, Transient Name Server AstroNote, 120, 1

Perna, R., Duffell, P., Cantiello, M., & MacFadyen, A. I. 2014, *Astrophys. J.*, 781, 119, doi: 10.1088/0004-637X/781/2/119

Pettini, M., & Pagel, B. E. J. 2004, *Mon. Not. Roy. Astron. Soc.*, 348, L59, doi: 10.1111/j.1365-2966.2004.07591.x

Pledger, J. L., & Shara, M. M. 2023, arXiv e-prints, arXiv:2305.14447, doi: 10.48550/arXiv.2305.14447

Poole, T. S., Breeveld, A. A., Page, M. J., et al. 2008, *Mon. Not. Roy. Astron. Soc.*, 383, 627, doi: 10.1111/j.1365-2966.2007.12563.x

Pooley, D., Lewin, W. H. G., Fox, D. W., et al. 2002, *Astrophys. J.*, 572, 932, doi: 10.1086/340346

Popov, D. V. 1993, *Astrophys. J.*, 414, 712, doi: 10.1086/173117

Postma, J. E., & Leahy, D. 2017, *Pub. Astron. Soc. Pac.*, 129, 115002, doi: 10.1088/1538-3873/aa8800

—. 2021, Journal of Astrophysics and Astronomy, 42, 30, doi: 10.1007/s12036-020-09689-w

Poznanski, D., Prochaska, J. X., & Bloom, J. S. 2012, *Mon. Not. Roy. Astron. Soc.*, 426, 1465, doi: 10.1111/j.1365-2966.2012.21796.x

Pumo, M. L., Zampieri, L., Spiro, S., et al. 2017, *Mon. Not. Roy. Astron. Soc.*, 464, 3013, doi: 10.1093/mnras/stw2625

Pun, C. S. J., Kirshner, R. P., Sonneborn, G., et al. 1995, *Astrophys. J. Suppl.*, 99, 223, doi: 10.1086/192185

Qin, Y.-J., Zhang, K., Bloom, J., et al. 2023, arXiv e-prints, arXiv:2309.10022, doi: 10.48550/arXiv.2309.10022

Quimby, R. M., Wheeler, J. C., Hoflich, P., et al. 2007, The Astrophysical Journal, 666, 1093, doi: 10.1086/520532

Quimby, R. M., Wheeler, J. C., Höflich, P., et al. 2007, *Astrophys. J.*, 666, 1093, doi: 10.1086/520532

Rho, J., Geballe, T. R., Banerjee, D. P. K., et al. 2018, *Astrophys. J. Lett.*, 864, L20, doi: 10.3847/2041-8213/aad77f

Riess, A. G., Yuan, W., Macri, L. M., et al. 2022, *Astrophys. J. Lett.*, 934, L7, doi: 10.3847/2041-8213/ac5c5b

Rodrigo, C., & Solano, E. 2020, in XIV.0 Scientific Meeting (virtual) of the Spanish Astronomical Society, 182

Rodríguez, Ó. 2022, *Mon. Not. Roy. Astron. Soc.*, 515, 897, doi: 10.1093/mnras/stac1831

Rodríguez, Ó., Clocchiatti, A., & Hamuy, M. 2014, *Astron. J.*, 148, 107, doi: 10.1088/0004-6256/148/6/107

Rodríguez, Ó., Pignata, G., Anderson, J. P., et al. 2020, *Mon. Not. Roy. Astron. Soc.*, 494, 5882, doi: 10.1093/mnras/staa1133

Roming, P. W. A., Kennedy, T. E., Mason, K. O., et al. 2005, Space Science Reviews, 120, 95, doi: 10.1007/s11214-005-5095-4

Roy, R., Kumar, B., Moskvitin, A. S., et al. 2011, *Mon. Not. Roy. Astron. Soc.*, 414, 167, doi: 10.1111/j.1365-2966.2011.18363.x

Sagar, R., Kumar, B., & Omar, A. 2019, Current Science, 117, 365. https://arxiv.org/abs/1905.12896

Sahu, D. K., Anupama, G. C., & Chakradhari, N. K. 2013, *Mon. Not. Roy. Astron. Soc.*, 433, 2, doi: 10.1093/mnras/stt647

Sahu, D. K., Anupama, G. C., Srividya, S., & Muneer, S. 2006, *Mon. Not. Roy. Astron. Soc.*, 372, 1315, doi: 10.1111/j.1365-2966.2006.10937.x

Sánchez-Sáez, P., Reyes, I., Valenzuela, C., et al. 2021, *Astron. J.*, 161, 141, doi: 10.3847/1538-3881/abd5c1

Schlafly, E. F., & Finkbeiner, D. P. 2011, *Astrophys. J.*, 737, 103, doi: 10.1088/0004-637X/737/2/103

Schmidt, B. P., Kirshner, R. P., & Eastman, R. G. 1992, *Astrophys. J.*, 395, 366, doi: 10.1086/171659

Schneider, S. E., Thuan, T. X., Mangum, J. G., & Miller, J. 1992, *Astrophys. J. Suppl.*, 81, 5, doi: 10.1086/191684

Sim, S. A. 2017, in Handbook of Supernovae, ed. A. W. Alsabti & P. Murdin (Springer International Publishing AG 2017), 769, doi: 10.1007/978-3-319-21846-5_28

Singh, A. 2021, RedPipe: Reduction Pipeline. http://ascl.net/2106.024

Singh, A., Kumar, B., Moriya, T. J., et al. 2019a, *Astrophys. J.*, 882, 68, doi: 10.3847/1538-4357/ab3050

Singh, A., Srivastav, S., Kumar, B., Anupama, G. C., & Sahu, D. K. 2018, *Mon. Not. Roy. Astron. Soc.*, 480, 2475, doi: 10.1093/mnras/sty1957

Singh, A., Sahu, D. K., Anupama, G. C., et al. 2019b, *Astrophys. J. Lett.*, 882, L15, doi: 10.3847/2041-8213/ab3d44

Singh, A., Teja, R. S., Moriya, T. J., et al. 2024, arXiv e-prints, arXiv:2405.20989, doi: 10.48550/arXiv.2405.20989

Singh, D., Visweswaran, G., Kagy, C., et al. 2023, The Astronomer's Telegram, 16054, 1

Skrutskie, M. F., Cutri, R. M., Stiening, R., et al. 2006, *Astron. J.*, 131, 1163, doi: 10.1086/498708

Smartt, S. J. 2009, *Ann. Rev. Astron. Astrophys.*, 47, 63, doi: 10.1146/annurev-astro-082708-101737

—. 2015, *Publications of the Astronomical Society of Australia*, 32, e016, doi: 10.1017/pasa.2015.17

Smartt, S. J., Eldridge, J. J., Crockett, R. M., & Maund, J. R. 2009, *Mon. Not. Roy. Astron. Soc.*, 395, 1409, doi: 10.1111/j.1365-2966.2009.14506.x

Smith, N. 2014, *Ann. Rev. Astron. Astrophys.*, 52, 487, doi: 10.1146/annurev-astro-081913-040025

—. 2017, in Handbook of Supernovae, ed. A. W. Alsabti & P. Murdin, 403, doi: 10.1007/978-3-319-21846-5_38

Smith, N., Pearson, J., Sand, D. J., et al. 2023, arXiv e-prints, arXiv:2306.07964, doi: 10.48550/arXiv.2306.07964

Smithsonian Astrophysical Observatory. 2000, SAOImage DS9: A utility for displaying astronomical images in the X11 window environment, Astrophysics Source Code Library, record ascl:0003.002

Soker, N. 2022, arXiv e-prints, arXiv:2205.09560. https://arxiv.org/abs/2205.09560

Sollerman, J., Yang, S., Schulze, S., et al. 2021, *Astron. Astrophys.*, 655, A105, doi: 10.1051/0004-6361/202141374

Soraisam, M. D., Szalai, T., Van Dyk, S. D., et al. 2023, arXiv e-prints, arXiv:2306.10783, doi: 10.48550/arXiv.2306.10783

Sparks, W. B. 1994, *Astrophys. J.*, 433, 19, doi: 10.1086/174621

Spiro, S., Pastorello, A., Pumo, M. L., et al. 2014, *Mon. Not. Roy. Astron. Soc.*, 439, 2873, doi: 10.1093/mnras/stu156

Srinivasaragavan, G. P., Sfaradi, I., Jencson, J., et al. 2021, arXiv e-prints, arXiv:2109.02159. https://arxiv.org/abs/2109.02159

Stalin, C. S., Hegde, M., Sahu, D. K., et al. 2008, Bulletin of the Astronomical Society of India, 36, 111. https://arxiv.org/abs/0809.1745

Steer, I. 2020, The Astronomical Journal, 160, 199, doi: 10.3847/1538-3881/abafba

Stephenson, F. R., & Green, D. A. 2005, in Astronomical Society of the Pacific Conference Series, Vol. 342, 1604-2004: Supernovae as Cosmological Lighthouses, ed. M. Turatto, S. Benetti, L. Zampieri, & W. Shea, 63–70

Stetson, P. B. 1987, *Pub. Astron. Soc. Pac.*, 99, 191, doi: 10.1086/131977

Stritzinger, M., Valerin, G., Elias-Rosa, N., et al. 2023, Transient Name Server AstroNote, 145, 1

Sukhbold, T., Ertl, T., Woosley, S. E., Brown, J. M., & Janka, H. T. 2016, *Astrophys. J.*, 821, 38, doi: 10.3847/0004-637X/821/1/38

Szalai, T., Vinkó, J., Könyves-Tóth, R., et al. 2019, *Astrophys. J.*, 876, 19, doi: 10.3847/1538-4357/ab12d0

Taddia, F., Stritzinger, M. D., Sollerman, J., et al. 2012, *Astron. Astrophys.*, 537, A140, doi: 10.1051/0004-6361/201118091

Takáts, K., & Vinkó, J. 2012, *Mon. Not. Roy. Astron. Soc.*, 419, 2783, doi: 10.1111/j.1365-2966.2011.19921.x

Takáts, K., Pignata, G., Pumo, M. L., et al. 2015, *Mon. Not. Roy. Astron. Soc.*, 450, 3137, doi: 10.1093/mnras/stv857

Tandon, S. N., Subramaniam, A., Girish, V., et al. 2017, *Astron. J.*, 154, 128, doi: 10.3847/1538-3881/aa8451

Tandon, S. N., Postma, J., Joseph, P., et al. 2020, *Astron. J.*, 159, 158, doi: 10.3847/1538-3881/ab72a3

Tartaglia, L., Sand, D. J., Groh, J. H., et al. 2021, *Astrophys. J.*, 907, 52, doi: 10.3847/1538-4357/abca8a

Teja, R. S., Goldberg, J. A., Sahu, D. K., et al. 2024, arXiv e-prints, arXiv:2407.13207. https://arxiv.org/abs/2407.13207

Teja, R. S., Singh, A., Sahu, D. K., et al. 2022, *Astrophys. J.*, 930, 34, doi: 10.3847/1538-4357/ac610b

—. 2023a, *Astrophys. J.*, 954, 155, doi: 10.3847/1538-4357/acdf5e

Teja, R. S., Singh, A., Basu, J., et al. 2023b, *Astrophys. J. Lett.*, 954, L12, doi: 10.3847/2041-8213/acef20

Terreran, G., Jerkstrand, A., Benetti, S., et al. 2016, *Mon. Not. Roy. Astron. Soc.*, 462, 137, doi: 10.1093/mnras/stw1591

Terreran, G., Jacobson-Galán, W. V., Groh, J. H., et al. 2022, *Astrophys. J.*, 926, 20, doi: 10.3847/1538-4357/ac3820

Thomas, R. C., Nugent, P. E., & Meza, J. C. 2011, *Pub. Astron. Soc. Pac.*, 123, 237, doi: 10.1086/658673

Tikhonov, N. A., Lebedev, V. S., & Galazutdinova, O. A. 2015, Astronomy Letters, 41, 239, doi: 10.1134/S1063773715060080

Tody, D. 1993, in Astronomical Society of the Pacific Conference Series, Vol. 52, Astronomical Data Analysis Software and Systems II, ed. R. J. Hanisch, R. J. V. Brissenden, & J. Barnes, 173

Tomasella, L., Cappellaro, E., Pumo, M. L., et al. 2018, *Mon. Not. Roy. Astron. Soc.*, 475, 1937, doi: 10.1093/mnras/stx3220

Tonry, J. L., Denneau, L., Flewelling, H., et al. 2018a, *Astrophys. J.*, 867, 105, doi: 10.3847/1538-4357/aae386

Tonry, J. L., Denneau, L., Heinze, A. N., et al. 2018b, *Pub. Astron. Soc. Pac.*, 130, 064505, doi: 10.1088/1538-3873/aabadf

Tsvetkov, D. Y., Shugarov, S. Y., Volkov, I. M., et al. 2018, Astronomy Letters, 44, 315, doi: 10.1134/S1063773718050043

Turatto, M., Mazzali, P. A., Young, T. R., et al. 1998, *Astrophys. J. Lett.*, 498, L129, doi: 10.1086/311324

Tutui, Y., & Sofue, Y. 1997, *Astron. Astrophys.*, 326, 915, doi: 10.48550/arXiv.astro-ph/9706280

Utrobin, V. P., & Chugai, N. N. 2024a, *Mon. Not. Roy. Astron. Soc.*, 527, 6227, doi: 10.1093/mnras/stad3633

—. 2024b, *Astrophys. Space Sci.*, 369, 49, doi: 10.1007/s10509-024-04311-9

Valenti, S., Elias-Rosa, N., Taubenberger, S., et al. 2008, *Astrophys. J. Lett.*, 673, L155, doi: 10.1086/527672

Valenti, S., Sand, D., Pastorello, A., et al. 2014, *Mon. Not. Roy. Astron. Soc.*, 438, L101, doi: 10.1093/mnrasl/slt171

Valenti, S., Sand, D., Stritzinger, M., et al. 2015, Monthly Notices of the Royal Astronomical Society, 448, 2608, doi: 10.1093/mnras/stv208

Valenti, S., Sand, D., Stritzinger, M., et al. 2015, *Mon. Not. Roy. Astron. Soc.*, 448, 2608, doi: 10.1093/mnras/stv208

Valenti, S., Howell, D. A., Stritzinger, M. D., et al. 2016, *Mon. Not. Roy. Astron. Soc.*, 459, 3939, doi: 10.1093/mnras/stw870

Valerin, G., Pumo, M. L., Pastorello, A., et al. 2022, *Mon. Not. Roy. Astron. Soc.*, 513, 4983, doi: 10.1093/mnras/stac1182

Van Dyk, S. D. 2017, Philosophical Transactions of the Royal Society of London Series A, 375, 20160277, doi: 10.1098/rsta.2016.0277

Van Dyk, S. D., Li, W. D., & Filippenko, A. V. 2002, in American Astronomical Society Meeting Abstracts, Vol. 201, American Astronomical Society Meeting Abstracts, 99.01

Van Dyk, S. D., Zheng, W., Maund, J. R., et al. 2019, *Astrophys. J.*, 875, 136, doi: 10.3847/1538-4357/ab1136

Van Dyk, S. D., Srinivasan, S., Andrews, J. E., et al. 2023, arXiv e-prints, arXiv:2308.14844, doi: 10.48550/arXiv.2308.14844

Vannini, & Julio. 2023a, Transient Name Server AstroNote, 156, 1

—. 2023b, Transient Name Server AstroNote, 161, 1

Vannini, J. 2023, Transient Name Server AstroNote, 141, 1

Vasylyev, S. S., Filippenko, A. V., Vogl, C., et al. 2022, *Astrophys. J.*, 934, 134, doi: 10.3847/1538-4357/ac7220

Vasylyev, S. S., Vogl, C., Yang, Y., et al. 2023, arXiv e-prints, arXiv:2304.06147, doi: 10.48550/arXiv.2304.06147

Vink, J. S., de Koter, A., & Lamers, H. J. G. L. M. 2001, *Astron. Astrophys.*, 369, 574, doi: 10.1051/0004-6361:20010127

Virtanen, P., Gommers, R., Oliphant, T. E., et al. 2020, Nature Methods, 17, 261, doi: 10.1038/s41592-019-0686-2

Vogl, C., Sim, S. A., Noebauer, U. M., Kerzendorf, W. E., & Hillebrandt, W. 2019, *Astron. Astrophys.*, 621, A29, doi: 10.1051/0004-6361/201833701

Waskom, M. L. 2021, Journal of Open Source Software, 6, 3021, doi: 10.21105/joss.03021

Waxman, E., Meszaros, P., & Campana, S. 2007, The Astrophysical Journal, 667, 351, doi: 10.1086/520715

Weiler, K. W., Sramek, R. A., Panagia, N., van der Hulst, J. M., & Salvati, M. 1986, *Astrophys. J.*, 301, 790, doi: 10.1086/163944

Wes McKinney. 2010, in Proceedings of the 9th Python in Science Conference, ed. Stéfan van der Walt & Jarrod Millman, 56 – 61, doi: 10.25080/Majora-92bf1922-00a

Wiggins, P. 2018, Transient Name Server Discovery Report, 2018-53, 1

Williams, R. E. 1967, *Astrophys. J.*, 147, 556, doi: 10.1086/149035

Woosley, S. E., Heger, A., & Weaver, T. A. 2002, Reviews of Modern Physics, 74, 1015, doi: 10.1103/RevModPhys.74.1015

Yamanaka, M., Fujii, M., & Nagayama, T. 2023, arXiv e-prints, arXiv:2306.00263, doi: 10.48550/arXiv.2306.00263

Yaron, O., & Gal-Yam, A. 2012, *Pub. Astron. Soc. Pac.*, 124, 668, doi: 10.1086/666656

Young, D. R. 2020, plot_atlas_fp.py, doi: 10.5281/zenodo.10978968

Yuan, F., Jerkstrand, A., Valenti, S., et al. 2016, *Mon. Not. Roy. Astron. Soc.*, 461, 2003, doi: 10.1093/mnras/stw1419

Zacharias, N., Finch, C. T., Girard, T. M., et al. 2013, *Astron. J.*, 145, 44, doi: 10.1088/0004-6256/145/2/44

Zampieri, L. 2017, in Handbook of Supernovae, ed. A. W. Alsabti & P. Murdin (Springer), 737, doi: 10.1007/978-3-319-21846-5_26

Zampieri, L., Pastorello, A., Turatto, M., et al. 2003, *Mon. Not. Roy. Astron. Soc.*, 338, 711, doi: 10.1046/j.1365-8711.2003.06082.x

Zhang, J., Wang, X., József, V., et al. 2020, *Mon. Not. Roy. Astron. Soc.*, 498, 84, doi: 10.1093/mnras/staa2273

Zhang, K., Kennedy, D., Oostermeyer, B., Bloom, J., & Perley, D. A. 2023, Transient Name Server AstroNote, 125, 1

Zhang, T., Wang, X., Li, W., et al. 2006, *Astron. J.*, 131, 2245, doi: 10.1086/500972

Zhang, X., Wang, X., Sai, H., et al. 2022, *Mon. Not. Roy. Astron. Soc.*, 509, 2013, doi: 10.1093/mnras/stab3007

Zimmerman, E. A., Irani, I., Chen, P., et al. 2023, arXiv e-prints, arXiv:2310.10727, doi: 10.48550/arXiv.2310.10727